Hadronic correlators at high temperature:

Spectral and transport properties

Dissertation

Florian Meyer

Fakultät für Physik
Universität Bielefeld

Februar 2016

Erster Gutachter: Prof. Dr. Edwin Laermann
Zweiter Gutachter: Dr. Olaf Kaczmarek

Gedruckt auf alterungsbeständigem Papier nach DIN-ISO 9706

Abstract

In the present thesis we approach the questions of deconfinement properties as well as transport properties of mesons in the Quark Gluon Plasma close to the transition temperature in the framework of Lattice QCD. Expectations for the underlying mesonic spectral functions are substantiated by combining non-interacting spectral functions and phenomenological results. Especially, non-interacting meson spectral functions are presented, in the continuum and on the lattice for degenerate quark masses, and the computations extended to the case of non-degenerate quark masses. With these expectations at hand, we extract spectral information from meson correlator data obtained in numerical computations of Lattice QCD, both in the quenched approximation and with $2 + 1$ dynamical flavors.

In the light quark sector quenched correlation function data at three temperatures $T = 1.1T_c, 1.2T_c$ and $1.4T_c$, with three increasingly finer lattices per temperature, are extrapolated to the continuum. At finite cutoff, large lattices with clover-improved Wilson valence fermions were used, which permits stable continuum extrapolations in a^2. The electrical conductivity, the dilepton rate and the soft photon rate are computed by extracting the underlying spectral function from the extrapolated correlation function data via a phenomenologically motivated fit Ansatz. Systematic uncertainties of the Ansatz and the fit procedure are investigated and discussed, notably by using additional perturbative input of the spectral function shape, and with a glance at possible quasiparticle and hydrodynamical descriptions, respectively. As an additional exploratory study we also utilize the method of Backus and Gilbert as a model independent approach to the reconstruction of spectral functions from correlator data at the lowest temperature $T = 1.1T_c$. The results are compared to the results from the fit procedure. Additionally, the Backus Gilbert method yields an estimate for the resolution of the procedure, given the statistical uncertainty of the correlation function data, which is compared to the results obtained by the systematic checks conducted in the fit procedure.

In the heavy quark sector deconfinement properties are analyzed by performing a $2+1$ dynamical flavor study on $64^3 \times 64$ and $64^3 \times 16$ lattices at two values of the coupling, using a HISQ sea quark action and a Standard Wilson valence quark action, extracting meson correlation functions of strange ($s\bar{s}$), strange-charmed ($s\bar{c}$) and charm ($c\bar{c}$) quark content. Comparing temporal as well as screening correlation functions around the transition region with corresponding vacuum correlation functions, in conjunction with phenomenological expectations, facilitates statements about the shapes of the corresponding spectral functions, and thus the properties of the investigated mesons with respect to the chiral/deconfinement transition. Screening masses are extracted, and the results are compared to a pure HISQ computation on slightly smaller lattices, especially with respect to cutoff effects and possible systematic effects due to the mixing of different actions.

Contents

1 Introduction

The Standard Model (SM) of particle physics, as we know it today, describes the smallest constituents of matter, their ways of interacting in conjunction with their corresponding force carriers, and the particles that arise from these interactions and are held together by these forces. As such, the four known forces in nature are the gravitational force, the electromagnetic force, the weak force and the strong force. Except for the first one, all of these are successfully set up as quantum field theories, namely Quantum Chromo Dynamics (QCD) and the unification of weak and electrodynamical interaction, the Glashow-Salam-Weinberg model. They are *gauge theories*, and therefore share a fundamental symmetry, the invariance under global gauge transformations acting on the theory's respective fields. Demanding this symmetry to hold locally, i.e. for each point in space time separately, provides a compelling mechanism to generate the fundamental interactions that can occur between these particles. This is the reason why,

Generation	Particles				
	Fermions				Bosons
	Quarks		Leptons		Mediators
1^{st}	u	d	e	ν_e	γ
2^{nd}	c	s	μ	ν_μ	$W^{+/-}, Z$
3^{rd}	t	b	τ	ν_τ	g

Table 1.1: Elementary particles in the Standard Model. Note that the quarks have fractional electromagnetic charge, with the left column having $e = 2/3$ and the right column $e = -1/3$.

albeit being called a 'model', the SM constitutes our most fundamental knowledge of nature, and computations and arguments based on this model are usually referred to as 'from first principles'. In general, it turns out that all force carrying particles are spin-1 *bosons*, thus obeying the Bose statistics, while the rest of the elementary particles are fermions, featuring a half integer spin and obeying the Fermi statistics. To sum up the elementary particle content of the SM, shown in Tab. 1.1, the forces of the electroweak interactions are mediated by the massless photon (the force carrier of the electromagnetic part of that theory), one massive and uncharged boson, the Z_0, and two charged and massive bosons W_+ and W_-. In fact, the latter are extremely heavy, $m_Z \approx 90.1\text{GeV}$ and $m_W \approx 80.4\text{GeV}$ [1]. Massive gauge bosons are only possible due to the presence of an additional particle, the Higgs boson, which was found in 2012 at LHC after a long search [2, 3]. The strong force is carried by eight massless *gluons*. The fermionic section of the SM is subdivided into *leptons* and *quarks*. The former class contains electrons,

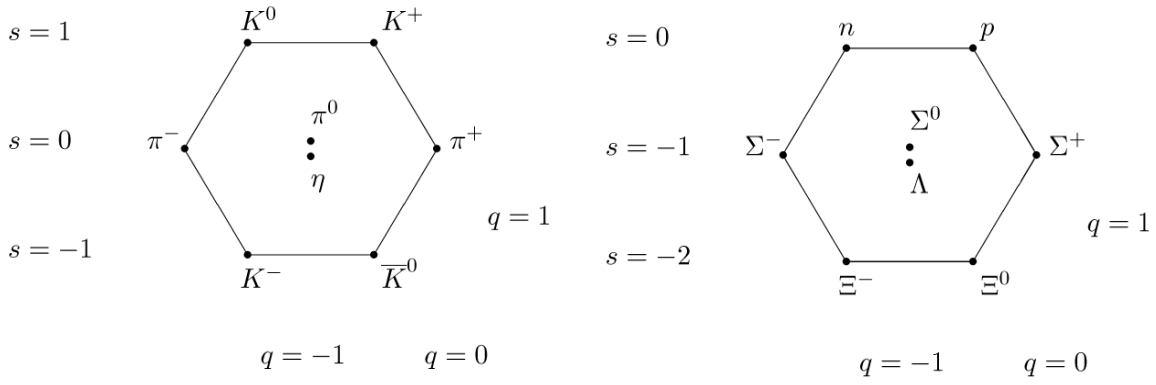

Figure 1.1: The meson (*left*) and baryon (*right*) octets according to the eightfold way. Pictures taken from [4].

muons and taus, together with their corresponding neutrinos. Analogously, there are three families of quarks, with two flavors per family, which are, ordered by increasing mass, the up and down, the strange and charm and the bottom and top quarks. While the up and down quarks are very light, $m_u \approx 2.3\text{MeV}$ and $m_d \approx 4.8\text{MeV}$, the strange quark has an intermediate mass of $m_s \approx 95\text{MeV}$. The c, b and t quark come with much higher masses of $m_c \approx 1,275\text{GeV}$, $m_b \gtrsim 4\text{GeV}$ and $m_t \gtrsim 160\text{GeV}$ [1].

The strong force binds the *hadrons*, which in turn can be subdivided into *mesons* as a (bosonic) bound state of quark and antiquark ($q\bar{q}$), and *baryons*, which are fermionic bound states of three quarks. A remarkably simple way to classify these quark bound states was found in 1964 by Gell-Mann and Ne'eman independently, called the eightfold way [5]. It categorizes composite particles by their quark content, especially strangeness (the abundance of a strange quark) and electric charge, see for example the *meson octet* and the *baryon octet* in Fig. 1.1. Such patterns are manifestations of the underlying flavor $SU(N_f)$ symmetry of a theory with N_f quark flavors, which would be perfectly realized only if the quarks were all mass-degenerate. However, even in this case a part of the flavor symmetry, the *chiral symmetry*, is spontaneously broken by the QCD dynamics, and with the masses of the light quarks in nature being comparatively small, at least the pions may be viewed as the occurring *Goldstone* bosons, which goes along with their relatively small masses of $m_\pi \approx 135 - 140\text{MeV}$ [6, 7]. The quarks are characterized, in addition to their fractional electrical charge, by a quantum number called *color*, without which baryon states, like the proton or the neutron, would be forbidden by the Pauli exclusion principle. The underlying symmetry is the defining $SU(N_c)$ gauge symmetry of the theory, which, with $N_c = 3$ color degrees of freedom termed red, green and blue, leads to a total of eight two-colored gluon states mediating between the quarks. It turns out that color is not a directly observable quantum number, unlike the electric charge, and indeed the meson ($q\bar{q}$) and baryon qqq structures are allowed because they are color neutral.

This phenomenon is known as *confinement*, and so far not rigorously proven. However, it can be qualitatively understood by noting that the gluons, themselves carrying color charge, can interact with each other, which is a consequence of the non-Abelian nature of the gauge group $SU(3)$. The electric field, mediated by the (not electrically charged) photon spreads out in space when emitted from an electric charge, but the gluon field between two (color charged) quarks can be pictured to form a narrow *flux tube*, with its energy content increasing as the distance between the two quarks increases. Because it is thus not possible to separate two color charges by an infinite amount, confinement can be seen as a long range feature of the theory. The space-time discretized formulation of the above gauge theory, Lattice Gauge Theory, can determine this long range behavior of a quark-antiquark pair, but in that case the connection to the continuous physics of nature is far from trivial [6, 8, 9]. At short ranges, on the other hand, QCD shows the remarkable feature of *asymptotic freedom*, which states that the force loses its attribute of being 'strong' at short distances, or, equivalently, large energy scales. This implies that the coupling constant really is a function of the energy scale involved in the process under consideration, a fact that can be observed in Deep Inelastic Scattering (DIS) experiments [10, 11].

The above considerations are very idealistic in the sense that they describe QCD in the vacuum, which is completely empty apart from quantum fluctuations. It is a complicated theory, far from being completely understood, and thus a research field in its own right. In addition, there are phenomena that can be investigated only when understanding QCD in a more thermodynamical context, i.e. not only considering single, fundamental processes, but also systems of many particles at finite temperature and particle densities. As such, it turns out that theoretically there is a rich phase structure as a function of temperature and density, with phase transition lines separating these different phases. A phase that has long been speculated about is the Quark Gluon Plasma, a state of matter that would be realized at extremely high temperatures of $T \gtrsim 150\text{MeV}$, roughly $150,000$ times the temperature of the sun's core [12], and vanishing net baryon density. In contrast to the 'hadronic phase' laid out above, it features liberated quark degrees of freedom inside the hot spatial volume, which are not confined to hadrons. Such a state is expected to have existed in the early universe [13], and has been discovered to occur in collision experiments colliding heavy nuclei [14]. The properties of the transition between the two phases are hence under intense research, with respect to the details of the deconfinement mechanism that takes place, as well as the restoration of chiral symmetry.

A complete description of the Quark Gluon Plasma calls not only for the determination of its equilibrium properties, but also of its transport properties, which parameterize the relaxation into equilibrium. Of special interest in the current work are the *transport coefficients*, specifically the electrical conductivity, of the Quark Gluon Plasma, as well as the fate of mesons in the plasma, thus addressing the question of existence and stability of particles inside the hot medium. Transport coefficients are fundamental properties of the medium, and allow for a more detailed view on the nature of interactions that

take place. For example, a low shear viscosity and electrical conductivity generally hint at the medium being a strongly coupled plasma, which behaves more like an ideal liquid. Especially the observation of large elliptic flow, i.e. the reaction of the Quark Gluon Plasma to pressure anisotropies created by nuclei colliding non-centrally, in conjunction with the success of its description by hydrodynamics, gives rise to a small shear viscosity to entropy ratio η/s [15, 16]. The fate of mesons in the plasma is of great interest, because the absence of states that otherwise exist in the hadronic medium signals the onset of deconfinement and chiral transition, and can, for example, serve as temperature probes in the experiment [17, 18, 19].

Both transport properties and the existence or absence of particles in the plasma are linked to *spectral functions*, which encode the spectrum of the theory with respect to given quantum numbers. They are thus central quantities to obtain, and there are different approaches to extract them from QCD [12, 20, 21]. In the current work, we extract spectral functions from numerical Lattice QCD data, which constitutes a non-perturbative and mathematically rigorous approach to QCD, to help alleviating the addressed questions.

2 Quantum Chromo Dynamics on the lattice

2.1 Fundamentals of QCD

The following is a short outline of QCD in a continuous space time. It quickly introduces the necessary concepts and quantities to be able to introduce the discretized formulation of QCD in the next section. Great sources that include the following, and everything that is missing, are introductory standard textbooks [6, 8, 11].

The fundamental Lagrangian of QCD at vanishing temperature and density in a Minkowski space time is given, with all indices and sums explicitly written, by

$$\begin{aligned}\mathcal{L}_{\mathrm{QCD}} = &\sum_{f=1}^{N_f}\sum_{a=b=1}^{N_c}\sum_{\alpha=\beta=1}^{4}\bar{\psi}^f_{a\alpha}(x)\left(i\not{D}^{\alpha\beta}_{ab} - m_f\delta_{\alpha\beta}\delta_{ab}\right)\psi^f_{b\beta}(x)\\ &-\frac{1}{4}\sum_{a=1}^{N_c^2-1}F^a_{\mu\nu}(x)F^{\mu\nu}_a(x).\end{aligned} \tag{2.1}$$

To shorten the notation, we switch to Einstein convention, thus summing over pairs of equally named indices and dropping the summation symbols. The first term constitutes the fermionic part of the action, with the coupling to gauge fields realized by the covariant derivative

$$\not{D}^{\alpha\beta}_{ab} = \gamma^\mu_{\alpha\beta}D_{\mu,ab} = \gamma^\mu_{\alpha\beta}\left(\partial_\mu\delta_{ab} - ig\frac{\lambda^c_{ab}}{2}A^c_\mu(x)\right), \tag{2.2}$$

with the bare gauge coupling g and the Dirac matrices fulfilling the anticommutation relation in Minkowski time through the flat metric $g_{\mu\nu} = \mathrm{diag}(1,-1,-1,-1)$

$$\{\gamma_\mu,\gamma_\nu\} \equiv \gamma_\mu\gamma_\nu + \gamma_\nu\gamma_\mu = g_{\mu\nu}. \tag{2.3}$$

In the covariant derivative, the gauge field $A_\mu(x) \equiv \frac{\lambda^a}{2}A^a_\mu(x)$ consists of the $SU(N_c)$ generators λ^a, which are elements of the algebra $su(3)$ and define the group via their commutation relations

$$\left[\lambda^a,\lambda^b\right] \equiv \lambda^a\lambda^b - \lambda^b\lambda^a = if^{abc}\lambda^c \tag{2.4}$$

and their structure constants f^{abc}. Thus, the single top index labels the generator, while the two bottom indices label its respective matrix element. Usually, in this work we

adapt three colors, $N_c = 3$. The covariant derivative results from the postulate that the Lagrangian should be invariant with respect to local, i.e. space time dependent, gauge transformations

$$\begin{aligned} &\psi_{a\alpha}(x) \to V_{ab}(x)\psi_{b\alpha}(x), \quad \bar{\psi}_{a\alpha}(x) \to \bar{\psi}_{b,\alpha}(x)V^\dagger_{ba}(x) \\ &A^\mu_{ab}(x) \to V(x)A^\mu_{ab}(x)V^\dagger(x) - \frac{i}{g}\left[\partial_\mu V(x)\right]V^\dagger(x). \end{aligned} \tag{2.5}$$

The gauge dynamics is contained in the second term, with the field strength tensor explicitly reading

$$F^a_{\mu\nu} = \partial_\mu A^a_\nu - \partial_\nu A^a_\mu + g f^{abc} A^b_\mu A^c_\nu. \tag{2.6}$$

To connect to Lattice QCD, we perform a Wick rotation $t \to -i\tau$ to Euclidean time, which affects the above relations. In Euclidean space time, the flat metric is a unit matrix, $g_{\mu\nu} \to \delta_{\mu\nu}$, the Dirac matrices change to the Euclidean Dirac matrices, and the Lagrangian is given by

$$\mathcal{L}^E_{\mathrm{QCD}} = \sum_{f=1}^{N_f} \bar{\psi}^f_{a\alpha}(x)\left(\not{D}^{\alpha\beta}_{ab} + m_f\delta_{\alpha\beta}\delta_{ab}\right)\psi^f_{b,\beta}(x) \tag{2.7}$$

$$+ \frac{1}{4}F^a_{\mu\nu}(x)F^a_{\mu\nu}(x), \tag{2.8}$$

with the covariant derivative now reading

$$\not{D}^E_{ab,\alpha\beta} = \gamma^E_{\mu,\alpha\beta}D^E_\mu = \gamma^E_{\mu,\alpha\beta}\left(\partial_\mu\delta_{ab} - ig\frac{\lambda^c_{ab}}{2}A^c_\mu(x)\right). \tag{2.9}$$

The partition function can be written as a path integral, Boltzmann-weighted with the action S_E. Keeping the temporal and spatial extends of space time finite, and dropping the Euclidean 'E' on the quantities under consideration, we write

$$S = \int_0^\beta \mathrm{d}\tau \int_V \mathrm{d}^3x\mathcal{L} \tag{2.10}$$

and thus have the partition function

$$\mathcal{Z} = \int \prod_\mu \mathcal{D}A_\mu \int \prod_f \mathcal{D}\psi_f\bar{\psi}_f \mathrm{e}^{-\int_0^\beta \mathrm{d}\tau \int_V \mathrm{d}^3x\mathcal{L}}. \tag{2.11}$$

With finite extends β and V in space time, the theory is interpreted as a system at finite temperature $T = 1/\beta$ and a finite volume V. In analogy to statistical mechanics, expectation values of an operator, which in general is a function of gauge and Dirac fields, are defined by

$$\langle\mathcal{O}(A,\psi,\bar{\psi})\rangle = \frac{1}{\mathcal{Z}}\int \prod_\mu \mathcal{D}A_\mu \int \prod_f \mathcal{D}\psi_f\bar{\psi}_f \mathrm{e}^{-S}\mathcal{O}(A,\psi,\bar{\psi}). \tag{2.12}$$

2.2 Lattice QCD building blocks

The considerations of the last section provide the basis to introduce the foundational method utilized in this work to actually compute results in the theory of QCD. We start with the introduction of a suitable discretized gauge action and a naive construct for the fermionic part of the action. Certain pathologies of the latter will have to be cured, leading to the Wilson Dirac action and the formulation of staggered fermions. A discussion on the discretization errors and principal issues regarding the respective action's symmetries is followed by systematic improvements of the former. More detailed treatments of the presented foundations can be found in e.g. [6, 8, 9].

On top of the theory presented above, we introduce a discretization of space time by demanding that the, formerly continuous, four vector x_μ satisfies

$$x_\mu = an_\mu, \qquad n_\mu \in [0, N_\mu - 1] \; \forall \; \mu = 1, 2, 3, 4. \tag{2.13}$$

The space time locations are thus restricted to the points, or sites, n_μ on the lattice, being homogeneously scattered with distance a across the whole four volume $a^4 \Pi_\mu N_\mu$. In practice the three spatial extents are chosen to be equal, $N_1 = N_2 = N_3 \equiv N_\sigma$, and the theory thus is set in a spatial volume of $V = (aN_\sigma)^3$, while the temporal extent, together with the lattice spacing, defines the temperature of the system $T = 1/(aN_\tau)$. As a consequence of discretizing space time, the effect of a Fourier transform on an arbitrary function of x_μ,

$$\begin{aligned} f\left(p_\mu\right) &= \int_{-\infty}^{\infty} \mathrm{d}x_\mu \mathrm{e}^{-ip_\mu x_\mu} f\left(x_\mu\right) \longrightarrow \sum_{n_\mu} \mathrm{e}^{-ip_\mu a n_\mu} f\left(a n_\mu\right) \\ &\Rightarrow f\left(p_\mu + \frac{2\pi}{a}\hat{e}_\nu\right) = \sum_{n_\mu} \mathrm{e}^{-ip_\mu a n_\mu} \mathrm{e}^{2\pi i n_\nu} f\left(a n_\mu\right) = f\left(p_\mu\right), \end{aligned} \tag{2.14}$$

with $\hat{e}_\nu$ being a unit vector in the specific direction ν, constrains the corresponding momenta to the finite *Brillouin Zone*. Effectively, the maximum momentum $p \sim 1/a$ acts as a regulator and renders computations on the lattice UV safe. The same idea 'reversed',

$$f(x_\mu) \stackrel{!}{=} s f(x_\mu + aN_\nu \hat{e}_\nu) = \mathrm{e}^{iap_\nu N_\nu} f(x_\mu), \tag{2.15}$$

where the index ν is arbitrary and not summed over, shows that putting the system in a box of finite volume, yields discretized momenta. By adjusting the parameter s, the corresponding allowed momenta for different boundary conditions are

periodic boundary conditions $(s = +1)$**:** $ap_\nu N_\nu = 2\pi k \Rightarrow p_\nu = \frac{2\pi}{aN_\nu} k$,

antiperiodic boundary conditions $(s = -1)$**:** $ap_\nu N_\nu = (2k+1)\pi \Rightarrow p_\nu = \frac{(2k+1)\pi}{aN_\nu}$.

Note that, as the temporal extent is fixed in a theory with definite temperature, the discretization in temporal Fourier space is manifest, and leads to the *Matsubara frequencies* $\omega_n = 2\pi kT$ for Bosonic fields and $\omega_n = 2\pi(2k+1)T$ for fermionic fields. Another direct consequence of introducing a lattice structure is that the continuous space time symmetry is broken down to the discrete symmetries of a four dimensional cube.

2.2.1 Gauge action

A suitable discrete expression for the continuum gauge action in (2.1) can be given by the standard Wilson action

$$S_G(U) = \frac{2N_c}{g^2} \sum_n \sum_{\mu<\nu} \Re \operatorname{tr} \left(1 - U_{\mu\nu}(n)\right), \tag{2.16}$$

where the *plaquette* is the smallest possible closed loop build by the link variables,

$$\begin{aligned} U_{\mu,\nu}(n) &\equiv U_\mu(n) U_\nu(n+\hat{e}_\mu) U_{-\mu}(n+\hat{e}_\mu+\hat{e}_\nu) U_{-\nu}(n+\hat{e}_\nu) \\ &= U_\mu(n) U_\nu(n+\hat{e}_\mu) U_\mu^\dagger(n+\hat{e}_\nu) U_\nu^\dagger(n). \end{aligned} \tag{2.17}$$

The link itself is given by

$$U_\mu(n) = \mathcal{P} \mathrm{e}^{ig\int_n^{n+a\hat{e}_\mu} \mathrm{d}x_\nu A_\nu(x)} \approx \mathrm{e}^{iagA_\mu(n)}. \tag{2.18}$$

This means that the $su(3)$ algebra valued gauge fields $A_\mu(n)$ are, in the lattice version of the theory, represented by $SU(3)$ matrices, which themselves transform under local gauge transformations,

$$U_\mu(n) \longrightarrow V(n) U_\mu(n) V^\dagger(n+\hat{e}_\mu). \tag{2.19}$$

The action S_G is gauge invariant, because (2.17) constitutes a closed loop of gauge links and their transformation behavior implies that the trace of this object is gauge invariant. Apart from this necessary condition, furthermore the naive limit $a \to 0$ of S_G can be taken by utilizing the Baker-Campbell-Hausdorff formula $\mathrm{e}^A \mathrm{e}^B = \mathrm{e}^{A+B+\frac{1}{2}[A,B]}$ on the plaquette (2.17), using (2.18), and Taylor expanding the fields $A_\mu(n+\hat{e}_\nu) = A_\mu(n) + a\partial_\nu A_\mu(n) + \mathcal{O}\left(a^2\right)$. The result is

$$U_{\mu,\nu}(n) = \mathrm{e}^{iga^2\{\partial_\mu A_\nu(n) - \partial_\nu A_\mu(n) + ig[A_\mu(n), A_\nu(n)]\} + \mathcal{O}\left(a^3\right)}, \tag{2.20}$$

which can be plugged in the above expression for S_G to show

$$S_G(U) \longrightarrow a^4 \sum_n \sum_{\mu,\nu} \operatorname{tr} \left\{F_{\mu\nu}(n) F_{\mu\nu}(n)\right\} + \mathcal{O}\left(a^2\right) + \mathcal{O}\left(g^2 a^2\right). \tag{2.21}$$

This not only demonstrates the recovery of the correct expression, but also eludicates the discretization errors, compared to the correct continuum expression in (2.1), to be of the order a^2, and loop corrections to enter as $\mathcal{O}(g^2)$. Note that the sum relates to the continuous space time integral as

$$a^4 \sum_n \xrightarrow{a\to 0} \int_0^\beta \mathrm{d}\tau \int_V \mathrm{d}^3 x. \tag{2.22}$$

2.2.2 The Wilson fermion action

In order to add fermions to the discretized theory, a gauge invariant expression for the fermionic part in (2.1) has to be found, which of course should as well reduce to the continuum expression in the naive limit. By simply discretizing the derivative of the fermion field, $\partial_\mu \psi(n) \longrightarrow \frac{\psi(n+\hat{e}_\mu)-\psi(n-\hat{e}_\mu)}{2a}$, and introducing link variables to render the construct gauge invariant, the fermionic part in (2.1) naively yields

$$S_F = a^4 \sum_n \sum_f \bar{\psi}^a_{f,\alpha}(n) \left(\gamma_\mu^{\alpha\beta} \frac{U_\mu^{ab}(n)\psi^b_{f,\beta}(n+\hat{e}_\mu) - U_{-\mu}^{ab}\psi^b_{f,\beta}(n-\hat{e}_\mu)}{2a} + \delta_{ab} m \psi^b_{f,\beta}(n) \right). \tag{2.23}$$

Analogous to the standard gauge action above, the continuum action can be retrieved by expanding

$$\begin{aligned} &U_\mu(n) \approx \mathrm{e}^{igaA_\mu(n)} = 1 + igaA_\mu(n) + \mathcal{O}\left(a^2 g^2\right) \\ &\text{and} \quad \psi(n \pm a\hat{e}_\mu) = \psi(n) \pm a\partial_\mu \psi(n)\hat{e}_\mu + \mathcal{O}\left(a^2\right) \end{aligned} \tag{2.24}$$

to yield

$$S_F \longrightarrow a^4 \sum_n \sum_f \bar{\psi}^f_{a\alpha}(n) \left(\not{D}^{\alpha\beta}_{ab} + m_f \delta_{\alpha\beta}\delta_{ab} \right) \psi^f_{b,\beta}(n) + \mathcal{O}\left(a^2\right). \tag{2.25}$$

While this is a very simple and handy expression, it suffers from a fundamental flaw. The inverse of the Dirac matrix $M \equiv \left(\not{D}^{\alpha\beta}_{ab} + m_f \delta_{\alpha\beta}\delta_{ab} \right)$ is the fermion propagator, which in momentum space on the lattice for massless, non-interacting fermions is given by

$$M^{-1}(p) = \frac{-ia^{-1}\sum_\mu \gamma_\mu \sin(ap_\mu)}{a^{-2}\sum_\mu \sin^2(ap_\mu)}. \tag{2.26}$$

With the extend of the Brillouin zone given by $2\pi/a$ as seen above, and the allowed momenta ranging from $-\pi/a$ to π/a symmetrically around zero momentum, we find that this propagator not only has one pole at vanishing momentum, but in fact blows up for any combination of momentum components of 0 or $\pm\pi/a$. These additional, unphysical poles are called *doublers*. In order to cure this problem, Wilson proposed to add another operator to the Dirac matrix, which reads

$$\delta M^{ab}_{SW}(n,m) = -a \sum_\mu \frac{U_\mu^{ab}(n)\delta_{n+\hat{e}_\mu,m} - 2\delta_{ab}\delta_{nm} + U_{-\mu}^{ab}(n)\delta_{n-\hat{e}_\mu,m}}{2a^2} \tag{2.27}$$

and (technically) is a discretized version of the Laplace operator. Note that, on the one hand it vanishes linearly in the continuum limit and thus leads to the continuum action with discretization errors of order $\mathcal{O}(a)$, while on the other hand it lifts the doubler contributions in the edges of the Brillouin zone, by making them very heavy (see the

term without gauge links in the middle of (2.27)). In terms of the momentum space propagator, the full *standard Wilson* version of (2.26) reads

$$M_{SW}^{-1}(p) = \frac{-ia^{-1}\sum_\mu \gamma_\mu \sin(ap_\mu) + 4a^{-2}\sum_\mu \sin^2(ap_\mu/2)}{a^{-2}\sum_\mu \sin^2(ap_\mu) + 4a^{-2}\left[\sum_\mu \sin^2(ap_\mu/2)\right]^2}, \tag{2.28}$$

which explicitly shows how the additional poles are lifted. The fermion mass in lattice units is usually expressed via the so called *hopping parameter*

$$am \equiv \frac{1}{2}\left(\frac{1}{\kappa} - \frac{1}{\kappa_c}\right), \tag{2.29}$$

where κ_c is the critical hopping parameter, i.e. the parameter where the fermions become massless. For the free theory $\kappa_c = 1/8$, while in the interacting theory the value has to be found by tuning the pion to vanishing mass. The standard Wilson Dirac matrix is commonly written in terms of the hopping parameter and rescaled fermion fields, $\psi(n) \to \psi(n)/\sqrt{am+4}$, such that the final expression reads

$$\begin{aligned} M_{SW}^{\alpha\beta,ab}(n,m) &= \delta_{nm}\delta_{\alpha\beta} \\ &\quad - \kappa \sum_\mu \left\{ \left(\delta_{\alpha\beta} - \gamma_\mu^{\alpha\beta}\right) U_\mu^{ab}(n)\delta_{n+\hat{e}_\mu,m} + \left(\delta_{\alpha\beta} + \gamma_\mu^{\alpha\beta}\right) U_{-\mu}^{ab}(n)\delta_{n-\hat{e}_\mu,m} \right\}. \end{aligned} \tag{2.30}$$

The errors of the standard Wilson action are of the order $\mathcal{O}(a)$, which can be improved by the *Symanzik improvement programme*. The general idea is to formally expand the action of the system in a power series of the lattice spacing a. To improve a given order, all (continuum) operators with the corresponding dimension are collected and reduced to a minimal set using symmetries or equations of motion. The remaining set of operators is then discretized and added to the action, that is to be improved [6, 22]. The improvement is then done up to constants multiplying the newly found improving operators. They have to be tuned by a suitable procedure, which depends on the theory under consideration, see e.g. [23].

In the current work we can partly take advantage of the fact that it is relatively simple to improve the standard Wilson action to yield errors of order $\mathcal{O}\left(a^2\right)$ [24]. First, only one operator is needed to improve the action, which is given by

$$\delta S = c_{sw} a^5 \sum_n \sum_{\mu<\nu} \bar{\psi}(n) \frac{1}{2} \sigma_{\mu\nu} \widetilde{F}_{\mu\nu}(n) \psi(n), \tag{2.31}$$

where $\sigma_{\mu\nu} = \left[\gamma_\mu, \gamma_\nu\right]/(2i)$, and the operator $\widetilde{F}_{\mu\nu}(n)$ is given by

$$\begin{aligned} \widetilde{F}_{\mu\nu}(n) &= -\frac{i}{8a^2}\left(Q_{\mu,\nu}(n) - Q_{\nu,\mu}(n)\right), \\ \text{with} \qquad Q_{\mu,\nu}(n) &\equiv U_{\mu,\nu}(n) + U_{\nu,-\mu}(n) + U_{-\mu,-\nu}(n) + U_{-\nu,\mu}(n) \end{aligned} \tag{2.32}$$

and $U_{\mu,\nu}(n)$ being the corresponding plaquette of links (2.17). The four plaquettes of the sum $Q_{\mu,\nu}(n)$ are arranged around the space time point n like the four quadrants in a two dimensional function plot around the zero point, and thus somewhat reminiscent of a four leaf clover. Second, the constant to tune, c_{sw}, also called the *Sheikoleslami–Wohlert coefficient*, has been computed for a theory without dynamical sea quarks in the framework of the *Schroedinger functional*, both perturbatively and non-perturbatively on the lattice [25, 26], with the non-perturbative expression given by

$$c_{sw}(g^2) = \frac{1 - 0.656g^2 - 0.152g^4 - 0.054g^6}{1 - 0.922g^2}. \tag{2.33}$$

Note that the coefficient c_{sw} depends on the bare coupling g^2 of the theory. For completeness, we mention that there exist also non-perturbative computations of the coefficient for two and three flavors of dynamical Wilson quarks, which have the same rational structure, see [27, 28]. The value at tree level is thus, independent of the number of dynamical flavors, given by $c_{sw} = 1$. Perturbation theory on the lattice suffers from bad convergence behavior, which is caused by ultraviolet divergencies of specific diagrams, the *tadpoles* [29, 30]. These can be cured by substituting the link variables $U_\mu(x) \to U_\mu(x)/u_0$, with u_0 the *tadpole factor*. It is not unique, but a definition that utilizes the plaquette and allows to measure u_0 in a numerical computation is $u_0^4 = (\langle U_{\mu\nu}\rangle/N)$. The gauge action can be improved by using this, and the Wilson-clover action can be tadpole improved at tree level by choosing $c_{sw} = 1/u_0^3$ [30].

2.2.3 The staggered formulation

By adding the Wilson term to remove the doublers, note that we explicitly broke chiral symmetry in the action, because the additional term $\sim \delta_{ab}\delta_{nm}/a$ behaves like a mass term and at finite lattice spacing thus spoils chiral symmetry, as $\{\gamma_5, 1\} \neq 0$. There is a no-go theorem by Nielsen and Ninomiya [31], which states that it is in fact impossible to have both properties, an action that is doubler free and at the same time chirally symmetric, in a lattice discretization. However, note that in the Wilson action the doublers really are completely removed, and the whole chiral symmetry is explicitly broken. A less extreme course would be to accept contributions from doublers to a small extent, but at the same time retain a certain amount of chiral symmetry. This is for example given in the staggered formulation of lattice fermions, which is presented in the following.

Instead of lifting the doublers from the theory, like done in the Wilson approach described above, the idea of the staggered action is to reduce the size of the Brillouin zone so the doublers are simply removed from the momentum domain of the theory. This is possible by starting out with a lattice and placing different *components* of spinors on different lattice sites [6, 8, 32]. Because this mixes space time and Dirac indices, the space time dimension fixes the number of quarks described by such an action to $N_f = 2^{\frac{d}{2}}$,

where d is the space time dimension. Concretely, we introduce a transformation

$$\begin{aligned}\psi(n) &\to \left(\prod_{i=1}^{4}\gamma_i^{n_i}\right)\psi(n) \equiv \Gamma(n)\psi(n)\\ \bar{\psi}(n) &\to \bar{\psi}(n)\left(\prod_{i=4}^{1}\gamma_i^{n_i}\right) \equiv \bar{\psi}\Gamma^{\dagger}(n)\end{aligned} \tag{2.34}$$

on the spinors of the (free) naive action (2.23), leading to

$$\begin{aligned}S = a^4\sum_n \bar{\psi}(n)\left(\sum_{\mu=1}^{4}\eta_\mu(n)\frac{\psi(n+\hat{\mu})-\psi(n-\hat{\mu})}{2a} + m\psi(n)\right)\\ \text{where } \eta_\mu(n) = (-1)^{\sum_{j=0}^{\mu-1} n_j},\quad n_0 \equiv 0.\end{aligned} \tag{2.35}$$

Instead of the γ matrices, the action now features phases η, and thus the whole Lagrangian is diagonal in Dirac space, which implies that 3 of the 4 components can be dropped as well. Introducing gauge fields the interacting staggered action then reads

$$S = a^4\sum_n \bar{\chi}(n)\left(\sum_{\mu=1}^{4}\eta_\mu(n)\frac{U_\mu(n)\chi(n+\hat{\mu}) - U_{-\mu}(n)\chi(n-\hat{\mu})}{2a} + m\chi(n)\right), \tag{2.36}$$

where χ and $\bar{\chi}$ are one-component of ψ and $\bar{\psi}$, respectively. This means that there are now 16 one component fields, that are in turn interpreted as 4 fermionic flavors, each with 4 components. Technically, the degrees of freedom described by this action are now distributed over the sites of a *hypercube* of the original lattice, and the reinterpretation as quark degrees of freedom can be done by constructing linear combinations of χ and $\bar{\chi}$. Assuming an even number of sites in each direction of the lattice, different sites can be addressed via $2h_\mu + s_\mu$, the first four vector labeling the hypercube, the latter one labeling the corners of the corresponding hypercube, hence $s_\mu = 0$ or $s_\mu = 1$. Due to $\gamma_\mu^2 = 1\ \forall\ \mu$, the phases and especially transformation (2.34) are independent of the position of the hypercube,

$$\Gamma(2h+s) = \Gamma(s),\quad \eta(2h+s) = \eta(s). \tag{2.37}$$

One then defines new quark fields via

$$\begin{aligned}q^{\alpha,t}(h) &\equiv \frac{1}{4}\sum_s \Gamma^{\alpha,t}(s)U_s(2h+s)\chi(2h+s)\\ \bar{q}^{\alpha,t}(h) &\equiv \frac{1}{4}\sum_s \bar{\chi}(2h+s)U_s^{\dagger}(2h+s)\left(\Gamma^{\alpha,t}\right)^{\dagger}(s),\end{aligned} \tag{2.38}$$

where α is a Dirac index and t labels four different quark degrees of freedom, called *tastes* in order to distinguish them from usual *flavour*. The staggered action can then be written as [6, 32]

$$S_{\text{staggered}} = b^4\sum_h \bar{q}_a^{\alpha,t}(h)\left\{m\delta_{tt'}\delta_{\alpha\beta}\delta_{ab} + \gamma_\mu^{\alpha\beta}D_\mu^{ab}\delta_{tt'} + \gamma_5^{\alpha\beta}\left(\xi_\mu\xi_5\right)^{tt'}C_\mu^{ab}\right\}q_b^{\beta,t'}(h), \tag{2.39}$$

where $b = 2a$ is the new lattice spacing, and using $V_\mu^{ab}(h, h') = U_\mu^{ac}(h+\hat{e}_\mu)U_\mu^{cb}(h)\delta_{n+2\hat{e}_\mu,h'}$ without summing μ, the operators are given by

$$\begin{aligned} D_\mu^{ab} &= \frac{1}{4}\left(V_\mu^{ab} - \left(V_\mu^{ab}\right)^\dagger\right), \\ C_\mu^{ab} &= \frac{1}{4}\left(V_\mu^{ab} - 2\delta_{ab}\hat{e}_\mu + \left(V_\mu^{ab}\right)^\dagger\right). \end{aligned} \tag{2.40}$$

Hence one has four fermion tastes on each hypercube, being separated from neighboring hypercubes by two lattice spacings. Thus the Brillouin zone is effectively cut in half, and the four tastes do not have doublers themselves.

However, apart from pure discretization errors, this action is also plaqued by mixing of the different tastes, caused by the third term. These effects are drastically reduced in the *Highly Improved Staggered Quark action* (HISQ), which is used in this work to perform computations with dynamical quarks. Details can be looked up in [33]. The action generally has the same structure as (2.39), but is Symanzik improved and features heavily smeared gauge links, which greatly reduce the interaction of the tastes, and leave the action to be free of $\mathcal{O}(a^2)$ errors at tree level. Additionally, a conceptual problem is that there are four tastes when using the action (2.39), and it is principally desirable to be able to work with single fermion flavors. With a glance at Sec. 2.4, which deals with the details of how to conduct a numerical computation in more technical detail, we state here merely that fermions enter the path integral as the determinant of the Dirac matrix, and the power of the determinant determines the fermion content. Thus, a typical measure to get rid of the three other tastes/flavors is to take the fourth root of the fermion determinant. While this *fourth root trick* was and is still today debated [34], continuum extrapolations from lattice studies with different quark discretizations, or comparisons to experimental results, show that the staggered formulation works in principal, and in fact it is often used with small dynamical quark masses and reasonably large lattices for its numerical cheapness, see e.g. [35, 36, 37].

2.3 Extracting physics from Lattice QCD

Computations performed with a lattice regulator are an outstanding tool for the theory of strong interactions. However, the theory, as outlined in the foregoing sections, is not strictly a theory that can make predictions, or can be compared to experimental results. First, the lattice has a finite volume. This is a disadvantage in the sense that, at too small lattice extents, one could face finite volume effects that affect observables under consideration. Especially, from statistical mechanics it is known that e.g. studies of critical phenomena only capture the essential features of the latter in the limit of infinite volume, see e.g. [38, 39]. For this reason the limit of infinite volume is addressed as the *thermodynamic limit*. However, in practice it often suffices to choose the volume in a lattice computation to be large enough. Second, and much more fundamental and intricate, the continuum limit of measured observables has to be performed in order to recover

the physics we are actually interested in. As such, it amounts to the removal of the regulator and thus constitutes the necessary renormalization of the theory, which renders otherwise divergent computations finite. In the derivation of the discretized actions this limit was taken simply by sending the lattice spacing $a \to 0$ in the corresponding analytical expressions. This *naive continuum limit* cannot be performed directly in a numerical computation, as the only input parameters are the bare coupling $g_0^2 = 6/\beta$ in pure gauge theory, and additionally the bare quark masses $am_{u,0}, am_{d,0}, am_{s,0}...$ in a dynamical theory. Note that the bare coupling constant in QCD is massless, as can be verified by counting the powers of terms in the Lagrangian that explicitly contain the coupling. To quantify the relation of observables to the lattice spacing, consider an observable in lattice units that, for simplicity, only depends on the bare coupling g_0,

$$\hat{\mathcal{O}}(g_0) = a^d \mathcal{O}(g_0, a) \qquad \Leftrightarrow \qquad \mathcal{O}(g_0, a) = a^{-d} \hat{\mathcal{O}}(g_0), \tag{2.41}$$

with d the dimension of the observable. By explicitly separating the dimensionful factor, it is clear that in order for the dimensionful observable to be finite in the limit of vanishing lattice spacing,

$$\mathcal{O}(g_0, a) \xrightarrow{a \to 0} \mathcal{O}_{\text{cont}} \quad \text{(finite)}, \tag{2.42}$$

the bare gauge coupling needs to be a function of the lattice spacing, $g_0 = g_0(a)$, and has to be tuned accordingly. Details about the a-dependence of $g_0(a)$ can be inferred by noting that the continuum result is of course independent of a, and close enough to the continuum limit almost a constant, such that for small a we find the *Renormalization Group Equation* (RGE)

$$\begin{aligned} a\frac{\mathrm{d}}{\mathrm{d}a}\mathcal{O}(g_0(a), a) &= \left(a\frac{\partial}{\partial a} + a\frac{\partial g_0}{\partial a}\frac{\partial}{\partial g_0} \right) \mathcal{O}(g_0(a), a) \\ &\equiv \left(a\frac{\partial}{\partial a} - \beta(g_0)\frac{\partial}{\partial g_0} \right) \mathcal{O}(g_0(a), a). \end{aligned} \tag{2.43}$$

The *beta function* $\beta(g_0) = -a\frac{\partial g_0}{\partial a}$ controls the change of $g_0(a)$ with varying lattice spacing and can be computed perturbatively for small a as a power series in g_0, and the result leads to the differential equation

$$\beta(g_0) = -a\frac{\partial g_0}{\partial a} = -\beta_0 g_0^3 - \beta_1 g_0^5 + \mathcal{O}\left(g_0^7\right), \tag{2.44}$$

where the coefficients are given by [9, 40]

$$\begin{aligned} \beta_0 &= \frac{1}{16\pi^2}\left(\frac{11N_c}{3} - \frac{2N_f}{3} \right), \\ \beta_1 &= \left(\frac{1}{16\pi^2} \right)^2 \left(\frac{34N_c^2}{3} - \frac{10N_cN_f}{3} - \frac{(N_c^2-1)N_f}{N_c} \right). \end{aligned} \tag{2.45}$$

The solution to the differential equation is given by

$$a(g_0^2) = \frac{1}{\Lambda} \left(\beta_0 g_0^2\right)^{-\frac{\beta_1}{2\beta_0^2}} \mathrm{e}^{-\frac{1}{2\beta_0 g_0^2}} \left(1 + \mathcal{O}\left(g_0^2\right)\right), \tag{2.46}$$

where Λ is the constant from the integration. It generates a scale for the lattice spacing, which depends on the details of the renormalization like the discretization of the gauge action. This is sometimes termed *dimensional transmutation* [9], and opens the possibility to assign physical units to the results of lattice computations, which can carry over to the continuum limit and thus allow for absolute predictions. Without this property, the only predictive power of Lattice QCD would be reduced to ratios of observables, in which the scales cancel.

From (2.44) we see that the slope of the beta function around $g_0 = 0$ is negative, which means that for small enough lattice spacing, the bare coupling decreases with a, and clearly one possibility is $g_0 \overset{a\to 0}{\longrightarrow} 0$ as the lattice spacing vanishes. Conversely, the continuum limit on the lattice is reached by sending the bare coupling to zero. Additionally, the fields in the theory, and thus the operators composed out of them, need to be renormalized in order to yield correct results upon removal of the cutoff in the continuum limit. In our case, the only operator that needs to be renormalized is the (point-to-point) electromagnetic current on the lattice, which will be introduced later. Here we only mention that it can be renormalized by multiplying with the hopping parameter and the renormalization factor Z_V,

$$J_{ren} = \frac{2\kappa}{a^3} Z_V J_0. \tag{2.47}$$

The computation of renormalization factors can be done perturbatively or non-perturbatively on the lattice, and especially for the vector current there exists a non-perturbatively determination for the quenched theory [41], valid in a range of $6.0 \leq \beta \leq 24.0$ given by

$$Z_V(g_0) = \frac{1 - 0.7663 g_0^2 + 0.0488 g_0^4}{1 - 0.6369 g_0^2}. \tag{2.48}$$

The scale entering the relation of lattice spacing and bare coupling (2.46) has to be fixed at finite lattice spacing. In general this can be done by matching lattice results to already known, dimensionful results, e.g. the proton mass from experiment, estimators of the string tension $\sqrt{\sigma}$ of the heavy quark potential,

$$V_{\bar{q}q}(r) = -\frac{\alpha}{r} + \sigma r, \tag{2.49}$$

or the Kaon decay constant f_K. In this work, several lattices are used where the scale has been set differently. We refer to the corresponding discussion of lattice setups in Sec. 6 and Sec. 7 for details.

2.4 Numerical approach to Lattice QCD

With the discretized actions presented in Sec. 2.2, we now shortly address the question how to evaluate the expectation value

$$\langle \mathcal{O}(U,\psi,\bar{\psi})\rangle = \frac{1}{\mathcal{Z}} \int \prod_{\mu} \mathcal{D}U_{\mu} \int \prod_{f} \mathcal{D}\psi_f \bar{\psi}_f \mathrm{e}^{-S(U,\psi,\bar{\psi})} \mathcal{O}(U,\psi,\bar{\psi}) \tag{2.50}$$

in a numerical setup. The details of the material can be looked up in standard literature, e.g. [6, 11, 32, 42].

2.4.1 General considerations

Splitting the action into its pure gauge part and a part governing the dynamics of fermions, $S = S_G(U) + S_F(U,\psi,\bar{\psi})$, and noting that the fermionic part has a bilinear structure $S_F \sim \bar{\psi} M \psi$, the integration of the Grassmannian fermion fields can be done analytically. Since the operator $\mathcal{O}(U,\psi,\bar{\psi})$ in our context will always be a function of fermionic and corresponding antifermionic fields, the *Wick theorem* allows to express the operator $\mathcal{O}(U,\psi,\bar{\psi})$ by contractions of inverse Dirac matrices $M^{-1}(U)$, see e.g. [11, 42]. The resulting expression is given by

$$\langle \mathcal{O}(U,\psi,\bar{\psi})\rangle = \frac{1}{\mathcal{Z}} \int \prod_{\mu} \mathcal{D}U_{\mu} \mathrm{e}^{-S_G(U)} \det M(U) \mathcal{O}(M^{-1}(U)). \tag{2.51}$$

The integration over the $SU(3)$ valued gauge fields $U_\mu(n)$ cannot be performed analytically and is done numerically in the framework of Lattice QCD. Because the integral is highly dimensional, the basic tool to use is a Monte Carlo integration in gauge field space [6, 8]. The general idea is to draw configurations of gauge links $U_\mu(n)$ connecting all sites on the lattice at random, with a distribution weighted by the Boltzmann factor

$$\frac{1}{\mathcal{Z}} \mathrm{e}^{-S_G(U)} \det M(U). \tag{2.52}$$

The acquired configurations of gauge links are then used to perform the MC integration, i.e. the resulting integral is just the average of the operator under consideration with respect to the statistical ensemble $\{U_\mu^{(i)}(n)\}$ of size N,

$$\langle \mathcal{O}(U)\rangle = \frac{1}{N} \sum_{i} \mathcal{O}(U^{(i)}). \tag{2.53}$$

Technically, the evolution in the configuration space is done by forming a *Markov chain* of gauge link configurations, for which it can be proven that, starting from an initial configuration, it is possible to drive the chain to resembling the probability distribution (2.52). This process is called *thermalization*, and a thermalized chain of configurations is then used to evaluate the integral according to (2.53).

2.4.2 Methods without fermions

The concrete procedure, and the algorithms used, in the production of gauge field samples depend on the choice of how to handle the fermion determinant. One possibility is to discard the fermion determinant altogether, called the *quenched approximation*, leaving only e^{-S_G} as the Boltzmann factor in the integral and probability distribution, which in turn is treatable by basic Markov chain generating algorithms like the Metropolis algorithm, and a combination of the heatbath algorithm and overrelaxation steps [43, 44, 45], with the latter combination used in this work for a study performed on quenched lattices. It should suffice here to note that the general procedure of these algorithms is to input a (thermalized or unthermalized) configuration of gauge fields, perform small changes to a patch of single gauge fields $U_\mu(n)$, and then check how the Boltzmann factor subsequently got affected by these changes, i.e. if $S_G^{(i)} \geq S_G^{(i+1)}$, then the change is accepted and the new gauge configuration in the chain is $\{U_\mu^{(i+1)}(n)\}$. If the action increases under the changes, then with a probability $p \sim \mathrm{e}^{-\left(S_G^{(i+1)} - S_G^{(i)}\right)}$ the change is still accepted, otherwise the new configuration is discarded.

2.4.3 A Method including fermions

However, these *local updates* of small patches are unfeasible for a non vanishing fermion determinant, because it is highly non local, and thus the whole determinant has to be recomputed per local update. This makes *global updates*, i.e. changes to all gauge links in a given configuration, the preferred way to go. These cannot be done by simply changing all links at once, as the probability of acceptance would drop close to zero. The strategy in this case is to rewrite the determinant as an exponentiated *bosonic* action [46],

$$\det M(U) = \sqrt{\det M^\dagger M} = \int \mathcal{D}\Phi^\dagger \mathcal{D}\Phi \mathrm{e}^{-\Phi^\dagger (M^\dagger(U)M(U))^{-1/2}\Phi}, \tag{2.54}$$

with $M^\dagger(U)M(U)$ being used to ensure hermiticity of the construct in the bosonic integral. Introducing momenta P_μ, conjugate to these *pseudofermions* and with a gaussian distribution, the total action becomes

$$H(U, \Phi, \Phi^\dagger, P) = \frac{1}{2}\sum_{n,\mu} P_\mu^2(n) + S\left(U, \Phi, \Phi^\dagger\right), \tag{2.55}$$

with the sum running over all lattice sites. The thus obtained expression is a classical Hamiltonian, and the corresponding equations of motion yield a set of differential equations to be solved along a surface of (up to numerical uncertainties) constant energy, see [6, 8, 47] for a more detailed description of the procedure and the algorithms used. The dynamics of the pseudofermion and gauge fields, performed across the whole lattice, thus constitutes a global update of the gauge configuration. The energy difference δH between two subsequent configurations can be used to also perform an acceptance test at the end of one such *trajectory* in $SU(3)$ gauge link space, rendering the procedure

exact. The acceptance rate then depends on the length of the trajectory and the details, e.g. the step size, of the algorithm that solves the differential equations emerging from (2.55). A rule of thumb is to keep it at a reasonable rate of $\sim 50 - 80\%$ [47].

In the current work, some of our gauge ensembles are produced using the *Hybrid Monte Carlo* algorithm described above. However, in order to work with an uneven number of dynamical fermions, expression (2.54) shows the need to approximate fractional powers of the (products of the) Dirac matrix. This is done by approximating

$$M^{-\alpha} \approx r(M) = \sum_n \frac{\alpha_n}{M + \beta_n}, \tag{2.56}$$

to which the algorithm owes its given name *Rational Hybrid Monte Carlo* (RHMC) [48]. The same is also needed when reducing the number of quarks in the staggered/HISQ formulations by the fourth root trick, as explained in Sec.2.2.3. The algorithm that computes the coefficients of the approximation was invented by Remez [48], and for definiteness we state here that the dynamical computations in the course of this work are performed with the MILC codebase [49], which includes the used HISQ and RHMC and Remez algorithm implementations.

2.5 Statistical methods for data analysis

Numerical lattice gauge theory computations are intrinsically statistical by nature. The use of Monte Carlo techniques for the integration of equation (2.50) leaves us with statistical samples, i.e. one number for each observable to compute per gauge configuration. The result is then in theory obtained by averaging over all obtained samples,

$$\frac{\int \mathrm{d}\mathcal{U} e^{-S(\mathcal{U})} \mathcal{O}(\mathcal{U})}{\int \mathrm{d}\mathcal{U} e^{-S(\mathcal{U})}} \equiv \langle \mathcal{O} \rangle. \tag{2.57}$$

In the following we present necessary and useful methods for error estimation of statistical estimators. They can be found in many fundamental texts, e.g. [6, 30].

2.5.1 Single quantity estimators

At this point the r.h.s. of (2.57) represents an expectation value with respect to the underlying theoretical distribution of $\mathcal{O}$. A suitable estimator for this quantity, in order to infer (2.57) from a finite sample in the context of Monte Carlo integration, is given by the usual (unbiased) average, or mean,

$$\langle \mathcal{O} \rangle \longleftarrow \hat{\mathcal{O}} \equiv \frac{1}{N} \sum_n^N \mathcal{O}_n, \tag{2.58}$$

with $\mathcal{O}_n$ the observed value of the $n - th$ sample and N the total number of samples. It is unbiased because the expectation of a single measurement is $\langle \mathcal{O}_n \rangle = \langle \mathcal{O} \rangle$, and thus

also $\langle\hat{\mathcal{O}}\rangle = \langle\mathcal{O}\rangle$. A measure of the deviation of each sample $\mathcal{O}_n$ from the theoretical expectation value, or the *spread* of the measurements, can be defined via

$$\langle(\delta\mathcal{O})^2\rangle \equiv \langle(\mathcal{O} - \langle\mathcal{O}\rangle)^2\rangle \longleftarrow \frac{1}{N}\sum_n^N \left(\mathcal{O}_n - \hat{\mathcal{O}}\right)^2 \equiv \tilde{\sigma}^2. \tag{2.59}$$

Care has to be taken when using this estimator, as $\langle\tilde{\sigma}^2\rangle = \frac{N-1}{N}\langle(\delta\mathcal{O})^2\rangle$, and thus it is biased. It is included here as a prestep to an unbiased estimator for the variance, because it will become important in the context of the bootstrap method. Rendering (2.59) unbiased is easily done by choosing

$$\hat{\sigma}^2 \equiv \frac{N}{N-1}\tilde{\sigma}^2 = \frac{1}{N-1}\sum_n^N \left(\mathcal{O}_n - \hat{\mathcal{O}}\right)^2. \tag{2.60}$$

At present, a more interesting quantity is the expected deviation of the estimator $\hat{\mathcal{O}}$ from its theoretical expectation value, which constitutes the statistical error that one has to state when computing observables via (2.57). For uncorrelated measurements, i.e. $\langle\mathcal{O}_n\mathcal{O}_m\rangle = \langle\mathcal{O}_n\rangle\langle\mathcal{O}_M\rangle = \langle\mathcal{O}\rangle^2$, one finds

$$\langle\left(\hat{\mathcal{O}} - \langle\mathcal{O}\rangle\right)^2\rangle = \frac{1}{N}\langle(\delta\mathcal{O})^2\rangle \longleftarrow \frac{1}{N\,(N-1)}\sum_n^N \left(\mathcal{O}_n - \hat{\mathcal{O}}\right)^2, \tag{2.61}$$

with the last expression being an unbiased estimator obtained from (2.59) and (2.60). This shows that the estimator for the expectation value is *consistent*, meaning that it approaches zero with increasing number of samples. If one has more than one observable that one wants to infer from a given statistics of data, then one can read (2.60) or (2.61) in a more general way and write e.g.

$$\begin{aligned}\langle\left(\hat{\mathcal{O}}_1 - \langle\mathcal{O}_1\rangle\right)\left(\hat{\mathcal{O}}_2 - \langle\mathcal{O}_2\rangle\right)\rangle &= \frac{1}{N}\langle\delta\mathcal{O}_1\delta\mathcal{O}_2\rangle \\ &\longleftarrow \frac{1}{N\,(N-1)}\sum_n^N \left(\mathcal{O}_{1,n} - \hat{\mathcal{O}}_{1,n}\right)\left(\mathcal{O}_{2,n} - \hat{\mathcal{O}}_{2,n}\right)\end{aligned} \tag{2.62}$$

for (2.62) and denote it as the *covariance* of the data. Non vanishing statistical covariance should be taken into account in many computational tasks such as χ^2 fitting. Also, there are many applications where it plays an essential role, see e.g. MEM or the method of Backus and Gilbert.

2.5.2 Estimators for composite quantities

In many cases one wants to infer a theoretical quantity that is a function of, for the sake of simplicity, say, two different variables. Hence, in practice these two variables

correspond to two different ensembles of measurements. Let $f(a,b)$ be a function of two different random variables a and b, while e.g. $\delta a = a - \langle a \rangle$ denotes the deviation of the variable a from its expectation value, and analogously for b. Then the squared total deviation of $f(a,b)$ can be computed by Taylor expanding

$$\begin{aligned}\langle (\delta f)^2 \rangle &= \langle [f(a+\delta a, b+\delta b) - f(a,b)]^2 \rangle \\ &= \langle \left[f(a,b) + \frac{\partial f}{\partial a}\delta a + \frac{\partial f}{\partial b}\delta b - f(a,b) + \mathcal{O}\left(\delta^2\right) \right]^2 \rangle \\ &= \langle \left[\frac{\partial f}{\partial a}\right]^2 (\delta a)^2 + \left[\frac{\partial f}{\partial b}\right]^2 (\delta b)^2 + 2\frac{\partial f}{\partial a}\frac{\partial f}{\partial b}\delta a \delta b + \mathcal{O}\left(\delta^3\right) \rangle.\end{aligned} \tag{2.63}$$

Dropping terms of order $\mathcal{O}(\delta^3)$ and higher, as well as identifying $\langle (\delta a)^2 \rangle$, $\langle (\delta b)^2 \rangle$, $\langle \delta a \delta b \rangle$ with the variances and the covariance of a and b, respectively, one arrives at the general error formula

$$\langle (\delta f)^2 \rangle = \left[\frac{\partial f}{\partial a}\right]^2 \langle (\delta a)^2 \rangle + \left[\frac{\partial f}{\partial b}\right]^2 \langle (\delta b)^2 \rangle + 2\frac{\partial f}{\partial a}\frac{\partial f}{\partial b}\langle \delta a \delta b \rangle. \tag{2.64}$$

Note that without the covariance term, this result is just the gaussian propagated error. Equation (2.64) is especially useful for constructing errorbands of extrapolating or interpolating fits, as long as the covariance term is available or computable.

With respect to the last remark, there are two resampling techniques that are used in this work and which should be addressed here, namely the Bootstrap and the Jackknife. Both are very powerful tools to infer statistics of (essentially arbitrary) functions of random variables. Denote such a function of N_{rv} random variables $f\left(\mathcal{O}^{(1)}, \ldots, \mathcal{O}^{(N_{\mathrm{rv}})}\right)$. Further assume that there are N given samples, or measurements, for each random variable $\mathcal{O}^{(r)}$. Then the Jackknife works by subdividing each sample set into M groups of size $n = N/M$. Defining the average of each group

$$\hat{\gamma}_i^{(r)} \equiv \frac{1}{n} \sum_{j=(i-1)n}^{in} \mathcal{O}_j^{(r)} \quad \forall\, i = 1, \ldots, M, \;\; r = 1, \ldots, N_{\mathrm{rv}}, \tag{2.65}$$

and further defining the average of all M subsets but one,

$$\hat{\Gamma}_i^{(r)} \equiv \frac{1}{M-1} \sum_{\substack{j=1 \\ j \neq i}}^{M} \hat{\gamma}_j^{(r)}, \quad \forall\, r = 1, \ldots, N_{\mathrm{rv}}, \tag{2.66}$$

the function $f(\mathcal{O}^{(1)}, \ldots, \mathcal{O}^{(N_{\mathrm{rv}})})$ is then evaluated using estimators $\hat{\Gamma}_i^{(r)}$,

$$f_i^{\mathrm{JK}} \equiv f(\hat{\Gamma}_i^{(1)}, \ldots, \hat{\Gamma}_i^{(N_{\mathrm{rv}})}) \quad \forall\, i = 1, \ldots, M. \tag{2.67}$$

The M latter quantities f_i^{JK} are called *partial Jackknife estimators*, and are used to construct estimators for the average $\langle f \rangle$ and the deviation $\langle (\delta f)^2 \rangle$ as follows. Denoting the usual mean of the function by

$$\langle f \rangle \longleftarrow \hat{f} \equiv f(\hat{\mathcal{O}}^{(1)}, \ldots, \hat{\mathcal{O}}^{(N_{\mathrm{rv}})}), \tag{2.68}$$

the Jackknife estimators for mean and deviation are

$$\langle f \rangle \longleftarrow \hat{f}^{\mathrm{JK}} \equiv M\hat{f} - \frac{M-1}{M} \sum_{i=1}^{M} f_i^{\mathrm{JK}}, \tag{2.69}$$

$$\langle (\delta f)^2 \rangle \longleftarrow \frac{M-1}{M} \sum_{i=1}^{M} \left(f_i^{\mathrm{JK}} - \hat{f}^{\mathrm{JK}} \right)^2. \tag{2.70}$$

The Jackknife estimator for the mean is unbiased in the sense that corrections corresponding to the finite size of the sample are of second order in the sample size,

$$\langle f \rangle = \hat{f}^{\mathrm{JK}} + \mathcal{O}\left(\frac{1}{N^2} \right), \tag{2.71}$$

while in general the naive estimator (2.68) has corrections of order $\mathcal{O}(1/N)$. In practice, this affects mainly cases where the sample size is small, e.g. $N \ll 100$, whence the bias becomes as large as the statistical error or even larger.

Considering the same function f, random variables $\mathcal{O}^{(r)}$ and their respective samples of size N each, the Bootstrap starts by drawing, with repetition, N values from each sample, thus creating N_{rv} new samples. This process is repeated N_{bs} times, until one is left with N_{bs} different 'dummy' samples of size N for each of the N_{rv} random variables. A blocking procedure, as in the Jackknife method, can be used analogously by subdividing each 'original' sample in M groups beforehand and always drawing whole groups of size N/M with repetition. Using the 'dummy' samples one can now infer

$$f_i^{\mathrm{BS}} \equiv f\left(\mathcal{O}_i^{(1)}, \ldots, \mathcal{O}_i^{(N_{\mathrm{rv}})} \right) \quad \forall\, i = 1, \ldots, N_{\mathrm{bs}}. \tag{2.72}$$

The original sample does not play a role anymore and is explicitly excluded. The $\mathcal{O}_i^{(r)}$ mimic independent measurements of the $\mathcal{O}^{(r)}$ and thus the f_i^{BS} mimic independent determinations of f, as well. As an estimator $\hat{f}$ for the mean of f one can use either (2.68), average the bootstrap ensemble f_i^{BS}, or use a bias corrected estimator

$$\hat{f}^{\mathrm{BS}} \equiv \hat{f} + \hat{f} - \frac{1}{N_{\mathrm{bs}}} \sum_{i=1}^{N_{\mathrm{bs}}} f_i^{\mathrm{BS}}. \tag{2.73}$$

An unbiased estimator for the deviation of $\hat{f}^{\mathrm{BS}}$ can be obtained by computing the spread of these new measurements, compare (2.59),

$$\langle (\delta f)^2 \rangle \longleftarrow \frac{1}{N_{\mathrm{bs}}} \sum_{i=1}^{N_{\mathrm{bs}}} \left(f_i^{\mathrm{BS}} - \hat{f} \right)^2. \tag{2.74}$$

Note here that this really is the deviation of the *bootstrap measurements* from the mean and thus does not have a prefactor $1/N_{bs}^2$ but merely $1/N_{bs}$. Analogously we can define the generalized covariance with two different quantities f_1 and f_2, sharing the same underlying statistical ensemble, to be

$$\langle \delta f_1 \delta f_2 \rangle \longleftarrow \frac{1}{N_{\mathrm{bs}}} \sum_{i=1}^{N_{\mathrm{bs}}} \left(f_{1,i}^{\mathrm{BS}} - \hat{f}_1 \right) \left(f_{2,i}^{\mathrm{BS}} - \hat{f}_2 \right). \tag{2.75}$$

Care has to be taken when the observables $\mathcal{O}^{(r)}$ are correlated among each other. This is the case when observing e.g. correlator data $G(t) \to G(t_i) \equiv G^{(i)}$, with the whole correlator consisting of $i = 1, \ldots, N_t$ different random variables. Then each $G^{(i)}$ corresponds to an observable $\mathcal{O}^{(i)}$, and, independent of the details of the operations done to or functions used on the correlator, the resampling should always be done with all correlator points involved *as a whole*, i.e. a new sample should be drawn with all $i = 1, \ldots, N_t$ corresponding to the same statistical sample. Although this remark might seem trivial, it is well worth mentioning, as the resampling methods then respect the statistical correlation between the different correlator points and e.g. the results of a fit, done within the resampling process, will reflect the correlation of the data points and thus be more reliable. To make this a bit more explicit, consider that both resampling methods probe the underlying probability distribution by systematically leaving out a part of the drawn ensemble, in case of the Jackknife, or by randomly shifting the relative weight of single samples, as done in the bootstrap by drawing from the original ensemble with repetition. When statistically correlated observables are resampled together, then features that appear for a given subsample or bootstrap sample in one observable, will also appear in the other observables, dependent on the amount of correlation.

2.5.3 Non vanishing autocorrelation

As has already been mentioned in the beginning of this chapter, the raw data used in this work stems from Monte Carlo integrations, and the samples drawn from those are snapshots of a time series. This implies that the samples are generally subject to *autocorrelations*. Considering the $i-th$ sample of an observable $\mathcal{O}_i$, its covariance with the same observable sampled at a later stage $i+t$ in the time series is given by

$$\begin{aligned} A_t(\mathcal{O}) &= \langle (\mathcal{O}_i - \langle \mathcal{O}_i \rangle)(\mathcal{O}_{i+t} - \langle \mathcal{O}_{i+t} \rangle) \rangle \\ &= \langle \mathcal{O}_i \mathcal{O}_{i+t} \rangle - \langle \mathcal{O}_i \rangle \langle \mathcal{O}_{i+t} \rangle = \langle \mathcal{O}_i \mathcal{O}_{i+t} \rangle - \langle \mathcal{O}_i \rangle^2. \end{aligned} \tag{2.76}$$

Normalizing this with the variance $\langle \mathcal{O}^2 \rangle - \langle \mathcal{O} \rangle^2 = A_0(\mathcal{O})$, its leading term is expected to be exponentially suppressed in t,

$$\frac{A_t(\mathcal{O})}{A_0(\mathcal{O})} \sim \mathrm{e}^{-t/\tau_0} + \mathrm{e}^{-t/\tau_1} + \cdots. \tag{2.77}$$

The quantities τ_n are called *autocorrelation times*, where the sum on the r.h.s. is dominated by the exponential with the largest autocorrelation time. The occurrence of non vanishing autocorrelation times in observables should be checked, as both the standard estimators (2.58, 2.60) and the estimators obtained from resampling methods generally require uncorrelated data as input. The latter have the advantage that choosing a fixed group size $n = N/M$ larger than the autocorrelation time is a way to get rid of correlations in an intrinsic way. Of course, this amounts to effectively reducing the sample sizes to n from the original N. For the former, one can compute the *integrated autocorrelation time*

$$\tau_{\text{int}} = \frac{1}{2} + \frac{1}{A_0\left(\mathcal{O}\right)} \sum_{i=1}^{N} A_i\left(\mathcal{O}\right) \tag{2.78}$$

and scale the fluctuation of the data (2.60)

$$\left\langle \left(\delta\mathcal{O}\right)^2 \right\rangle \longrightarrow 2\tau_{\text{int}} \left\langle \left(\delta\mathcal{O}\right)^2 \right\rangle \tag{2.79}$$

in order to account for these additional correlations.

2.6 Spectroscopy

The lattice regularization of a theory really serves two purposes. First of all, it renders the theory well-defined with regards to ambiguities in the evaluation of the path integral [8, 9]. In this sense it is a prestep of the necessary renormalization procedure. Second, it yields the theory in a form that is naturally tractable by numerical methods, and thus potentially calculable *without* any approximations made. A very fundamental job of Lattice QCD is to determine the properties of the hadrons in the spectrum, e.g. the occurring bound and excited states depending on number of flavors, number of colors, values of the quark masses etc, as well as decay constants, form factors and parton distribution functions, see for example [6, 30, 32, 50, 51, 52, 53] for introductions, reviews and concrete examples.

We present in this chapter the very basic methods of Lattice QCD spectroscopy. They constitute the foundation from which advanced methods are developed to compute a multitude of quantities such as (excited) hadron masses. As we use methods of spectroscopy for the very specific purpose of tuning valence quark masses, to fit masses of the sea quarks, used in the production of the gauge configurations, we only cover a rather small range of methods and very basic principles to perform the needed fits to extract ground state masses from correlation function data.

2.6.1 Extraction of energies

The bound states of QCD are naturally characterized by their quantum numbers, i.e. their behavior under symmetry operations. This classification scheme is used in exper-

channel	Dirac structure	particle example
S	1	$a_0,\ K^*$
V	γ_i	$\rho,\ K^*,\ J/\psi$
PS	γ_5	$\pi,\ K,\ \eta$
AV	$\gamma_i\gamma_5$	$a_1,\ K_1$

Table 2.1: The naming scheme of the Dirac structure and examples of corresponding physical particles.

iments to identify measured particles, and encompasses the quantum numbers of total spin (J), parity (P) and charge conjugation (C). On the lattice, mesons are modeled as quark-antiquark bound states and can be classified with respect to their Dirac structure to be either scalars (S), vectors (V), pseudoscalars (PS) or axial vectors (AV), see Tab. 2.1 for an overview of the Dirac structure and the associated physical particle states. Since the vector and axial vector have three spatial components $i = 1, 2, 3$, which are degenerate at zero momentum due to homogeneity of space, we usually average over the three spatial directions. The Dirac structure fixes the spin and parity of the meson, while the behavior under charge conjugation is related to the charge of the particle, and hence the quark content. In order to measure a certain mesonic state, it is necessary to construct interpolating operators $\mathcal{O}$ that have the quantum numbers of the physical particle under consideration, and at the same time have a strong overlap with the physical states. This is generally a non trivial task, as can be seen in spectroscopy of excited states, where superpositions of operators as well as more complicated operators in general, are used to improve the signal [6, 32]. The most simple operators, however, suffice for the extraction of ground state masses as performed in the course of this work. They generally consist of two Dirac spinors and an insertion point for gamma matrices,

$$\mathcal{O}_H(x) = \bar{\psi}_1(x)\Gamma_H\psi_2(x). \tag{2.80}$$

In order to make this interpolator represent a certain physical state, we have to set the gamma matrix and the quark content, such that the symmetry properties of the physical state are fulfilled. As an example, consider the ρ particle. The physical ρ is a spin-1 particle, so the Γ_H has to at least contain a matrix γ_i, to account for the spin-1 Dirac structure. From the negative parity of the state, we know that the interpolator thus needs to have a vector structure, as opposed to an axial vector structure, and hence $\Gamma_H = \gamma_i$ with no further modification. Considering the quark content, the ρ consists of a u and a d quark, which is a realization of an isospin-$\frac{1}{2}$ system. Addition of the isospins thus yields a triplet of total isospin $I = 1$, containing three states, and a singlet of total isospin $I = 0$, containing one state. The singlet configuration is attributed to the physical ω state, which leaves the three triplet states to constitute the sought ρ. Indeed, the three possible values of the z-component of the isospin, $I_z = -1, 0, +1$, amount to quark contents [54]

$$\mathbf{I_z = -1}:\ a_{-1}\bar{u}\gamma_i d$$

$$\mathbf{I_z = 0}: \; a_0 \bar{u}\gamma_i u + b_0 \bar{d}\gamma_i d$$

$$\mathbf{I_z = +1}: \; a_{+1} \bar{d}\gamma_i u,$$

which realize states of total charge -1 (the ρ^-), total charge 0 (the ρ^0) and total charge $+1$ (the ρ^+), respectively. The factors a and b are the Clebsch-Gordan coefficients for addition of two spin-$\frac{1}{2}$ states. In Lattice computations the up and down quark are usually taken to have degenerate masses, which in turn degenerates ρ^+ and ρ^-, and simplifies the structure of the ρ^0.

The basic techniques used to extract information from correlation functions of interpolating operators, however, are oblivious of the structure of the operators as well as the nature of the physical states. The desired initial and final state are expressed as their respective interpolating operators, i.e. $|S_{i,f}\rangle = \mathcal{O}^\dagger_{i,f}|0\rangle$. By inserting a unit operator in energy basis between the overlap of final and initial state as well as making explicit the time translation of the final state, we obtain [6, 9, 32]

$$\langle S_f||S_i\rangle = \langle 0|\mathcal{O}_f(\tau)\mathcal{O}_i^\dagger(0)|0\rangle = \sum_n A_n \langle 0|\mathrm{e}^{H\tau}\mathcal{O}_f(0)\mathrm{e}^{-H\tau}|n\rangle\langle n|\mathcal{O}_i^\dagger(0)|0\rangle. \tag{2.81}$$

Evaluating the (hermitian!) Hamiltonian H on the respective energy states, $H|n\rangle = E_n|n\rangle$, and choosing by convention $E_0 \equiv 0$, we arrive at

$$\langle S_f||S_i\rangle = \sum_n A_n \mathrm{e}^{-E_n\tau}\langle 0|\mathcal{O}_f|n\rangle\langle n|\mathcal{O}_i^\dagger|0\rangle. \tag{2.82}$$

Note that by choosing the vacuum energy to be zero, the energy of the state is actually an energy difference, namely the energy needed to produce a particle in the ground state. This formula has a very vivid interpretation. It states that the overlap of the initial state and the final state is really a superposition of contributions. The unit operator sums over all states in the Hilbert space, and thus the term $\langle 0|\mathcal{O}_f|n\rangle\langle n|\mathcal{O}_i^\dagger|0\rangle$ potentially couples to every state in the spectrum that is compatible with the quantum numbers of $\mathcal{O}$. Specifically, when the energy of the state that we want to measure is high enough to open decay channels, intermediate scattering states are expected to be dominating contributions in (2.82). This has serious implications for the extraction of energies and masses via this approach, see e.g. [55]. However, if the state we are looking for is clearly separated from other contributions, the exponential suppresses the latter at large times and the sum can be truncated after the first term to obtain an estimate for the ground state,

$$\langle S_f||S_i\rangle \overset{\tau\to\infty}{\longrightarrow} A_1 \mathrm{e}^{-E_1\tau}\langle 0|\mathcal{O}_f|1\rangle\langle 1|\mathcal{O}_i^\dagger|0\rangle. \tag{2.83}$$

By fitting the numerical correlator data to an Ansatz manifesting this exponential decay for large enough times, one may hope to extract both the matrix element as well as the ground state energy. Note however that in general this depends on the value of the overlap, characterized by the matrix element; having on the lattice only a finite time extent,

it may well happen that the ground state is contaminated by higher states, making it challenging to extract even the first energy level with good accuracy [32].

When explicitly choosing an Ansatz to fit the correlator data, then on the lattice one has to take into account the finite lattice extent in time direction, which is written in terms of the temperature as $T = 1/(aN_\tau)$. The consequence of this is twofold, namely [56]

1. because of the periodicity one not only has the contribution (2.83) propagating from the source forward in time, $A\mathrm{e}^{-m\tau}$, but also a contribution going backward from the source, $A\mathrm{e}^{-m(1/T-\tau)}$.

2. both backward and forward contribution actually appear infinitely often, coming with additional factors $\mathrm{e}^{-(m/T)n}$, with $n = 1, 2, \ldots$, which represent their respective contributions when wrapping n times *around* the lattice.

The full resulting expression, which is used for meson correlator fits throughout this thesis, is given by

$$\begin{aligned} G(\tau) &\equiv \left(A\mathrm{e}^{-m\tau} + A\mathrm{e}^{-m(1/T-\tau)}\right) \sum_{n=0}^{\infty} \mathrm{e}^{-(m/T)n} \\ &= \frac{A}{1-\mathrm{e}^{-m/T}} \left(e^{-m\tau} + \mathrm{e}^{-m(1/T-\tau)}\right) \\ &= A\frac{\cosh\left[m(\tau - 1/(2T))\right]}{\sinh\left[m/(2T)\right]}. \end{aligned} \tag{2.84}$$

As a side remark, this obviously leads to the correlator being a symmetric or antisymmetric function of the time variable around $\tau = 1/(2T)$. Up to statistical fluctuations the correlator data of course also has to show this behavior, and hence all of our correlator data are (anti)symmetrized with respect to the midpoint unless otherwise noted.

The representation of Euclidean correlation functions via their respective spectral density is the topic of Sec. 4.1, but it is instructive in the context of equations (2.82) and (2.84) to anticipate one point already here. For a finite temporal extent, the correlation function results from the spectral function via the integral

$$G(\tau) = \frac{1}{2\pi} \int_0^\infty \mathrm{d}\omega \frac{\cosh\left[\omega(\tau - 1/(2T))\right]}{\sinh\left[\omega/(2T)\right]} \rho(\omega). \tag{2.85}$$

Assuming a spectral density consisting of a series of δ peaks, located at respective frequencies ω_n, the correlation function becomes

$$\begin{aligned} G(\tau) &= \frac{1}{2\pi} \int_0^\infty \mathrm{d}\omega \frac{\cosh\left[\omega(\tau - 1/(2T))\right]}{\sinh\left[\omega/(2T)\right]} \sum_n A_n \delta(\omega - \omega_n) \\ &= \sum_n A_n \frac{\cosh\left[\omega_n(\tau - 1/(2T))\right]}{\sinh\left[\omega_n/(2T)\right]}, \end{aligned} \tag{2.86}$$

i.e. Dirac delta peaks are a way to represent well defined particle states in the corresponding spectral function. Note however, that this is somewhat idealized at finite temperature. In the limit $K(\omega, T) \xrightarrow{T\to 0} \mathrm{e}^{-\omega_n \tau}$, the strict zero temperature result (2.82) is recovered.

As already mentioned above, there can be difficulties when attempting to extract a ground state mass using a fit Ansatz with only one state. A superposition as in (2.86) can help to catch the effects of not yet decayed excited state signals. However, *extracting* excited states in this manner usually suffers from large uncertainties on the coefficients A_n and ω_n, and combinations of different operators are used to obtain reliable estimators [57].

There is another very common way to compute ground state masses of bound states, which will be addressed here. Instead of merely looking at the correlator, one can consider the ratio of correlators

$$\frac{G(\tau + l)}{G(\tau)} \approx \frac{\mathrm{e}^{-m(\tau+l)}}{\mathrm{e}^{-m\tau}} \quad \Leftrightarrow \quad m_{\mathrm{eff}} \equiv -\frac{1}{l} \ln \frac{G(\tau + l)}{G(\tau)}, \tag{2.87}$$

by taking (2.83) at two points separated by a lag l, or by taking all finite size effects into account and solving the expression

$$\frac{G(\tau + l)}{G(\tau)} = \frac{\cosh\left[m\left(\tau + l - 1/(2T)\right)\right]}{\cosh\left[m\left(\tau - 1/(2T)\right)\right]} \tag{2.88}$$

numerically for the so called *effective mass* m_{eff}. The effective mass is usually computed with a lag $l = 1$ or $l = 2$ and saturates at large enough times τ to the ground state mass value. A constant can then be fitted in order to extract the mass. Another application of this quantity is to look closely where it starts to saturate in order to identify a suitable fit range for τ in (2.84).

2.6.2 A general remark on χ^2 fits

When extracting quantities like bound state masses via one of the techniques mentioned above, the question about their reliability immediately arises. One way to assign a measure of uncertainty to any statistically obtained quantity is of course to employ the statistical tools presented in Section 2.5. Generally, the fit should in such a case be performed fully correlated,

$$\chi^2 = \sum_{ij} \left(G(\tau_i) - f(\tau_i, \vec{p})\right) C^{-1}(\tau_i, \tau_j) \left(G(\tau_j) - f(\tau_j, \vec{p})\right), \tag{2.89}$$

i.e. including the off diagonal terms of the covariance matrix $C(\tau_i, \tau_j)$ of the data points, because then we get a reliable estimate of the χ^2, as well as the errors and correlations of the fit parameters $\vec{p}$. The importance of properly computed errors on the fit parameters

is evident, while e.g. proper correlations of the fit parameters enable us to perform a correct error propagation for composite quantities, as in (2.64). The value of χ^2/dof is an indicator of whether the input data and the model used are compatible. A value of $\chi^2/\text{dof} \ll 1$ means that probably there are non negligible terms that have not been accounted for (correlations in the data), while a $\chi^2/\text{dof} \gg 1$ simply means that the model does not describe the data. Thus, it is very desirable to have access to these quantities.

There are cases in which the inclusion of the covariance matrix in the fit is not possible, and thus we need to find another way to properly estimate the quantities sought above. One such situation can arise in the case of fits to correlator data via the Ansatz (2.84), where the condition number $\kappa \sim \sigma_{\max}/\sigma_{\min}$ of the covariance matrix in the interesting fit region $[\tau_{min}, 1/(2T)]$ can grow very large, e.g. $\kappa \gtrsim 10^{15}$. The condition number corresponds to the fraction of largest and smallest eigenvalue of the covariance matrix. Inverting such an ill-conditioned matrix can introduce large fluctuations and leads to a very unstable fit. One possible solution is given in [58], where a smoothing or averaging of the smallest eigenvalues is proposed in order to achieve an increase in $\sigma_{\min}$. This method has the disadvantage of altering the χ^2 term, which of course means that the fit-problem itself is altered. This introduces an unknown systematical error. Another approach is to enclose the fitting procedure in a bootstrap as described in Sec. 2.5. By choosing N_{bs} bootstrap samples and fitting every single one of those, we obtain N_{bs} estimators for the fit parameters. From these, estimators for average and variance can be obtained. By combining the samples of different fit parameters via (2.75) we can even compute the correlation of the fit parameters. The only quantity that is unfortunately lost during such a procedure is the sum of squares, χ^2, and its meaningfulness with respect to statements about the quality of the fit. Nevertheless, the bootstrap provides a very stable and reliable method of performing error analysis of fits to sets of correlated data, like lattice correlation function data $G_(\tau)$, and is thus the preferred fitting method within this work when the covariance matrix is (too) ill-conditioned.

2.6.3 Construction of correlation functions

In the following section we discuss how the interpolating fields $\mathcal{O}$ are combined to correlation functions, given the gauge configurations produced according to the methods reviewed in section 2.4, and we refer to the same standard textbooks and review articles for more details and context.

The interpolating fields are inserted to form a two point function between the source and sink points x_i and x_f, respectively, in space time. In practical lattice calculations, the source operator is located to $(\tau_i, \vec{x}_i) = (0, \vec{0})$, while the sink is 'probed' at any desired point $(\tau, \vec{x})$ on the lattice. The most general case is to have the operators at both the source and sink points contain identical quarks, i.e. to drop the indices attached to the spinors in (2.80). Starting from the definition of the path integral, the integral with respect to the fermionic degrees of freedom is carried out analytically via the Wick

theorem,

$$\begin{aligned}\langle \mathcal{O}_H(x)\mathcal{O}_H^\dagger(0)\rangle &= \frac{1}{Z}\int \mathcal{D}\mathcal{U}\mathcal{D}\bar{\psi}\mathcal{D}\psi \left(\mathcal{O}_H(x)\mathcal{O}_H^\dagger(0)\right) \mathrm{e}^{-(S_\mathrm{G}+S_\mathrm{F})} \\ &= \frac{1}{Z}\int \mathcal{D}\mathcal{U}\mathrm{e}^{-S_\mathrm{G}} \det(M)\,\mathrm{tr}\left[M^{-1}(x,0)\Gamma_H M^{-1}(0,x)\Gamma_H^\dagger\right] \\ &- \frac{1}{Z}\int \mathcal{D}\mathcal{U}\mathrm{e}^{-S_\mathrm{G}} \det(M)\,\mathrm{tr}\left[M^{-1}(0,0)\Gamma_H^\dagger\right]\mathrm{tr}\left[M^{-1}(x,x)\Gamma_H\right]\end{aligned} \tag{2.90}$$

with the traces running over both color and spinor indices. The result for degenerate quark flavors in the interpolator thus yields a contribution that depicts the quarks propagating from the source to the sink, and a contribution in which one quark is associated with the sink and source, respectively. The latter is known as the quark line disconnected contribution, and only occurs if the quarks and antiquarks used in the interpolating field have the same flavor. This is a consequence of the Wick contractions, which reflects that physics does not allow a change of flavor. In many lattice calculations the disconnected part is left out, because it is very noisy and thus requires very high statistics in the gauge field average to be accurately determined. Luckily, the OZI rule states that contributions, which can be split by only cutting gloun lines, are increasingly suppressed with increasing quark mass [54], and especially for charmonia are very small compared to the connected part [59]. For masses closer to the strange quark mass, such contractions are small for the vector channel, while the pseudoscalar channel could show a stronger dependence on disconnected parts due to mixing of the underlying physical states, see [60]. However, in this study we still drop disconnected contributions also in this case.

The connected part of (2.90) consists of two inverted Dirac matrices, one connects the source with the sink and the other one connects the sink with the source, and thus goes backward. Using the γ_5 hermiticity, rewrite

$$M^{-1}(0,x) = \gamma_5\left[M^{-1}(x,0)\right]^\dagger\gamma_5, \tag{2.91}$$

and thus one inversion on a given gauge background field suffices for such simple observables. In order to have states of definite momentum, we take the Fourier transform of the correlation function, and obtain the mixed representation,

$$G(\tau T,\vec{p}) = \frac{1}{\sqrt{V}}\sum_{\vec{x}} \mathrm{e}^{-i\vec{x}\cdot\vec{p}} G(\tau T,\vec{x}). \tag{2.92}$$

This implies that a projection to vanishing momentum is just a sum over all spatial lattice sites,

$$G(\tau T,\vec{0}) = \frac{1}{\sqrt{V}}\sum_{\vec{x}} G(\tau T,\vec{x}). \tag{2.93}$$

3 Phenomenology of the thermal medium

The Quark Gluon Plasma, or QGP, is a state of matter that has long been speculated about. QCD is, by all experimental evidence known to be, while theoretically strongly conjectured to be, a theory that confines its elementary degrees of freedom in composite particles. However, depending on the temperature and the density of a system, strongly interacting matter can be in different phases, with fundamentally different properties. See Fig. 3.1 for a sketch of the phase diagram in temperature and baryon density, focusing on the two phases that are relevant for the current work. In the following we want to characterize these different phases in more detail, mainly from the theoretical side, but as well as experimentally. With respect to theory, we want to present the main ideas behind QCD at vanishing, small and high temperature, along with the important theoretical probes that are argued to allow for a qualitative and quantitative understanding of nature in the framework of lattice field theory. Regarding experiments and phenomenology, it is imperative to identify different stages of heavy ion collisions and to subsequently develop an understanding of processes happening when crossing the boundaries of different phases, in order to connect them to the theoretical expectations.

3.1 Heavy Ion Collisions

Experimentally the properties of the QGP are sought by conducting particle collisions. The most important and largest facilities are the Large Hadron Collider (LHC) in Geneva at CERN, the Relativistic Heavy Ion Collider (RHIC) at the Brookhaven National Laboratory, the developing FAIR project at the Gesellschaft für Schwerionenforschung (GSI) and the Nuclotron based Ion Collider fAcility (NICA) at the Joint Institute for Nuclear Research. Experiments to test the strong interactions are in these institutions usually performed by building up two particle beams running concurrently in accelerator rings, ionized by stripping off most of the electrons, and made to collide at special points in the ring. These points are surrounded by detector chambers, detecting different particles, which originate as the end products from reactions between the two colliding ion beams. The energies reached suffice to create a state of matter that is observed at very high temperatures and particle densities. The existence of such a phase was speculated about for decades [62, 63, 64], and finally in the early 2000s it was found in experiments performed at RHIC [14].

In a particle collision one encounters several different regimes after the two Lorentz

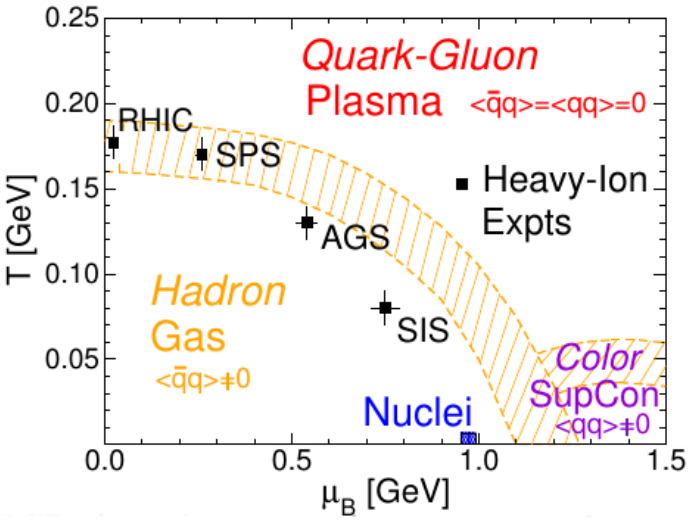

Figure 3.1: A rough sketch of the phases, expected in HIC, that are relevant for the current work. Shown are the hadronic and the QGP phase, as well as the transition line, as a function of temperature and density, separating them. The computations conducted in this work are at vanishing baryon density, i.e. to the very left of the plot. The picture is taken from [61].

contracted discs have approached on another. For two colliding protons (pp collision) one finds that, with a spatial extension of $l \approx 1\text{fm}$ for each collision partner in its rest-frame, due to the Lorentz contraction in the detector frame we have $l \ll 1\text{fm}$. Due to time dilation, the time it takes for the information of the collision to propagate through the nucleons, depend on the energy of the collision, $\sqrt{s}/(2m)\tau_0 \gg \tau_0$, and with a high enough energy the two protons move through each other while interacting. This leaves a trail of energetic bubbles along the beam axis, which cool down after initial expansion and hadronize to yield particles hitting the detector far away from the original collision region [39]. Concretely, they estimate an energy density of $\epsilon_{pp} \approx 0.36\text{GeV/fm}^3$ for a realistic beam energy of $\sqrt{s} = 20\text{GeV}$ inside the bubbles. While this is twice as high as nuclear matter, and certainly can be made larger by operating the collider at higher energies, the volume of the interacting matter will be rather small for thermodynamical purposes. However, the energy density is also proportional to the third root of the number of nucleons participating in the collision, $\epsilon \sim \sqrt[3]{A}$, and utilizing heavy nuclei like gold or lead (AA collisions) thus leads to both a larger reaction region and a higher energy density at the same input energy. The further qualitative expectation of the droplet is that quarks and gluons from the nucleons, forming the incident nuclei, are essentially percolating and it becomes increasingly difficult, with higher and higher beam energies $\sqrt{s}$, to consider them as single, well defined partons. Correspondingly, the resulting matter is a strongly correlated 'Glasma', which subsequently cools and expands [39]. The basic idea is that, the medium becoming increasingly dilute, it again makes sense to speak of partons in the droplet, and a thermalized patch of quarks and

gluons appears, which form the QGP. Upon further cooling and expansion, the temperature and density of the plasma decrease, and quarks of the plasma start to form light hadron states such as pions and kaons. This reorganization of the plasma's light quark background into colorless particles is the point of the confinement/deconfinement transition. Because the net baryon density in the collision region decreases with the center of mass energy $\sqrt{s}$, and thus in experiments there is the possibility to tune the baryon density accordingly [42, 65], we assume from here on a vanishing density. This is the region typically explored by the experiments performed at RHIC and LHC, while the FAIR project and NICA aim at higher baryon densities [66, 67]. Somewhat interestingly, due to the smallness of the light quark masses, the appearance of pions also marks the spontaneous breaking of chiral symmetry, where they play the role of the corresponding Goldstone bosons. These two transitions thus happen at the pseudocritical temperature of $T_c = 154(9)$MeV, determined by continuum extrapolated, non-perturbative lattice QCD results [36]. The errors in this estimate stem mainly from the fact that at zero baryon density the transition is a smooth crossover, so the very definition of the transition *point* itself is problematic, and one rather faces a transition *region*.

Generally, at the end of the QGP evolution, the frozen out hadrons (e.g. pions and kaons) are detected in the experiment, as well as particles that come from earlier stages of the collisions. Examples are highly energetic single quarks or gluons that hadronize into jets [11, 68], and dilepton (e^+e^- and $\mu^+\mu^-$) pairs and photons that are created at all stages of particle collisions. Because dileptons and photons interact electromagnetically, after being produced in a process they cross the interaction region mostly without further modification [12]. This makes them ideal probes and in the following we will concentrate on how an experimental dilepton yield can be accessed theoretically, and what we can learn from it about the QGP.

3.2 Probes of Heavy Ion Collisions

In order to study the phenomena happening in particle collisions, and especially the properties of the QGP formed in Heavy Ion Collisions (HIC), physical probes are needed. As already indicated in the foregoing section, the only probes available are the particles produced during the whole collision process, which escape the interaction region and are examined in the detector. Also, as pure *pp* collisions do not create a QGP, the observed yields in this case are the outcomes of vacuum processes. In order to observe possible effects stemming from a Quark Gluon Plasma, an important observable in experiments is the *Nuclear Modification Factor* R_{AA}, which is just the value of an observable from an HIC (i.e. an AA collision) divided by the (up scaled) value of that observable coming from a *pp* collision. In the following we will introduce the concepts behind charmonium as a probe (and the same holds essentially also for bottomonium), which is generally susceptible to in-medium dynamics that directly relate to the deconfinement properties of the medium, due to the large mass of its constituent charm quarks. Particles with

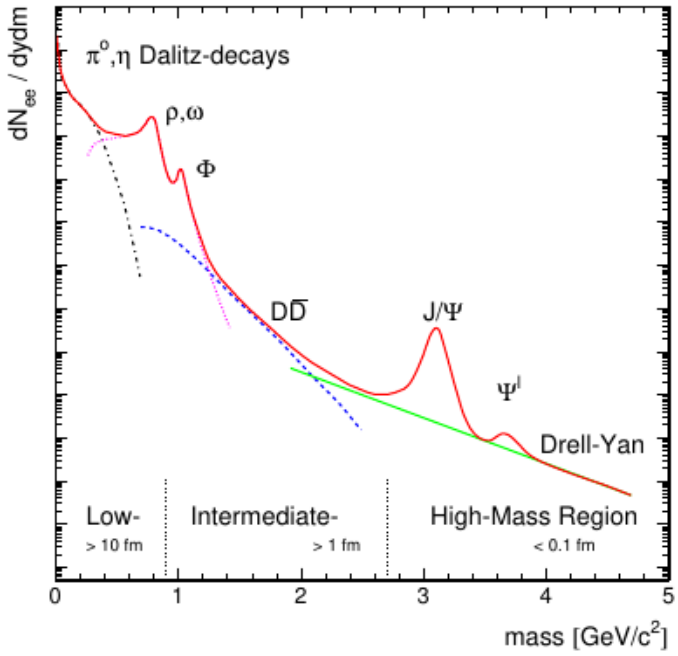

Figure 3.2: A sketch of the dilepton production rate in highly energetic Heavy Ion Collisions. The picture is taken from [69].

lighter constituent quarks, like the up and down, and, to some degree, the strange quark, are naturally more susceptible to the chiral aspect of the transition, see e.g. [70, 71]. Also, we introduce in-medium, or thermal, low mass dileptons and photons, which are in the present study investigated as probes for dissipative features of the Quark Gluon Plasma. Because low mass dileptons stem from hadrons comparatively lighter than e.g. charmonium, their study effectively probes the chiral aspect of the Quark Gluon Plasma, as mentioned above. Additionally, since heavy quark pairs usually have high branching ratios to decay into dileptons, from the point of view of experiments, charmonia yield strong signals in the dilepton production rate as a function of the dilepton pair mass, see the sketch in Fig. 3.2 from [69], and thus the measured dilepton rate is the central experimental evidence for both of the probes treated in this work.

3.2.1 Dilepton and photon rates

The low mass dileptons and photons, that are emitted from the QGP phase, stem mainly from quark-antiquark annihilation processes inside the plasma [69]. The number of leptons produced per phase space volume inside the heat bath of quarks and gluons can

be factored into a leptonic and a hadronic part, such that [69, 72]

$$\frac{\mathrm{d}^8 N_{l^+l^-}}{\mathrm{d}^4x\mathrm{d}^4q} = L^{\mu\nu}(q)W_{\mu\nu}(q), \tag{3.1}$$

with the leptonic part

$$\begin{aligned} L^{\mu\nu}(q) = \frac{(4\pi\alpha)^2}{M^4}\int\frac{\mathrm{d}^3p_+}{(2\pi)^3 2p_{0,+}}\int\frac{\mathrm{d}^3p_-}{(2\pi)^3 2p_{0,-}}\times \\ \times\,\mathrm{tr}\left\{\left(\not{p}_+ - m\right)\gamma_\mu\left(\not{p}_- + m\right)\gamma_\nu\right\}\delta^{(4)}(q-p_+-p_-) \\ = -\frac{\alpha^2}{6\pi^3M^2}\left(g_{\mu\nu}-\frac{q_\mu q_\nu}{M^2}\right), \end{aligned} \tag{3.2}$$

where $\alpha = 1/137$ is the electromagnetic fine structure constant, the lepton energies $p_{0,\pm} = \sqrt{m_l^2 + \vec{p_\pm}^{\,2}}$ and the dilepton invariant mass $M^2 = (p_+ + p_-)^2$. The coupling to the hadronic sector is realized by the other part, which connects the production rate (3.1) with the QCD electromagnetic current,

$$j_\mu^{em} = \sum_f Q_f \bar{q}\gamma_\mu q, \tag{3.3}$$

via the Fourier transform of the (real time) electromagnetic current correlator [72]

$$W_{\mu\nu}(q) = \int \mathrm{d}^4x \mathrm{e}^{-iqx}\langle j_\mu^{em}(x) j_\nu^{em}(0)\rangle. \tag{3.4}$$

Note that in the current (3.3) the sum runs over all flavors, where Q_f is the electric charge of the corresponding quark, and by restricting the sum to light flavors, for example, the hadronic contribution is sensitive to low mass dileptons from the plasma phase. As will be elaborated later in more detail in Sec. 4.1, the real time current correlation function is directly related to the underlying spectral function, and hence the space integrated dilepton rate in turn is given by [72, 73]

$$\frac{\mathrm{d}^4 N_{l^+l^-}}{\mathrm{d}q^4} = C_{em}\frac{\alpha^2 g^{\mu\nu}\rho_{\mu\nu}(q)}{6\pi^3 q^2(\mathrm{e}^{\beta q_0}-1)}. \tag{3.5}$$

Note that the Dirac delta in the leptonic expression (3.2) enforces $M^2 = q^2$. Similarly, the photon rate is [64, 72]

$$q_0\frac{\mathrm{d}^3 N_\gamma}{\mathrm{d}q^3} = C_{em}\frac{\alpha\rho_T(q_0 = |\vec{q}|, T)}{4\pi^2\,(\mathrm{e}^{\beta q_0}-1)}, \tag{3.6}$$

with ρ_T the component of the spectral function polarized transversally with respect to spatial momentum $\vec{q}$, and $C_{em} = \sum_f Q_f^2$ is the sum of squared charges of the quarks contained in the current. Note that we have explicitly inserted it in these formulas, i.e. in this work the correlation functions obtained from lattice computations, and therefore

generally the spectral functions, do not carry this factor by convention. However, for physical predictions, we can just multiply e.g. 5/9 for two flavors or 6/9 for three flavors. The dependence of expression (3.1) on (the Fourier transform of) the QCD electromagnetic current is a central relation in the current work. The Euclidean time version of this current correlator can be calculated in Lattice Gauge Theory, and thus is non-perturbatively accessible from theory. However, the problem in that case is to relate the Euclidean correlator to the spectral density. Unlike the direct relation (3.5), the spectral function yields the Euclidean (imaginary time) correlator from an integral equation,

$$G(\tau) = \frac{1}{2\pi} \int_0^\infty \mathrm{d}q_0 \rho(q,T) K(\tau, q_0, T), \tag{3.7}$$

which weights the spectral function with a kernel

$$K(\tau, q_0, T) = \frac{\cosh\left(q_0\left[\tau - 1/(2T)\right]\right)}{\sinh\left(q_0/(2T)\right)}. \tag{3.8}$$

This equation is the pillar on which deep theoretical understanding of the features of the Quark Gluon Plasma is based. Its solution, i.e. obtaining the spectral density $\rho(q_0)$ from a given correlation function $G(\tau)$, is a highly nontrivial problem, and especially the extraction of non-perturbative information from a discrete set of input data, obtained from lattice computations, is the topic of the rest of this work. The intimate and direct connection of the spectral density with the measured dilepton production rate sketched above demonstrates how signals, that show up as bumps for e.g. J/ψ particle and the ρ resonance in Fig. 3.2, will also be visible in the spectral density. In fact, for vanishing momentum, $M^2 = q_0^2$, the dilepton rate equals the spectral density as a function of q_0 apart from a constant factor and the Bose distribution $n_B(q_0) = 1/\left(\mathrm{e}^{\beta q_0} - 1\right)$. This illustrates how definite particle states will appear as peaks in the spectral function, with a width antiproportional to the state's lifetime.

3.2.2 Charmonium as a probe

Before the QGP was finally discovered, a now famous paper proposed to use the suppression of charmonium ($c\bar{c}$) yields in heavy ion collisions as an indicator of QGP formation [63]. The authors argued that the anti-screening mechanism in vacuum QCD, which supposedly leads to confinement of color charges, would be replaced in a thermalized medium by a screening mechanism analogous to Debye screening in a plasma. Taking the potential that binds the charm and anti-charm quarks together at zero temperature to be the Cornell potential,

$$V(r) = -\frac{\alpha(r)}{r} + \sigma r, \tag{3.9}$$

we see from the component linear in the binding radius r that for $\sigma > 0$ liberation of the quarks into single particles as such can never occur. However, embedded in a deconfined

medium the interactions would be modified by color charges that surround it, to yield

$$V(r) \longrightarrow V(r)\mathrm{e}^{-r/r_D(T)}. \tag{3.10}$$

Here $r_D(T)$ is the effective screening radius, and from the above expression we see that the interactions between the charm and anti-charm quarks are strongly suppressed for $r \gtrsim r_D(T)$, compared to the vacuum potential. The Debye radius shrinks with rising temperature, leading to a dissociation of the quark antiquark pair as soon as the Debye radius becomes smaller than the corresponding binding radius of the meson. Considering that there is a series of well known excited bound states, which have a higher energy and generally exhibit a larger binding radius r_n, the higher their energy is, these are thus expected to dissociate as soon as $r_n > r_D(T)$. If one can theoretically determine the radii r_n of the states as well as the Debye radius r_D induced by the medium, or alternatively directly compute the dissociation temperatures T_n of the corresponding states, the abundance or absence of such states at different times in a HIC event would constitute a simple thermometer to measure the temperature of the QGP [17]. The theoretical idea of Debye screening in the QGP is very pictorial and simple, and our presentation on the matter remains rather qualitative. However, it suffices to outline a number of important points to be addressed in the first place, if charmonia and their suppression are to be utilized as a probe in the experiment:

1. Are there other mechanisms that affect charmonium states inside a QGP, i.e. additional suppression or competing enhancement effects?

2. What about the other stages of a HIC event? Is there any suppression/enhancement of $c\bar{c}$ pairs before the equilibrated plasma phase or afterwards, upon the freezeout to hadrons?

3. How to precisely define dissociation temperatures?

An example for the first point is the expected *Loss of Feed-Down* in an equilibrated QGP, see [74, 75] and references therein. Excited charmonium states in the vacuum have finite branching fractions to decay into the charmonium ground state. When a ground state charmonium yield is compared in R_{AA}, then one has to take into account that not all of the measured charmonia in the vacuum correspond to primary charmonia produced in the initial collision, but also stem from decay of higher excited states. This is complicated by the fact that in a QGP, because of the *sequential melting* picture laid out above, this feed-down is decreased, as the excited states may dissociate before being able to feed the lower states. This also emphasizes the need for an accurate and consistent definition of dissociation temperatures.

The second point constitutes a large class of effects, which are all together termed *Cold Nuclear Matter* (CNM) effects. These include modifications of the parton distribution function (pdf) of the nucleon inside the colliding hadrons, compared to the pdf of a single nucleon in a *pp* collision, scattering contributions inside the nuclei, and the early absorption of produced charmonia before they reach the QGP phase, see e.g. [74,

76]. Because these effects are all caused by the much larger size of a gold or led nucleus compared to a proton, they can be studied by performing proton on nucleus (pA) collisions.

Concerning the definition of a dissociation temperature, one has many different possibilities. As examples we give here the free energy of a heavy quark-antiquark pair, which saturates at some distance r, and the value $F(r = \infty, T)$ can serve as an indicator when the state has melted. A definition that is very close to this idea is revolving the interquark potential $V(r, T)$, which can be computed in QCD in the framework of a *hard thermal loop resummation* [77, 78]. The result is in general complex, with the real part governing the screening behavior, and the imaginary part describing scattering of the light medium constituents with the heavy quarks. This is a very active area of research in the context of non-relativistic heavy quark physics, and the potential can also be matched to, or used in conjunction with, Lattice QCD results. See e.g. [79] for a quantitative description and application. Another possibility relies on directly extracting (at least the relevant part of) the spectral function of corresponding correlation functions and monitoring the disappearance of a peak [74]. For more details on the physics of heavy quarks and an extensive review on the corresponding approaches, see e.g. [52].

The complications presented above are very conceptual, and a lot of experimental knowledge, theoretical models and careful argumentation is needed to successfully compare results obtained from purely theoretical QCD to experimental yields, which renders it a field in its own right. In Lattice QCD, we have the Quark Gluon Plasma at hand in a non-perturbative fashion, that is yet unspoiled by the above complications. Therefore, we can directly explore the theory using numerical techniques, and, for example, the determination of dissociation temperatures of quarkonium bound states already embodies a very tough problem on its own, see e.g. [12].

4 Spectral functions

Spectral functions are the central quantity to study in this work. As we have seen explicitly in Sec. 2.6.1, physical particles of certain quantum numbers are related to different correlation function channels. A spectral function encodes the entire underlying properties of a given channel, and in the following sections we eludicate, in a very general framework, the connections of the unique, channel specific spectral function to different correlation functions. The latter hence constitute, from this perspective, different ways to view the underlying spectral function. From there, we present and perform computations of non-interacting spectral functions for a range of channels in QCD, both in the continuum formulation, as well as in a discretized lattice framework using Wilson fermions. They already contain basic features and shapes, which are, as a next step, combined with phenomenological computations in order to develop an idea what the spectral functions should look and behave like in the fully interacting case. Finally, we will provide solutions for the light quark vector current from perturbative methods in hot QCD, and quickly review a possible solution from the AdS/CFT correspondence.

4.1 Correlators and spectral functions

The relations that are presented in this section are worked out in many basic textbooks on finite temperature quantum field theory and review articles/papers [12, 19, 42, 80] and doctoral theses [81, 82], which we follow closely. The goal is to introduce the real time correlator, which we already encountered shortly in the last section, the retarded correlator, which is conceptually important for the use of *linear response theory* treated in Sec. 4.3.2 to estimate our expectations on the approximate behavior of spectral functions, and finally the Euclidean correlator, which is an important output observable of numerical computations of Lattice QCD.

To start, note that every expectation value in this section is to be understood as a thermal average at inverse temperature β, i.e. we define

$$\langle A(x)\rangle \equiv \langle A(x)\rangle_\beta = \sum_n \langle n|\hat{\rho}(\beta)A(x)|n\rangle, \tag{4.1}$$

with the statistical ensemble density

$$\hat{\rho}(\beta) = Z^{-1}\exp(-\beta\hat{H}), \tag{4.2}$$

which is not to be confused with the spectral function ρ, the partition function Z, and the sum counting all eigenstates of the Hamiltonian $\hat{H}$. For convenience, we drop the hats on all other operators, as they should be identifiable from context. Furthermore, we exemplarily show the connections for operators that depend only on one time coordinate, as opposed to a four dimensional space time. This keeps the discussion simpler, and we will reintroduce it when coming to the Euclidean correlator. In the last section we have already seen the real time correlation function of the electromagnetic current in QCD, and more generally we can write

$$G^{>}(t) \equiv \langle A(t)A(0)\rangle, \qquad G^{<}(t) \equiv \langle A(0)A(t)\rangle = G^{>}(-t), \tag{4.3}$$

where the last equality follows from homogeneity of time. Time translation $A(t) = \mathrm{e}^{iHt}A(0)\mathrm{e}^{-iHt}$ and a unit operator $\mathbf{I} = \sum_n |n\rangle\langle n|$ can be used to express $G^{>}(t)$ as a sum over states,

$$G^{>}(t) = \frac{1}{Z}\sum_{mn} \mathrm{e}^{-\beta E_n}\mathrm{e}^{it(E_n - E_m)} \left\|\langle n|A(0)|m\rangle\right\|^2, \tag{4.4}$$

with the Boltzmann weight $\exp(-\beta E_n)$ and the (real) time dependence showing as oscillations. However, note that allowing t to take complex values, the correlator diverges unless $-\beta \leq \mathrm{Im}(t) \leq 0$ for $G^{>}(t)$ and $0 \leq \mathrm{Im}(t) \leq \beta$ for $G^{<}(t)$. From translation in imaginary time we additionally have the Kubo-Martin-Schwinger (KMS) relation,

$$G^{>}(t) = G^{<}(t + i\beta). \tag{4.5}$$

We form the linear combination

$$G(t) = i\left(G^{>}(t) - G^{<}(t)\right), \tag{4.6}$$

with the spectral function being defined as its Fourier transform,

$$\begin{aligned}\rho(\omega) = \frac{1}{2\pi i}\int_{-\infty}^{\infty} \mathrm{d}t \mathrm{e}^{i\omega t} G(t) &= \frac{1}{2\pi}\int_{-\infty}^{\infty} \mathrm{d}t \mathrm{e}^{i\omega t}\left(G^{>}(t) - G^{<}(t)\right) \\ &= G^{>}(\omega) - G^{<}(\omega).\end{aligned} \tag{4.7}$$

Using the KMS relation, it follows for the Fourier transforms that $G^{<}(\omega) = G^{>}(-\omega) = \mathrm{e}^{-\beta\omega}G^{>}(\omega)$, and thus they can be written as

$$G^{>}(\omega) = \frac{\mathrm{e}^{\beta\omega}}{\mathrm{e}^{\beta\omega} - 1}\rho(\omega), \qquad G^{<}(\omega) = \frac{1}{\mathrm{e}^{\beta\omega} - 1}\rho(\omega). \tag{4.8}$$

This leads to the Fourier transform of the explicit expression (4.4)

$$\rho(\omega) = \frac{1}{Z}\sum_{m,n} \mathrm{e}^{-\beta E_n}\left\{\delta(\omega + E_n - E_m) - \delta(\omega + E_m - E_n)\right\}\left\|\langle n|A(0)|m\rangle\right\|^2, \tag{4.9}$$

which reveals the general peak structure of the spectral function, as well as its symmetry properties $\rho(-\omega) = \rho(\omega)$ and $\mathrm{Im}(\rho(\omega)) = 0$. The *retarded correlator* is defined as the Fourier transform of $G(t)$ over the positive half axis,

$$\begin{aligned} G^R(\omega) = \int_0^\infty \mathrm{d}t \mathrm{e}^{i\omega t} G(t) &= \frac{i}{2\pi} \int_0^\infty \mathrm{d}t \int_{-\infty}^\infty \mathrm{d}\omega' \mathrm{e}^{i(\omega-\omega'+i\epsilon)t} \left[G^>(\omega') - G^<(\omega')\right] \\ &= \int_{-\infty}^\infty \mathrm{d}\omega' \frac{\rho(\omega')}{\omega - \omega' + i\epsilon}, \end{aligned} \tag{4.10}$$

where we introduced a small but finite quantity ϵ to ensure convergence of the integral. By using (4.7) and the definition of the retarded correlator (4.10) we can write equation (4.7) as

$$\rho(\omega) = \frac{1}{2\pi i} \left(G^R(\omega) - G^{R\dagger}(\omega)\right) = \frac{1}{\pi} \mathrm{Im} G^R(\omega), \tag{4.11}$$

which is the desired connection between the retarded correlation function and the spectral density.

Coming to the Euclidean correlation function, note that the structure of the correlators above in imaginary direction is characterized by the finite size β of the interval, the periodicity and thus the KMS relation. As such, the Euclidean correlator is defined as the forward real time correlator on the imaginary axis,

$$G_E(\tau) = G^>(-it), \tag{4.12}$$

and to make a connection to the Euclidean correlation functions from lattice computations, we generalize to a $3+1$ dimensional space time, $x = (t, \vec{x})$ and $p = (\omega, \vec{p})$. The Euclidean version of the current correlator (3.4) reads

$$G_H(\tau, \vec{x}) = \langle J_H(\tau, \vec{x}) J_H^\dagger(0, \vec{0}) \rangle, \tag{4.13}$$

where the symbolic index H denotes different Dirac structures in the current J, see Sec. 2.6. The Euclidean correlator is most useful when projected to definite momentum,

$$G_H(\tau, \vec{p}) = \int \mathrm{d}^3 x \mathrm{e}^{-i\vec{p}\vec{x}} \langle J_H(\tau, \vec{x}) J_H^\dagger(0, \vec{0}) \rangle, \tag{4.14}$$

and it is straightforward to connect it to the forward propagator in momentum space by expressing it as its Fourier transform,

$$\begin{aligned} G_H(\tau, \vec{p}) = \int \mathrm{d}^3 x \mathrm{e}^{-i\vec{p}\vec{x}} G^>(-it, \vec{x}) &= \int \mathrm{d}^3 x \int_{-\infty}^\infty \frac{\mathrm{d}\omega}{2\pi} \int \mathrm{d}^3 q \ \mathrm{e}^{i(\vec{q}-\vec{p})\vec{x} - \omega\tau} G^>(\omega, \vec{q}) \\ &= \int_{-\infty}^\infty \frac{\mathrm{d}\omega}{2\pi} \mathrm{e}^{-\omega\tau} G^>(\omega, \vec{p}). \end{aligned} \tag{4.15}$$

Splitting the integration at zero and transforming the integral over the negative half axis to be over the positive half axis, we utilize equation (4.8) and $G^{>}(-\omega) = \mathrm{e}^{-\beta\omega} G^{>}(\omega)$ to arrive at

$$\begin{aligned} G_H(\tau, \vec{p}) &= \int_0^\infty \frac{\mathrm{d}\omega}{2\pi} \left(\frac{\mathrm{e}^{\omega(\beta-\tau)} + \mathrm{e}^{\omega\tau}}{\mathrm{e}^{\beta\omega} - 1} \right) \rho(\omega, \vec{p}) \\ &= \int_0^\infty \frac{\mathrm{d}\omega}{2\pi} \frac{\cosh\left(\omega(\tau - \beta/2)\right)}{\sinh(\omega\beta/2)} \rho(\omega, \vec{p}) \\ &\equiv \int_0^\infty \frac{\mathrm{d}\omega}{2\pi} K(\tau, \omega, T) \rho(\omega, \vec{p}), \end{aligned} \tag{4.16}$$

where the spectral function still depends on the spatial momentum we wish to project to; in this work this is generally $\vec{p} = 0$. Note that we left the temperature dependence of the spectral function implicit. Sometimes it is more useful to consider the relation written in units of temperature,

$$\frac{G_H(\tau, T)}{T^3} = \frac{1}{2\pi T^2} \int_0^\infty \mathrm{d}\left(\frac{\omega}{T}\right) K\left(\tau T, \omega/T\right) \rho(\omega/T). \tag{4.17}$$

In these derivations, the spatial coordinates were treated on the same footing, but it is possible to follow an analogous idea and project out two spatial directions (by convention these are the x and y coordinates) and the temporal direction, leaving the z direction as the relevant space time coordinate. This approach leads to the *screening correlator*, with $\vec{p}_T = (p_x, p_y), \vec{x}_T = (x, y)$,

$$G_H^{\mathrm{scr}}(z, T) = \int_0^{1/T} \mathrm{d}\tau \int \mathrm{d}x \mathrm{d}y \mathrm{e}^{i(\omega_n \tau - \vec{p}_T \vec{x}_T)} \left\langle J_H(\tau, \vec{x}) J_H^\dagger(0, \vec{0}) \right\rangle \Big|_{\omega_n = 0, \vec{p}_T = 0}, \tag{4.18}$$

and is sketched in e.g. [19]. In order to derive it, note that the periodicity implied by the KMS relation (4.5) leads to the discrete Matsubara frequencies $\omega_n = 2\pi n T$ when Fourier transforming the Euclidean correlator in frequency, and the resulting expression reads

$$G_H(i\omega_n, \vec{p}) = \int \mathrm{d}^3 x \int \mathrm{d}\tau \mathrm{e}^{i\omega_n \tau - i\vec{p}\vec{x}} G_H(\tau, \vec{x}). \tag{4.19}$$

With $G_H(\tau, \vec{x}) = G^{>}(-i\tau, \vec{x})$ from (4.12), and its connection to the spectral function (4.8), we arrive at

$$\begin{aligned} G_H(i\omega_n, \vec{p}) &= \int \mathrm{d}^3 q \int_{-\infty}^\infty \mathrm{d}\omega \delta(\vec{p} - \vec{q}) \frac{e^{(i\omega_n - \omega)\beta} - 1}{1 - \mathrm{e}^{-\beta\omega}} \frac{\rho(\omega, \vec{q})}{i\omega_n - \omega} \\ &= \int_{-\infty}^\infty \mathrm{d}\omega \frac{\rho(\omega, \vec{p})}{\omega - i\omega_n}. \end{aligned} \tag{4.20}$$

Comparing this expression with the integral connection between $G_R(\omega)$ and $\rho(\omega)$ in equation (4.10), we can connect it with the Euclidean correlator $G_H(i\omega_n)$ via analytic continuation,

$$G_H(i\omega_n \to \omega + i\epsilon) = G_R(\omega). \tag{4.21}$$

Correspondingly, the imaginary part of the Euclidean correlator is related to the spectral function analogously to (4.11),

$$\rho(\omega) = \frac{1}{\pi}\mathrm{Im}G_H(i\omega_n \to \omega + i\epsilon). \tag{4.22}$$

Returning to the computation of the screening correlator, we can put equation (4.20) to good use in the following. Performing the integrations (4.18) by inserting appropriate Fourier transforms, the screening correlator reads,

$$\begin{aligned} G_H^{\mathrm{scr}}(i\omega_n, \vec{p}_T, z) &= \int_0^\beta \mathrm{d}\tau \int \mathrm{d}^2x_T \mathrm{e}^{i\omega_n\tau - i\vec{P}_T\vec{x}_T} G_H(\tau, \vec{x}) \\ &= \int \mathrm{d}p_z \int \mathrm{d}^2q_T \frac{1}{\beta}\sum_{n'} \delta_{n,n'}\delta(\vec{p}_T - \vec{q}_T)\mathrm{e}^{ip_z z} G_H\left(i\omega_{n'}, \vec{q}_T, p_z\right) \\ &= \int \mathrm{d}p_z \mathrm{e}^{ip_z z} G_H\left(i\omega_n, \vec{p}\right), \end{aligned} \tag{4.23}$$

where $\int_0^\beta \mathrm{e}^{i\tau(\omega_n - \omega_{n'})} = \beta\delta_{n,n'}$ from the frequency transform yields the Kronecker Delta. Inserting (4.20) and writing

$$G_H(i\omega_n, \vec{p}) = \int_{-\infty}^{\infty} \mathrm{d}\omega \frac{\rho(\omega, \vec{p})}{\omega - i\omega_n} = 2\int_0^\infty \mathrm{d}\omega \frac{\rho(\omega, \vec{p})}{\omega^2 + \omega_n^2}\omega, \tag{4.24}$$

in the limits $\vec{p}_T \to 0$ and $\omega_n \to 0$, we finally have an expression that is to be contrasted to (4.16),

$$G_H^{\mathrm{scr}}(z, T) = \int_0^\infty \frac{2}{\omega}\mathrm{d}\omega \int_{-\infty}^{\infty} \mathrm{d}p_z \mathrm{e}^{ip_z z}\rho(\omega, p_z, T). \tag{4.25}$$

4.2 Non-interacting spectral functions

With the theoretical concept of the spectral function at hand, as introduced in the foregoing section, and its connection with the retarded and the Euclidean correlation functions, respectively, we can present computations of mesonic spectral function in the non-interacting limit. Because of asymptotic freedom, this corresponds to evaluating

correlation functions at infinitely high temperature. These free spectral functions are an important intermediate step towards the extraction of spectral information from interacting correlation functions. In this section we derive expressions for free mesonic spectral functions in the continuum, which can be computed analytically and thus allow for an analysis of the general structure of spectral functions and correlation functions, respectively. These computations have been first done in [83, 84] for degenerate quark masses, and will be extended to non-degenerate quark masses in the next section.

4.2.1 Free continuum spectral functions – degenerate quark masses

Starting out with a general correlation function in the channel H,

$$G_H(\tau, \vec{x}) = \langle J_H(\tau, \vec{x}) J_H^\dagger(0, \vec{0}) \rangle, \tag{4.26}$$

we can write to lowest order in the loop expansion in Fourier space

$$G_H(P) = -T \sum_n \int \frac{d^3k}{(2\pi)^3} \mathrm{tr} \left[S(K) \Gamma_H S(P+K) \gamma_0 \Gamma_H^\dagger \gamma_0 \right], \tag{4.27}$$

with $P = (i\omega_l, \vec{P})$ and ω_l the (bosonic) Matsubara frequencies $\omega = 2\pi l T$ of the meson. The momentum dependent quantity

$$S(P) = -\frac{1}{i\widetilde{\omega}_n \gamma_0 - \gamma_i p_i - m} = -\int_{-\infty}^{\infty} \frac{d\omega}{2\pi} \frac{\rho_F(P)}{i\widetilde{\omega}_n - \omega} \tag{4.28}$$

is the quark propagator with its corresponding fermionic Matsubara frequency $\widetilde{\omega}_n = (2n+1)\pi T$. The underlying non interacting quark spectral function is easily obtained by comparing the left hand side and the right hand side, giving

$$\rho_F(K) = \rho(K)(\not{K} + m) = 2\pi \mathrm{sgn}(k_0) \delta(K_0^2 - \omega_K^2)(\not{K} + m), \tag{4.29}$$

with $\rho(K)$ being free of any γ structure and the energy of a propagating quark given by $\omega_K = \sqrt{\vec{K}^2 + m^2}$. As has been shown in section 4.1, from the Euclidean correlator in 4-momentum space (4.27) we can arrive at an expression for the free meson spectral function by considering its imaginary part, analytically continued to the real frequency axis. Plugging in the spectral representation of the fermionic propagator yields

$$\begin{aligned} &\rho_H(P = (\omega, \vec{p}), m) = 2\mathrm{Im} G_H(i\omega_n \to \omega + i0^+, \vec{p}) \\ &= N_c \int \frac{d^4k}{(2\pi)^4} \rho(K)\rho(R) \mathrm{tr} \left\{ (\not{K} + m) \Gamma_H (\not{R} + m) \gamma_0 \Gamma_H^\dagger \gamma_0 \right\} \left\{ n_F(k_0) - n_F(r_0) \right\}, \end{aligned} \tag{4.30}$$

where $R = K + P$ and $n_F(k_0)$ is the Fermi distribution at temperature T. Apart from the tree level approximation, this is a very general result, which results in the non interacting mesonic spectral function as a function of the frequency ω, the meson's momentum $\vec{p}$, the temperature T, the quark mass m and the specific channel $\Gamma_H = 1, \gamma_i, \gamma_\mu, \gamma_5, \gamma_5\gamma_i, \gamma_5\gamma_\mu$.

	Γ_H	$a_H^{(1)}$	$a_H^{(2)}$	$a_H^{(3)}$
ρ_S	$\mathbb{I}$	1	-1	1
ρ_{PS}	γ_5	1	-1	-1
$\rho_{V,00}$	γ_0	1	1	1
$\rho_{V,ii}$	γ_i	3	-1	-3
$\rho_{V,\mu\mu}$	γ_μ	2	-2	-4
$\rho_{AV,00}$	$\gamma_5\gamma_0$	1	1	-1
$\rho_{AV,ii}$	$\gamma_5\gamma_i$	3	-1	3
$\rho_{AV,\mu\mu}$	$\gamma_5\gamma_\mu$	2	-2	4

Table 4.1: The coefficients of the Dirac structure occurring in the non interacting spectral functions.

It is easier to consider certain special cases, namely vanishing momentum, vanishing mass, and the simplest case of vanishing mass and momentum, although in principle the integrals can be performed and expressed in terms of polylogarithms. Since in this work we exclusively investigate spectral functions at vanishing external spatial momentum $\vec{p} = 0$, we will start from formula (4.30). An additional advantage of starting out so early in the computation is, that we will gain inside into how the different regimes of the spectral function arise mathematically, and can try to draw conclusive implications for the physics of meson states. The computation involves several different steps, starting with the trace over the γ-matrices, which we conventionally take to be defined by

$$\gamma^{0\dagger} = \gamma^0,\ \gamma^{i\dagger} = -\gamma^i,\ \gamma_5^\dagger = \gamma_5,\ \{\gamma^\mu, \gamma^\nu\} = 2g^{\mu\nu}, \tag{4.31}$$

and the metric tensor having the 'mostly minus' signature $g^{\mu\nu} = \mathrm{diag}(1, -1, -1, -1)$. Since in the trace only the terms proportional to $\sim \not{K}\not{R}$ and $\sim m^2$ yield an even number of γ-matrices, the result can be cast into the form

$$\mathrm{tr}\left\{(\not{K} + m)\Gamma_H(\not{R} + m)\gamma_0\Gamma_H^\dagger\gamma_0\right\} = a_H^{(1)}K_0R_0 + a_H^{(2)}\vec{K}\cdot\vec{R} + a_H^{(3)}m^2, \tag{4.32}$$

with the coefficients $a_H^{(i)}$ for the corresponding channel H given in Tab. 4.2.1. Next, the fermion propagators contain Dirac delta functions which cancel most of the integrals. In order to see this, rewrite

$$\begin{aligned}\delta(K_0^2 - \omega_K^2)\delta(R_0^2 - \omega_R^2) = \frac{1}{4\omega_K\omega_R}&\left[\delta(K_0 - \omega_K) + \delta(K_0 + \omega_K)\right] \\ &\times\left[\delta(R_0 - \omega_R) + \delta(R_0 + \omega_R)\right],\end{aligned} \tag{4.33}$$

and the expression for the meson spectral function becomes

$$\begin{aligned}\rho_H(\omega) = 2\pi N_c \int_{\vec{K}} \Bigg\{ & \\ & + \left(a_H^{(1)} + a_H^{(2)} \frac{\vec{K}\cdot\vec{R}}{\omega_K \omega_R} + a_H^{(3)} \frac{m^2}{\omega_K \omega_R} \right) \left[n_F(\omega_K) - n_F(\omega_R) \right] \delta(\omega + \omega_K - \omega_R) \\ & + \left(a_H^{(1)} - a_H^{(2)} \frac{\vec{K}\cdot\vec{R}}{\omega_K \omega_R} - a_H^{(3)} \frac{m^2}{\omega_K \omega_R} \right) \left[1 - n_F(\omega_K) - n_F(\omega_R) \right] \delta(\omega - \omega_K - \omega_R) \\ & - (\omega \to -\omega) \Bigg\}.\end{aligned} \tag{4.34}$$

In the limit $\vec{p} \to 0$ the two energies degenerate, $\omega_K \to \omega_R$, and the integration in the second and fourth line of (4.34) can be performed by standard techniques. The Dirac delta function fixes the quark energies to be $\omega_{K/R} = \omega/2$ each, and thus this part of the spectral function describes the state of a quark-antiquark pair at a total energy ω. In the first and third line of the spatial integration, however, the Dirac delta function contains no integration variable anymore in the case $\omega_K \to \omega_R$. To investigate this, for now leave a small momentum $\vec{p}$ in ω_R and Taylor expand around $\vec{p} = 0$,

$$\begin{aligned}\omega_R = \sqrt{(\vec{k}+\vec{p})^2 + m^2} = \omega_K \sqrt{1 + \frac{2kpx + p^2}{\omega_K^2}} &= \omega_K + \frac{kpx}{\omega_K} + \mathcal{O}(p^2) \\ &\equiv \omega_K + \alpha + \mathcal{O}(p^2),\end{aligned} \tag{4.35}$$

with $x = \cos(\theta)$ the angle between the two vectors. Applying this to the product of Dirac delta function and difference of Fermi distributions above, we find

$$\left[n_F(\omega_K) - n_F(\omega_K + \alpha) \right] \delta(\omega - \alpha) = -\frac{n_F(\omega_K + \alpha) - n_F(\omega_K)}{\alpha} \alpha \delta(\omega - \alpha), \tag{4.36}$$

and we can identify the difference quotient with the derivative,

$$\frac{d}{d\omega_K} n_F(\omega_K) = \lim_{\alpha \to 0} \frac{n_F(\omega_K + \alpha) - n_F(\omega_K)}{\alpha}. \tag{4.37}$$

On the other hand, we can identify in the other term

$$\alpha \delta(\omega - \alpha) \equiv \omega \delta(\omega - \alpha), \tag{4.38}$$

in the sense that the integration (4.17), which finally yields the Euclidean correlator from the spectral function, for small frequencies reads

$$\int \mathrm{d}\omega \frac{1}{\omega} \alpha \delta(\omega - \alpha) f(\omega) = f(\alpha) \overset{\alpha \to 0}{\longrightarrow} f(0) = \int \mathrm{d}\omega \frac{1}{\omega} \omega \delta(\omega) f(\omega) \tag{4.39}$$

for an arbitrary function $f(\omega)$. Collecting all factors and performing the above procedures for all four terms in (4.34), we arrive at the massive free spectral function in the limit of vanishing momentum,

$$\begin{aligned}\rho_H(\omega,m) = &\frac{N_c}{8\pi}\sqrt{1-\frac{4m^2}{\omega^2}}\omega^2\left(n_F(-\omega/2)-n_F(\omega/2)\right)\\ &\times\left\{\left(a_H^{(1)}-a_H^{(2)}\right)+\frac{4m^2}{\omega^2}\left(a_H^{(2)}-a_H^{(3)}\right)\right\}\Theta(\omega^2-4m^2)\\ &+2\pi\omega\delta(\omega)N_c\left\{\left(a_H^{(1)}+a_H^{(3)}\right)I_1+\left(a_H^{(2)}-a_H^{(3)}\right)I_2\right\}.\end{aligned} \tag{4.40}$$

The coefficients $a_H^{(n)}$ are the results of the traces over the different possible products of gamma matrices. They are hence channel dependent and can be computed via (4.32). For brevity, the results are given in Tab. 4.2.1. The integrals

$$I_1 = -2\int\frac{d^3K}{(2\pi)^3}\frac{d}{d\omega_{\vec{K}}}n_F(\omega_{\vec{K}}), \qquad \text{and} \qquad I_2 = -2\int\frac{d^3K}{(2\pi)^3}\frac{\vec{K}^2}{\omega_{\vec{K}}^2}\frac{d}{d\omega_{\vec{K}}}n_F(\omega_{\vec{K}}), \tag{4.41}$$

can be analytically computed in the case of vanishing mass. Owing to the Dirac delta function multiplying both I_1 and I_2, they only contribute to the behavior of the spectral function at zero frequency. Observe that this contribution vanishes identically in the pseudoscalar channel due to the coefficients $a_H^{(n)}$ canceling completely, while all other channels maintain a finite contribution. Comparing the integrands of (4.41), we see that $\vec{K}^2/(\vec{K}^2+m^2) < \vec{K}^2/\vec{K}^2 = 1$, and hence $I_2 < I_1$. Inserting the corresponding coefficients into (4.40), the vector current spectral function ρ_V thus exhibits a negative Delta peak at zero frequency, while the remaining channels show a positive peak.

Sending the mass to zero, utilizing the free dispersion relation $\omega_{\vec{K}}^2 = \vec{K}^2 + m^2$, we see that the remaining integrals degenerate, $I_1 = I_2 = T^2/6$, and equation (4.40) yields that also in the scalar channel the contribution at $\omega = 0$ vanishes identically at vanishing mass. This is an effect of the restauration of chiral symmetry above the chiral transition temperature, which degenerates the scalar and pseudoscalar spectral functions, and hence also their correlation functions. More generally for massless quarks, rewriting the term involving the fermi distribution,

$$\begin{aligned} n_F(\omega) &= \frac{1}{1+\mathrm{e}^{\omega/T}}\\ \Rightarrow 1-2n_F(\omega/2) &= \frac{\mathrm{e}^{\omega/(2T)}-1}{\mathrm{e}^{\omega/(2T)}+1} = \tanh(\omega/(4T)),\end{aligned} \tag{4.42}$$

we get in the zero mass limit of equation (4.40)

$$\rho_H(\omega) = \frac{N_c}{8\pi}\omega^2\tanh(\omega/(4T))\left(a_H^{(1)}-a_H^{(2)}\right)+\frac{\pi N_c}{3}T^2\omega\delta(\omega)\left(a_H^{(1)}+a_H^{(2)}\right). \tag{4.43}$$

Since the coefficient $a_H^{(3)}$ drops out, also the spectral functions for the vector and axialvector degenerate. The integration of this expression can be performed analytically to

yield the corresponding free, massless correlation functions at zero momentum. Inserting (4.43) into the mixed representation relationship (4.17), we obtain

$$\begin{aligned} &G_H(\tau, \vec{p}=0, m=0) \\ &\qquad = \frac{N_c T^3}{6}\left\{(a_H^{(1)}+a_H^{(2)}) + \frac{3}{2}(a_H^{(1)}-a_H^{(2)})\frac{3u+u\cos(2u)-2\sin(2u)}{\sin^3(u)}\right\}, \end{aligned} \tag{4.44}$$

with $u = 2\pi T(\tau - 1/(2T))$. The first term in this expression originates from the Dirac delta term in the spectral function, and thus constitutes the constant contribution of the free correlation function. As can be seen from the coefficients, it vanishes for the pseudoscalar, the scalar and the full vector channel. The second term carries the imaginary time dependence and diverges in the limit $u \to -\pi$ ($\tau \to 0$). At the midpoint, Taylor expansion to the order $\mathcal{O}(u^3)$ in both nominator and denominator yields

$$G_H(u) \xrightarrow{u\to 0} \frac{N_c T^3}{3} a_H^{(1)}, \tag{4.45}$$

showing that all correlation functions remain strictly positive. Of special interest in the context of the current work is the vector channel with its single components $\rho_{V,00} \equiv \rho_{00}$, $\rho_{V,ii} \equiv \rho_{ii}$ and $\rho_{V,\mu\mu} \equiv \rho_V$. Working with the coefficients from Tab. 4.2.1, we find for $N_c = 3$

$$\begin{aligned} \rho_{00} &= 2\pi T^2 \omega \delta(\omega), \\ \rho_{ii} &= \frac{3}{2\pi}\omega^2 \tanh(\omega/(4T)) + 2\pi T^2 \omega\delta(\omega), \\ \rho_V &= \frac{3}{2\pi}\omega^2 \tanh(\omega/(4T)) \end{aligned} \tag{4.46}$$

Apparently, the contribution proportional to the Dirac delta function appears in the temporal and the spatial channels, but exactly cancels out in the combination $\rho_V = \rho_{ii} - \rho_{00}$. Because the temporal direction is determined by charge conservation, the corresponding correlation function, given by (4.26) with $H = 0$ and Fourier transformed to the mixed representation, is a constant and defines the charge susceptibility χ_q,

$$G_{00}(\tau, \vec{p}=0) = \int_0^\infty \frac{d\omega}{2\pi}\rho_{00}(\omega)K(\omega,\tau,T) = T^3 \equiv \chi_q T. \tag{4.47}$$

4.2.2 Free continuum spectral functions – non-degenerate quark masses

The results developed so far describe so called *hidden* flavor meson states at both finite and zero quark mass, as two quarks of equal flavor are involved. However, *open* flavor

mesons contain two different quark flavors, and therefore different quark masses, so that for the two fermionic frequencies we get

$$\begin{aligned}\omega_K &= \sqrt{\vec{K}^2 + m_1^2} \\ \omega_R &= \sqrt{\vec{R}^2 + m_2^2} \overset{\vec{p}\to 0}{\longrightarrow} \sqrt{\vec{K}^2 + m_2^2} \neq \omega_K\end{aligned} \tag{4.48}$$

in the limit of vanishing momentum. The effects of non-degenerate quark masses in a free meson should now, for the first time, be investigated by extending the computations of the free continuum spectral functions [83, 84], keeping this difference in mind. Note, however, that we take the external spatial momentum to be zero from the beginning. We first focus on the structure of the Dirac delta functions and the sign functions and define for the rest

$$f(K_0, \vec{K}) \equiv \mathrm{tr}\left\{(\not{K} + m_1)\Gamma_H(\not{R} + m_2)\gamma_0\Gamma_H^\dagger\gamma_0\right\}\{n_F(K_0) - n_F(K_0 + \omega)\} \tag{4.49}$$

The frequency integration is carried out strictly over K_0 by using $R_0 = K_0 + \omega$, and the resulting expression is given by

$$\begin{aligned}\rho_H(\omega) = \frac{N_c}{(2\pi)^2}\int_{-\infty}^{\infty} \mathrm{d}K_0 \mathrm{d}^3K f(K_0, \vec{K}) \\ \times\delta(K_0^2 - \omega_K^2)\delta((K_0+\omega)^2 - \omega_R^2)\mathrm{sgn}(K_0)\mathrm{sgn}(K_0+\omega).\end{aligned} \tag{4.50}$$

The sign functions yield an overall minus for $K_0 \in [-\omega, 0]$, so we decompose

$$\begin{aligned}&\int_{-\infty}^{\infty}\mathrm{d}K_0 f(K_0,\vec{K})\delta(K_0^2-\omega_K^2)\delta((K_0+\omega)^2-\omega_R^2)\mathrm{sgn}(K_0)\mathrm{sgn}(K_0+\omega) \\ &= +\int_{-\infty}^{-\omega}\frac{\mathrm{d}K_0}{2\omega_K}f(K_0,\vec{K})\left[\delta(K_0-\omega_K)+\delta(K_0+\omega_K)\right]\delta((K_0+\omega)^2-\omega_R^2) \\ &\quad -\int_{-\omega}^{0}\frac{\mathrm{d}K_0}{2\omega_K}f(K_0,\vec{K})\left[\delta(K_0-\omega_K)+\delta(K_0+\omega_K)\right]\delta((K_0+\omega)^2-\omega_R^2) \\ &\quad +\int_{0}^{\infty}\frac{\mathrm{d}K_0}{2\omega_K}f(K_0,\vec{K})\left[\delta(K_0-\omega_K)+\delta(K_0+\omega_K)\right]\delta((K_0+\omega)^2-\omega_R^2).\end{aligned} \tag{4.51}$$

Because in every integral we exclusively have either $K_0 < 0$ or $K_0 > 0$, one of the two Dirac deltas always evaluates to zero, and Heaviside functions need to be inserted to keep track of whether $0 < \omega_K < \infty$, or $\omega < \omega_K < \infty$, or $0 < \omega_K < \omega$ follows from the other Dirac delta function. The resulting expression for the whole spectral function reads

$$\begin{aligned}\rho_H(\omega) = +\frac{N_c}{(2\pi)^2}\int\frac{\mathrm{d}^3K}{2\omega_K}\Big\{&f(K_0=-\omega_K,\vec{K})\delta((-\omega_K+\omega)^2-\omega_R^2)\Theta(\omega_K-\omega) \\ &-f(K_0=-\omega_K,\vec{K})\delta((-\omega_K+\omega)^2-\omega_R^2)\left[\Theta(\omega_K)-\Theta(\omega_K-\omega)\right] \\ &+f(K_0=\omega_K,\vec{K})\delta((\omega_K+\omega)^2-\omega_R^2)\Theta(\omega_K)\Big\}.\end{aligned} \tag{4.52}$$

Since one of the quarks must be heavier than the other, without loss of generality we assume $m_1 > m_2$ for the rest of the computation. This implies $\omega_K > \omega_R$ for all $\vec{K}$ in the integration range, and thus the last line of (4.52) vanishes upon evaluation of the Dirac delta function. The remaining Dirac delta function is transformed to read

$$\delta\left((-\omega_K+\omega)^2-\omega_R^2\right) \to \frac{\omega_K}{\omega}\delta\left(\vec{K}^2 - \left[\frac{1}{4\omega^2}\left(m_1^2-m_2^2+\omega^2\right)^2-\omega^2\right]\right), \tag{4.53}$$

and since $f(-\omega_K, \vec{K})$ only depends on $\vec{K}^2$, the angular integration is trivial. The Heaviside functions can be combined to yield an overall plus sign for $\omega_K > \omega$ and an overall minus sign for $0 < \omega_K < \omega$. Changing the integration variable to be $\vec{K}^2$ instead of $|\vec{K}|$, we get

$$\begin{aligned}\rho_H(\omega) = \frac{4\pi N_c}{(2\pi)^2}\int_0^\infty \mathrm{d}\vec{K}^2 \frac{|\vec{K}|}{4}\delta\left(K^2 - [\frac{1}{4\omega^2}(m_1^2-m_2^2+\omega^2)^2 - m_1^2]\right) \\ \times f(K_0=-\omega_K, K^2)\left[\Theta(\omega_K-\omega)-\Theta(\omega-\omega_K)\right].\end{aligned} \tag{4.54}$$

From here the Dirac delta function determines the value of $|\vec{K}|$, and the conditions in the stepfunctions can be rewritten in terms of m_1, m_2 and ω. Notice that, depending on the masses, the expression for $\vec{K}^2$ can become negative. To avoid imaginary parts showing up in the spectral function, we introduce another constraint,

$$\Theta\left(\frac{1}{4\omega^2}(m_1^2-m_2^2+\omega^2)^2-m_1^2\right) = \Theta\left(\omega-(m_1+m_2)\right)+\Theta\left(m_1-m_2-\omega\right), \tag{4.55}$$

and by furthermore rearranging the expression to be directly comparable to the mass-degenerate case (4.40), we arrive at the final expression

$$\begin{aligned}\rho_H(\omega) = {}& \frac{N_c}{32\pi}\sqrt{\left(\frac{m_1^2-m_2^2}{\omega^2}+1\right)^2-\frac{4m_1^2}{\omega^2}}\omega^2\left[n_F(-\omega_K)-n_F(-\omega_K+\omega)\right] \\ & \times\left[(a_H^{(1)}-a_H^{(2)})+2a_H^{(2)}\frac{m_1^2+m_2^2}{\omega^2}-4a_H^{(3)}\frac{m_1m_2}{\omega^2}-(a_H^{(1)}+a_H^{(2)})\left(\frac{m_1^2-m_2^2}{\omega^2}\right)^2\right] \\ & \times\left[\Theta\left(\omega-\sqrt{m_1^2-m_2^2}\right)-\Theta\left(\sqrt{m_1^2-m_2^2}-\omega\right)\right] \\ & \times\left[\Theta\left(\omega-(m_1+m_2)\right)+\Theta\left(m_1-m_2-\omega\right)\right],\end{aligned} \tag{4.56}$$

with $\omega_K = \frac{1}{2\omega}|m_1^2-m_2^2+\omega^2| \overset{m_1\geq m_2}{=} \frac{1}{2\omega}(m_1^2-m_2^2+\omega^2)$.

An especially intriguing feature in the mass-degenerate case is the appearance of a Dirac delta peak, or *zero mode*, at vanishing frequency in the limit of zero external momentum. As discussed in the derivation of that result, the peak with its prefactors I_1 and I_2 appears, because the two frequencies ω_K and ω_R become degenerate when the external 3-momentum $\vec{p}$ vanishes. In the case of non-degenerate quark masses, this

never happens and all Dirac delta functions are completely integrated out. From a physical point of view, this means that in the corresponding correlation functions there is *no* constant mode, independent of the channel under consideration. But if there is no constant contribution in the free case, then we do not expect one to arise upon the onset of interactions. Concretely, we can see on the level of the spectral function, that the 'mixed' vector current is not conserved in this case.

Comparing the results (4.40) and (4.56), it becomes clear that in the limit $m_1 \to m_2$, we reobtain the correct expression for all $\omega > 0$. The corresponding expression at degenerate masses for the Dirac delta peak obviously cannot be obtained anymore from (4.56), since the integration over the momentum is already carried out. However, it is very instructive to look at the spectral functions of the vector and pseudoscalar channels for several different masses m_1/T at fixed $m_2/T = 1$ in Fig. 4.1, and at fixed $m_2/T = 0$ in Figs. 4.2. The former allows us to study the limit of finite, but degenerate masses, while the latter gives insight of how a meson with one massless quark connects to the massless free spectral function (4.43).

For the spatially polarized vector channel spectral function $\rho_{V,ii}$, at high frequencies we see in Fig. 4.1 the same 'typical continuum' behavior as in the case of degenerate masses, starting at $\omega/T = (m_1 + m_2)/T \overset{m_1 \to m_2}{\longrightarrow} 2m/T$. While the region between $(m_1 + m_2)/T$ and $(m_1 - m_2)/T$ is zero, as here the square root would yield imaginary values, there exists a finite contribution below $(m_1 - m_2)/T$. This regime merely arises due to a difference in the quark masses, and thus is not present otherwise. Following the plotted functions of decreasing m_1/T, we see how this contribution forms an increasingly sharp peak, with its center moving towards zero frequency. This is the mechanism that in the strict limit $m_1 \to m_2$ constitutes the Dirac delta peak at zero frequency. Essentially the same behavior is observed in the axialvector and scalar channels, with the 'bump' contribution at low frequencies being a bit larger than in the vector channel.

In Fig. 4.1 we show the very same plots also for the temporal component of the vector current correlator. It becomes apparent that the Dirac delta peak at low frequency appears in the same way as for the spatial part when taking the limit of degenerate masses. At high frequencies the spectral function stays finite and saturates for $\omega \to \infty$, which can be seen from the general large frequency limit of (4.56),

$$\rho_H(\omega, m_1, m_2) \overset{\omega \to \infty}{\longrightarrow} \frac{N_c}{32\pi} \left[2a_H^{(2)}(m_1^2 + m_2^2) - 4a_H^{(3)} m_1 m_2 + (a_H^{(1)} - a_H^{(2)})\omega^2 \right] \tag{4.57}$$

with $a_H^{(1)} = a_H^{(2)} = a_H^{(3)} = 1$ for the temporal component $H = 00$. This part cleanly vanishes for $m_1 \to m_2$, leaving only the Dirac delta peak as predicted by equation (4.40).

Because the contribution below $\omega/T = m_1 - m_2$ is systematically larger for ρ_{00} than for ρ_{ii}, we find that their difference ρ_V is indeed negative in this frequency region, and forms the negative zero mode in the limit of degenerate masses, as predicted by (4.40).

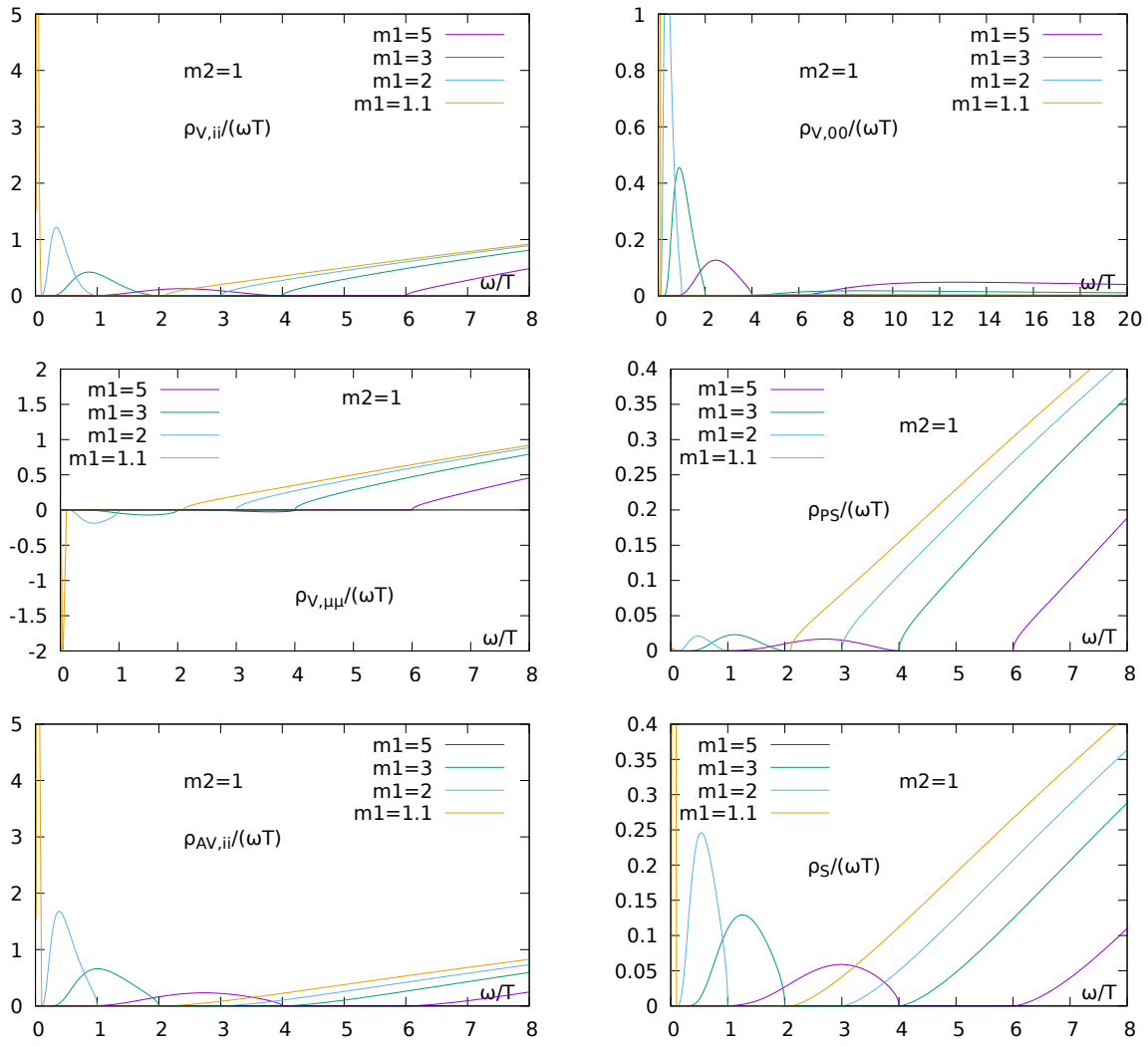

Figure 4.1: The free spectral function ρ/ω of different quantum number channels in the continuum and with non-degenerate quark masses. The second mass is fixed to $m_2/T = 1$. Note that the pseudoscalar channel does not build up a Dirac delta contribution for $m_1 \to m_2$.

The pseudoscalar channel shows a positive contribution below $\omega = m_1 - m_2$. In contrast to the scalar, axialvector or vector channels, ρ_{PS} at degenerate masses does not exhibit a Dirac delta peak at vanishing frequency, and accordingly we see in Fig. 4.1 how the positive contribution becomes very small and finally vanishes for $m_1 \to m_2$. However, it is intriguing to see that for non degenerate masses, there is an enhancement in the low frequency region, although it is much smaller compared to the corresponding enhancements in the vector channel.

After having investigated how the limit $m_1 \to m_2 \neq 0$ works to yield equation (4.40),

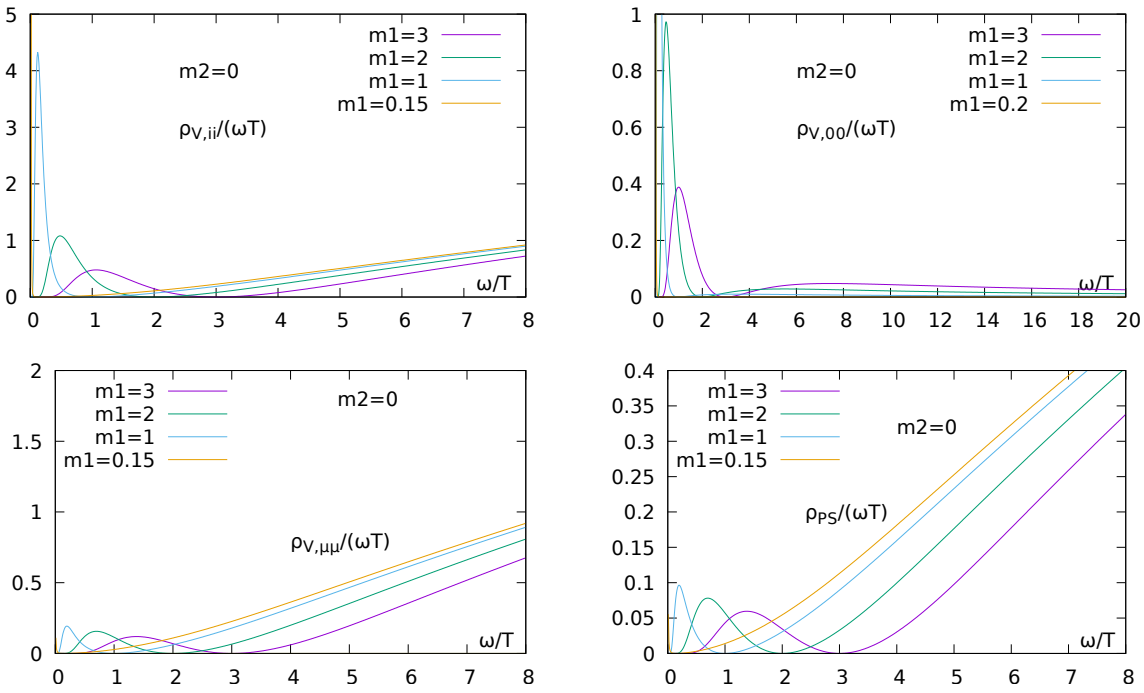

Figure 4.2: The free spectral function ρ/ω in the continuum and with non-degenerate quark masses, for vanishing fixed mass $m_2/T = 0$. Note that $m_2 \to 0$ constitutes the chiral limit, and hence we only show the pseudoscalar and the vector, since their positive parity partners, scalar and axialvector, are exactly the same, also at finite m_1.

we take another step and also consider this limit with $m_2 = 0$. This case is interesting because it fits in as an intermediate step between the fully massive, but mass-degenerate, spectral function and the massless spectral function. Physically, this might be an idealization of a heavy-light quark pair in the chiral limit. Many features in this case are analogous to the case of finite m_2, but an intriguing exception is found in the vector current spectral function ρ_V, see Fig. 4.2. Where in the former case the limit $m_1 \to m_2$ was achieved with a negative contribution for $\omega < m_1 - m_2$, leading to a negative peak, the spectral function stays strictly positive for all frequencies when one massless quark is involved. Note that $m_2 \to 0$ is indeed the formal chiral limit, as then the coefficient $a_H^{(3)}$ drops out and consequently the pseudoscalar and scalar, and the vector and axialvector channels, respectively, degenerate.

4.2.3 Free lattice spectral functions for Wilson quarks

While the preceding section dealt with meson spectral functions at infinite temperature in the continuum, the purpose of this chapter is to introduce the same quantities in a lattice regularized version. To be specific, the discretization scheme adopted is that of standard Wilson fermions on a lattice. As we will see, certain features are present in

both formulations of QCD, while especially the cutoff, introduced by putting the quarks on a lattice, will lead to a drastically different behavior in the region of large frequencies compared to the continuum results. Because lattice artifacts are also seen in correlators resulting from fully interacting numerical lattice computations, the free lattice correlator is more comparable to the latter than the free continuum expression would be. Free spectral functions on the lattice have first been computed by Stickan et. al. [84, 85] as well as Aarts and Resco [83], and the notation in this section is that of Aarts, although the differences between the notation in above works are minor.

The starting point is (4.27) in the mixed representation, i.e. in terms of τ instead of the Matsubara frequency ω_l. Discretization in space-time introduces bounds in the integration over the momenta, while introducing a finite size also in the spatial direction, additionally to the already present bound in temporal direction, discretizes the momenta in the integration. The free Euclidean meson correlation function for Wilson fermions is thus given by

$$G_H(\tau, \vec{P}) = -\frac{N_c}{L^3} \sum_{\vec{K}} \mathrm{tr} \left[S(\tau, \vec{K}) \Gamma_H S(-\tau, \vec{P} + \vec{K}) \gamma_0 \Gamma_H^\dagger \gamma_0 \right], \tag{4.58}$$

where $\vec{K}_i = 2\pi n / N_\sigma$ with integer $n_i \in [-N_\sigma/2+1, N_\sigma]$ and periodic boundary conditions for $S(\tau, \vec{K})$ in these directions. The latter can be decomposed to read [86]

$$S(\tau, \vec{K}) = \gamma_4 S_4(\tau, \vec{K}) + \sum_{i=1}^{3} \gamma_i S_i(\tau, \vec{K}) + \mathbb{I} S_u(\tau, \vec{K}), \tag{4.59}$$

with the single components given by

$$\begin{aligned} S_4(\tau, \vec{K}) &= S_4(\vec{K}) \cosh\left(\left[\tau T - \frac{1}{2} \right] E_{\vec{K}} \right), \\ S_i(\tau, \vec{K}) &= S_i(\vec{K}) \sinh\left(\left[\tau T - \frac{1}{2} \right] E_{\vec{K}} \right), \\ S_u(\tau, \vec{K}) &= S_u(\vec{K}) \sinh\left(\left[\tau T - \frac{1}{2} \right] E_{\vec{K}} \right) - \frac{\delta_{\tau,0}}{2(1 + \mathcal{M}_{\vec{K}})}. \end{aligned} \tag{4.60}$$

In this mixed representation, the particle energy $E_{\vec{K}}$ is given by

$$\cosh(E_{\vec{K}}) = 1 + \frac{\mathcal{K}_{\vec{K}}^2 + \mathcal{M}_{\vec{K}}^2}{2(1 + \mathcal{M}_{\vec{K}}^2)}, \tag{4.61}$$

with $\mathcal{K}_{\vec{K}} = \sum_{i=1}^{3} \gamma_i \sin(K_i)$ and $\mathcal{M}_{\vec{K}} = \sum_{i=1}^{3} (1 - \cos(K_i)) + m$, while the purely mo-

mentum dependent components of the propagator are

$$\begin{aligned} S_4(\vec{K}) &= \frac{\sinh(E_{\vec{K}})}{2\mathcal{E}_{\vec{K}}\cosh(E_{\vec{K}}/2T)}, \\ S_i(\vec{K}) &= \frac{i\sin(K_i)}{2\mathcal{E}_{\vec{K}}\cosh(E_{\vec{K}}/2T)}, \\ S_u(\vec{K}) &= -\frac{1-\cosh(E_{\vec{K}})+\mathcal{M}_{\vec{K}}}{2\mathcal{E}_{\vec{K}}\cosh(E_{\vec{K}}/2T)}, \end{aligned} \tag{4.62}$$

with $\mathcal{E}_{\vec{K}} = (1+M_{\vec{K}})\sinh(E_{\vec{K}})$. Using the relation $S(-\tau,\vec{K}) = \gamma_5 S^\dagger(\tau,\vec{K})\gamma_5$, and computing the traces over the Dirac matrices as in the continuum case, the free lattice correlation function is given by

$$\begin{aligned} G_H(\tau,\vec{p}) = \frac{4N_c}{L}\sum_{\vec{K}}\Bigg\{ & a_H^{(1)} S_4(\tau,\vec{K})S_4^\dagger(\tau,\vec{K}+\vec{P}) - a_H^{(2)}\sum_i S_i(\tau,\vec{K})S_i^\dagger(\tau,\vec{K}+\vec{P}) \\ & - a_H^{(3)} S_u(\tau,\vec{K})S_u^\dagger(\tau,\vec{K}+\vec{P})\Bigg\}, \end{aligned} \tag{4.63}$$

with the coefficients $a_H^{(n)}$ from Tab. 4.2.1. With the purely momentum dependent components (4.62) of the quark propagators, the spectral function of the lattice correlator can be written analogous to (4.34), with the very same structure of Dirac delta functions,

$$\begin{aligned} \rho(\omega,\vec{P}) = \frac{2N_c}{L^3}\sum_{\vec{K}}\sinh\left(\frac{\omega}{2T}\right)\Bigg\{ & \\ + \left[a_H^{(1)} S_4(\vec{K})S_4^\dagger(\vec{R}) + a_H^{(2)}\sum_i S_i(\vec{K})S_i^\dagger(\vec{R}) + a_H^{(3)} S_u(\vec{K})S_u^\dagger(\vec{R})\right]\delta(\omega+E_{\vec{K}}-E_{\vec{R}}) & \\ + \left[a_H^{(1)} S_4(\vec{K})S_4^\dagger(\vec{R}) - a_H^{(2)}\sum_i S_i(\vec{K})S_i^\dagger(\vec{R}) - a_H^{(3)} S_u(\vec{K})S_u^\dagger(\vec{R})\right]\delta(\omega-E_{\vec{K}}-E_{\vec{R}}) & \\ +(\omega\to-\omega)\Bigg\} & \end{aligned} \tag{4.64}$$

with $\vec{R} \equiv \vec{K}+\vec{P}$. Both the expressions (4.63) and (4.64) can be evaluated numerically to yield the discretized free correlation and spectral functions, respectively, for given N_σ and N_τ.

When evaluating the spectral function, the Dirac delta functions are used to pick those contributions from the sum over momenta, which fit the correct energy difference. As such, they are unity for a small frequency range $[\omega, \omega+\Delta\omega]$, and zero otherwise, an approach known as the *Binning method*. Because of the discreteness of the sum, the number of sums and differences of energies which fall into this interval depends strongly on N_σ, and too small a spatial extent leads to strong fluctuations in the resulting spectral function. To circumvent this, values of $N_\sigma = 4098$ with a sufficiently good resolution of

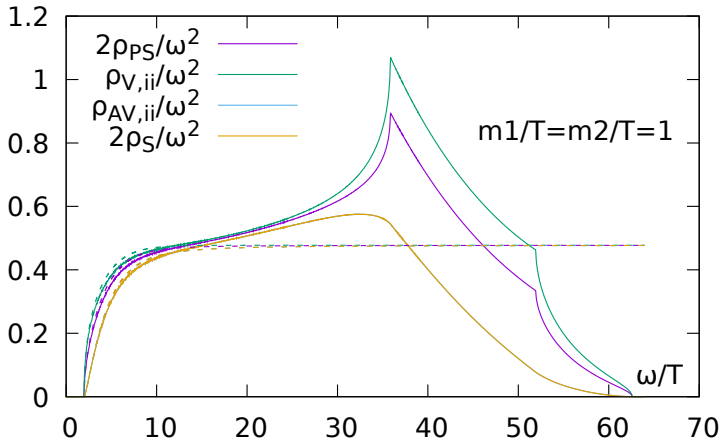

Figure 4.3: The free spectral functions as obtained from formula (4.64) via binning, for degenerate quark masses $m_1 = m_2 = T$ and in units of the temperature. The dashed lines denote the corresponding free continuum spectral functions. Note that the non-interacting scalar and axial vector lie on top of each other, as the scalar (and also the pseudoscalar) spectralfunction is multiplied by two.

$\Delta\omega = 1/500$ are used in the following demonstrations. The temporal extent is fixed to $N_\tau = 16$, but can be essentially chosen arbitrarily.

Extensive discussions on the features of non-interacting spectral functions in Lattice QCD and especially the lattice effects can be found in [83, 85]. Here, we only want to discuss some features of the free lattice spectral functions in comparison with the continuum one, and thus choose to keep the frequency in units of the temperature. For definiteness, we choose to set $N_\tau = 16$ to fix the value of the cutoff. To start, we show the massive lattice spectral functions with $m_1/T = m_2/T = 1$ for the pseudoscalar, scalar, vector and axial vector channels in Fig. 4.3. The dashed lines of the respective same colors denote the free continuum result (4.40). We normalize the spectral functions by the square of the frequency to stress the difference of the large frequency behavior between the continuum and the lattice. The influence of the cutoff becomes explicit at very large frequencies, leads to kinks in the spectral shape of the pseudoscalar and vector, and finally drops $\rho(\omega)/\omega^2 \to 0$, compared to the quadratic behavior $\rho(\omega)/\omega^2 \sim 1$ seen in the continuum at arbitrarily high frequencies. At very low frequencies, however, the structure of the free spectral functions is very similar in the continuum and on the lattice. In contrast to the continuum expressions, the expressions evaluated numerically on the lattice via the binning method can be easily adjusted from the case of degenerate masses in (4.64) to yield the free lattice spectral functions of open flavor mesons, simply by picking different quark masses in $\mathcal{M}_{\vec{K}}$ and $\mathcal{M}_{\vec{R}}$. In Fig. 4.4 (*left*) we show the same spectral functions as above, but set $m_1/T = 5$. In the low frequency region appear structures very similar to the corresponding continuum case at non-degenerate quark

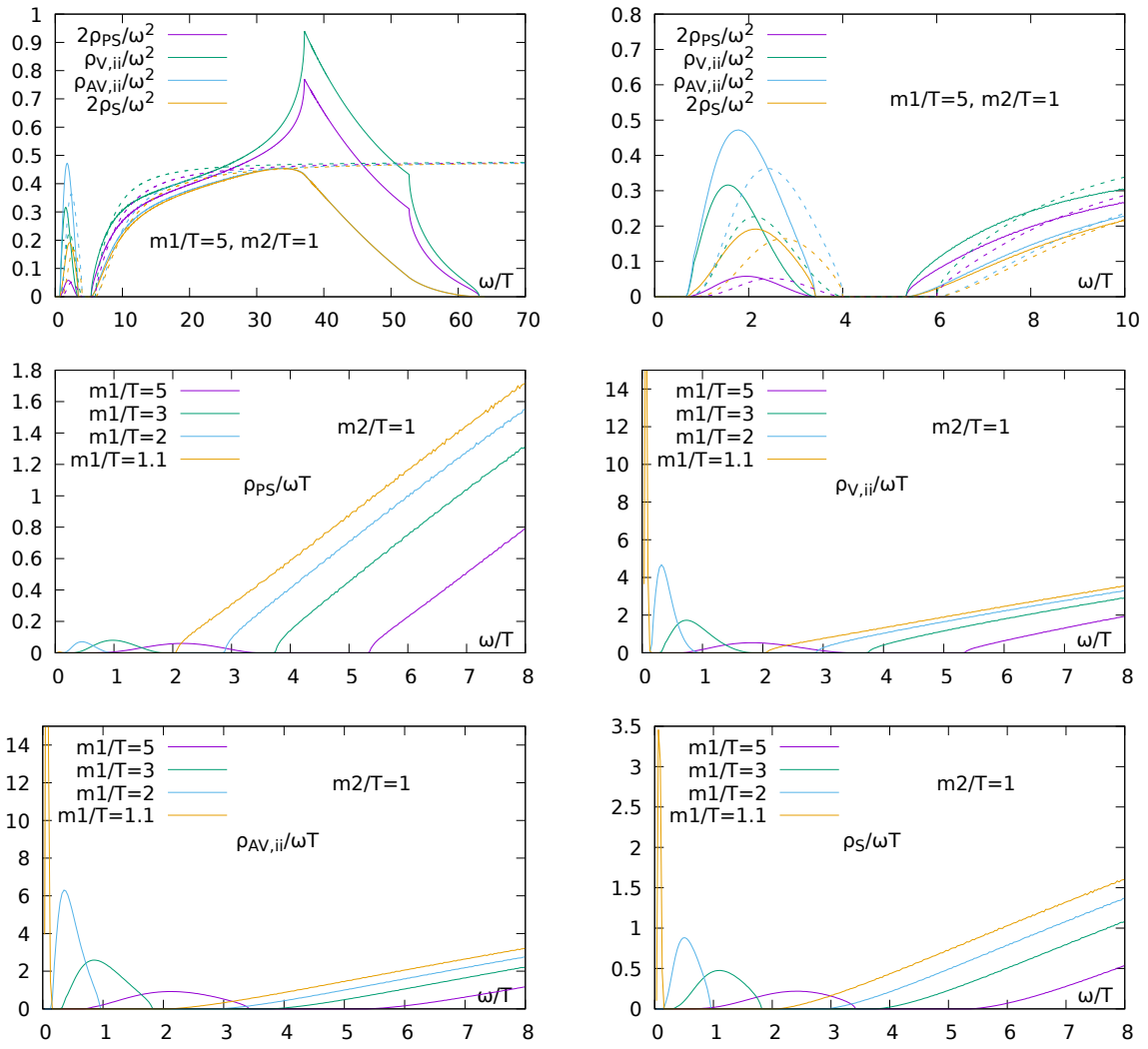

Figure 4.4: The free lattice spectral functions as obtained from formula (4.64) via binning for non-degenerate quark masses. *Top*: The whole frequency range and a blowup, the dashed lines are the corresponding free continuum results. *Middle and bottom*: Illustration of the limit $m_1/T \to m_2/T$ for a range of channels. Note that it works in the same way as for the free continuum spectral functions.

masses, and a blowup of the region $0 \leq \omega/T \leq 10$ is shown in Fig. 4.4 (*right*). There are two interesting points to note, namely

- the gap between the bump at low frequency and the onset of the large frequency behavior is shifted to smaller frequencies on the lattice, compared to the continuum,
- and the spectral function of the axialvector channel $\rho_{AV,ii}$ now deviates from $2\rho_S$, especially at low frequencies, in the characteristic bump contribution, where the

deviation is quite pronounced.

Overall, it becomes clear that the free spectral functions on the lattice are, apart from the cutoff, qualitatively very comparable to the free spectral functions in the continuum, both for degenerate and non-degenerate quark masses. As a side remark, shifts of structures between the continuum and discretized versions of free spectral functions, as we find them in case of non-degenerate quark masses above, also occur similarly for free spectral functions at finite momenta, see [83, 84, 85]. To conclude, we study the limit of degenerate masses, as done in Fig. 4.1 for the continuum spectral functions, and show the same channels as above, for different m_1 and fixed $m_2/T = 1$, in Fig. 4.4. The spectral functions shown are normalized as $\rho/(\omega T)$, and it becomes apparent that the limit of degenerate quark masses is reached in the same way as in the continuum, with the the frequency structure becoming increasingly peaked.

4.3 Towards interacting spectral functions

While the preceding section dealt with the analytically tractable case of free mesonic spectral functions, we now formalize our expectations of spectral functions which are subjected to a finite interaction strength. We identify elementary building blocks of which spectral functions can generally consist, and present phenomenological results for light and heavy quarks utilizing kinetic theory and linear response theory. As a result, these motivations yield continuum formulas for how the shapes of *mesonic* spectral functions change under the influence of interactions, compared to the free case. Even stronger, these hints can in turn serve as definite Ansaetze for the low frequency region of mesonic spectral functions, thus helping to extract them from non-perturbative lattice data. We conclude the discussion with a presentation of *thermal moments* and their relevance for the low frequency region of spectral functions.

4.3.1 Spectral function structure

In section 4.2 we have seen two distinct parts that the meson spectral functions at infinite temperature can generally be made of. First, there is a zero mode at vanishing frequency and, second, a continuum contribution which sets in after a threshold given by the sum of the two constituent quark masses. On the other hand, at the zero temperature the spectral functions consists of structures that reflect the presence of particle states. These can be either narrow peaks, as motivated in equation (2.85) for well defined bound states, or rather broad Lorentz structures, as in the case of the ρ resonance. Especially the bound states in the spectrum are thus given by Dirac delta peaks located in energy space at the mass of the corresponding states. Furthermore, a heavy meson, which just above the transition temperature might still be bound, will have disappeared at infinite temperature, as the corresponding free spectral functions do not show any bound state peaks. Since this process will not be discontinuous, it is intuitive to assume

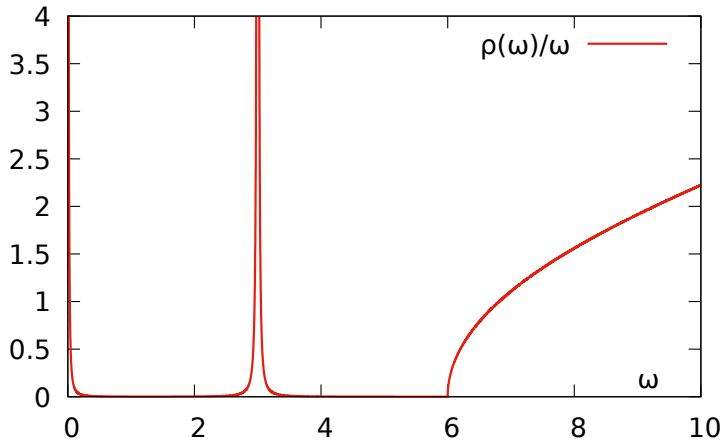

Figure 4.5: The schematic expectation of the interacting spectral function. The plot illustrates the different building blocks (zero mode, bound state, continuum). Note that the units of ω here are arbitrary and the plot carries no quantitative information.

that bound state peaks of heavy quark states deform gradually at increasing temperature, getting smaller in magnitude and broader in extent, until one cannot recognize a bound state at the corresponding frequency anymore. Note that meson states consisting of lighter quarks, e.g. pions, will already in the transition region be heavily affected, as they are closely linked to the chiral aspects of the transition. We will solidify this melting behavior of peaks in the next section. Note that there still is a continuum contribution at zero temperature, which dominates the correlator at small distances. The asymptotic behavior is given by $\rho(\omega) \sim \omega^2$ for large frequencies, see e.g. [87], and thus the same as at infinite temperature. The threshold for the onset of this continuum is heuristically given by the energy at which light quark antiquark pair creation permits the decay into other colorless hadron pairs [88], e.g. $c\bar{c} \longrightarrow D\bar{D}$ in the case of charmonium, where $D \sim u\bar{c}$. Conversely, adding a medium and increasing the temperature from zero to higher values will make the continuum contribution shift to lower frequencies with rising temperature, until it reaches its minimum threshold $2m_q$, which is the threshold at infinite temperature, see Sec. 4.2.

Putting it all together, by physical arguments we assume the shape of the interacting spectral function at finite temperature to be that of a peak structure in the low frequency region, a number of bound state peaks in the intermediate and high frequency region, and finally the continuum contribution. This result is schematically plotted in Fig. 4.5.

4.3.2 Light and heavy quarks from kinetic theory

After this rather pictorial discussion, which formed a first picture of what features are to be expected in a mesonic spectral function at finite temperature, we now want to tweak

the details of this picture. A very important conclusion will be drawn about the shape of the transport peak, as well as the connection made between the low frequency regime of the spectral function and transport properties of the system. These considerations are described in standard textbooks [42, 64, 80, 89], as well as important works and review papers [12, 20, 90].

When a physical system is somehow pulled out of equilibrium, it is generally expected to relax back into the stable equilibrium state. In the framework of *linear response* it is possible to quantify the first order reaction of a system to a time dependent perturbation. Let the full Hamiltonian be

$$H'(t) = H + V(t), \tag{4.65}$$

with H the unperturbed Hamiltonian and $V(t)$ encodes the details of how exactly the perturbation disturbs the system. If we are interested in the time evolution of a certain operator $A(t)$, denote a state, modified by the perturbation, in the Schroedinger picture as

$$|\bar{\psi}_S(t)\rangle = \mathrm{e}^{-iHt}U(t,t_0)|\psi_S(0)\rangle, \tag{4.66}$$

with the influence of the perturbation over time, starting at t_0, encoded in the operator

$$U(t,t_0) = 1 - i\int_{t_0}^{t} \mathrm{d}t' V_H(t') + \mathcal{O}\left(V_H^2\right) \tag{4.67}$$

and the usual transition from Heisenberg picture to Schroedinger picture governed by the unperturbed Hamiltonian, $\psi_S(t) = \mathrm{e}^{-iHt}\psi_S(0) \equiv \mathrm{e}^{-iHt}\psi_H$, and analogous for operators. Then we can quantify the influence of $V(t)$ on an expectation value of an operator $O(t)$ by subtracting the unperturbed expectation value and using (4.67),

$$\begin{aligned}\delta\langle O(t)\rangle &\equiv \langle\bar{\psi}_S(t)|O(t)|\bar{\psi}_S(t)\rangle - \langle\psi_S(t)|O(t)|\psi_S(t)\rangle \\ &= -i\int_{t_0}^{\infty} \mathrm{d}t'\Theta(t'-t)\langle\psi_H|\left[O_H(t), V_H(t')\right]|\psi_H\rangle.\end{aligned} \tag{4.68}$$

Since this holds especially for all eigenstates of the operator H, the relation holds also with expectation values corresponding to the thermal bath, i.e.

$$\sum_n \langle n|\hat{\rho}\left[O_H(t), V_H(t'\right]|n\rangle = \mathrm{tr}\hat{\rho}\left[O_H(t), V_H(t')\right] \equiv \langle[O_H(t), V_H(t')]\rangle. \tag{4.69}$$

The commutator together with the restricting step function is another way to define the retarded correlator that was encountered earlier, in time t,

$$G_R(t-t') = \Theta(t'-t)\langle[O_H(t), V_H(t')]\rangle. \tag{4.70}$$

Choosing the perturbation to entail a specific time dependence , $V_H(t) \to f(t)V_H(t)$, the change of $O(t)$ in (4.68) is technically just a convolution of the retarded correlator and

$f(t)$, and in Fourier space thus just becomes the product of the two. In this context, we define the static susceptibility to be the retarded correlator at vanishing frequency,

$$\delta\langle O(\omega=0)\rangle = G_R(\omega=0)f(\omega=0) \equiv \chi_s f_0, \tag{4.71}$$

and with an *adiabatic* perturbation $f(t) = f_0 \mathrm{e}^{\epsilon t}\Theta(-t)$ we obtain the retarded correlation function by integrating with $\int_0^\infty \mathrm{d}t \mathrm{e}^{i\omega t}$,

$$G_R(\omega) = \chi_s + \frac{i\omega}{f_0}\int_0^\infty \mathrm{d}t \mathrm{e}^{i\omega t}\delta\langle O(t)\rangle. \tag{4.72}$$

This shows how, conversely, the behavior of the system relaxating back from the perturbed state to equilibrium, to first order determines the retarded correlator and thus, via equation (4.11), carries information about the spectral function. Very concretely, this formalism opens the possibility to input model assumptions and gain information on the spectral function, where the validity of the results of course strongly depends on the nature of the model. In a macroscopic framework, hydrodynamics describes the relaxation via transport coefficients, which appear as the proportionality prefactors of the first order perturbations. Thus, the first order responses of the system can be obtained from the underlying spectral function.

As a simple example, consider the diffusion of a massive particle subject to a thermal medium. A simple hydrodynamic model treats this via number density conservation,

$$\frac{\partial n(t,\vec{x})}{\partial t} = -\nabla\cdot\vec{j}, \tag{4.73}$$

with the reaction to a change given as the spatial flux that drives the system back into equilibrium, i.e. $\vec{j} = -D\nabla n(t,\vec{x})$, and thus the particle number is determined by the diffusion equation

$$\frac{\partial n(t,\vec{x})}{\partial t} = D\nabla^2 n(t,\vec{x}). \tag{4.74}$$

In this context the coefficient D is the diffusion constant, a transport coefficient that describes how strong the original perturbation is washed out by the dynamics of the system. Perturbing the system with a chemical potential as the source of imbalance, which amounts to choosing $f(t)V_H(t) = -\mathrm{e}^{\epsilon t}\Theta(-t)\int \mathrm{d}^3x\mu(\vec{x})n(t,\vec{x})$ as the perturbation, we thus identify

$$O \mathrel{\hat{=}} n, \qquad V \mathrel{\hat{=}} n, \qquad f_0 \mathrel{\hat{=}} \mu. \tag{4.75}$$

The solution to (4.74) is given in Fourier space by

$$n(\omega,\vec{p}) = \frac{n(0,\vec{p})}{-i\omega + D\vec{p}^2}, \tag{4.76}$$

and writing the initial condition in terms of equation (4.71), we arrive via the central relation (4.72) at the predicted retarded correlation function

$$G_R(\omega,\vec{p}) = \chi_s(\vec{p}) + i\omega\frac{\chi_s(\vec{p})}{-i\omega + D\vec{p}^2} = \chi_s(\vec{p})\frac{\left(D\vec{p}^2\right)^2 + i\omega D\vec{p}^2}{\omega^2 + \left(D\vec{p}^2\right)^2}. \tag{4.77}$$

The imaginary part of this expression corresponds to the density current spectral function, and by projecting it to the longitudinal spectral function, $\rho_L(\omega,\vec{p}) = \frac{\omega^2}{\vec{p}^2}\rho(\omega,\vec{p})$, we can obtain the diffusion constant D in the limit of low frequency and momentum,

$$\begin{aligned} \rho_L(\omega,\vec{p}) &= \frac{\chi_s}{\pi}\frac{D\omega^3}{\omega^2 + \left(D\vec{p}^2\right)^2} \\ \Leftrightarrow D\chi_s &= \pi\lim_{\omega\to 0}\lim_{\vec{p}\to 0}\frac{\rho_L(\omega,\vec{p})}{\omega}. \end{aligned} \tag{4.78}$$

An analogous computation, see e.g. [12, 20] involves the electromagnetic current j_μ^{em} (3.3) and is based on extending the current $\vec{j}$ with Ohm's law $\vec{j}^{\text{em}} = \sigma\vec{E}$. Since the current correlator is related to the dilepton rate, as seen in Sec. 3.2.1, so is the electrical conductivity, and the resulting expression is

$$\sigma = \frac{C_{em}}{6}\lim_{\omega\to 0}\frac{\rho_{V,ii}(\omega,\vec{p}=0)}{\omega}. \tag{4.79}$$

Note that we explicitly put a factor of C_{em}, see Sec. 3.2.1. Note also that this result is exact, in the sense that the conductivity is a first order coefficient by definition and the hydrodynamical approach is a low energy/long distance approach, anyway, that encodes microscopic features in the macroscopic concept of transport. Relations like (4.79) and (4.78), which relate transport coefficients to the spectral functions at zero frequency, are called *Kubo formulas* [64]. Thus, having the electrical conductivity as the slope of the spectral function at zero frequency leaves the determination of the spectral function itself, if possible in an *ab-initio* way, as a formidable challenge.

The thoughts followed above utilized rather general, macroscopic hydrodynamical arguments. Note how the resulting expression for the longitudinally polarized spectral function $\rho_L(\omega,0)/\omega$ resembles a constant at low frequencies. When we introduce further assumptions, we might be able to get another impression on the subsequent low frequency behavior. As such, assume that the mean free path of the transported charges is long compared to the thermal scale, i.e. the interaction of the charges under consideration with the medium is to be characterized as rather weak. This implies that they form definite quasiparticle states, which demands further assumptions about their properties.

To start out, assume that the particle under consideration is much more massive than the surrounding medium constituents, e.g. a heavy quark. The characteristic time scale for diffusion processes is M/T^2 [12, 90], and hence, with the above assumption, is easily larger than the characteristic time scale of the medium, $1/T$. This statement

implies that the transport process will show up in the spectral function at frequencies $\omega \sim 1/(M/T^2) = T^2/M \ll T$, and hence we can again utilize the linear response formula to relate corresponding model assumptions to the shape of the spectral density at small frequencies. A classical model that describes the movement of a particle distinctly heavier than its surrounding medium is given by the classical Langevin equations [12, 89, 90]. They constitute a set of equations of motion,

$$\frac{\partial \vec{x(t)}}{\partial t} = \frac{\vec{p(t)}}{M}, \qquad \frac{\partial \vec{p}}{\partial t} = \vec{\xi(t)} - \eta p(t), \tag{4.80}$$

with different components of the noise vector $\vec{\xi}$ taken to be uncorrelated at differing times, i.e. $\langle \xi_i(t)\xi_j(t')\rangle = \kappa\delta_{ij}\delta(t-t')$, where κ is the fluctuation coefficient and the strength of the (directed) drag is given by η. The latter two are related by the fluctuation-dissipation relation $\eta = \kappa/(2MT)$. For times that are long compared to the inverse drag $1/\eta$, the diffusion equation (4.74) holds and can be expressed by a probability distribution, as the heavy quark moves via Brownian motion induced by the Langevin equation. The probability $P(\vec{x},t)$ to meet it at a distance $\vec{x}$ at time t from the origin $(\vec{0},0)$ is known to be a gaussian,

$$\begin{aligned} P(\vec{x},t) &= \frac{1}{\left(2\pi\sigma^2(t)\right)^{3/2}} \mathrm{e}^{-\frac{\vec{x}^2}{\sigma^2(t)}} \\ \text{with} \qquad \sigma(t) &= 2Dt - \frac{2D}{\eta}\left(1-\mathrm{e}^{-\eta t}\right). \end{aligned} \tag{4.81}$$

Here D is the diffusion constant from the diffusion equation, which is related to the fluctuation coefficient and the drag coefficient by the Einstein relation $D = T/(M\eta) = 2T^2/\kappa$. The particle number as a function of time and space is thus given by the convolution

$$N(t,\vec{x}) = \int \mathrm{d}x' P(t,\vec{x}-\vec{x'})N(0,\vec{x'}), \tag{4.82}$$

and the relation to the corresponding retarded correlation function can be made by plugging the probability distribution into equation (4.72). The static susceptibility χ_s can be found by assuming that initially the distribution of the heavy quarks is given by

$$f(0,\vec{x},\vec{p}) = \mathrm{e}^{\beta\left(\mu(\vec{x})-M-\vec{p}^2/(2M)\right)}, \tag{4.83}$$

with a small perturbing chemical potential $\mu(\vec{x}) = \mu + \delta\mu(\vec{x})$, and can be shown to read

$$\chi_s = 4N_c\left(\frac{M}{2\pi\beta}\right)^{\frac{3}{2}} \mathrm{e}^{-\beta M}\cosh\left(\beta\mu\right). \tag{4.84}$$

The important result in the context of this thesis is the shape of the spectral function of the corresponding current correlation function, which for vanishing momentum reads

$$\frac{\rho_{JJ}(\omega)}{\omega} \sim \chi_s \frac{\eta}{\omega^2+\eta^2}. \tag{4.85}$$

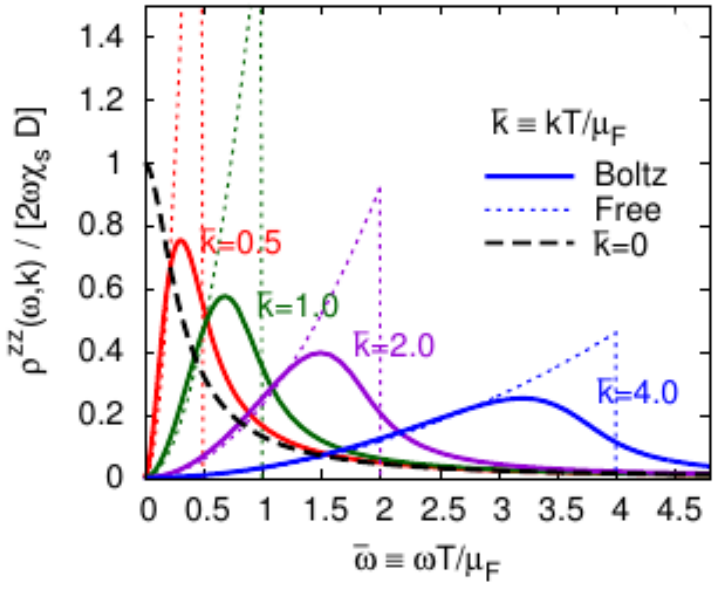

Figure 4.6: The solution for the longitudinal spectral function of the light quark current correlator, as predicted by the corresponding Boltzmann equation. We are especially interested in the zero momentum limit $\bar{k} = 0$, the thick dashed line. The picture is taken from [20].

Thus, the assumption of a heavy quasiparticle, on top of the hydrodynamical constitutive equations, leads to a Breit-Wigner peak centered around $\omega = 0$. This feature is very interesting to compare to the findings of the low frequency structure of free mesonic spectral functions in Sec. 4.2. The low frequency region in the spatially polarized vector channel (as well as the axialvector and scalar channels) was found to be characterized by a sharp Dirac delta peak at vanishing frequency. The Breit-Wigner peak for small drift η is an approximating representation of the Dirac delta function,

$$\delta_\eta(\omega) \equiv \frac{1}{\pi}\frac{\eta}{\eta^2+\omega^2} \overset{\eta\to 0}{\longrightarrow} \delta(\omega), \tag{4.86}$$

and becomes an exact Dirac delta in the limit of vanishing drift. Conversely, this shows an explicit possibility of how an exact Dirac delta peak in the free theory can become washed out, or smeared out, by effects of interactions. We want to merely refer here to a computation that shows the same result for the case of light quarks. Just as a diffusing heavy quark is characterized by a different time scale than its surrounding plasma, M^2/T compared to $1/T$, so is the central assumption in the case of light quarks, that subsequent particle collisions occur on a time scale large compared to the medium scale. In this case the former is characterized by $1/(g^4T)$, with g being the coupling constant of QCD [20, 91]. To be large compared to $1/T$, clearly $g \ll 1$. A weakly interacting

picture like this can be dealt with in the form of a linearized Boltzmann equation, as done in [20]. There, the resulting equation is solved numerically and the spectral density of the quark current correlator is shown in Fig. 4.6. Clearly, for vanishing momentum, which is the interesting case for us, it exhibits a very similar shape as we found in the case of a diffusing heavy quark. However, also the cases of finite momenta are of interest for us, since we explicitly see how the discontinuities of the free cases are washed out in the respective solutions from the Boltzmann equation, to yield smooth structures.

Concerning the structure of spectral functions under investigation, already outlined in the former section, this insight solidifies the idea that the Dirac delta peaks, which we found at low and intermediate frequencies for infinite and zero temperature, respectively, gradually deform and acquire a finite width and height. These results have serious implications for the analysis of light and heavy quark spectral functions in the course of the current work, for the obtained shape of a Breit-Wigner peak can be explicitly used as an Ansatz of the spectral shape in the low frequency region, and also for heavy mesons we thus expect contributions to the correlator to arise from the low frequency region, and the intermediate frequency region, stemming from molten Dirac delta structures. Concerning modifications of the free meson spectral functions at non-degenerate quark masses, we do not have explicit phenomenological predictions of what should happen to the characteristic bump structure at low to intermediate frequencies. However, as a first approximation we expect that, while interactions will certainly modify the structure, it will generally still remain at finite interactions.

4.3.3 Analytical results

The free theory results for the spectral function computed in Sec. 4.2 are the spectral functions at infinite temperature. From a perturbative point of view, these are the *leading order* results of corresponding expansions in the coupling g. Without going into the details of perturbative methods in QCD, we want to mention some important results for light/massless quarks, and try to bring them into the context of the current work. We will utilize some of these to compare our own results to, while some will be incorporated into our approaches as additional input to perform systematic checks and/or improvements. We merely mention here, that there exist also recent perturbative results for the massive vector current in thermal QCD, see [92].

Compared to perturbation theory at zero temperature, a new feature at finite temperature is that the scale of the temperature T plays an additional role. It turns out that external momenta in the expansion need to be classified by two momentum scales, the so called *hard scale*, $p \sim T$, and the *soft scale* $p \sim gT$. It can be shown that if the momenta of all external legs are hard, then loop corrections are of the order $\mathcal{O}(g^2)$, as is the case in zero temperature perturbative QCD, and subsequently the expansion can be performed order by order [80, 93]. However, if at least one of the external legs has a momentum of the order of the soft scale, then loop corrections contribute already

at the order $\mathcal{O}(g)$, i.e. at the same order as the tree level contributions. These contributions can be extracted from the corresponding diagrams, and the entirety of these *hard thermal loops* need to be taken into account in order to fully describe all effects of order $\mathcal{O}(g)$. This procedure is called *Hard Thermal Loop resummation* (HTL), and the systematic treatment of such resummations has been developed in [93]. To be specific, the three different perturbative results that are used in the course of this work are listed in the following.

1. The first is a longstanding result which computes the soft dilepton rate to full leading order in the QCD coupling constant [94], and hence was an immediate followup of the development of the HTL resummation techniques.

2. Another perturbative result for the spectral function is given in [95], where an approximation of the spectral function is achieved by combining the perturbative zero temperature result [87] which is known up to 5-loop order, with the thermal contribution being merely the free thermal result,

$$\rho_{ii}(\omega) = \frac{3\omega^2}{2\pi} \tanh\left(\frac{\omega}{2T}\right) R(\omega^2) + 2\pi\chi_q^{\text{free}}\omega\delta(\omega), \tag{4.87}$$

   where $R(\omega^2)$ is the 5-loop vacuum contribution. Note that the latter leads to a very accurate behavior in the regime of large frequencies $\omega/T \gg 3$, while due to the lack of HTL resummation the thermal effects incorporated in the low frequency region is the Dirac delta structure at $\omega = 0$, that is already in the free result.

3. Somewhat different in its philosophy, we show in Fig. 4.7 (*left*) the result of a thermal computation to 2-loop order, valid in higher frequency region $\omega/T \gtrsim 3$ [96], and a treatment of the low frequency regime $\omega/T \ll 1$, done in [73], which relies on the assumption of a weakly coupled surrounding plasma. Because there is no systematic treatment for the region $\omega/T \sim 1$, an interpolation between these two computations is used, but of course does not strictly arise from physical reasoning[1].

Plots of these solutions are shown in Fig. 4.7 (*left*). As can be seen, the HTL spectral function (1) diverges when plotted as ρ/ω, and thus it has a behavior $\rho \sim \omega^x$ with $x < 1$ for small frequencies. Solution (2) accomplishes the limit with $x > 1$, as it simply vanishes in ρ/ω, while solution (3) indeed fulfills $x = 1$ and yields a finite intercept.

An entirely different approach to computing the underlying spectral functions is based on the famous AdS/CFT correspondence, which is a statement about the connection of conformal field theories on the one hand, and black hole dynamics in $\text{AdS}_5 \times S^5$ space on the other hand. Thus, theories that exhibit a gravity dual can serve as models to investigate the features of field theories using string theory techniques. Since QCD does not have a gravity dual (theories with energy dependent coupling are not conformal

[1] Thanks to Mikko Laine for providing the solution.

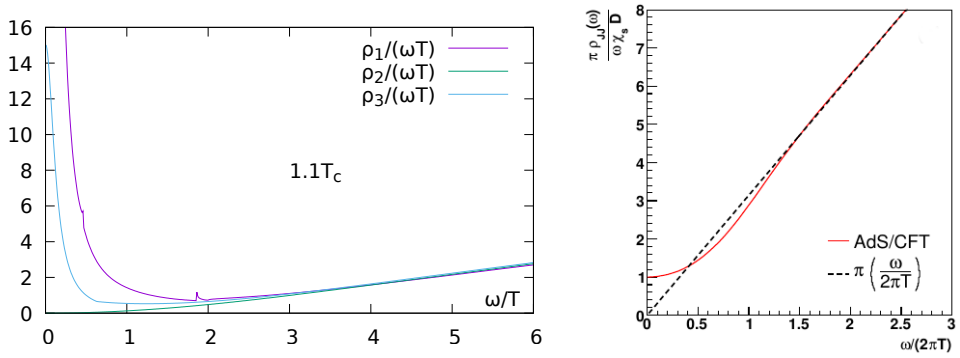

Figure 4.7: *Left*: The perturbative solutions ρ/ω of the current current correlator from listings (1)-(3) for $T = 1.1T_c$. *Right*: The shape of the spectral function in the strongly interacting case as obtained from the AdS/CFT correspondence. The plot is taken from [97]. Note that all spectral functions exhibit a distinctly different behavior in the low frequency region.

[98]), one popular model is $N = 4$ Super Yang-Mills (SYM) theory, where the relevant coupling on the AdS side is the 't Hooft coupling, which can be related to the SYM coupling and the number of colors as $\lambda = g^2_{\mathrm{SYM}} N_c = g_s N$. It turns out that for large λ, the correspondence is strongest, and the string theory proofs to be very effective to compute, as it results in a weakly coupled string theory on $\mathrm{AdS}_5 \times S^5$, that, in this limit, becomes classical supergravity. However, the corresponding field theory is strongly coupled, and due to the conjectured duality it thus becomes accessible by solving the supergravity theory [98, 99, 100]. A current-current correlator, similar to the electromagnetic current correlator considered above, can be computed in this framework [97], and is shown in Fig. 4.7 (*right*). Note that while ρ/ω features a finite intercept at $\omega = 0$, it also exhibits a flat behavior at small frequencies, which is attributed to the nature of a strongly interacting system, see [12, 20] and references therein. Thus, this 'featurelessness' in the low frequency region of the spectral density seems generally to be associated with theories which are strongly coupled, while a pronounced peak structure is typical for computations originating from a description via quasiparticles, see the discussion in Sec. 4.3.2 and e.g. [12]. Since there are strong experimental hints that the QGP is a strongly interacting medium, both paradigms are under discussion, motivating to see how well a quasiparticle description works out from the perspective of Lattice QCD.

5 Approaches to reconstructing spectral functions

With the expectations for interacting mesonic spectral functions at hand, we proceed to elaborate in more detail the problems faced when extracting spectral functions in QCD, and also try to work out the problems more generally with a view on the method of Backus and Gilbert. Finally we describe the methods that are actually used in this work to extract information from meson correlation functions for both light and heavy quarks.

5.1 A short primer on ill-posed problems

5.1.1 The integration kernel

The integration kernel in units of the temperature,

$$K(\tau T, \omega/T) = \frac{\cosh(\omega/T\,[\tau T - 1/2])}{\sinh(\omega/(2T))}, \tag{5.1}$$

acts as a weight in the mixed representation connection (4.17) of the Euclidean correlator and its corresponding spectral function. As can be seen in Fig. 5.1, $K(\tau T, \omega/T) \gg 0$ for a large range of frequencies, which means that operation (4.17) is effectively a *smearing operation*, and the translation from the level of the spectral function to the correlator level is in this sense distorted. From a mathematician's viewpoint, this identifies the problem of obtaining the spectral function from Euclidean correlator data as being *ill-posed*. Additionally, because usually $\mathcal{O}(10)$ correlator data points are available as a product of state of the art numerical lattice computations, while the spectral function needs to be resolved much finer, and this lack of information makes the problem even more severe [101, 102]. However, even with a continuous input correlation function, no exact method of inverting relation (4.17) is known, and the correlation function is generally found to be quite insensitive to the detailed features of the spectral function in the small frequency region [73, 103, 104]. This can be seen by Taylor expanding the kernel (5.1) around $\omega/T = 0$ for small frequencies,

$$\begin{aligned} K(\tau T, \omega/T) &= \frac{1 + (\omega/T)^2\,(\tau T - 1/2)^2/2 + \mathcal{O}((\omega/T)^4)}{\omega/(2T) + \mathcal{O}((\omega/T)^3)} \\ &= \frac{2T}{\omega} + \frac{\omega}{T}\left((\tau T)^2 - \tau T + \frac{1}{4}\right) + \mathcal{O}\left[\left(\frac{\omega}{T}\right)^3\right], \end{aligned} \tag{5.2}$$

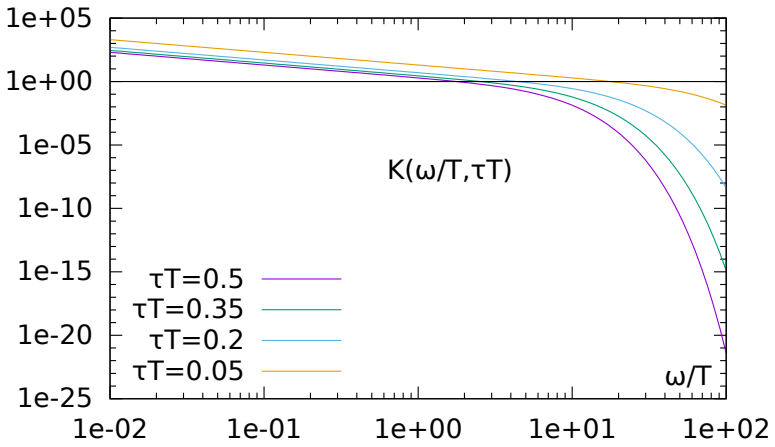

Figure 5.1: The integration kernel as a function of ω/T, shown for several values of τT in a double logarithmic plot. Note the much stronger suppression of large frequencies at $\tau T = 0.5$ compared to $\tau T = 0.05$. The horizontal line marks unity.

which reveals the power of the divergence of the weighting kernel at zero frequency to be of $\mathcal{O}(1/\omega)$. Obviously, a nonzero and finite limit is only possible for $\rho(\omega) \sim \omega$ for small frequencies. However, this also implies that the integral (4.17) in the low frequency region takes the shape

$$\int_{\text{small }\omega} \mathrm{d}\left(\frac{\omega}{T}\right) \rho(\omega/T) K(\omega/T, \tau T) \sim \int_{\text{small }\omega} \mathrm{d}\left(\frac{\omega}{T}\right) \frac{\rho(\omega/T)}{\omega/T}. \tag{5.3}$$

It turns out that this expression constitutes a sum rule, and hence its resulting value is fixed [73]. The authors compute an explicit expression in the framework of kinetic theory, which however is independent of the value of the coupling, and is given by

$$\int_{\text{small }\omega} \mathrm{d}\left(\frac{\omega}{T}\right) \frac{\rho\left(\frac{\omega}{T}\right)}{\omega T} = \frac{2\pi}{3} N_c C_{em} T^2. \tag{5.4}$$

Note that the integration is restricted to the region of the transport peak at low frequencies. Also, we want to cite here the original result, but *note that in our convention the factor C_{em} would be absent*. With the contribution of the small frequency region to the correlator fixed, *independent* of the actual shape of the spectral function, it is possibly very difficult to constrain it from correlation function data.

In order to assess the kernel's further effects on the integration, for large frequencies ω/T we expand it to yield

$$K(\tau T, \omega/T) \overset{\omega\to\infty}{\longrightarrow} \mathrm{e}^{-\omega\tau}, \tag{5.5}$$

which also constitutes the zero temperature limit for fixed frequency ω. The exponential decay of the kernel for large frequencies implies that the regime of large frequencies is

highly suppressed in the integration and thus does not yield a contribution to the correlation function. This effect becomes stronger with increasing distance τ, such that the correlation function at the midpoint is, out of all distances, least affected by the large frequency regime. For this reason, information that resides in the small frequency region of the spectral function is most explicitly contained in the large distance region of the correlation function.

5.1.2 Model independent approaches to ill-posed problems

The above considerations referred to the very specific problem that we face in Lattice QCD when trying to extract spectral information from finite, discrete correlation function data. However, it is generally worthwhile to consider the problem also from a different, more general, angle, and the following ideas will be especially useful to have when discussing and using the method of Backus and Gilbert.

The problem of extracting the spectral function, as we face it in QCD, is one special case of a very broad class of problems. Generalizing far enough, we can imagine two operations, with one of them being the opposite of the other. In mathematical terms we thus have a mapping and its inverse. Let the problem of performing one of the two operations be straightforward in the sense that it might be *technically* difficult to solve, i.e. the mapping is cumbersome to perform, but conceptually possible without restriction. Hadamard sorted out three criteria to define, from the conceptual side, whether a problem is to be considered as such, and he called those problems *well-posed* [105]:

1. the solution to the problem *exists*,
2. the solution to the problem is *unique*,
3. the solution to the problem depends continuously on the input data.

We name this operation the forward problem. It turns out that many inverse problems, as described above, suffer from the fact that the second operation, called the inverse problem, does not meet at least one of those three points. The act of inversion is then declared as an ill-posed problem. The need to handle these inversion problems led to a rich and increasingly general mathematical theory [106]. Examples of ill-posed problems in modern science and technology can be found in many areas, be it computer tomography in medicine, tomography in crystallographics, earth crust scans in geology, image deblurring, etc. An interesting overview and discussion of specific applications can be found in [107].

The problem that we face in course of this work is classified as an inverse problem, and can be mathematically described as a *Fredholm equation of* 1^{st} *kind*. Such an equation

is generally given by [108]

$$\int_a^b dt K(s,t) f(t) = g(s). \tag{5.6}$$

The parallel to the connection between the Euclidean correlator and the spectral function, equation (4.17), is immediate, by simply setting $a = 0$, letting $b \to \infty$ and choosing the kernel accordingly. Thus, for a given r.h.s. $g(s)$, we are looking for a function $f(t)$ that reproduces it when acted upon by the operation $\int dt K(s,t)$. The Kernel $K(s,t)$ is called a smoothing kernel, because it has the general property of integrating out small scale effects in f. This can be seen by considering 'high modes' in $f(t)$, i.e. quickly oscillating contributions $\delta f(t) = a \sin(\omega t)$. The Riemann-Lebesgue Lemma states that $\int dt K(s,t) \delta f(t)$ can become arbitrarily small for arbitrarily high oscillation frequency ω, and thus 'high modes' lead to an arbitrarily small change in $g(s)$ [109, 110]. This constitutes a loss of information when going from $f(t)$ to $g(s)$, and correspondingly, one generally cannot hope to reconstruct the details when reversing the operation and reconstructing $f(t)$ from $g(s)$. Quite the opposite, turning around the situation and attempting to find $f(t)$ by a standard inversion method, we face the same effect and small changes on $g(s)$ might lead to a huge influence on $f(t)$ that is hard to pin down. In this sense it is especially an admixture of the last two criteria above, which make these problems so difficult to solve.

The above statement and the general problems when inverting integral equations can be made explicit by first discretizing the problem and rewriting it as a system of equations,

$$\int_a^b dt K(s,t) f(t) = g(s) \longrightarrow \sum_j A_{ij} x_j = b_i. \tag{5.7}$$

The matrix $A \in \mathbb{R}^{m \times n}$ inhibits an expansion called *Singular Value Decomposition* (SVD) [111], which is given by

$$A \equiv U \Sigma V^T = \sum_i^n \vec{u}_i \sigma_i \vec{v}_i^T, \tag{5.8}$$

where the matrices fulfill $U^T U = \mathbb{I}$, $V^T V = \mathbb{I}$ and $\Sigma = \mathrm{diag}\,(\sigma_1, \sigma_2, ..., \sigma_n)$. The column vectors $\vec{u}_i, \vec{v}_i$ are called *left and right singular vectors*, while the σ_i are the *singular values* of the matrix A. The ill-posedness of a problem shows in this discretized framework by the fact that the singular values of the smoothing matrix A decrease to zero with rising index i. Expanding the solution vector $\vec{x} = \sum_i \left(\vec{v}_i^T \cdot \vec{x}\right) \vec{v}_i$ into a basis of right singular vectors, we get from (5.8)

$$A\vec{x} = \sum_{ij}^n \vec{u}_i \sigma_i \left(\vec{v}_j^T \cdot \vec{x}\right) \delta_{ij} = \sum_i^n \vec{u}_i \sigma_i \left(\vec{v}_i^T \cdot \vec{x}\right). \tag{5.9}$$

Thus, the smaller the singular values σ_i become, the more damped out the corresponding contribution of $A\vec{x}$ to $\vec{b}$. Inverting the matrix A, we see the expected amplification of details presented above, namely

$$\vec{x} = A^{-1}\vec{b} = V\Sigma^{-1}U^T\vec{b} = \sum_i^n \frac{\vec{u}_i^T \cdot \vec{b}}{\sigma_i}\vec{v}_i. \tag{5.10}$$

In this context the smallness of the singular values causes of course numerical problems, which in practice can have a strong impact on the stability of a solution: the modes with smallest singular values dominate the solution, small perturbations lead to huge fluctuations in the solution. To be more precise, this phenomenon arises as soon as the modulus of the expansion coefficients $|\vec{u}_i^T \cdot \vec{b}|$ remains much larger than the singular values, and the matrix A is said to be *ill-conditioned* [111].

Another tool in this context is Tikhonov Regularization. It is useful for solving ill-posed problems numerically, as well as for analytic investigation of general properties of ill-posed problems. In the current work we are mainly interested in the latter, instead of actually performing computations with the Tikhonov method, and extract general features of model independent approaches to solving ill-posed problems. Its framework consists of solving the least squares problem [106, 112]

$$\min_{\vec{x}} \left(\left\| A\vec{x} - \vec{b} \right\|^2 + \lambda^2 \left\| L\vec{x} \right\|^2 \right) \tag{5.11}$$

with respect to $\vec{x}$. The operator L can be essentially any operator, typical choices include the unit matrix and the first or second derivative operator. Thus, the additional operator poses constraints of smoothness or differentiability on the solution, and this way regularizes a wildly oscillating $\vec{x}$. The amount of regularization added to the solution is controlled via the parameter λ. There are plenty of algorithmic methods to solve a given problem in this way, but in order to draw generic conclusions, we have to invoke an extension of the SVD, the *Generalized Singular Value Decomposition* (GSVD), which makes a statement about a pair of matrices $(A, L) \in (\mathbb{R}^{m\times n}, \mathbb{R}^{p\times n})$, involving corresponding *generalized singular values* γ_i [111]. It can be shown that, for a sufficiently ill-conditioned matrix A and well conditioned regulator L as in(5.11), the generalized singular values are in correspondence to the singular values, $\gamma_i = \sigma_i\sqrt{1-\sigma_i^2} \approx \sigma_i$ for small enough σ_i, and the solution to (5.11) is given by

$$\vec{x}_{\mathrm{reg}}(\vec{b}, \lambda) = \sum_{i=1}^{p} f_i \frac{\vec{u}_i^T \cdot \vec{b}}{\sigma_i}\vec{w}_i + \sum_{i=p+1}^{n} \left(\vec{u}_i^T \cdot \vec{b} \right) \vec{w}_i. \tag{5.12}$$

Here, the numbers f_i are so called filter factors, given by $f_i = \frac{\gamma_i^2}{\gamma_i^2+\lambda^2}$ for $L \neq \mathbb{I}$, which cancel the contributions from small singular values for a large enough regularization parameter λ. The vectors w_i are the columns of a well conditioned matrix $W \in \mathbb{R}^{n\times n}$, appearing in the corresponding decomposition of A and L.

So far we have mainly used discretized problems and solution strategies explicitly to both make the matter mathematically easier, and account for the discrete nature of the inverse problem we are facing in QCD. One very crucial fact is missing in our presentation so far: the data that we obtain from a Monte Carlo computation are in general the results of a statistical process, and thus subject to statistical errors. Writing the right hand side as $\vec{b}_e = \vec{b} + \vec{e}$, with $\vec{b}$ being the unperturbed r.h.s. as appearing in the considerations above, and $\vec{e}$ being a vector of errors on the data, one can show that the expectation value of the modulus of the perturbed coefficients, i.e. $|\vec{u}_i^T \cdot \vec{b}_e|$, levels off and thus is dominated by the errors $|\vec{u}_i^T \cdot \vec{e}| \sim \|e\|$ [111], independent of the unperturbed r.h.s. $\vec{b}$. This implies that the errors on the input data are actually the prime source of ill-posedness of the problem. However, there exists a very general statement, called the *Discrete Picard Condition* [113]. It states that, if the modulus of the unperturbed coefficients $|\vec{u}_i^T \cdot \vec{b}|$ in (5.12) on average decay to zero faster than the singular values σ_i, then the regularized solution $x_{\text{reg}}(\vec{b}_e, \lambda)$ approximates the unperturbed and unregularized solution $x_{\text{exact}} = x_{\text{reg}}(\vec{b}, 0)$. To make this more specific, the difference of these two solutions is given by [111]

$$\begin{aligned} &\vec{x}_{\text{reg}}(\vec{b}_e, \lambda) - \vec{x}_{\text{reg}}(\vec{b}, 0) = \\ &\left(\sum_{i=1}^{p} f_i \frac{\vec{u}_i^T \cdot \vec{e}}{\sigma_i} \vec{w}_i + \sum_{i=p+1}^{n} \left(\vec{u}_i^T \cdot \vec{e} \right) \vec{w}_i \right) + \sum_{i=1}^{p} \left(f_i - 1 \right) \frac{\vec{u}_i^T \cdot \vec{b}}{\sigma_i} \vec{w}_i. \end{aligned} \tag{5.13}$$

The above is a measure of the error made as a function of the amount of regularization applied to the problem. If there is a large degree of regularization, i.e. λ is large, then the filter factors $f_i \sim 0$, and the dominating term is the last one, reflecting a large error due to the applied regularization, while the terms related to the errors of the data are suppressed. Choosing a small λ we force the filter factors to be close to unity, thus filtering out the last term in (5.13) and ending up with an error that is dominated by the error on the input data, which signals the instabilities of the unregularized, ill-posed problem. The framework of Tikhonov regularization minimizes the sum of the problem norm $\left\| A\vec{x} - \vec{b} \right\|^2$ and the scaled regulator norm $\lambda \left\| L\vec{x} \right\|^2$, and one sees that, with larger regularization factor λ, the regularizing term dominates and thus gains more weight in the minimization. This introduces the *regularization error* on the level of the minimizing functional (5.11). When plotting $\|L\vec{x}\|^2$ against $\left\| A\vec{x} - \vec{b} \right\|^2$, the resulting curve, parameterized by λ, is called *L-curve*. It directly reflects how in an almost unregularized solution the regularizing term grows large, and vice versa. The name stems from its characteristic shape when viewed in a $\log - \log$ fashion, as shown in Fig. 5.2. This is usually used as a method to determine an 'ideal' regularization parameter λ_0, by choosing it such that the resulting point of the L-curve is close to the kink of the 'L', thus keeping both norms close to a simultaneous minimum. See [114] for a more elaborate treatment of the L-curve.

To sum up, in the course of solving an ill-posed problem in the framework of Tikhonov

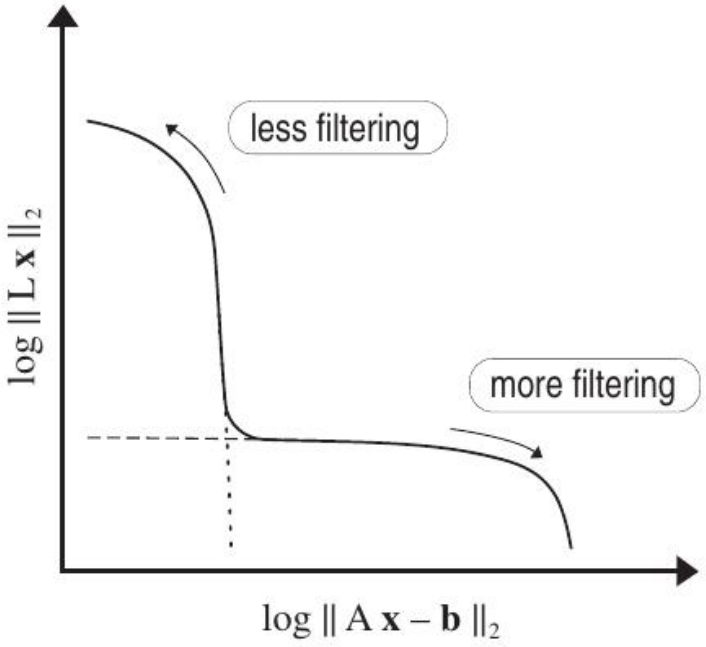

Figure 5.2: The L-curve as a function of λ. A balanced solution would be located at the kink, i.e. close to the intersection of the two dotted lines. The picture is taken from [111].

regularization, the arguments above show that we are always computing a wrong solution, in the sense that we always suffer from at least one kind of error. Only by tuning the regularization parameter we decide, according to (5.13), which error is realized to what extent. The L-curve is often called *tradeoff curve*, for apparent reasons, and the tradeoff is always between an underregularized solution, suffering from instabilities of the underlying original problem, and an overregularized solution, which is smoothed by the regularization term, but is further away from the problem we are actually interested in to solve. The method of Backus and Gilbert, which is presented in Sec. 5.5, is of a very similar nature, as one also tries to minimize a sum of two terms, of which one is the actual problem, and the other is a reglulator, and as a consequence one can construct tradeoff curves and observe the phenomena of overregularization and underregularization. The treatment of Tikhonov regularization laid out in this chapter is thus useful to gain an understanding also of the method of Backus and Gilbert.

Finally, we mention another model-independent, numerical method that became very popular and has been widely used to extract spectral functions in QCD, given correlation function data, which is the Maximum Entropy Method (MEM) [115] and its successive improvements [116, 117, 118]. The method is *Bayesian*, i.e. fundamentally probabilistic, and takes additional input information via a *default model*, on which the final solution then depends. A characteristic feature of this method is that the quality of the obtained solution is quantifiable, in the sense that MEM yields the *most probable* solution to a

problem. We will compare the results of our studies to corresponding results obtained by the Maximum Entropy Method.

5.2 Thermal moments and the transport contribution

Thermal moments are defined as the coefficients of the Taylor expansion of the correlation function around the midpoint [119],

$$G_H(\tau T) = \sum_{n=0}^{\infty} G_H^{(n)} \left(\frac{1}{2} - \tau T\right)^n , \tag{5.14}$$

$$\text{where} \quad G_H^{(n)} = \frac{1}{n!} \frac{d^n G_H(\tau T)}{d(\tau T)^n}\bigg|_{\tau T = 1/2} = \frac{1}{n!} \int_0^{\infty} \frac{\mathrm{d}\omega}{2\pi} \left(\frac{\omega}{T}\right)^n \frac{\rho_H(\omega)}{\sinh(\omega/(2T))}. \tag{5.15}$$

Because the correlation functions under consideration in this work are symmetric with respect to the midpoint, all odd thermal moments vanish identically. Essentially we are interested in the first two non vanishing thermal moments. The zeroth moment $G_H^{(0)}$ is simply the value of the correlation function at the midpoint, while the second moment $G_H^{(2)}$ is the curvature of the correlation function at the midpoint. There is a very physical reason in considering thermal moments in the analyses to come, as they are especially sensitive to the low frequency region of the spectral function. On the one hand, the weight function

$$K^{(n)}(\omega/T) \equiv \frac{(\omega/T)^n}{n! \sinh(\omega/(2T))}, \tag{5.16}$$

for $n = 0$ equal to the kernel $K(\tau T = 1/2, \omega/T)$, generally falls off faster than the kernel at $\tau T < 1/2$ for large frequencies ω/T, thus it filters out more contribution from the spectral functions at high frequencies than the latter. On the other hand, at small frequencies the weights for $n > 0$ have a vanishing intercept at $\omega/T = 0$, but then first increase before gradually going over into their exponentially decaying behavior at large frequencies. This is depicted in Fig. 5.3 (*left*), which explains their sensitivity to the region of low frequencies. As can be seen in the plot, the corresponding maxima of the weight functions shift to the right with increasing n. In order to quantify this point, consider the derivative with respect to ω/T to find the maximum as a function of the order n,

$$\frac{\mathrm{d}}{\mathrm{d}(\omega/T)} \frac{(\omega/T)^n}{\sinh(\omega/(2T))} = \frac{n(\omega/T)^{n-1}}{\sinh(\omega/(2T))} - \frac{(\omega/T)^n}{2\sinh(\omega/(2T))\tanh(\omega/(2T))} \stackrel{!}{=} 0 \tag{5.17}$$

$$\Leftrightarrow 2n \tanh(\omega/(2T)) \stackrel{!}{=} \omega/T, \tag{5.18}$$

thus leading to a self-consistent equation. Graphical solutions for $n = 0, 2, 4$ are shown in Fig. 5.3 (*right*), with the maxima thus lying at $\omega/T = 0$ for $n = 0$ and $\omega/T \approx 3.8, 8.0$ for $n = 2, 4$, respectively. From both pictures we see that the zeroth moment is sensitive

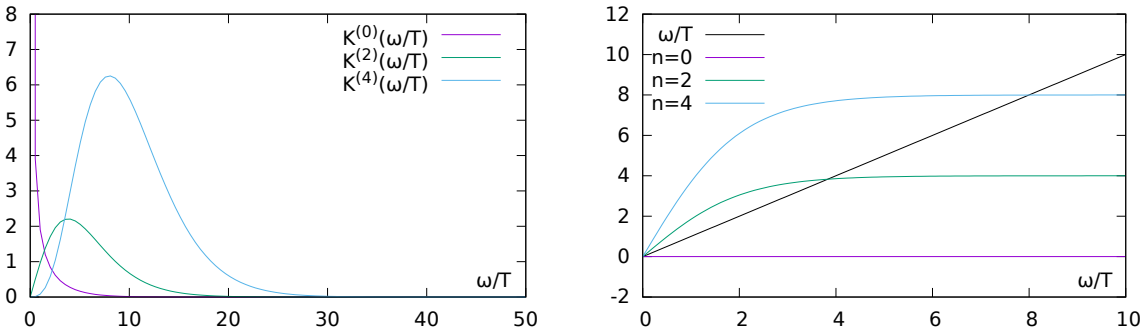

Figure 5.3: *Left*: The integrations kernels of the thermal moments for $n = 0, 2, 4$. *Right*: The solutions of the self consistent equation (5.18) for $n = 0, 2, 4$.

to the region $\omega/T = 0$, and falls off quite rapidly. The second thermal moment rises steeply to its maximum value, and thus we expect it to still contain a large amount of information concerning the region of low frequencies. Contrasting this with the large value of $\omega/T \approx 8$ for the location of the maximum of the fourth thermal moment, and the course of the corresponding weight function $K^{(4)}(\omega/T)$, which becomes larger than $K^{(2)}(\omega/T)$ only around $\omega/T \approx 3.5$, i.e. when the latter reaches its maximum and starts to fall off, we qualitatively expect it to not grasp the details of the low frequency region as well as the second thermal moment does.

The thermal moments are not only helpful to gain more information about the low frequency region of the spectral function, but can be linked directly to physical modes in the spectrum. When considering the free spectral functions as in Sec. 4.2, we found that some of them, in the massive case specifically in the vector, axialvector and scalar channels, while in the massless case only the former two channels, gave rise to contributions proportional to a Dirac delta function, $\rho_{\text{low}} \sim \omega\delta(\omega)$. As such, this zero mode is located exactly at $\omega/T = 0$ and upon integration leads to a constant contribution to the respective correlation function [120]. To put it explicitly, the reason for this is the behavior of the kernel for low frequencies, given by equation (5.2), such that

$$\omega\delta(\omega)K(\omega, \tau, T) \overset{\omega\to 0}{\longrightarrow} 2T\delta(\omega). \tag{5.19}$$

Upon evaluation of the Dirac delta, the constant $2T$ remains and obviously affects the correlator at all distances τ. We follow [120] closely to pictorially explain the physical origin of this contribution. Consider a quark-antiquark pair of degenerate quarks with zero spatial momentum, as a *free quark system*, i.e. while strictly there is no interaction in the system to form a mesonic bound state, we still formally consider them to be a meson-like system with an energy $E = 2m_q$, hence lacking any interaction energy. Looking at the sketch of this meson-like temporal correlation function in Fig. 5.4 (a), we see that it thus exhibits a behavior

$$G(\tau) \sim \exp(-m_q\tau)\exp(-m_q\tau) = \exp(-2m_q\tau). \tag{5.20}$$

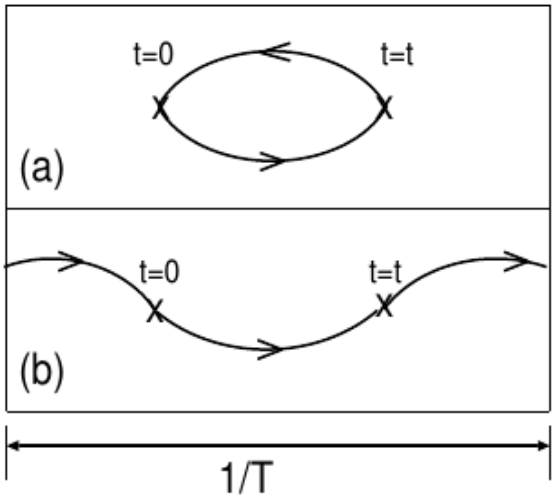

Figure 5.4: The two possible contributions to the meson-like correlator. Note that the contribution in (b) really denotes the wrapping of only *one* quark propagator; the wrapping of both propagators corresponds to the backwards contribution (see Sec. 2.6.1), which does not play a role in this qualitative discussion. The picture is taken from [120].

This contribution directly joins the quarks' source and sink and is independent of the temporal extent of the system. However, if the temporal extent of the system is finite, $L_t = 1/T$, then either of the two quarks can connect to the other by wrapping around the boundary, see Fig. 5.4 (b), which leads to a correlation of the form

$$G(\tau) \sim \exp(-m_q \tau) \exp(-m_q(1/T - \tau)) = \exp(-m_q/T). \tag{5.21}$$

This contribution is independent of the time variable, thus can strongly affect the correlation function at large distances, and directly results from the finiteness of the temporal direction. While arguing this way is a bit hand-waving due to the idealization of a free quark system, and thus purely qualitative, it nevertheless connects the appearance of zero modes in the free spectral functions to the finiteness of the temporal extent of the system. Since consequently the wrapping contribution influences the structure of the spectral function at low frequencies, it certainly will influence the transport properties of the interacting system. Consider, however, that a more detailed picture, e.g. the question why this contribution is absent in some quantum number channels, can only be acquired by computing the free spectral function from first principles, as we did in Sec. 4.2.

In the non-interacting case the zero mode, if present, is entirely contained in the zeroth thermal moment, i.e. the midpoint of the correlation function, because of the exact Dirac delta function in the spectral function at $\omega/T = 0$. A practical consequence

is that by subtracting the midpoint value from a free correlation function, i.e. writing

$$G_H^{\text{free,sub}}(\tau) = G_H^{\text{free}}(\tau) - G_H^{(0),\text{free}}, \tag{5.22}$$

we are guaranteed to have subtracted the entire zero mode contribution from the correlation function. However, we emphasize that generally also contributions from larger frequencies are subtracted in this manner, already in the free case, as can be seen from the definition of the moments (5.15).

So far the discussion referred solely to the case of no interactions between the particles of the system. Turning on interactions has a very profound effect on the shape of the spectral function, as we have seen in the foregoing section. Consider here the expected effects on the level of the correlation function. As such, the discussion above for the origin of the constant mode in the free quark system resulted from the absence of any interaction term mixing the two exponential quark correlations, with the time dependent contribution of the backward running 'wrapping' quark propagator just canceling the corresponding contribution of the forward running quark, leaving the constant. In an interacting theory, the two quarks are expected to form physical bound states, with an interaction energy that certainly depends on the distance between the two quarks. We correspondingly modify (5.21) to read

$$\begin{aligned} E(\tau) &= m_q\tau + m_q\left(\frac{1}{T} - \tau\right) + E_{\text{bind}}(\tau) \\ &\Rightarrow G(\tau) \sim \exp\left(-\frac{m_q}{T} - E_{\text{bind}}(\tau)\right). \end{aligned} \tag{5.23}$$

From the simple wrapping picture we thus obtain a binding energy of the two quarks which depends on the time variable, and the factorization into two distinct contributions does not work anymore. An immediate consequence of this is that the zero mode contribution is not strictly a constant in that case, which we have seen in the last section on more formal grounds, as, on the level of the spectral function, the zero mode is expected to be modified to become a peak of finite width upon the onset of interactions. If, in practice, the peak is very narrow, then the integration yields a merely weakly time dependent term, which is consequently called a *smeared zero mode* [119, 120]. Lattice studies have shown in the past that this mode constitutes a large share of the temperature dependence of Euclidean temporal meson correlators [120, 121], to an extent that modifications of bound states yield a comparatively weak signal in studies of the temperature dependence of correlation functions [122, 123, 124].

For the thermal moments this means that, as opposed to the non-interacting case, the transport contribution is not solely contained in the zeroth thermal moment, but due to the smearing also higher moments carry their share. Consequently, while in the free case the subtraction of the zeroth thermal moment (5.22) canceled all of the transport contribution, this feature is lost in the interacting case. To sum up, by performing a midpoint subtraction on interacting correlation functions,

$$G_H^{\text{sub}}(\tau) = G_H(\tau) - G_H^{(0)}, \tag{5.24}$$

we can effectively reduce the impact of the wrapping contribution on the correlation function data, while suffering from two distinct uncertainties:

1. We subtract contributions from the correlator that originate from regions higher up in the spectrum, instead of only the zero mode. This happens already in the free case.

2. We merely subtract a part of the zero mode contribution, and are not able to make precise quantitative statements about how much information is left unsubtracted in the higher moments, e.g. the second and fourth thermal moment. This is an effect of non-vanishing interactions.

These will have to be kept in mind when performing midpoint subtractions, and the identification of these two effects will help to understand the behavior of the corresponding correlation functions. Also, for correlators of open flavor mesons, we expect that a subtraction of the midpoint is even less effective, because the characteristic bump contribution is located at a frequencies strictly larger than zero, i.e. not centered around $\omega/T = 0$ like the smeared zero mode.

5.3 Analysis of heavy quark correlators

Previous sections dealt with an analysis of free spectral functions, as well as phenomenological computations and motivations, that constitute our rough expectations of the effects of an interacting medium. Because the free case is analytically computable and thus well understood in terms of the low frequency structure of the spectral functions, this is a natural way to interpret and to build up first expectations of measurements of observables. In order to asses the changes that happen to the spectral function when the corresponding particle is subject to a thermal medium, as opposed the the zero temperature vacuum, we can compare their corresponding temporal and screening correlation functions, which are the most immediate observables to extract from a lattice computation.

5.3.1 The reconstructed correlator

Because (4.17) has a generally simple structure, as it is a one dimensional weighted integration, with the structure of the weighting kernel presented in section 4.3, it is possible to make indirect statements about features of the underlying spectral function just from the temporal correlation function data. However, a direct comparison suffers from a fundamental obstacle with regard to the extraction of information from the underlying spectrum. Concerning temporal correlation functions for different temperatures, the kernel functions in the integration (4.17), which converts the spectral function to the corresponding correlation function, generally differ due to their explicit temperature dependence. This means that the temperature dependence of correlation functions really is

a mix of the temperature dependence of the spectral density and the integration kernel. Thus, comparing two correlation functions $G(\tau, T)$ and $G(\tau, T')$ at temperatures $T > T'$ directly thus does not guarantee that observed changes really stem solely from differences in the underlying spectral distributions $\rho(\omega, T)$ and $\rho(\omega, T')$. A way to circumvent this problem is to define the so called *reconstructed correlator* [122, 125]

$$G_{\mathrm{rec}}(\tau, T, T') = \frac{1}{2\pi} \int_0^\infty \mathrm{d}\omega K(\omega, \tau, T)\rho(\omega, T'), \tag{5.25}$$

which substitutes the kernel dependence of $G(\tau, T')$ with that from $G(\tau, T)$, while leaving the spectral function untouched. Comparing $G(\tau, T)$ to $G_{\mathrm{rec}}(\tau, T, T')$ then implies that any difference in the correlators must result from differences in the spectral functions alone. Since equation (5.25) already requires knowledge of the complete spectral function to compute the reconstructed correlator, we utilize a general relation between integration kernels at different temperatures [119, 126], which for temporal distances τ, τ' and frequency ω implicitly in lattice units, reads

$$\begin{aligned} K(\tau, T) = \frac{\cosh(\omega\,[\tau - N_\tau/2])}{\sinh(\omega N_\tau/2)} &= \sum_{\tau'=\tau, \tau'+=N_\tau}^{N'_\tau - N_\tau + \tau} \frac{\cosh(\omega\,[\tau' - N'_\tau/2]}{\sinh(\omega N'_\tau/2)} \\ &= \sum_{\tau'=\tau, \tau'+=N_\tau}^{N'_\tau - N_\tau + \tau} K(\tau', T') \end{aligned} \tag{5.26}$$

where the temperature is proportional to the inverse number of points in temporal direction. A restriction of this formula is that the higher temperature needs to be an integer multiple of the lower one, i.e. $N'_\tau = nN_\tau$, and τ and τ' range from 0 to $N_\tau - 1$ and $N'_\tau - 1$, respectively. Inserting (5.26) into (5.25) immediately yields

$$G_{\mathrm{rec}}(\tau, T) = \sum_{\tau'=\tau, \tau'+=N_\tau}^{N'_\tau - N_\tau + \tau} G(\tau', T'), \tag{5.27}$$

and hence the reconstructed correlator can be computed directly from the correlator data in the vacuum. As a remark, note that in a ratio of an in-medium correlator and its corresponding vacuum correlator we can expect cancellations of cutoff effects present in both correlators.

It is instructive to quickly prove relation (5.26). We shift the starting value of the sum to $\tau' = 0$, and get

$$\frac{\cosh(\omega\,[\tau - N_\tau/2])}{\sinh(\omega N_\tau/2)} = \sum_{\tau'=0}^{N'_\tau - N_\tau} \frac{\cosh\left[\omega\left(\tau - N_\tau/2\right) + \omega\left(\tau' - (N'_\tau - N_\tau)/2\right)\right]}{\sinh(\omega N'_\tau/2)}. \tag{5.28}$$

The argument of the hyperbolic cosine on the r.h.s. can be split to yield

$$\begin{aligned} \cosh(\dots) = &\cosh\left[\omega(\tau' - (N'_\tau - N_\tau)/2)\right] \cosh\left[\omega(\tau - N_\tau/2)\right] \\ &+ \sinh\left[\omega(\tau' - (N'_\tau - N_\tau)/2)\right] \sinh\left[\omega(\tau - N_\tau/2)\right], \end{aligned} \tag{5.29}$$

of which the term involving the hyperbolic sine completely cancels when summed over,

$$\sum_{\tau'=0}^{N'_\tau - N_\tau} \sinh\left[\omega(\tau' - (N'_\tau - N_\tau)/2)\right] = 0, \tag{5.30}$$

due to symmetry, and the result is

$$\begin{aligned} K(\tau, T) &\stackrel{!}{=} \frac{\cosh(\omega\left[\tau - N_\tau/2\right])}{\sinh(\omega N'_\tau/2)} \sum_{\tau'=0}^{N'_\tau - N_\tau} \cosh\left[\omega(\tau' - (N'_\tau - N_\tau)/2\right] \\ \iff \sum_{\tau'=0}^{N'_\tau - N_\tau} &\cosh\left[\omega(\tau' - (N'_\tau - N_\tau)/2\right] \sinh(\omega N_\tau/2) \stackrel{!}{=} \sinh(\omega N'_\tau/2). \end{aligned} \tag{5.31}$$

Writing the l.h.s. as exponentials and multiplying out, many terms cancel and the remaining ones can be written as

$$\sinh(\omega N'_\tau/2) = \frac{1}{2} \sum_{\tau'=0}^{N'_\tau - N_\tau} \left\{\sinh\left[\omega(\tau' - N'_\tau/2 + N_\tau)\right] - \sinh\left[\omega(\tau' - N'_\tau/2)\right]\right\}, \tag{5.32}$$

which in turn cancel to a large degree when summed, because

$$\begin{aligned} \sum_{\tau'=0}^{N'_\tau - N_\tau} \sinh\left[\omega(\tau' - N'_\tau/2)\right] &= -\sinh(\omega N'_\tau/2), \\ \sum_{\tau'=0}^{N'_\tau - N_\tau} \sinh\left[\omega(\tau' - N'_\tau/2 + N_\tau)\right] &= \sinh(\omega N'_\tau/2). \end{aligned} \tag{5.33}$$

This proves relation (5.26) to be true for all integer $n = T/T'$.

5.3.2 The screening correlator

Addressing the complications of comparing temporal correlation functions in another way, note that the compactification of the time direction for a practical computation will generally imply $N_\tau \ll N_\sigma$. Thus, investigating the screening correlation functions instead has the advantage to yield more data points, which potentially increases the accuracy of further analyses. Apart from this purely numerical benefit, the extent in the spatial directions is of course also larger in physical units, which makes the screening correlator a good probe for in-medium effects, which are expected to show up most clearly for $z > 1/T$ [37]. Also, this implies that ground state screening mass spectroscopy becomes possible at such large separations. Furthermore, the relation of the spectral function and the respective screening correlator, as presented in section 4.1 (specifically equation (4.25)), only depends on temperature through the spectral function itself. Hence, in contrast to the temporal correlation function, the former directly allows for a

meaningful comparison of different temperatures, without the need for a 'reconstructed screening correlator'. This also implies that the restriction of an integer temperature ratio can be dropped, and theoretically a continuous range of temperatures can be scanned using only one designated zero temperature lattice. As a last, but important point, note that a potential zero mode contribution $\sim \omega\delta(\omega)$ in $\rho(\omega, p_z)$, as it appears in the free continuum spectral function $\rho(\omega)$, does not in general lead to a z-independent constant contribution in the screening correlation function [37]. To see this, we explicitly split off this contribution from the spectral function by writing $\rho(\omega, p_z) \equiv \omega\delta(\omega) + \widetilde{\rho}(\omega, p_z)$, where $\widetilde{\rho}(\omega, p_z)$ denotes the spectral function without the zero mode contribution, and perform the integration (4.25) over the zero mode only,

$$\begin{aligned} \delta G_H^{\mathrm{scr}}(z,T) &= \int_0^\infty \frac{2}{\omega}\mathrm{d}\omega \int_{-\infty}^\infty \mathrm{d}p_z \mathrm{e}^{ip_z z}\omega\delta(\omega) \\ &= \int_0^\infty \mathrm{d}\omega 2\delta(\omega) \int_{-\infty}^\infty \mathrm{d}p_z \mathrm{e}^{ip_z z} = 2\pi\delta(z). \end{aligned} \tag{5.34}$$

This is merely a contact term and only contributes to $z = 0$. Indeed, it was found that screening correlators in dynamical lattice computations across the deconfinement/chiral restoration transition are much more sensitive to the forming medium and carry a strong temperature dependence across the transition [37].

Aside from merely comparing screening correlators directly, there is another way to extract details of the underlying spectral properties of spatial meson correlation functions. Note that equation (4.25) has a more complicated structure than the relation (4.17) of the spectral function to the temporal correlator in momentum space, which is just one weighted integral. A possible way to detect bound state modifications as a function of the temperature, when comparing screening correlators, lies in the corresponding change of their mass when subjected to a thermal medium. In the vacuum, the screening correlator and the temporal correlator are degenerate, with their ground state mass given by the characteristic exponential decay at large distances, $M_{scr} \equiv M_{q\bar{q}}$. Because at non vanishing temperature the temporal direction is compactified with antiperiodic boundary conditions for fermions, at infinite temperature the screening mass is then given by $M_{scr}^{\mathrm{free}} = 2\sqrt{m_q^2 + (\pi T)^2}$, where the fermionic Matsubara zero mode πT enters the expression due to the temporal integration [127]. These two cases are thus extreme cases, and by extracting screening masses from spatial correlation functions at finite temperature, the respective proximity to either of the two regimes serves as an indicator whether the system behaves more like in the free case or is still tightly bound.

5.4 Fitting to an Ansatz

We now come to a method that, instead of inferring features of the spectral function *indirectly*, and therefore merely qualitatively, allows for *direct* access to a functional

form of the spectral function. As was elaborated in Sec. 5.1.2, the inversion of equation (4.17) is an underdetermined problem. In the present work we choose the necessary additional information to enter in the form of an Ansatz, which is inspired and phenomenologically motivated by our elaborations in Sec. 4.2 and 4.3. Fixing the shape of the solution by supplying an Ansatz with two or three degrees of freedom is a very strong assumption, and the method of least squares fitting consequently is the natural tool to be employed. Because now the number of degrees of freedom determining the spectral function has drastically decreased, the problem has in this sense turned into an *over-determined* problem, where the choice of the Ansatz consequently plays an essential role, and will be assessed critically by using different functional shapes in the fit.

To be more concrete, the data supplied to the fit will be temporal Euclidean correlation functions, extrapolated to the continuum. Of special interest in this case is the vector channel spectral function and its components, $\rho_V = \rho_{ii} - \rho_{00}$, that relate via the QCD electromagnetic current to the dilepton rate and the electrical conductivity of the QGP, as described in Sec. 3.2.1. In order to extract the vector spectral function via equation (4.17) in this case, we can construct an Ansatz for its spatial part:

$$\begin{aligned}\rho_{\mathrm{ans}}(\omega,T) =& \chi_q c_{\mathrm{BW}} \frac{\omega\Gamma}{\omega^2+(\Gamma/2)^2} + \frac{3}{2\pi}(1+k)\omega^2 \tanh\left(\frac{\omega}{4T}\right) \\ \equiv& \rho_{\mathrm{BW}}(\omega,T) + (1+k)\rho_V^{\mathrm{free}}(\omega,T).\end{aligned} \tag{5.35}$$

It consists of two constituents: a Breit-Wigner peak, governing the behavior in the low ω region via its height c_{BW} and width Γ as fit parameters, and a modified version of the free, massless continuum spectral function, with a third fit parameter k. This Ansatz is inspired by the known relations for massless continuum spectral functions in the non-interacting case, derived in Sec. 4.2.1,

$$\rho_{ii}^{\mathrm{free}}(\omega,T) = 2\pi T^2\omega\delta(\omega) + \frac{3}{2\pi}\omega^2 \tanh(\frac{\omega}{4T}) \tag{5.36}$$

$$\rho_{00}^{\mathrm{free}}(\omega,T) = 2\pi T^2\omega\delta(\omega) \tag{5.37}$$

$$\rho_V^{\mathrm{free}}(\omega,T) = \rho_{ii}^{\mathrm{free}}(\omega,T) - \rho_{00}^{\mathrm{free}}(\omega,T). \tag{5.38}$$

The computations presented in Sec. 4.3 gave hints that the δ-functions in these expressions are expected to be washed out upon the onset of interactions, and yielded the functional shape of a Breit-Wigner peak with its maximum at $\omega/T = 0$ under this melting effect. These are very concrete hints at the expected shape of the spectral function for low frequencies, and especially lead to a nontrivial shape in this region. However, the temporal component of the vector channel correlator is the correlation of the net quark and antiquark number, and the net number of quarks is conserved at vanishing quark chemical potential. Hence, the correlator $G_{00}(\tau T)$, which was found to be a constant in the free case in Sec. 4.2.1, is also a constant in the interacting case, and thus the corresponding spectral function also remains an exact Dirac delta peak, with only the overall value of the quark number susceptibility χ_q being modified.

On the other hand, for large frequencies we know that with rising ω we can expect to enter the regime where perturbative computations show an increasingly better performance, and asymptotic freedom guarantees that for very large frequencies, the spectral function is approaching the free solution. Hence, for large frequencies we draw inspiration from the free case, and set the spectral function there to be the free spectral function ρ_V^{free}, corrected by a deviation factor $(1 + k)$. This solution of course never approaches the fully free case, and it can be shown that in leading order perturbation theory $k = \alpha_s/\pi$ [96]. Since asymptotic freedom really influences the physical coupling $\alpha_s \to 0$, choosing k to be a constant in ω is clearly only an approximation. However, since the set in of asymptotic freedom is to be expected at comparatively large frequencies, and the kernel suppresses the large frequency region in the integral the more, the larger τT, the dependence of k on ω will not play a crucial role in our fit procedure. This does not mean that there is no room for improvement, as is shown later by utilizing higher order perturbative input, as well.

5.5 The method of Backus and Gilbert

This section deals with a specific way of solving Fredholm equations, which was invented by Backus and Gilbert in the 60's for solving geophysical inverse problems [128]. This method has proven to be very successful in reconstructing the earth's internal properties given some 'gross earth data', and notably has been used in astrophysics for extracting γ-ray spectra of γ-ray bursts [129]. The derivation of the method presented here relies mainly on [108, 129].

It differs from Tikhonov regularization, presented heuristically in Sec. 5.1.2 to demonstrate some selected mathematical aspects of ill-posed problems, by the functionals that are to be minimized, as well as by being a linear method. The latter means that the reconstructed spectral function is built of the sum of the input data points $G_n \equiv G(\tau_n)$, each multiplied by a certain basis function $q_n(\omega)$,

$$\hat{\rho}(\omega) = \sum_{n=1}^{N} q_n(\omega) G_n. \tag{5.39}$$

Considering the initial problem, we can informally integrate over both sides with respect to τ and an integration kernel $H(\omega, \tau)$, such that

$$\begin{aligned} \int \mathrm{d}\tau H(\omega', \tau) G(\tau) &= \int \mathrm{d}\tau H(\omega', \tau) \int \mathrm{d}\omega K(\tau, \omega) \rho(\omega) \\ &= \int \mathrm{d}\omega \int \mathrm{d}\tau H(\omega', \tau) K(\tau, \omega) \rho(\omega) = \int \mathrm{d}\omega \delta(\omega', \omega) \rho(\omega) \end{aligned} \tag{5.40}$$

Ideally, the right hand side would yield $\rho(\omega')$, i.e. the kernel $H(\omega', \tau)$ would be the inverse of the problem's integration kernel $K(\tau, \omega)$. A linear method formulates this

idea in a discretized way,

$$\int \mathrm{d}\tau H(\omega',\tau)G(\tau) \sim \sum_n q_n(\omega')G(\tau_n) = \hat{\rho}(\omega') = \int \mathrm{d}\omega \hat{\delta}(\omega',\omega)\rho(\omega). \tag{5.41}$$

The last step describes the solution obtained by the numerical inversion procedure as a smeared out version of the correct solution. The weight function $\hat{\delta}(\omega',\omega)$ that performs this smearing operation is called the *resolution kernel* or *resolution function*. Comparing with (5.40), one has to find functions $q_n(\omega)$ for which

$$\sum_n q_n(\omega')K(\tau_n,\omega) = \hat{\delta}(\omega',\omega) \tag{5.42}$$

resembles a true δ-function as much as possible. Specifically, the method of Backus and Gilbert seeks to minimize the quantity

$$\mathcal{A} = \int \mathrm{d}\omega'(\omega-\omega')^2 \left[\hat{\delta}(\omega,\omega')\right]^2 = \int \mathrm{d}\omega'(\omega-\omega')^2 \left[\sum_n q_n(\omega)K_n(\omega')\right]^2 \tag{5.43}$$

$$= \sum_{n,m} q_n(\omega) \int \mathrm{d}\omega'(\omega-\omega')^2 K_n(\omega')K_m(\omega')q_m(\omega) \tag{5.44}$$

$$\equiv \vec{q}(\omega)\, \mathbf{W}\, \vec{q}(\omega). \tag{5.45}$$

This quantity is referred to as the *spread* of the solution. By choosing an appropriate function of ω and ω' as a weight in the integration over the resolution function $\hat{\delta}(\omega,\omega')$, in this case $(\omega-\omega')^2$, the minimization procedure suppresses $\hat{\delta}(\omega,\omega')$ for $\omega \neq \omega'$ and admits it more contribution when $\omega = \omega'$, thus leading to $\hat{\delta}(\omega,\omega')$ acquiring the shape of a smeared peak. As a δ-function in general is also required to have unit area, the integral

$$\int \mathrm{d}\omega' \hat{\delta}(\omega,\omega') = \sum_n q_n(\omega) \int \mathrm{d}\omega' K_n(\omega') \equiv \vec{q}(\omega)\cdot\vec{R} \tag{5.46}$$

is introduced as an additional constraint.

Minimizing the functional $\mathcal{A}$ alone is a direct approach of inversion, as can be seen from (5.40). Hence, only minimizing (5.45) will result in a completely unregularized treatment, because it lacks the needed regularizing term, see Sec. 5.1.2. The method of Backus and Gilbert seeks to additionally minimize the statistical variance of the solution that is caused by the statistical uncertainty of the data. Writing $\bar{G}_n = G_n + \delta G_n$, the latter is given by δG_n, which satisfies

$$\langle \bar{G}_n \rangle = G_n, \quad \langle \delta G_n \rangle = 0 \quad \text{and} \quad \langle \delta G_n \delta G_m \rangle = \mathrm{cov}(G_n, G_m) \tag{5.47}$$

under the statistical ensemble average $\langle\cdot\rangle$. To see the connection of the respective fluctuations of solution and data, consider

$$\begin{aligned}\langle\big[\bar{\hat{\rho}}(\omega)\big]^2\rangle &= \langle\sum_n q_n(\omega)\bar{G}_n \sum_m q_m(\omega)\bar{G}_m\rangle = \sum_{n,m} q_n(\omega)\langle\bar{G}_n\bar{G}_m\rangle q_m(\omega)\\ &= \sum_{n,m} q_n(\omega)\langle G_nG_m + \delta G_nG_m + G_n\delta G_m + \delta G_n\delta G_m\rangle q_m(\omega)\\ &= \hat{\rho}^2(\omega) + \sum_{n,m} q_n(\omega)S_{nm}q_m(\omega)\\ &= \hat{\rho}^2(\omega) + \vec{q}(\omega)\,\mathbf{S}\,\vec{q}(\omega),\end{aligned} \tag{5.48}$$

with $S_{nm} = \mathrm{cov}(G_n, G_m)$. The variance of the estimator of the solution is then given by

$$\begin{aligned}\mathrm{Var}(\bar{\hat{\rho}}(\omega)) &= \langle\big[\bar{\hat{\rho}}(\omega) - \hat{\rho}(\omega)\big]^2\rangle = \langle\big[\bar{\hat{\rho}}(\omega)\big]^2\rangle - \langle\hat{\rho}(\omega)\rangle^2\\ &= \hat{\rho}^2(\omega) + \vec{q}(\omega)\,\mathbf{S}\,\vec{q}(\omega) - \hat{\rho}^2(\omega)\\ &= \vec{q}(\omega)\,\mathbf{S}\,\vec{q}(\omega) \equiv \mathcal{B},\end{aligned} \tag{5.49}$$

and constitutes the needed regulator $\mathcal{B}$ of the solution. It is important to stress that this is the error on the solution as caused by the statistical uncertainty of the data. While it is an integral part of the uncertainty of the solution $\hat{\rho}$, it does not state anything about the uncertainties from the regularization, loss of information etc.

With the calculations done above, the core of the Backus-Gilbert method is set up and the solution vector $\vec{q}$ is obtained by forming the normal equations and introducing a Lagrange multiplier to take the constraint (5.46) into account. In order to have control over the amount of regularization, the functional that is to be minimized is chosen to be

$$\begin{aligned}\mathcal{A}\cos(\theta) + \nu\mathcal{B}\sin(\theta) = \vec{q}\,\mathbf{W}\,\vec{q}\cos(\theta) + \nu\vec{q}\,\mathbf{S}\,\vec{q}\sin(\theta) \equiv \vec{q}\,\mathbf{L}\,\vec{q},\\ \mathbf{L} \;=\; \mathbf{W}\;\cos(\theta) + \nu\,\mathbf{S}\;\sin(\theta),\end{aligned} \tag{5.50}$$

with $\theta \in [0, \frac{\pi}{2}]$. Hence, for each ω, the solution can be continuously tuned from being unregularized to being fully regularized within finite bounds of the parameter θ. The factor ν is supposed to make the two matrices $\mathbf{W}$ and $\mathbf{S}$ of roughly the same order by choosing $\nu = \mathrm{tr}\mathbf{W}/\mathrm{tr}\mathbf{S}$; the respective contributions of the two quadratic forms thus lie on a circle parameterized by θ, as opposed to lying on an ellipse. With these modifications the normal equations are given by

$$\nabla_q\left(\vec{q}\,\mathbf{L}\,\vec{q} + \lambda\left[\vec{q}\cdot\vec{R} - 1\right]\right) = \vec{q}\,\mathbf{L} \;+\; \mathbf{L}\,\vec{q} + \lambda\vec{R} = 0, \tag{5.51}$$

$$\frac{\mathrm{d}}{\mathrm{d}\lambda}\left(\vec{q}\,\mathbf{L}\,\vec{q} + \lambda\left[\vec{q}\cdot\vec{R} - 1\right]\right) = \vec{q}\cdot\vec{R} - 1 = 0. \tag{5.52}$$

From (5.51) we get, bearing in mind that $\mathbf{L}$ is a symmetric matrix,

$$\mathbf{L}\,\vec{q} = -\frac{\lambda}{2}\vec{R} \quad\Leftrightarrow\quad \vec{q} = -\frac{\lambda}{2}\,\mathbf{L}^{-1}\vec{R} \tag{5.53}$$

while multiplying this with $\vec{R}$ and using the constraint (5.52) yields the Lagrange multiplier and, by eliminating it, the solution:

$$\begin{aligned} \vec{R}\cdot\vec{q} = -\frac{\lambda}{2}\vec{R}\,\mathbf{L}^{-1}\vec{R} \quad &\Leftrightarrow \quad \lambda = -2(\vec{R}\,\mathbf{L}^{-1}\vec{R})^{-1} \\ &\Rightarrow \quad \vec{q} = \frac{\mathbf{L}^{-1}\vec{R}}{\vec{R}\,\mathbf{L}^{-1}\vec{R}}. \end{aligned} \tag{5.54}$$

The expected spectral function $\hat{\rho}$ can then be constructed via (5.39).

As $\vec{q}$ depends on ω and θ through the matrix $\mathbf{L}$, note that first, $\mathcal{A}$ and $\mathcal{B}$ depend implicitly on the angle θ, and second, for every point in frequency space at which we want to construct the spectral function, one such solution has to be computed. Especially, for each frequency we have to make a choice about the regularizing parameter θ. From this point of view, the challenge in utilizing the method of Backus and Gilbert lies in finding a suitable mapping $\theta(\omega)$, that

- brings us as close as possible to the 'real' solution $\rho(\omega)$, with the spread kernel $\hat{\delta}(\omega,\omega')$ being as narrow in ω' as possible and thus the spread (5.45) being as small as possible for that frequency ω,
- at the same time provides a minimum statistical variance $\mathrm{Var}(\hat{\rho})$ for all ω.

To connect to the theory on Fredholm equations and other methods for solving these, as presented earlier, consider choosing a value $\theta \gtrsim 0$ for a fixed ω. Then the regulating term $\sim \mathcal{B}$ will be suppressed in (5.50), and accordingly, mainly the spread term $\sim \mathcal{A}$ will be minimized *at that specific frequency*. Thus, the resolution will be high. On the other hand, the statistical variance of the solution will be rather large, which displays that our solution is dominated by the errors of the input data. According to (5.13), this is expected if the solution is *underregularized*. If, in contrast, we choose $\theta \lesssim \frac{\pi}{2}$, then the variance will generally be small but we lose the resolution, i.e. the value of $\hat{\rho}(\omega)$ will be very different from the true solution $\rho(\omega)$. This analogously displays *overregularization*, and the solution is not dominated by the error on the input data, but by a regularization error that we introduce. Hence, the choice of the regularizing parameter θ is a tradeoff between both kinds of errors. The L-curve for that specific frequency ω in this case is built by plotting, in $\log-\log$ scale, the variance of the solution $\mathcal{B}$ against the spread of the solution $\mathcal{A}$.

6 Analysis of strange and charm mesons on dynamical lattices

6.1 Tuning of the quark masses

6.1.1 Lattice setup

In this section the behavior of heavy flavor bound states across the deconfinement transition is studied using lattice computations featuring two dynamical light and one dynamical strange degree of freedom. The lattice action used to generate the sea quarks is the Highly Improved Staggered Quark (HISQ) action, presented in Sec. 2.2. The gauge field samples used in the integration over the $SU(3)$ manifold are produced using the Rational Hybrid Monte Carlo (RHMC) algorithm, discussed in Sec. 2.4. The trajectory length in all production runs is tuned to yield an acceptance rate of the RHMC of $65 - 70\%$. In contrast to similar studies recently performed in Lattice QCD with dynamical quarks [37, 60], we choose to use a different formulation of valence quarks, the (unimproved) standard Wilson formulation of Lattice QCD. The reasons for this are the conceptually easier spectroscopy that can be done, compared to the staggered formulation, and the resulting intrinsic complications like mixing of different states in taste space [8, 130]. A very immediate problem is also posed by the periodic boundary conditions when doing staggered spectroscopy, because the correlation functions generally have both oscillating and non-oscillating contributions. To separate these, the backwards propagating correlator needs to be neglected, and thus correlators of definite physical quantum numbers cannot be reliably constructed at large distances [60]. However, we crosscheck our findings to similar studies using HISQ for both sea and valence quarks, in order to check for possible effects due to using different actions for sea and valence quarks.

The scale used in this study was set in [36, 131] by fitting data of the Kaon decay constant f_K to an Ansatz

$$af_K(\beta) = \frac{c_0 f(\beta) + c_2(10/\beta) f^3(\beta)}{1 + d_2(10/\beta) f^2(\beta)}, \tag{6.1}$$

where $f(\beta)$ is the scaling function from the renormalization group (2.46), and here $\beta = 10/g^2$. The setup used featured $N_\sigma = 32 - 48$ lattices with $2 + 1$ dynamical HISQ fermions and a light to strange quark mass ratio of $m_l/m_s = 1/20$. For the conversion to physical units, a value of $f_K = 156.1/\sqrt{2}$MeV, measured by the PDG, was used, and the f_K scale is reported to absorb cutoff effects into the scale to a significant amount

T	N_s	N_τ	β	c_{sw}	a^{-1}	$\frac{m_l}{m_s}$
$0.24T_c$	64	64	7.010	0.0	2.319 GeV	1/27
$0.95T_c$	64	16	7.010	0.0	2.319 GeV	1/27
$0.28T_c$	64	64	7.188	0.0	2.736 GeV	1/27
$1.11T_c$	64	16	7.188	0.0	2.736 GeV	1/27

Table 6.1: The lattices used in the study of strange mesons and charmonia using $2+1$ dynamical quarks.

[131]. The corresponding critical temperature was determined in [36], with the ratio of sea quark masses down scaled to $m_l/m_s = 1/27$ via a scaling analysis, by locating the peak positions of the chiral susceptibility, and subsequently extrapolating the resulting values to the continuum, yielding $T_c = 154(9)$MeV. The corresponding lattice spacings and temperatures for the lattices used in this study are shown in Tab. 6.1.

Returning to our study using a Wilson quark action, the computations are performed on different lattices with spatial extent $N_\sigma = 64$ and $N_\tau = 16, 64$ at two couplings. For the lattices with smaller time extent, this corresponds to $T \sim 0.95T_c$ and $T \sim 1.1T_c$, respectively. Details about the lattices are collected in Tab. 6.1. Correlation functions of mesons are studied for strange flavor ($s\bar{s}$), charmonium ($c\bar{c}$) and strange charmed open flavor ($s\bar{c}$) by setting the corresponding bare quark masses in the inversion of the Dirac matrix. Because of the different nature of the bare quark mass parameters in the staggered and Wilson formulation of Lattice QCD, one has to find a definite way to compare them and find corresponding hopping parameters κ for each quark to serve as an input in the valence Wilson quark action. The way this correspondence is found is described in the next section.

In order to investigate the behavior of strange mesons and charmonia through the QGP transition, the different quark mass parameters need to be set for each value of the coupling, such that they yield the same physics when translating observables from lattice units to physical units. This defines a Line of Constant Physics (LCP). In practice, each quark mass parameter is tuned, at zero temperature, to reproduce a certain observable which can be measured by lattice computations, with a typical choice being (combinations of) meson masses [36, 132]. A convention adopted in [36] tunes the strange quark mass for each coupling by requiring that the mass of the fictitious $\eta_{s\bar{s}}$ meson, which is the pseudoscalar strange meson state with $J^{PC} = 0^{-+}$, matches the mass of its lowest order chiral perturbation theory estimate, $M_{\eta_{s\bar{s}}} \equiv \sqrt{2M_K^2 - M_\pi^2}$. Note that the physical η and η' are known to demand to take into consideration disconnected diagrams, and hence it is usual practice in this case to tune to this fictitious particle [18, 60]. Having done this, the light quark mass is then obtained by taking shares of the strange quark mass, typical values used in thermodynamical studies being $m_l/m_s = 1/5, ...1/27$. This allows for a controlled approach to the physical mass value $m_l = m_s/27$, which is quite close to the chiral limit and thus very expensive to compute on large lattices. For every

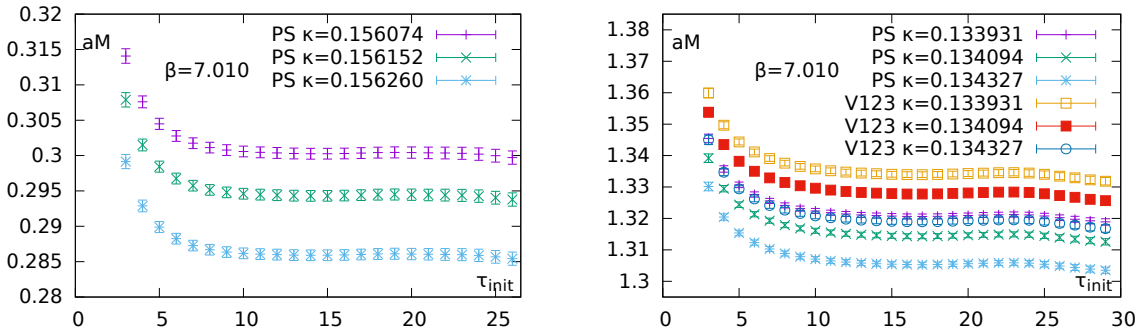

Figure 6.1: The masses resulting from one state fits to the zero temperature correlator data at $\beta = 7.010$ and different hopping parameters, as a function of the fit interval. *Left*: The pseudoscalar channel used to tune the bare strange quark mass. *Right*: The pseudoscalar and vector channels used to tune the bare charm quark mass.

other quark that is to be incorporated, another particle's mass has to be matched accordingly, with large freedom in the explicit choice of the particle to match to. For the value of the bare charm quark mass, a typical choice is the spin averaged charmonium mass $M_{c\bar{c}} \equiv \left(M_{\eta_c} + 3M_{J/\psi}\right)/4$.

In the present work we adopt the scheme outlined above for the light and strange sea quark masses. To be more precise, the strange (HISQ) sea quark mass is tuned along the LCP used in [36, 60], and then the light quark mass is chosen to be $m_l = m_s/27$. In order to find a correspondence between the bare quark masses of the HISQ action and our valence Wilson quark action, we follow the same idea and compute the physical masses of $\eta_{s\bar{s}}$, J/ψ and η_c in lattice units, given the respective lattice cutoff. For the value of the bare strange quark mass, we choose to match to the 'physical' fictitious $\eta_{s\bar{s}}$ meson mass $M_{\eta_{s\bar{s}}} = 686$ MeV, by using physical Kaon and Pion masses. For the bare charm quark mass, we choose to match to the physical spin averaged charmonium mass $M_{c\bar{c}} = 3.067$ GeV. We then tune the hopping parameter κ in the valence quark action to reproduce $M_{\eta_{s\bar{s}}}$ and $M_{c\bar{c}}$, yielding the corresponding hopping parameters κ_s and κ_{ch}, respectively.

6.1.2 Tuning of the masses

We now present the tuning of the Wilson valence quark masses to the HISQ sea quark masses at zero temperature. In order to tune the quark masses appropriately, we set up computations at several values of the hopping parameter κ scattered around the expected values corresponding to the quark mass that is to be tuned.

The meson masses themselves are obtained from the correlation functions of the corresponding channels by performing the one state fit technique described in section 2.6.1.

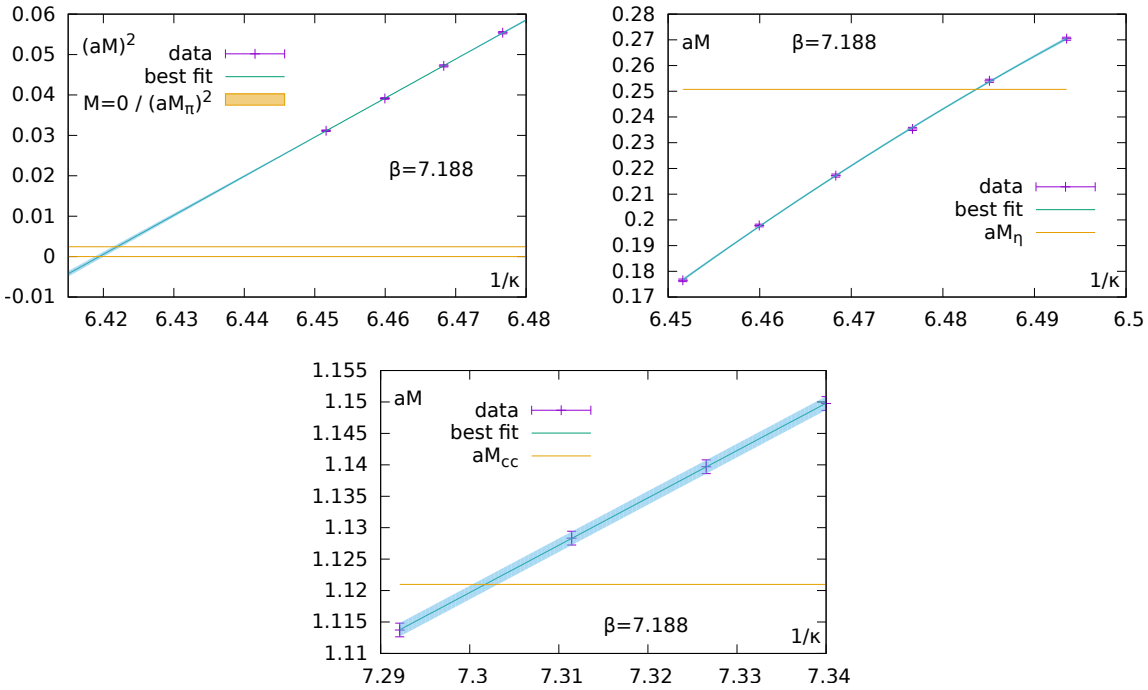

Figure 6.2: The tuning of the valence quark masses to reconstruct physical meson masses, at a inverse coupling of $\beta = 7.188$. *Top Left*: The extrapolation to the physical pion mass in lattice units, and the chiral critical point. *Top Right*: The interpolation that yields the correct strange quark mass to reproduce the $\eta_{s\bar{s}}$. *Bottom*: The hopping parameters in the case of the charm quark are scattered in a very small interval around the expected one, enabling us to perform a linear fit.

An exemplary plot of the resulting mass as a function of the fit boundary is shown in Fig. 6.1. The fits yield a broad and reliable fit interval around $\tau_{\text{init}} \sim 20$, which we use to fix the mass. However, we naturally expect the data points for different hopping parameters to be correlated, since they originate from the very same gauge field samples used in the Monte Carlo integration. To account for this correlation properly, we perform the fits for each hopping parameter on a large number N_{bs} of bootstrap samples, formed from the original data. The result is N_{bs} bootstrap estimators for the respective meson ground state mass for each κ. In the course of our tuning procedure the necessary interpolations and extrapolations between the different hopping parameters are then performed per sample, and the quantities resulting from this respect the original correlation of the data.

Because we scanned over a large range of hopping parameters for $\beta = 7.188$, it is in this case actually possible to additionally compute the critical hopping parameter κ_c, which determines the point of the chiral critical transition, as well as the hopping parameter κ_l, corresponding to the bare mass of the light quarks. Because in the chiral

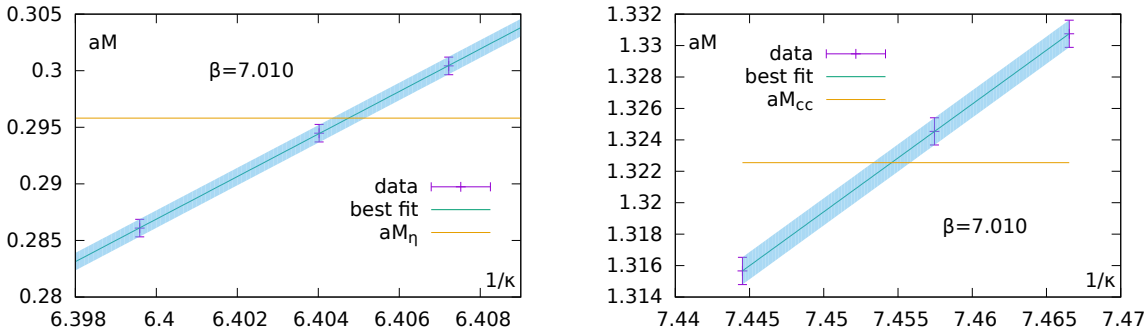

Figure 6.3: The tuning of the strange (*left*) and charm (*right*) valence quark masses to reconstruct physical meson masses, at an inverse coupling of $\beta = 7.010$.

limit the mass of the pion will vanish, κ_c is obtained by extrapolating the pseudoscalar mass to zero. To determine κ_l, we choose to extrapolate to the physical pion mass value $m_\pi = 135$ MeV. All performed interpolations and extrapolations for $\beta = 7.188$ are shown in Fig. 6.2, while the corresponding interpolations for $\beta = 7.010$ are shown in Fig. 6.3. In the (*top left*) plot four estimations of the pion mass are used to extrapolate to the light quark mass and the chiral critical matching points. In order to perform a reliable extrapolation, we resort to the well known GMOR relation (see e.g. [7, 133])

$$M_\pi^2 \sim (m_u + m_d) = 2m_l, \tag{6.2}$$

which is valid for small quark masses, and actually is the tree level result of the pion mass from chiral perturbation theory [7, 134]. Using this as theoretical input, the extrapolation can be done linearly in $(aM(1/\kappa))^2$. Note that for all four points, the GMOR relation holds very well and allows for a clean extrapolation to the chiral limit and the pion mass. In Fig. 6.2 (*top right*) six different hopping parameters, scattered in the strange mass region, are shown. The GMOR relation does not hold here anymore and we choose to interpolate using a quadratic polynomial in $1/\kappa$, fitting to the data in aM, to tune the strange quark mass. Our approach is again a little bit different in Fig. 6.2 (*bottom*), where the tuning of the charm quark is shown. Because it is very cheap to perform inversions at such large hopping parameters, we can afford to first approximately locate the matching region and then generate four data points very closely scattered around the expected matching point. As can be seen, the data behave perfectly linear in the interpolation region, and thus we choose to interpolate using a linear fit in $1/\kappa$ to the data given in aM. In the case of $\beta = 7.010$, three data points were generated right away very close to the correct value also when tuning the strange quark mass, which allows linear interpolations, see Fig. 6.3.

The resulting values for the hopping parameters are shown in Tab. 6.2. As an easy crosscheck we use the fact that the light sea quarks were not tuned, but their mass set to $m_l = m_s/27$. Via the correspondence of mass and hopping parameters for Wilson quarks (2.29), we use the value of κ_c to find, neglecting possible additive renormalizations of

β	κ_c	κ_l	κ_s	κ_{ch}
7.010	–	–	0.156134(10)	0.134146(23)
7.188	0.155778(16)	0.155716(15)	0.154234(6)	0.136954(27)

Table 6.2: The hopping parameters resulting from the tuning procedure for the two couplings β considered. Note that the errors are statistical, but include the correlations of the original data.

N_s	N_τ	β	$s\bar{s}$	$s\bar{c}$	$c\bar{c}$
64	64	7.010	380	380	380
64	16	7.010	814	814	814
64	64	7.188	752	746	752
64	16	7.188	830	829	834

Table 6.3: The number of correlation function samples for the correctly tuned hopping parameters on different lattices.

the quark masses,

$$\kappa_l = \left(\frac{m_l}{m_s \kappa_s} + \frac{1 - \frac{m_l}{m_s}}{\kappa_c} \right)^{-1} = 0.155720, \tag{6.3}$$

which matches the value found by tuning to the physical pion mass quite well. To proceed with our analysis on strange and charm mesons in the transition region, the tuning results for κ_s and κ_{ch} are in the follwing used to generate large numbers of correlation function samples for both couplings, on both the zero temperature and the finite temperature lattices. The statistics acquired in these runs is shown in Tab. 6.3.

6.2 Indirect spectral information from correlation functions

With the prerequisites presented in the foregoing section, in the following we show the results of correlation function measurements on dynamical lattices, and discuss what can be inferred from them with respect to the structure of the underlying spectral function and a possible melting of the states at finite temperature. To be precise, we only look at ratios of correlation functions, which are computed from the underlying raw data samples by enclosing them in a bootstrap method as described in Sec. 2.5, which allows for a reliable computation of the statistical errors of the ratio forming procedure. The number of bootstrap samples drawn is large enough to ensure stability in all observables, and we usually used $N_{bs} = 10000 - 20000$.

	$PS(\gamma_5)$	$V12(\gamma_i)$	$S(\mathbb{I})$	$A12(\gamma_5\gamma_i)$
strange	$\eta_{s\bar{s}}$	Φ		$f_1(1420)$
strange/charm	D_s	D_s^*	D_{s0}^*	D_{s1}
charm	η_c	J/ψ	χ_{c0}	χ_{c1}

Table 6.4: The investigated channels and their corresponding physical states, dependent on the flavor content.

6.2.1 Screening correlators

We start with the presentation and discussion of the ratio of in-medium screening correlators to zero temperature screening correlators in Fig. 6.4. Deviations from unity thus correspond to a modification of the corresponding finite temperature screening correlator. Per figure a definite flavor content of the pseudoscalar (PS), vector (V12) and scalar (S), axialvector (A12) channels are shown in the left and the right plot, respectively. Each plot contains the two investigated temperatures $T = 0.95T_c$ and $T = 1.11T_c$. The flavor contents shown are purely strange mesons, (open) strange-charmed mesons, and charmonium. For a correspondence of the quantum channels to physical particle states see Tab. 6.4. From the figure, we can say that generally, the heavier the total quark content, the weaker the modifications of the finite temperature screening correlators turn out to be.

For the S-wave channels, the purely strange mesons and the mixed charmed strange mesons are affected already below T_c, with a maximum at the largest distance of roughly 20% and roughly 10%, respectively. The corresponding screening correlators above T_c shows in both cases a more drastic fall by roughly 60% and 40%, respectively. The purely charmed S-wave channels show no significant modification throughout all distances, and are within error bars independent of the temperature. While in almost all cases there are no visible differences between the modification of the pseudoscalar channel and the vector channel, for purely strange flavor content above T_c there is a clear enhancement at intermediate distances: the vector channel remains around unity until $z \approx 0.4$fm, then starts to decrease, staying well above the pseudoscalar ratio for $z \approx 2$fm, while the pseudoscalar ratio deviates from unity already at very small distances. This effect is not seen in the same channels below T_c. Note that for the charmed strange flavor content, the 10% deviation from unity at maximum distance, that is observed below T_c, is to be contrasted to a gradual decrease of the ratio above T_c to a maximum of 40%. This indicates that the charmed strange ground states are already quite strongly affected by the medium just above the transition. Dynamical lattice studies of quantum number fluctuations across the deconfinement transition have recently suggested that strange-charmed and purely strange mesons melt already at the transition [35, 135], which is in accord with the strong modifications of the screening correlators that we find on the lattices in this work. Conversely, the strong 20% effect of the purely strange mesons already below T_c shows how sensitive screening correlators are with respect to thermal modifications, especially in comparison to the temporal correlation functions investigated below. The

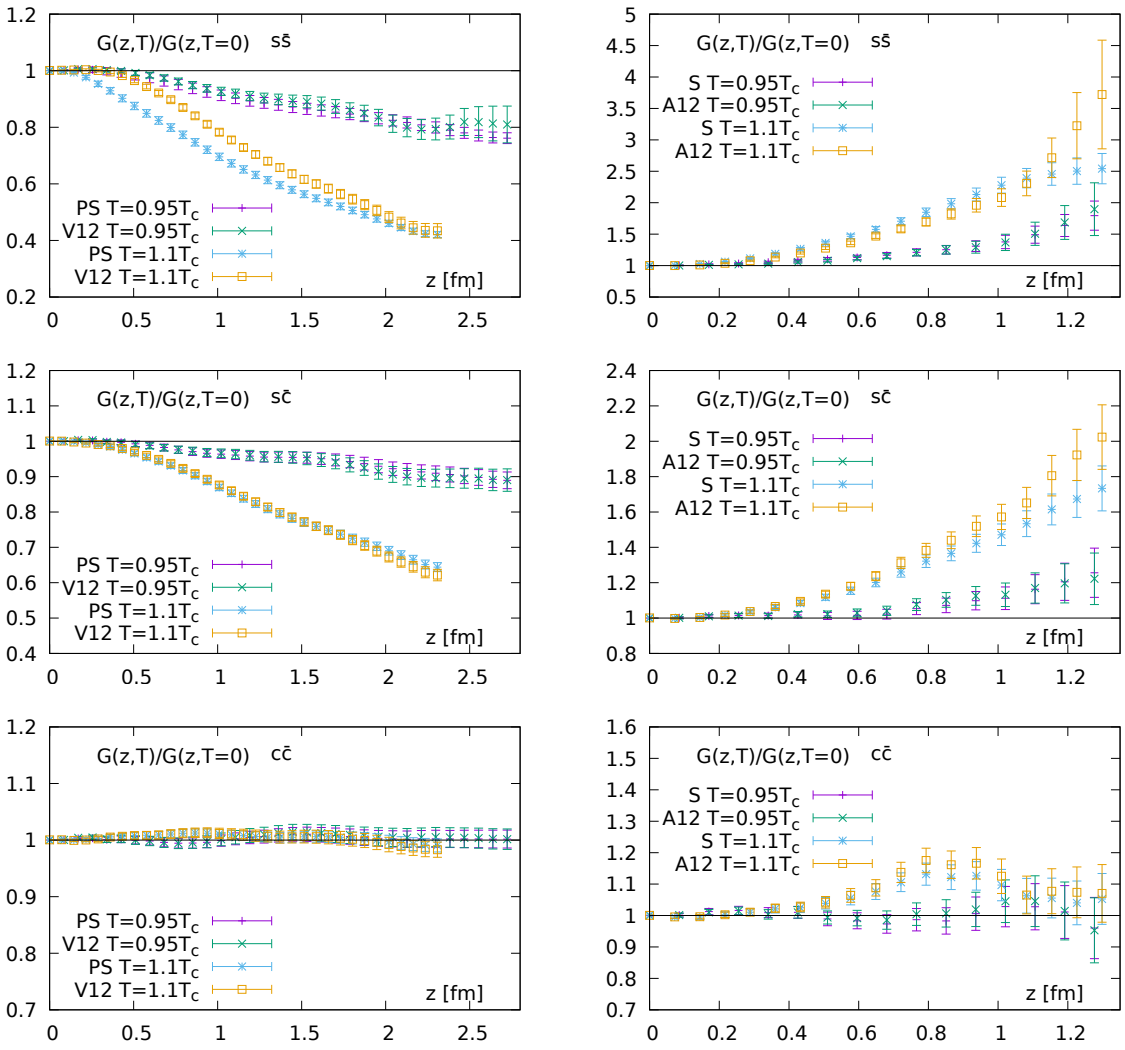

Figure 6.4: The ratios of the screening correlators at finite temperature and at zero temperature. The corresponding mesons consist of strange quarks only, one strange and one charm, and charm quarks only from *top* to *bottom*. On the *left* the S-wave channels are shown, while on the *right* P-wave channels are shown.

pseudoscalar and vector channels of purely charmed meson correlators are shown at the (*bottom left*) of Fig. 6.4. It is evident that there is no significant modification due to the thermal medium within the error. Hence, we argue that, given the apparent sensitivity of the measured screening correlators to such modifications, no temperature dependence of the corresponding physical states close to the transition region can be seen in our S-wave channels at charm quark mass.

Comparing our S-wave screening correlators to an extensive recent study [60], per-

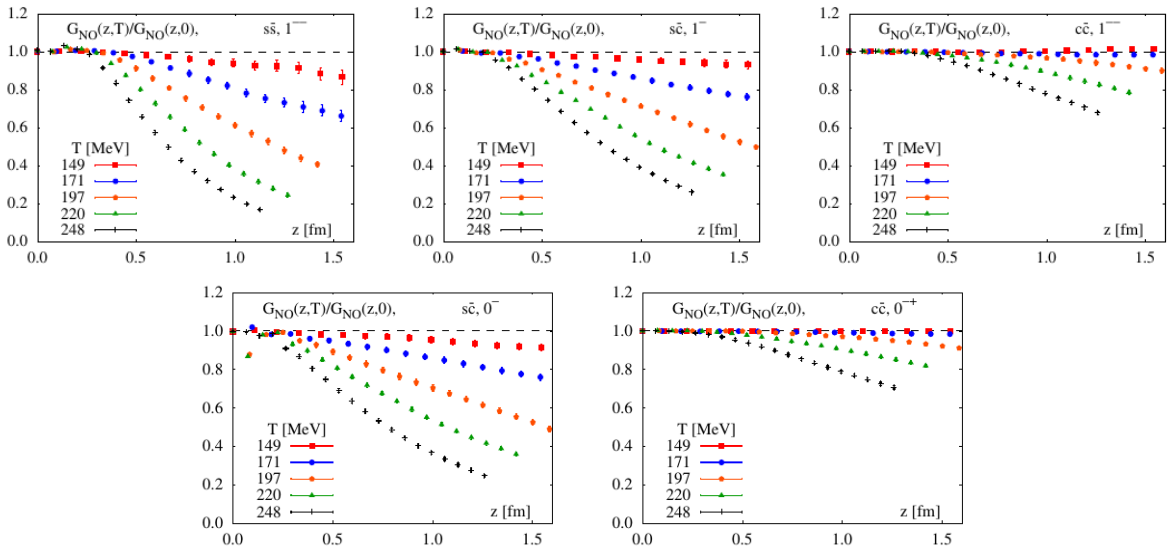

Figure 6.5: *Top*: The negative parity part of the vector screening correlators for several temperatures, taken from [60]. Note the smaller physical distance z in the x-axis, compared to our Wilson screening correlators. *Bottom*: The negative parity part of the pseudoscalar.

formed on slightly smaller lattices with size $48^3 \times 12$ and $2+1$ dynamical HISQ quarks in the sea and HISQ valence quarks, they find very similar behavior in all channels for two comparable temperatures, and we show their results of the vector and pseudoscalar screening correlation functions in Fig. 6.5 for comparison. Note that due to the use of HISQ valence quarks in their study, they have to avoid contributions of opposite parity showing up in the large distance region of their screening correlators, see [60]. In practice, their maximum distance for the two temperatures is $z \approx 1.5fm$ in case of S-wave correlators, which is roughly half of the maximum distance available in the current work. However, unfortunately the purely strange pseudoscalar correlator is not shown in their study.

Turning to the P-wave ratios, we show them in Fig. 6.4 (*right*) only up to $z \approx 1.3$fm, because at larger distances the signal becomes considerably worse. First of all their behavior differs from all S-wave states by the ratio being larger than unity throughout all temperatures and channels for strange and charmed strange mesons. Quite pictorially, a ratio growing with distance means a weaker falloff of the screening correlator above T_c compared to the vacuum correlator. This implies that for a ratio larger than unity the screening mass of the state is smaller than the mass in the vacuum, and vice versa a ratio smaller than unity predicts a larger screening mass compared to the particle's mass at zero temperature. Hence, without performing fits, we can state that our resulting P-wave screening masses shrink across the transition region.

However, we perform simple ground state fits to the S-wave screening correlators for

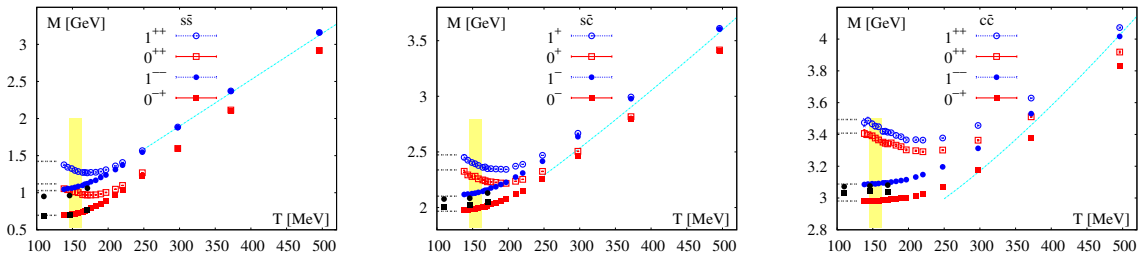

Figure 6.6: The screening masses of S-wave channels from [60], together with our findings in black. The yellow band marks the transition region. The horizontal lines on the left depict the corresponding zero temperature masses obtained from HISQ valence quarks. The leftmost black data points are our zero temperature masses obtained with Wilson valence quarks.

comparison with [60], and plot our found screening masses into their study[1] on the temperature dependence of screening masses across and above the transition, see Fig. 6.6. One sees that their screening masses in the P-wave channels decrease in the transition region, marked by the yellow band, to later bend over and increase towards their predicted free behavior. The masses in the S-wave channels increase already in the transition region, with the increase in the charm sector Fig. 6.6 (*right*) being visibly less pronounced than for smaller quark masses, which reflects that they are less modified in the transition region in comparison. The same behavior was also found in earlier dynamical $2+1$ flavor computations for light quark mesons [136] and 2 flavor computations [137] for the S-wave channels. Our fit results are shown as the black data points, with the circles corresponding to the vector channel and the rectangles corresponding to the pseudoscalar channel. The black data points to the very left depict the corresponding zero temperature results from our finest lattice, and the horizontal lines depict the corresponding zero temperature masses in the HISQ study.

Our findings are consistent with respect to the relative behavior of the screening masses in the older study, but all masses, except for the $s\bar{s}$ pseudoscalar, are shifted upwards (pseudoscalar) or downwards (vector) compared to the results of the HISQ study, effectively reducing the splitting between these to channels in comparison. These two studies are conceptually very comparable, in the sense that the same scale is used, and also the same definitions were used for the LCPs of the strange and the charm quark. This leaves two possible reasons for these deviations, namely the different volumes used in the studies, as well as different cutoff effects. Considering that the valence quark sector is in our study covered by the standard Wilson fermion action, which has cutoff errors of $\mathcal{O}(a)$, to be compared to the HISQ action, which leaves $\mathcal{O}(a^2)$ errors at tree level and has very strongly reduced taste breaking effects compared to the standard staggered action, see Sec. 2.2.3, we think it is plausible that a large share of the deviations in the meson masses come from actual cutoff effects that are present in our action. This

[1] Thanks to Yu Maezawa for providing the data.

is confirmed by the more pronounced mass shift in the $c\bar{c}$ pseudoscalar, compared to the shifts in the lighter quark sectors. Note also that the quite good agreement in the corresponding screening correlator ratios $G(z,T)/G(z,T=0)$ of the S-wave channels suggests that indeed cutoff errors seem to largely cancel in such ratios.

We return to the P-wave screening correlators and discuss the detailed behavior of the single screening correlation functions. Note that the deviations from unity for the purely strange and charmed strange mesons are quite large compared to the corresponding S-wave channels, considering that the maximum distance shown is $z \approx 1.3$fm. Also the error is larger in comparison, which shows that the signal is harder to extract for the P-wave channels already at comparatively small distances. Like for the S-wave channels, we find significant enhancements already below T_c, accompanied by corresponding stronger modifications above T_c. This is a clear sign that the P-wave states on our lattices are as well influenced by the thermal medium in the transition region. The charmonium correlator ratios show a slight enhancement of at maximum 20% at intermediate distances above T_c, which is not seen below the transition, and is comparable in magnitude to the deviation of the charmed strange P-wave correlators below T_c. Also, this signal decreases again towards $z \approx 1.3$fm, where after the signal is lost.

6.2.2 Temporal correlators

After the analysis of the screening correlators we turn to the analysis of the temporal correlation functions. As discussed in Sec. 5.3, for a study on the temperature dependence of the latter, the reconstructed correlator is the tool of choice. As the correspondence (4.17) is just an integration over the spectral function with respect to the frequency, to yield the correlation function, conclusions about the spectral function can be drawn by merely investigating the latter as a function of τT. Quite pictorially, because of the integrand structure, we expect modifications at large distances τT to reflect modifications in the low to intermediate frequency range of the spectral function. Of course, this does not allow for precise, quantitative statements, but a qualitative understanding of the behavior of different particles across the deconfinement transition can nevertheless be gained. Using the findings of the analytically solved free correlation functions from Sec. 4.2 in the continuum and on the lattice, we know that at finite, and degenerate, quark masses we expect smeared zero modes to arise in the vector, scalar and axialvector channel, while the pseudoscalar will not acquire a transport contribution above T_c. In the case of non-degenerate quark masses, we have seen that all four channels under consideration develop a contribution at low to intermediate frequencies, at strictly $\omega > 0$, whose magnitude depends on the difference of the quark masses and is not easily estimated. However, we expect them to be still present in the interacting case, though somewhat modified, analogous to the case of degenerate quark masses, see Sec. 4.3.2. Note that the distance in all plots is given in units of τT, in contrast to the study on screening correlators, which compared the distance in Fermi to facilitate a comparison to the corresponding HISQ study on slightly smaller lattices.

In Figs. 6.7-6.9 we show the ratios $G(\tau T)/G_{rec}(\tau T)$ of the temporal correlators at finite temperature to the corresponding reconstructed correlators, which were extracted from the respective vacuum correlator data by applying equation (5.26). As for the screening correlators, we have flavor contents of purely strange mesons, strange-charmed mesons and purely charm mesons. In each plot we show the ratios at both available temperatures. In addition to the ratio, we also plot the ratio with the respective midpoints subtracted from both correlation functions,

$$\frac{G^{sub}(\tau T)}{G^{sub}_{rec}(\tau T)} = \frac{G(\tau T) - G(\tau T = 0.5)}{G_{rec}(\tau T) - G_{rec}(\tau T = 0.5)}. \tag{6.4}$$

As has been discussed in Sec. 5.2, the midpoint subtraction procedure can subtract a part of the constant, or zero mode, contribution to the correlation function, which shadows the details of the bound state modifications. However, we will see in the analysis that in practice it turns out to be difficult to differentiate between effects in the correlator that come from modifications of the bound states, and effects that result from transport or, more generally, low frequency contributions in the spectral function. We thus introduce another observable which was used in [119]

$$\Delta G(\tau T) = G(\tau T) - G_{rec}(\tau T) = \int_0^\infty \frac{\mathrm{d}\omega}{2\pi} \Delta\rho(\omega/T) K(\omega/T, \tau T), \tag{6.5}$$

with $\Delta\rho(\omega/T) = \rho(\omega/T) - \rho(\omega/T')$, and T the temperature in the transition region and T' the temperature from the corresponding vacuum case. A negative correlator difference for some range of τT thus implies that there must be a range of frequencies where the difference in spectral functions $\Delta\rho(\omega/T)$ must be negative, i.e. contributions vanish at higher temperature compared to (nearly) zero temperature. On the other hand, a positive difference does not necessarily rule out that there are negative regions in $\Delta\rho(\omega/T)$. By expanding the correlator difference into its thermal moments,

$$\Delta G(\tau T) = \Delta G^{(0)} + \Delta G^{(2)} \left(\tau T - \frac{1}{2}\right)^2 + \mathcal{O}\left[\left(\tau T - \frac{1}{2}\right)^4\right], \tag{6.6}$$

with $\Delta G^{(n)} = G^{(n)} - G^{(n)}_{rec}$, we gain more insight in the structure of the dominating contributions at large distances. Since we generally expect the occurrence of contributions in the low frequency region, and the disappearance of contributions at larger frequency, we conclude that the former will lead to a positive spectral function difference $\Delta\rho(\omega/T)$ at a range of ω/T, while analogously the latter will lead to a negative $\Delta\rho(\omega/T)$. Because the thermal moments are essentially the correlation function, 'filtered' by the kernel to pass a certain frequency range (see Fig. 5.3 (*left*)), they give us a more fine grained handle on the sign of $\Delta\rho(\omega/T)$ than the complete difference of correlation functions $\Delta G(\tau T)$. Specifically, a value of $\Delta G^{(2)} < 0$ indicates a decrease in the spectral function across the transition, that can only be caused by vanishing bound state peaks, while $\Delta G(\tau T)$ as a whole might still be positive. In order to make quantitative statements about the signs of $\Delta G^{(0)}$ and $\Delta G^{(2)}$, in all cases we perform a fit to the difference correlator $\Delta G(\tau T)$,

with expression (6.6) as a fit Ansatz, which thus yields the intercept $\Delta G^{(0)}$ and the curvature $\Delta G^{(2)}$ as resulting fit parameters. The fits are performed on each bootstrap sample, and the resulting bootstrap intercepts and curvatures are used to obtain estimates that respect the correlation of the data. The results are listed in Tab. 6.5, and for some interesting cases we show the whole correlator difference $\Delta G(\tau T)$ in Fig. 6.10.

A very general feature of the ratios is, just as for the screening correlators, that with increasing quark mass the deviations from unity decrease, i.e. the heavier the particle, the less affected it is by the temperature. Furthermore, the P-wave channels clearly show a much stronger reaction at large distances τT than the corresponding S-wave channels, and with no exception are modified to be larger than unity, which per se hints at a dominating transport contribution, or the analogous low frequency contribution at non-degenerate quark masses.

We start to discuss mesons with pure strange quark content, which yields the clearest signal in the S-wave channels. The pseudoscalar ratio below the transition is modified very slightly at $\tau T \gtrsim 0.3$ to be smaller than unity, although the errors at the midpoint are almost as large as the deviation. Above the transition temperature we find a gradual decrease starting at $\tau T \approx 0.1$, resulting in a maximum deviation from unity of

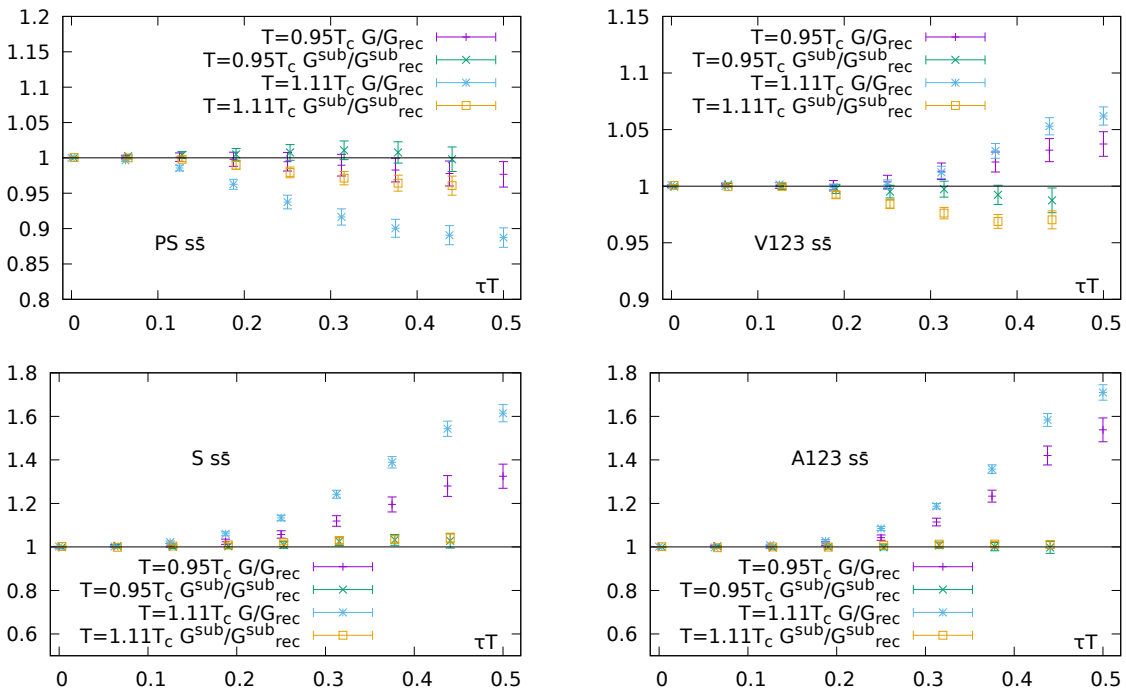

Figure 6.7: The ratio G/G_{rec} for all channels and $s\bar{s}$ flavor content. Note that, if needed, the points are offset in τT relatively to each other for visual clarity.

11% at the midpoint. Since there is no transport contribution arising in this channel, we interpret the observed drop as stemming solely from a modification of the bound

states. Interestingly, the corresponding midpoint subtracted ratio is again shifted upwards towards unity, which can be understood as follows. Because the spectral function above T_c is not expected to be modified by the medium at low frequencies, we could conclude that the zeroth thermal moment contains essentially the same contributions at both temperatures from this region. But this argument assumes a strong separation of scales in the structure of the spectral function, i.e. that there are no contributions to the midpoint coming from the region where the bound states are located. The upwards shift of the subtracted ratio shows that there are contributions in $G^{(0)}_{rec}$ that are not contained in $G^{(0)}$. Since the bound states have clearly been modified above T_c compared to $T = 0.95T_c$, we interpret this as bound state contributions that are contained in $G^{(0)}_{rec}$, have vanished above T_c, and are thus not present in $G^{(0)}$. This mechanism is essentially the first concluding remark from Sec. 5.2. The same effect is also seen in earlier quenched calculations of charmonium [119], but at comparatively higher temperatures of $T \gtrsim 1.4T_c$. For illustrative purposes, this is also reflected by the correlator difference $\Delta G(\tau T)$, which is entirely negative for $T = 1.11T_c$ as shown in Fig. 6.10, and also shows a statistically significant negative curvature, see Tab. 6.5. In the vector channel the ratio increases at both temperatures, reaching roughly 6% deviation above T_c, and roughly 4% below T_c. This is attributed to an appearing transport contribution, which apparently takes effect already just below the transition. The subtracted ratio at $T = 0.95T_c$ stays compatible with unity, while subtracted ratio above T_c drops below unity for $\tau T \gtrsim 0.15$ to a maximum deviation of $3 - 4\%$ from unity at the largest distance. This indicates that the midpoint subtraction indeed eliminates a large part of the appearing zero mode. However, since the appearance of a zero mode and also potential bound state modifications might happen simultaneously in the vector channel, we cannot draw such firm conclusions as for the pseudoscalar channel by looking at the ratios alone. We have found in Sec 6.2.1 that the corresponding screening correlators show a strong reaction to crossing the critical region, and furthermore we see from the fit to the corresponding difference correlator $\Delta G(\tau T)$ in Tab. 6.5 that $\Delta G^{(2)} < 0$, which is an unambiguous sign for a modification of the bound states in this channel. Although it is not possible to quantitatively determine whether the ground state has (completely) melted, we certainly see a modification and state here the possibility that the subtracted ratio suffers from contributions of the bound states in $G^{(0)}_{rec}$, similar to the pseudoscalar channel, and its deviation from unity might thus be underestimated. Additionally, the appearing smeared zero mode might contribute to the higher moment $G^{(2)}$, rendering $\Delta G^{(2)}$ larger than it actually would be if there was no smeared zero mode. This mechanism is the second remark from the end of Sec. 5.2.

The changes in the case of strange-charmed mesons, shown in Fig. 6.8, are much smaller than for purely strange mesons. In the pseudoscalar channel, we find no significant modification below T_c, and a very slight modification of G/G_{rec} above T_c around $\tau T \approx 0.3$, being compatible with unity around the midpoint again. The subtracted ratio above T_c shows a modification of $1 - 2\%$ at the largest distance. From the clear signal in the analysis of screening correlators above we concluded that the strange-charmed pseudoscalar meson has probably dissociated above the transition, which is not visi-

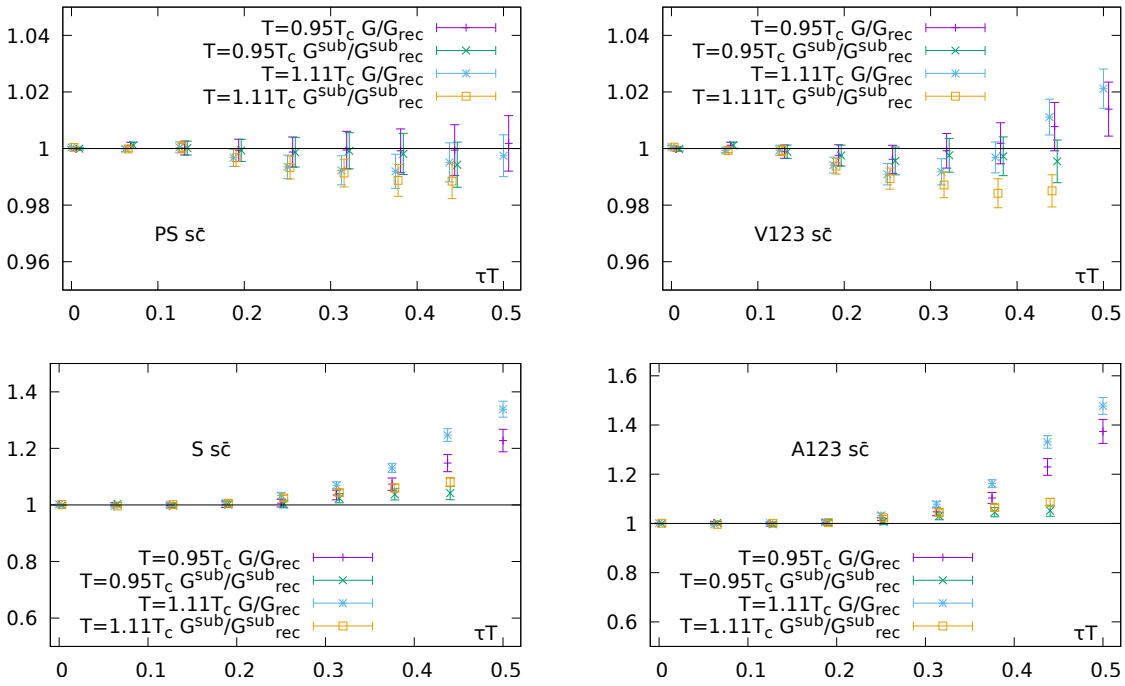

Figure 6.8: The ratio G/G_{rec} for all channels and $s\bar{c}$ flavor content. Note that, if needed, the points are offset in τT relatively to each other for visual clarity.

ble in the correlator ratio here. We find confirmation of this in the resulting value of $a^3\Delta G^{(2)} = -1.72(0.98) \cdot 10^{-03}$. A possible explanation for the weak signal is a cancellation of two effects: the modification of bound states is canceled by a modification of the low to intermediate frequency region of the spectral function. Here we assume that the contribution that arises at low to intermediate frequencies, computed in Sec. 4.2 and Sec. 4.2.3 for infinite temperature (and especially is found also in the pseudoscalar channel) is modified at finite temperature, but such that it still shows an effect in the correlator. That there is a remnant of this contribution in the correlator at finite interactions can be seen also in Fig. 6.10 (*bottom left*) compared to (*top left*), where the whole difference correlator is shifted upwards compared to the purely strange pseudoscalar. Because the contribution does not originate from a Dirac delta peak, and thus even in the free case does not lead to a constant in the correlator, one cannot argue that it is successfully removed to a large degree by midpoint subtraction. Indeed, we see that the midpoint subtracted ratios do not improve on this matter, but also above T_c stay almost compatible with unity. There is a slightly clearer signal in the vector channel above T_c, with G/G_{rec} at $T = 1.11T_c$ dropping below unity for $0.15 \lesssim \tau T \lesssim 0.4$, and rising above unity for $\tau T \gtrsim 0.4$. The corresponding subtracted ratio follows the decreasing trend, but stays below unity with a maximum of $1 - 2\%$ at the maximum distance. In Sec. 4.2 we found that the low frequency contribution appearing in the free case is generally smaller, for constant quark masses, in the pseudoscalar channel than in the other channels (see Fig. 4.1 and Fig. 4.2). Correspondingly, it is possible that the stronger signal

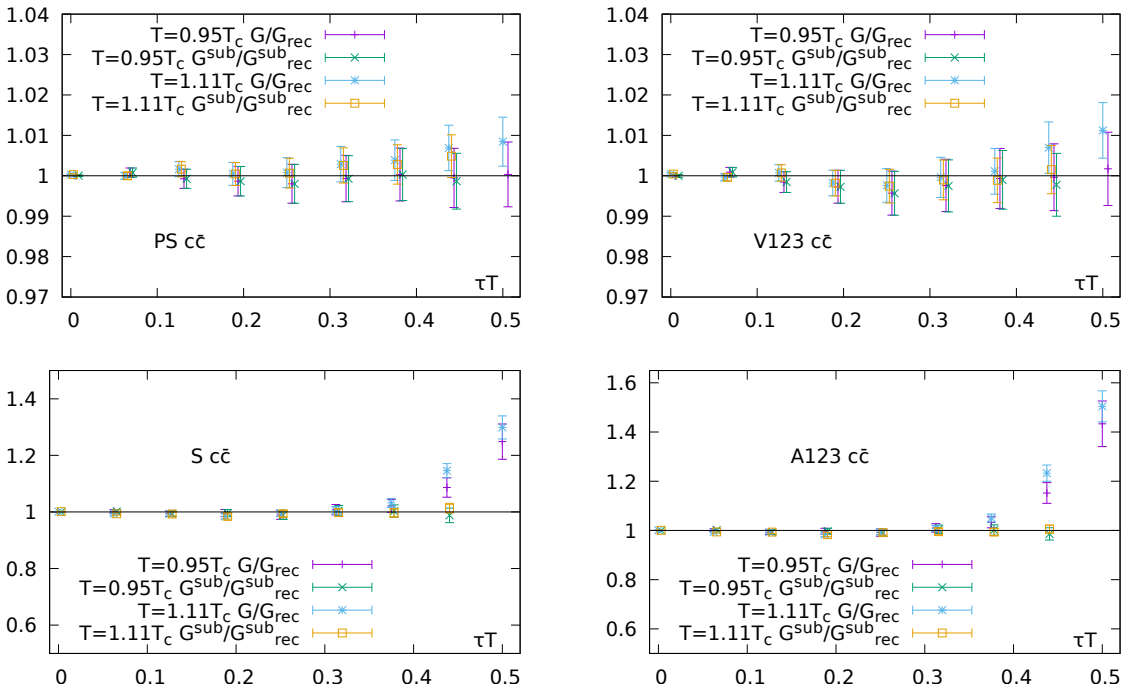

Figure 6.9: The ratio G/G_{rec} for all channels in the case of charmonium. Note that, if needed, the points are offset in τT relatively to each other for visual clarity.

in $G(\tau T)/G_{rec}(\tau T)$ at large distances, compared to the pseudoscalar channel, is caused by this contribution. Considering our earlier finding that the pseudoscalar and vector channel both show an equally strong deviation from unity in their screening correlators above T_c, the latter seem not to be as susceptible to such low frequency modifications as temporal correlators. This is the analogue of the statement for hidden mesons elaborated in Sec. 5.3, that the temperature dependence across the transition is carried mainly by the appearing smeared zero mode, which is absent in the screening correlator [37]. From the fit to the difference correlator we find $a^3\Delta G^{(2)} = -1.21(0.42) \cdot 10^{-03}$ above T_c and $a^3\Delta G^{(2)} = -1.67(4.42) \cdot 10^{-04}$ below T_c, which hints at vanishing contributions in the correlator when crossing the transition region. We conclude that we have a weak signal of bound state modifications in both S-wave channels, which is also predicted by a very recent study on QCD thermodynamics of open charmed mesons [135].

The ratios in the S-wave channels for pure charm quark content show a very faint signal, being almost compatible with unity for all τT. This is also reflected in the fits to the correlator difference, which yields both $\Delta G^{(0)}$ and $\Delta G^{(2)}$ compatible with zero for $T = 0.95T_c$ and $\Delta G^{(2)}$ compatible with zero for $T = 1.11T_c$. The slight rise of the ratios above T_c close to and at the midpoint could be a sign of a transport contribution in the vector channel, but it is hardly significant within errors, and it is observed in both the vector and the pseudoscalar channel, which should not exhibit a transport peak; we thus conclude that there is no significant signal in these two channels. There

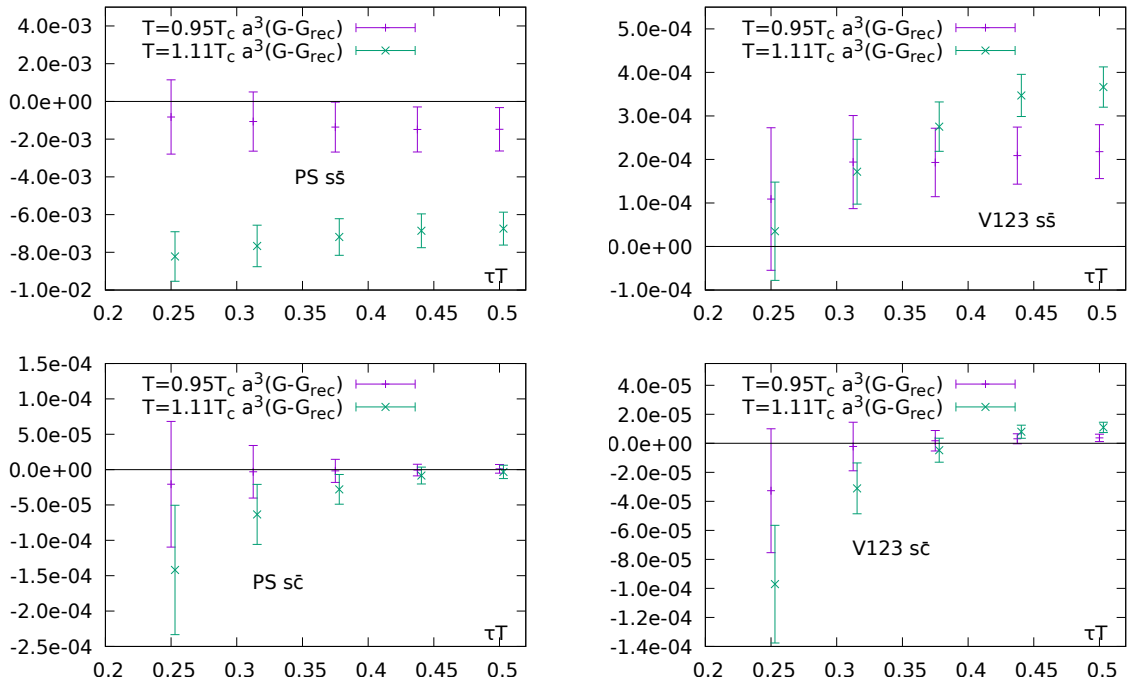

Figure 6.10: Plots of $(G - G_{rec})$ in lattice units, for pseudoscalar and vector channels of both strange and strange-charmed flavor content. We use this observable to essentially probe for the sign of the differences of thermal moments and its statistical significance, which are oblivious of the specific units. As such, especially a visible negative intercept or negative curvature at $\tau T = 0.5$ hint at disappearing contributions in the spectral function

are a number of lattice studies conducted on charmonium. While at higher temperature $T \gtrsim 1.4T_c$ recent studies, performed on large lattices in the quenched approximation and using either MEM and/or ratios to reconstructed correlators, find hints for both bound state modifications as well as appearing transport contributions in charmonia [119, 126], an earlier study performing MEM on anisotropic lattices [123] finds no modification of the pseudoscalar charmonium up to $T = 2T_c$. Two flavor computations on anisotropic lattices, also utilizing MEM, contrast this by finding bound state modifications up to roughly $T = 2T_c$, where the states finally melt [138]. Additionally, they also measure appearing transport contributions in the vector channel. A very recent $2 + 1$ flavor MEM study finds no variation in the pseudoscalar channel up to $1.5T_c$, and a transport contribution appearing above T_c [139, 140]. An interesting contrast to this is a study using MEM on a known sum rule for spectral functions [141], which yields continuous input data, and thus circumvents the use of the quenched approximation in conjunction with large lattices or the use of dynamical quarks on smaller, but anisotropic lattices. They find sizable S-wave bound state modifications already at $T \sim 1.1T_c$. These MEM results should be compared to very recent results from pNRQCD, utilizing $2 + 1$ flavor lattice input to extract both real and imaginary part of the interquark potential [79].

$\beta/q\bar{q}$	$s\bar{s}$	$s\bar{c}$	$c\bar{c}$
PS			
7.010	$-1.51(1.15)\cdot 10^{-03}$	$3.5(54.4)\cdot 10^{-07}$	$1.38(3.82)\cdot 10^{-07}$
7.010	$1.22(1.45)\cdot 10^{-02}$	$-1.04(9.20)\cdot 10^{-04}$	$-2.6(21.0)\cdot 10^{-05}$
7.188	$-6.76(0.87)\cdot 10^{-03}$	$-2.18(8.82)\cdot 10^{-06}$	$9.34(6.39)\cdot 10^{-07}$
7.188	$-2.60(0.86)\cdot 10^{-02}$	$-1.72(0.98)\cdot 10^{-03}$	$1.78(3.08)\cdot 10^{-04}$
V123			
7.010	$2.12(0.62)\cdot 10^{-04}$	$3.90(2.31)\cdot 10^{-06}$	$2.77(2.92)\cdot 10^{-07}$
7.010	$-6.34(18.0)\cdot 10^{-04}$	$-1.67(4.24)\cdot 10^{-04}$	$-6.05(15.6)\cdot 10^{-05}$
7.188	$3.66(0.46)\cdot 10^{-04}$	$1.23(0.33)\cdot 10^{-05}$	$1.12(0.43)\cdot 10^{-06}$
7.188	$-5.57(1.18)\cdot 10^{-03}$	$-1.21(0.42)\cdot 10^{-03}$	$-4.8(21.4)\cdot 10^{-05}$
S			
7.010	$1.59(0.24)\cdot 10^{-03}$	$1.39(0.22)\cdot 10^{-05}$	$3.55(2.18)\cdot 10^{-07}$
7.010	$7.96(6.01)\cdot 10^{-03}$	$7.50(5.05)\cdot 10^{-04}$	$1.72(6.65)\cdot 10^{-05}$
7.188	$4.06(0.22)\cdot 10^{-03}$	$6.17(0.44)\cdot 10^{-05}$	$2.85(0.42)\cdot 10^{-06}$
7.188	$9.57(4.28)\cdot 10^{-03}$	$2.42(0.64)\cdot 10^{-03}$	$-2.7(12.3)\cdot 10^{-05}$
A123			
7.010	$5.11(0.44)\cdot 10^{-04}$	$1.18(0.14)\cdot 10^{-05}$	$4.07(1.54)\cdot 10^{-07}$
7.010	$7.8(15.8)\cdot 10^{-04}$	$5.64(2.82)\cdot 10^{-04}$	$1.05(4.06)\cdot 10^{-05}$
7.188	$9.97(0.42)\cdot 10^{-04}$	$4.34(0.28)\cdot 10^{-05}$	$2.73(0.35)\cdot 10^{-06}$
7.188	$1.55(1.13)\cdot 10^{-03}$	$1.40(0.34)\cdot 10^{-03}$	$-3.11(7.21)\cdot 10^{-05}$

Table 6.5: Results of the fits to $a^3\left(G(\tau T) - G_{rec}(\tau T)\right)$. The first row of each β corresponds to $a^3\Delta G^{(0)}$, the second row corresponds to $a^3\Delta G^{(2)}$. All values are given in units of the lattice spacing for reference. Note that adopting another normalization in $\Delta G(\tau T)$ is a constant factor, and thus does not change the fit results relative to each other, and especially does not affect the sign.

They determine the melting temperature of the vector ground state of charm mesons to be $T \approx 1.37(^{+0.08}_{-0.07})T_c$. With an exception of the study utilizing sum rule input, which is based on an operator product expansion, our result that charmonium S-wave states show no significant modification across the transition region $T \sim 0.95 - 1.11T_c$ is thus in accord with results of other studies, obtained by different methods.

The P-wave channels of all quark contents show quite strong and very clear signals at all distances, as opposed to their corresponding screening correlators. The strong increases hint at dominating transport contributions that appear both below and above the transition temperature. Upon subtracting the midpoint, the deviations from unity are drastically reduced compared to the unsubtracted ratios, in part being perfectly compatible with unity, as in the case of charm quark mesons or the axialvector channel of purely strange mesons. For purely strange and strange-charmed quark contents, the fits to the correlator difference in Tab. 6.5 show $\Delta G^{(0)} > 0$ very significantly both above and below the transition, and, with larger relative errors, the same holds also for $\Delta G^{(2)}$.

This does not strictly imply that there are no negative contributions to $\Delta\rho(\omega/T)$, because the appearing strong low frequency contributions could shadow modifications of bound state peaks in the correlation function, as we have seen before in the S-wave channels. Indeed, the analysis of screening correlators in Sec. 6.2.1 revealed that there are modifications of bound states at the observed temperatures, and combining these information leads to the conclusion that P-wave states of purely strange and strange-charmed quark content, are, both for low frequencies, as well as concerning their bound state structure, strongly modified already in the transition region. This coincides with physical expectation, as the P-wave states should show an equal or stronger modification compared to corresponding S-wave states at the same temperature. For purely charmed P-wave states, we see modifications in the ratio $G(\tau T)/G_{rec}(\tau T)$ at very large distances $\tau T \gtrsim 0.38$, which are in magnitude at the midpoint similar to the strange-charmed P-wave states. However, the behavior of the corresponding screening correlators in Fig. 6.4 (*bottom* and *center*) is quite different over the range of z shown, and we conclude that if there is a modification of the charmonium screening correlators, it might not occur in the observed interval $z \lesssim 1.3$fm, and is thus expected to be less pronounced in magnitude compared to the strange-charmed case. The values of $\Delta G^{(2)}$ (in the (*bottom right*) section of Tab. 6.5) are all compatible with zero, and the intercepts $\Delta G^{(0)}$ are all significantly larger than zero, which confirms that there are definitely distinguishable low frequency modifications at play. Thus, concerning the bound state structure, we cannot make a statement whether it is modified or not at the highest temperature $T = 1.11T_c$ measured on the used lattices. Earlier quenched [123] and two flavor [138] lattice QCD computations combined with MEM find that P-wave channels of charmonium are heavily modified, i.e. dissolve, at $T \approx 1.1 - 1.2T_c$.

6.2.3 Conclusions

We summarize our procedure and results on the interpretation of correlator data measured in lattice computations with $2 + 1$ dynamical quark flavors. After tuning the strange and charm valence quark masses, used in the inversion of the Wilson Dirac matrix on gauge fields produced with HISQ sea quarks, to reproduce certain meson ground state masses, we perform computations of temporal and screening correlation functions of strange, charm, and mixed strange-charmed quark content, for pseudoscalar, vector, scalar and axial vector quantum numbers, both slightly below the pseudocritical temperature and slightly above. For strange and strange-charmed mesons we generally find significant modifications of screening correlators already in the transition region, which shows that they are indeed very sensitive probes compared to temporal correlation functions. A Comparison with a recent study using the HISQ action on smaller lattices reveals a very similar behavior in the screening correlators, and a qualitatively comparable behavior of screening masses through the transition region. However, systematic cutoff effects are identified in the extracted masses, which reduce the splitting between the vector and pseudoscalar channels, with the strongest effects in the charm quark sector.

Furthermore, we combine the results of screening correlator ratios $G_{scr}^{T\approx T_c}/G_{scr}^{T\approx 0}$, ratios to reconstructed temporal correlators, G/G_{rec} and $(G-G^{(0)})/(G_{rec}-G_{rec}^{(0)})$, as well as the differences between temporal and reconstructed correlator, $(G-G_{rec})$. We find that, except for the case of charmonium, all channels, which we expect from the free theory to develop a contribution at low frequencies, indeed do so in the vicinity of the transition. These turn out to be dominating effects in the P-wave channels. At the same time, we find modifications of the corresponding bound states in all channels of strange and strange charmed flavored mesons above the transition temperature. For charmonium, in case of the S-wave channels we detect no clear signal for any modification of the underlying spectral functions on the lattices investigated, while there is a small, but measurable, enhancement of the P-wave correlators around the transition temperature. It is argued to stem from arising transport contributions. There is no signal for bound state modifications, which however does not exclude them to take effect above the transition temperature.

7 Light quarks in the continuum from quenched lattices

After assessing the spectral function for strange and charm mesons in the last chapter, we now turn to the case of light quarks. Unlike in the former case, the lattices used in this study do not contain quarks in the sea, i.e. there are no inherent dynamical effects from virtual quarks. While the *quenched approximation* is a drawback compared to the former case, we are on the upside able to use its computational cheapness to gain a series of advantages. First, we have lattices at three different temperature scales above T_c, which enables us to investigate a possible temperature dependence of the physics. Second, we have gauge configurations with three different, rather fine, lattice spacings per temperature, which allows us to perform extrapolations to the continuum, thus removing the lattice cutoff, and to extract non perturbative continuum physics. Third, while the dynamical lattices with 16 data points in temporal direction at high temperatures are rather small, the temporal extents of the finest lattice for each temperature ranges from 48 to 64, a factor $3-4$ in comparison. This opens the possibility for an entirely different kind of analysis, which focuses on directly extracting details of the spectral function, instead of merely observing indirect information using the reconstructed correlator, which only sees the spectral function *after* integration, and thus results in a merely qualitative view on the underlying spectral structure.

In the following we will present our setup of quenched lattices and the details of the continuum extrapolation procedure. A central point is the extraction of thermal moments from the correlator data that, extrapolated to the continuum, provide information about the low frequency region of the spectral function. The obtained continuum correlators are then used to perform further fits with an Ansatz that was presented in Sec. 5.4. In order to assess systematics, we perform fits with different Ansaetze to do cross checks and gain additional information about the performance and stability of the fit procedure. In the end we present results for the dilepton rate, the soft photon rate and the electrical conductivity at all three temperatures. This work is going to appear in near future [142]. In the context of this work only vector correlation functions at vanishing momentum are considered and extrapolated to the continuum limit. However, we have also continuum extrapolated vector correlator data at finite momenta, which are used in [143] to extract, for the first time, the photon rate at non vanishing frequency.

7.1 Continuum correlation functions from the lattice

7.1.1 Lattice setup

The central observable used in this analysis is the Euclidean correlation function $G_V(\tau, \vec{p})$ of the light electromagnetic vector current of QCD,

$$J_\mu(\tau, \vec{x}) = \sum_f Q_f \bar{\psi}_f(\tau, \vec{x}) \gamma_\mu \psi_f(\tau, \vec{x}), \tag{7.1}$$

with f indexing the flavors. Having the quantum numbers of a vector, it corresponds to the physical ρ, ω and Φ particles. As discussed in Sec. 3, $G_V(\tau, \vec{p})$ also carries information about dilepton production inside the Quark Gluon Plasma. The connection between the current and the correlator on the lattice is given by considering the component $H = \{0, i, \mu\}$ of the renormalized vector channel, and combining it to yield the Euclidean correlation function in position space,

$$J_H = Z_V \bar{\psi}(x) \gamma_H \psi(x) \tag{7.2}$$

$$\rightarrow \quad G_{HH}(\tau, \vec{x}) = \langle J_H(\tau, \vec{x}) J_H^\dagger(0, \vec{0}) \rangle. \tag{7.3}$$

The indices $HH = ii$ and $HH = \mu\mu$ then are the sum of the spatial components and of all components of the vector correlation function, respectively. For notational convenience we often write $HH = \mu\mu \equiv V$ and call it the *full* vector correlator. The point to point correlators (7.3) are projected to definite momentum $\vec{p}$ by a discrete Fourier transform over all spatial coordinates on the lattice,

$$G_H(\tau, \vec{p}) = \sum_{\vec{x}} G_H(\tau, \vec{x}) e^{i\vec{p}\vec{x}}. \tag{7.4}$$

In this study we constrain ourselves to the case $\vec{p} = 0$ and thus set $\vec{p} = 0$ implicitly when dropping the momentum in the function arguments. The full vector correlator is

	$\mathbf{N_\tau}$	$\mathbf{N_\sigma}$	β	κ	$\mathbf{1/a[GeV]}$	$\mathbf{\#\ conf.}$
$\mathbf{T = 1.1T_c}$	32	96	7.192	0.13440	9.65	314
	48	144	7.544	0.13383	13.21	358
	64	192	7.793	0.13345	19.30	242
$\mathbf{T = 1.2T_c}$	28	96	7.192	0.13440	9.65	232
	42	144	7.544	0.13383	13.21	417
	56	192	7.793	0.13345	19.30	273
$\mathbf{T = 1.4T_c}$	24	128	7.192	0.13440	9.65	340
	32	128	7.457	0.13390	12.86	255
	48	128	7.793	0.13340	19.30	456

Table 7.1: Parameters of all lattices for all temperatures used in this study.

in Euclidean metric obtained from the correlation function (7.4) by summing spatially and temporally polarized components, i.e.

$$G_V(\tau) = \sum_{i=1}^{3} G_{ii}(\tau) + G_{00}(\tau) \equiv G_{ii}(\tau) + G_{00}(\tau). \tag{7.5}$$

In the following we do not consider single spatial components, and the index $HH = ii$ will always denote the sum over all spatial components. The temporal component $HH = 00$ is the quark number susceptibility $\chi_q = -G_{00}/T$. As we are especially interested in the spatial correlation function $G_{ii}(\tau)$, we form a ratio of correlation functions

$$R_{ii}(\tau) = \frac{T^2}{\chi_q} \frac{G_{ii}(\tau)}{G_V^{free,lat}(\tau)}, \tag{7.6}$$

where G_{ii} is normalized by both the free, massless correlator on the lattice, which can be computed similarly to the spectral function presented already in Sec. 4.2 [84, 85], and the quark number susceptibility χ_q/T^2 in units of temperature. The reason for this choice of normalization is purely technical, specifically the division by χ_q/T^2 rids us of the need to actually renormalize the spatial current correlator $G_{ii}(\tau)$, while the division by $G_V^{\mathrm{free,lat}}(\tau)$ cancels the exponential falloff of the interacting correlator to a large extent, which increases the numerical stability in the continuum extrapolation. Strictly speaking, any function resembling this exponential falloff works out for this task, but we specifically decided to use the free lattice correlator over the free continuum one in order to already cancel cutoff effects in the process of the extrapolation itself.

The lattice calculations of the vector correlator were performed in [144, 145], by using the standard Wilson gauge action to produce a background sea of purely ($SU(3)$) gluonic degrees of freedom, see Sec. 2.2 for details of the discretization. In order to equilibrate the ensemble, a mixture of local heatbath and overrelaxation steps was used, which provide an efficient way to equilibrate quickly and also reduce correlations between the resulting subsequent gauge configurations [43, 44, 45]. For the Dirac matrix, i.e. the realization of the valence quarks, we chose the non-perturbatively improved Wilson-Clover action, with the values of the corresponding improvement coefficient $c_{sw}(\beta)$ known for the quenched approximation as a function of the coupling $\beta = 6/g^2(a)$ in the chiral limit, see Sec. 2.2.2 and [26] for reference.

The lattice spacing was set in [144] for the lattices with temperatures $T = 1.1T_c$ and $T = 1.2T_c$ by using an Ansatz

$$\ln(r_0/a) = \ln(1/f(\beta)) \frac{1 + c_1/\beta + c_2/\beta^2}{1 + c_3/\beta + c_4/\beta}, \tag{7.7}$$

with $f(\beta)$ being a scaling function from the renormalization group, see equation (2.46), and the Sommer scale parameter $r_0 = 0.49(2)$fm, as determined in [146]. They obtained r_0/a on lattices with $\beta \lesssim 6.9$ by fixing the force $\mathrm{d}V/\mathrm{d}r$ between two static quarks,

$$r_0^2 F(r_0) \equiv 1.65. \tag{7.8}$$

Then equation (7.7) was used in [144] to extrapolate to the needed values of β in Tab. 7.1. To determine the critical temperature T_c in the continuum, the critical coupling $\beta_c(N_\tau)$ was obtained for several N_τ by finding the peak position of the Polyakov Loop susceptibility. At $1.4T_c$, the scale setting was done in [82]. The temperature scale was set by determining the string tension $\sqrt{\sigma}$ of the interquark potential (2.49), and using $\sqrt{\sigma} = 428\text{MeV}$ and $T_c/\sqrt{\sigma} = 0.630$ from [147]. The lattice spacing was fixed by parameterizing

$$a\sqrt{\sigma}(g) = f(g^2)\frac{1 + c_2 r^2(g) + c_4 r^4(g) + c_6 r^6(g)}{\lambda/\sqrt{\sigma}}, \tag{7.9}$$

with $r(g) = f(g^2)/f(g^2(\beta = 6.0))$ and $f(g^2)$ again being the scaling function from above. Note that these two methods of scale setting are performed by performing exclusively pure gauge computations, and thus yield a very precise scale for computations on quenched lattices.

The bare gauge couplings $g^2(a) = 6/\beta(a)$, on the lattices to be extrapolated to the continuum for the actual study of the vector current spectral function, are then tuned to yield the three different temperatures desired, $T = 1/(aN_\tau) = 1.1T_c$, $1.2T_c$ and $T = 1.4T_c$. As mentioned above, for each of these temperatures, three increasingly finer lattices were produced to allow for extrapolations to the continuum, see Tab. 7.1. Valence quark masses were estimated via the improved Axial Ward Identity (AWI) mass [26], and the corresponding hopping parameters κ were fixed for each lattice such that the valence quark masses are small, corresponding to $m_{\overline{MS}}(\mu = 2GeV) \sim \mathcal{O}(10MeV)$ in the $\overline{MS}$ scheme. Note that for the two lowest temperatures the aspect ratio is fixed to $N_s/N_t = 3$ and $N_s/N_t = 3.42$ for all lattices, respectively, ensuring a constant physical volume, while for the $T = 1.4T_c$ lattices the aspect ratio decreases with decreasing cutoff a. However, finite volume effects were verified to be small in the corresponding study [145].

7.1.2 Extrapolation to the continuum

In order to be able to compare the correlation functions on differently spaced lattices, we adopt a normalization of the Euclidean time $\tau \to \tau T \in [0, 1]$, as done in the study of the dynamical lattices. The continuum extrapolation itself contains several technical steps to ensure a high quality extrapolation, facilitate a robust and reliable estimation of the initial Monte Carlo error carrying over to the final statistical error of the continuum data, and also extract information about the statistical correlation of the continuum data between different lattice distances τT. As such, for each temperature

1. we form N_{bs} bootstrap samples of each of the original data sets at different lattice spacings a, as described in Sec. 2.5. Each bootstrap sample, labeled n, has the same size N_{data} as the original data set.

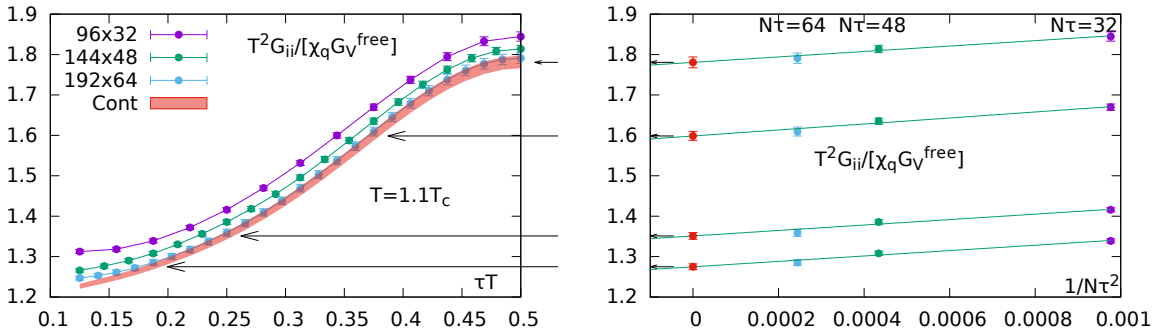

Figure 7.1: The extrapolation shown for a choice of temporal slices τT and the corresponding result.

2. We compute the average for each bootstrap sample per lattice distance

$$G_{ii}^{(n)}(\tau T, a)/T^3 \leftarrow \langle G_{ii}^{(n,k)}(\tau T, a)/T^3 \rangle_k \tag{7.10}$$

$$\text{and} \quad G_{00}^{(n)}(\tau T, a)/T^3 \leftarrow \langle G_{00}^{(n,k)}(\tau T, a)/T^3 \rangle_k, \tag{7.11}$$

where $k \in [1, N_{\text{data}}]$ numbers the configurations drawn within a boostrap sample, then perform a constant fit to $G_{00}^{(n)}$ to obtain the constant $\chi_q^{(n)}(a)/T^2$,

3. and compose the ratio

$$R_{ii}(\tau T, a) = \frac{1}{G_V^{\text{free,lat}}(\tau T, a)} \frac{G_{ii}^{(n)}(\tau T, a)}{\chi_q^{(n)}(a)/T^2}. \tag{7.12}$$

4. Because the temporal extents differ for all the temperatures considered, the maximum number of data points, and thus the maximum amount of information to obtain in the continuum, is the number of data points on the respective finest lattice, $N_\tau^{\max}$. Since for each τT available on the finest lattice we rarely find corresponding points at the same τT on the coarser lattices, we perform a natural cubic spline interpolation of the ratio $R_{ii}^{(n)}(\tau T, a)$ in τT.

5. With three data points, corresponding to the three different lattice spacings a, and the fact that our valence quark action has a cutoff error of $\mathcal{O}(a^2)$, we can perform a linear extrapolation in $a^2 \sim 1/N_\tau^2$, such that

$$R_{ii}^{(n)}(\tau T, a=0) = \lim_{N_\tau \to \infty} \left(1 + \frac{C(\tau T)}{N_\tau^2} + \mathcal{O}(\frac{1}{N_\tau^3})\right) R_{ii}^{(n)}(\tau T, a=0), \tag{7.13}$$

with $C(\tau T)$ parameterizing the slope of the linear extrapolation. In practice terms of order $\mathcal{O}(1/N_\tau^3)$ and higher are neglected.

At the end of this procedure, we are left with N_{bs} continuum extrapolated bootstrap samples $R_{ii}^{(n)}(\tau T)$ for each distance $\tau T = k/N_\tau^{\max}$, $k \in [0, N_\tau^{\max} - 1]$. The extrapolation

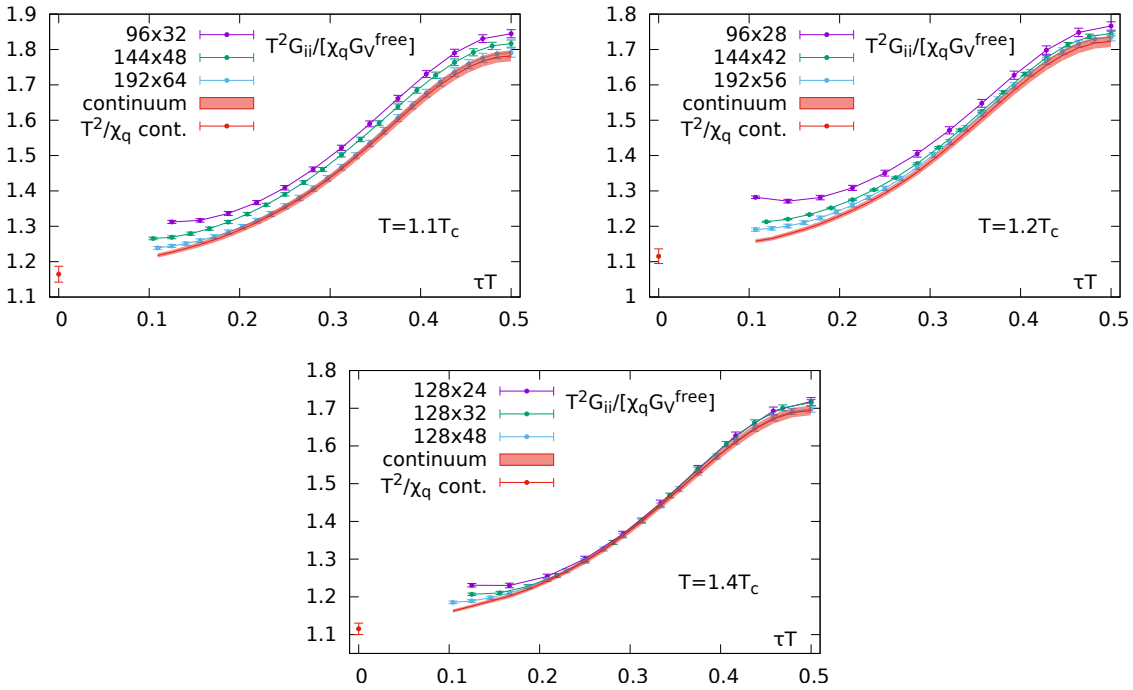

Figure 7.2: All three lattice correlators and the resulting continuum extrapolated correlator for the data sets at $T = 1.1T_c$, $T = 1.2T_c$ and $T = 1.4T_c$, respectively. Note that the finest lattice agrees with the continuum extrapolation down to $\tau T \sim 0.2$ in all cases. The single black data point at $\tau T = 0$ indicates the continuum extrapolated result for the inverted quark number susceptibility.

β	7.192	7.457	7.544	7.793
Z_V	0.8421	0.8512	0.8539	0.8612

Table 7.2: Non-perturbative renormalization constants of the vector channel Z_V, for the four values of the coupling used in this study.

is demonstrated in Fig. 7.1, where a collection of τT at different lattice spacings on the right hand side is linearly extrapolated in $1/N_\tau^2$ to become the result pointed to on the left hand side of the figure. The extrapolation itself works reliably, and the errors inferred by equation (2.74) are reasonable, and of the order of 1% or less.

For the quark number susceptibility the above procedure is repeated, bearing in mind that in this case the correlation function $G_{00}^{(n)}(\tau T)/T^3$ has to be renormalized for each single lattice spacing according to equation (2.47), with the renormalization constants, obtained from equation (2.48), given in Tab. 7.2 for convenience. The results for the continumm extrapolated quark number susceptibility χ_q are listed in Tab. 7.3.

For completeness, Fig. 7.2 shows the extrapolations for all three temperatures. The

T	$1.1T_c$	$1.2T_c$	$1.4T_c$
χ_q/T^2	0.8586(16)	0.8966(17)	0.8967(12)

Table 7.3: The values of the quark number susceptibility χ_q/T^2 in the continuum.

single red data point at $\tau T = 0$ is the continuum extrapolated inverse quark number susceptibility in units of temperature. Note that it is indeed approached by the extrapolated ratio in the limit $\tau T \to 0$,

$$\frac{G_{ii}}{G_V^{\text{free}}} = \frac{G_V - \chi_q T}{G_V^{\text{free}}} \overset{\tau T \to 0}{\longrightarrow} \frac{G_V^{\text{free}}}{G_V^{\text{free}}} - 0 = 1, \tag{7.14}$$

because the kernel fulfills

$$K(\omega/T, \tau T = 0) = [\tanh(\omega/(2T))]^{-1} \overset{\omega \to \infty}{\longrightarrow} 1 \tag{7.15}$$

for large frequencies, and thus the divergence of both the free and the interacting correlators, occurring at zero distance, is dominated on the spectral function level by the large frequency regime of the integration, with the consequence that the interacting correlator becomes free. In this sense asymptotic freedom governs the correlator at small distances, which reflects our argument to use the free spectral function as an Ansatz for the high frequency region. It is assuring that our extrapolated continuum data shows this behavior.

As outlined in Sec. 2.5, because the bootstrap encompasses the whole extrapolation procedure, the covariances/correlations between data points at different τT are preserved in the process and thus present in the continuum bootstrap samples $R_{ii}^{(n)}(\tau T)$. This enables us to compute the covariance matrix of the continuum data via (2.75), which in the current notation reads

$$M_{jk} = \frac{1}{N_{bs}} \sum_{n}^{N_{bs}} \left(R_{ii}^{(n)}(\tau T_j) - \hat{R}_{ii}(\tau T_j) \right) \left(R_{ii}^{(n)}(\tau T_k) - \hat{R}_{ii}(\tau T_k) \right), \tag{7.16}$$

with $\hat{R}_{ii}(\tau T_j)$ representing the sample averaged ratio at coordinate τT_j. In Sec. 2.6 we expressed a warning when performing fits with a full covariance matrix, because they tend to be unstable under certain circumstances. However, in this case the continuum covariance matrices we get from the extrapolation, are well behaved for all temperatures, and indeed permit stable fits. When we fit a spectral function Ansatz to the continuum data, of course we will have to choose a range to fit to, $\tau T \in [\tau T_{\text{min}}, 0.5]$. Without going into the details how to do this, which will be eludicated later, we state here that the covariance matrices for all three temperatures have a condition number $\kappa \sim \sigma_{\text{max}}/\sigma_{\text{min}} \sim \mathcal{O}(10^6)$, with σ_X being the largest and smallest eigenvalue of the matrix with the corresponding elements in $\tau T \in [\tau T_{\text{min}}, 0.5]$. Fig. 7.3 (*right*) shows the eigenvalues of the covariance matrix exemplarily for all temperatures, and it is clear that the eigenvalues

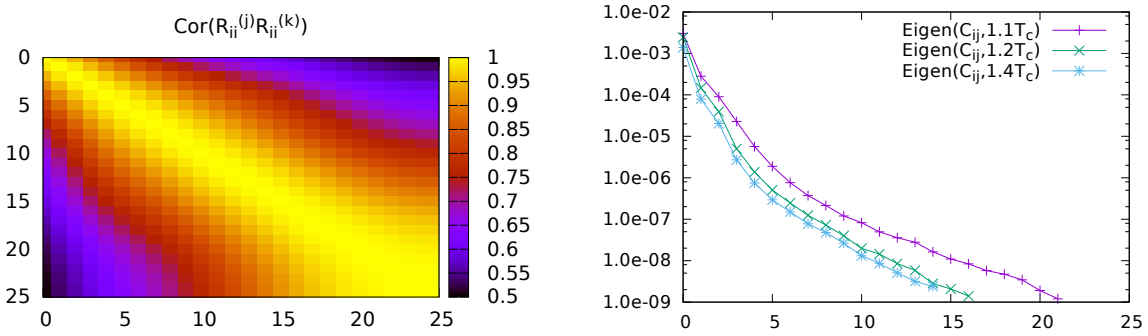

Figure 7.3: *Left*: A heat map of the entries of the estimated continuum correlation matrix for all points $\tau T > 0.1$ at $1.1T_c$. The axes label the row and column entry, resp. Hence, the midpoint $\tau T_j = \tau T_k = 0.5$ is located in the bottom right corner. *Right*: The eigenvalues of the covariance matrices of the data. Note that they decrease in a regular fashion, without strong fluctuations. The whole span covered is $\sim \mathcal{O}(10^6)$.

decrease in a regular fashion, without strong fluctuations. On the other hand, Fig. 7.3 (*left*) shows the corresponding normalized covariance matrix, or correlation matrix,

$$C_{ij} = \frac{M_{ij}}{\sqrt{M_{ii}M_{jj}}}, \qquad \text{(no sum)} \tag{7.17}$$

Clearly, the correlation, being unity along the diagonal by definition, is quite strong among several neighboring data points. Over the whole range shown in the heat map, the numerical value of the correlation remains strictly larger than 1/2, which serves as a strong indication that the correlations between the points should not be neglected in the fit procedure.

A comparison of the continuum ratios for all three temperatures is shown in Fig. 7.4 (*right*). The results for the two highest temperatures overlap to a large extent, while the extrapolation for $T = 1.1T_c$ lies distinctly higher than the former two. On the other hand, the continuum extrapolated correlator G_{ii}/T^3 can be obtained by multiplying the continuum ratio $R_{ii}(\tau T)$ by the extrapolated continuum χ_q/T^2 and the free continuum correlator. For all three temperatures G_{ii}/T^3 is shown in Fig. 7.4 (*left*). They show a nearly perfect overlap for a range of $\tau T \in [0.1 : 0.5]$. However, at large distances they differ distinctly from the free continuum correlator G_{ii}^{free}/T^3. Since neither G_{ii}/T^3, nor G_V^{free}/T^3 show a dependence on T, the reason for $R_{ii}^{1.1T_c}$ deviating from the almost overlapping $R_{ii}^{1.2T_c}$ and $R_{ii}^{1.4T_c}$ must be the quark number susceptibility χ_q/T^2 differing in the two cases. However, note that this difference is, although significant with respect to the errorbars, rather small. From this and the agreement of the correlators in Fig. 7.4 we expect the underlying spectral functions also to be very similar for all three temperatures, already indicating that temperature effects in the dilepton rates and the electrical conductivities will be rather small, as well.

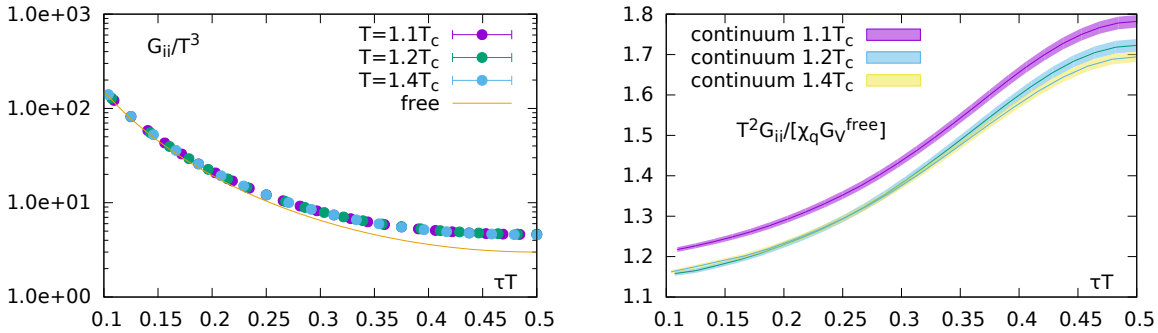

Figure 7.4: *Left*: Continuum extrapolated correlation functions for all three temperatures. Shown are the renormalized spatial components. The solid line is the corresponding free correlation function. *Right*: The continuum extrapolations for all three temperatures.

7.1.3 Extracting thermal moments from the data

As has been discussed in Sec. 5.2 and Sec. 5.1.1, the information about the small ω region resides in the large τT region of the correlator [104], i.e. around its midpoint $\tau T \sim 1/2$. Because we face a problem whose solution relies strongly on providing additional information, the idea is to gain knowledge also about the curvature of the correlation function, or, to be more specific, of the ratio $R_{ii}(\tau T)$. In order to supply this information, the idea is to also compute the second thermal moment (5.15) of the correlator data and account for it in the fit procedure as an additional data point. We choose to form a ratio of midpoint subtracted correlation functions,

$$\Delta_H(\tau T) = \frac{G_H(\tau T) - G_H^{(0)}}{G_H^{\text{free}}(\tau T) - G_H^{(0),\text{free}}}, \tag{7.18}$$

for the same reasons as in the case of the correlation function itself. By taking the expansion of the correlator into its thermal moments (5.15), plugging it into (7.18) and expanding the denominator, we arrive at

$$\begin{aligned}
\Delta_H(\tau T) &= \frac{G_H^{(2)}(\tau T - \frac{1}{2})^2 + G_H^{(4)}(\tau T - \frac{1}{2})^4 + \mathcal{O}\left[(\tau T - \frac{1}{2})^6\right]}{G_H^{(2),\text{free}}(\tau T - \frac{1}{2})^2 + G_H^{(4),\text{free}}(\tau T - \frac{1}{2})^4 + \mathcal{O}\left[(\tau T - \frac{1}{2})^6\right]} \\
&= \frac{G_H^{(2)}}{G_H^{(2),free}} \frac{1 + R_H^{(4,2)}\left(\tau T - \frac{1}{2}\right)^2 + \mathcal{O}\left[(\tau T - \frac{1}{2})^4\right]}{1 + R_{H,\text{free}}^{(4,2)}\left(\tau T - \frac{1}{2}\right)^2 + \mathcal{O}\left[(\tau T - \frac{1}{2})^4\right]} \\
&= \frac{G_H^{(2)}}{G_H^{(2),\text{free}}} \left\{1 + \left(R_H^{(4,2)} - R_{H,\text{free}}^{(4,2)}\right)\left(\frac{1}{2} - \tau T\right)^2 + \mathcal{O}\left[\left(\frac{1}{2} - \tau T\right)^4\right]\right\},
\end{aligned} \tag{7.19}$$

$$\text{with} \quad R_X^{(n,m)} = G_X^{(n)}/G_X^{(m)}. \tag{7.20}$$

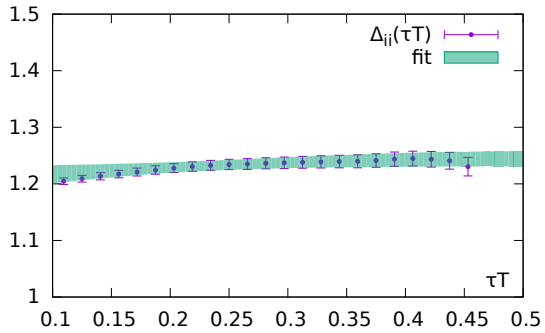

Figure 7.5: The necessary extrapolation in τT to obtain Δ_{ii} for the case $T = 1.1T_c$. The fit interval is $\tau T \in [0.2, 0.45]$, i.e. the point at the far right is not included in the fit.

At the midpoint this quantity obviously satisfies

$$\frac{T^2}{\chi_q}\Delta_H(\tau T) \overset{\tau T \to 1/2}{\longrightarrow} \frac{T^2}{\chi_q}\frac{G_H^{(2)}}{G_H^{(2),\mathrm{free}}}\,, \tag{7.21}$$

and we are left with a ratio similar to (7.6). This leaves us with two more steps that are to be performed to extract the thermal moments. First, we need to extrapolate the midpoint subtracted correlation function (7.18) to the continuum. This is done by computing $\frac{T^2}{\chi_q}\Delta_H(\tau T, a)$ at each lattice spacing for all available distances $\tau T < 0.5$, and subsequently extrapolating these to the continuum analogously to the extrapolation procedure outlined above. This yields $\frac{T^2}{\chi_q}\Delta_H(\tau T)$. Second, because we cannot evaluate the midpoint subtracted correlator for $\tau T = 1/2$ directly, the limit (7.21) has to be taken by using the expansion (7.19) as an Ansatz for an extrapolating fit to $\tau T = 0.5$. Note that all spatial and full thermal moments except for the first are degenerate, i.e.

$$G_{ii}^{(n)} = G_V^{(n)} \quad \forall\, n > 0 \quad \Leftrightarrow \quad \Delta_V(\tau T) = \Delta_{ii}(\tau T). \tag{7.22}$$

Working with the spatial channel $H = ii$ for definiteness, the two unknown parameters in the fit are the second thermal moment $G_{ii}^{(2),\mathrm{free}}/G_{ii}^{(2)}$ and the ratio of fourth thermal moment to the second thermal moment $R_{ii}^{(4,2)}$. Fig. 7.5 shows the extrapolation exemplarily for the case $T = 1.1T_c$.

The advantage in constructing the midpoint subtracted correlator ratio from the data from scratch, and consequently having to perform an additional continuum extrapolation, is that the desired second thermal moment then appears in the Ansatz (7.19) as

T	Δ_{ii}	$R_{ii}^{(4,2)}$	χ^2/dof
$1.1T_c$	1.244(14)	10.26(12)	0.67
$1.2T_c$	1.203(12)	10.06(11)	0.50
$1.4T_c$	1.200(9)	10.14(5)	0.89

Table 7.4: The results for the extrapolation in τT to obtain Δ_{ii}. The extrapolating fits have been performed using the full covariance matrix of the data.

the intercept. A quicker route might be to expand analogously

$$\begin{aligned}\frac{G_{ii}(\tau T)}{G_{ii}^{\text{free}}} &= \frac{G_{ii}^{(0)} + G_{ii}^{(2)}\left(\tau T - \frac{1}{2}\right)^2 + \mathcal{O}\left[(\tau T - \frac{1}{2})^4\right]}{G_{ii,\text{free}}^{(0)} + G_{ii,\text{free}}^{(2)}\left(\tau T - \frac{1}{2}\right)^2 + \mathcal{O}\left[(\tau T - \frac{1}{2})^4\right]} \\ &= \frac{G_{ii}^{(0)}}{G_{ii,\text{free}}^{(0)}}\left\{1 + \left(R_{ii}^{(2,0)} - R_{ii,\text{free}}^{(2,0)}\right)\left(\tau T - \frac{1}{2}\right)^2 + \mathcal{O}\left[(\tau T - \frac{1}{2})^4\right]\right\},\end{aligned} \tag{7.23}$$

and use it as an Ansatz to perform a fit to the ratio data $R_{ii}(\tau T)$ from (7.6). Note that, since the free continuum correlators are available analytically, the above ratio can be easily converted to be normalized by the full free correlator $G_V^{(0),\text{free}}$, and so in principal no additional continuum extrapolation is needed to extract $G_H^{(2)}$ from the data. However, the second thermal moment shows up in Ansatz (7.23) as its curvature, while the Ansatz (7.19) contains the second thermal moment as its intercept, which is simply more reliable to obtain from a fit. Also, analogously, higher thermal moments are better extracted from (7.19). Hence, we conclude that an extra continuum extrapolation of the midpoint subtracted correlator ratio is profitable to facilitate a reliable extraction of the thermal moments. The necessary thermal moments of the free theory are, for the vector channel, given by $G_H^{(2),\text{free}}/T^3 = 28\pi^2/5$ and $R_{H,\text{free}}^{(4,2)} = 155\pi^2/147$ [82]. The results for Δ_{ii} for all temperatures are shown in Tab. 7.4. See e.g. [82, 145] for other discussions on this method.

7.2 Spectral function via Ansatz and fit

In this section we present the results of fitting the Ansatz (5.35) to the continuum extrapolated lattice data, as presented in the foregoing section. To be more precise on the fit procedure itself, an estimator for the spectral function is obtained from relation (4.17) by χ^2-minimizing the Ansatz ρ_{ans} from (5.35) with respect to the continuum

extrapolated ratio data from equation (7.6), i.e.

$$\begin{aligned} R_{ii}(\tau T) &= \frac{T^2}{\chi_q G_V^{\text{free}}(\tau T)} \int_0^\infty \frac{\mathrm{d}\omega}{2\pi} \rho_{ii}(\omega, T) K(\omega, \tau, T) \\ &= \frac{T^3}{2\pi G_V^{\text{free}}(\tau T)} \int_0^\infty \mathrm{d}\Big(\frac{\omega}{T}\Big) \left\{ \frac{c_{BW} T}{\Gamma} \frac{\omega/T}{\left(\frac{\omega}{\Gamma}\right)^2 + \frac{1}{4}} + (1+k)\, \rho_V^{\text{free}}(\omega/T) \right\} K(\omega/T, \tau T) \\ &= \frac{T^3}{2\pi G_V^{\text{free}}(\tau T)} \int_0^\infty \mathrm{d}\Big(\frac{\omega}{T}\Big) \frac{c_{BW} T}{\Gamma} \frac{\omega/T}{\left(\frac{\omega}{\Gamma}\right)^2 + \frac{1}{4}} K(\omega/T, \tau T) + (1+k)\,. \end{aligned} \tag{7.24}$$

Note that the free, massless continuum correlation function $G_V^{\text{free}}(\tau T)$, given by

$$G_V^{\text{free}}(\tau T) = \frac{1}{2\pi} \int_0^\infty \mathrm{d}\Big(\frac{\omega}{T}\Big)\, \rho_V^{\text{free}}(\omega/T) K(\omega/T, \tau T) \tag{7.25}$$

appears in the numerator of the r.h.s. after the integration over ω/T is performed. It thus cancels with the normalizing free spectral function and the free part of the Ansatz simplifies to a constant in the fit.

Analogously to the Ansatz for the correlation function above, we also have to develop a corresponding expression for the second thermal moment, as it too is supposed to be included in the fit. This is done by replacing the structure of the integrand above by the defining structure of the second thermal moment, as given in (5.15) for $n = 2$. Explicitly, this amounts to replacing the kernel $K(\omega/T, \tau T) \to \frac{1}{2!} \frac{(\omega/T)^2}{\sinh(\omega/(2T))}$, leading to

$$\frac{T^2}{\chi_q} \Delta_{ii} = \frac{T^3}{2! 2\pi G_{ii}^{(2),\text{free}}(\tau T)} \int_0^\infty \mathrm{d}\Big(\frac{\omega}{T}\Big) \frac{c_{BW} T}{\Gamma} \frac{\omega/T}{\left(\frac{\omega}{\Gamma}\right)^2 + \frac{1}{4}} \frac{(\omega/T)^2}{\sinh(\omega/(2T))} + (1+k)\,. \tag{7.26}$$

The fit itself is performed by taking into account all statistical correlations among the data points, with the covariance matrix $\mathbf{M}$ of the extrapolated continuum ratio $\hat{R}_{ii}(\tau T)$ from (7.16). It became apparent in Sec. 7.1.2 that it is non-negligible in the construction of the χ^2 function. The same Ansatz has been used in [145], on the $1.4 T_c$ data set also used in this work, but with a slightly different extrapolation procedure, and a fit that was done with only the diagonal parts of the covariance matrix. It yielded a very small value of χ^2/dof, which was attributed by the authors to neglecting correlations among the data. The need for including covariances will be further backed in our analysis by a systematic cross check.

The electrical conductivity can be obtained from the spectral function at the origin via the Kubo relation (4.79), which is proportional to the ratio of the fit parameters C_{BW} and Γ/T, written as follows,

$$\frac{\sigma}{C_{em}T} = \frac{2}{3T}\chi_q \frac{c_{BW}}{\Gamma}. \tag{7.27}$$

Consequently, the soft photon rate can also be obtained and written in terms of the electrical conductivity, with (3.6) and $\rho_T = \rho_{ii}/3$,

$$\lim_{\omega\to 0} \omega \frac{\mathrm{d}R_\gamma}{\mathrm{d}^3 p} = \frac{\alpha_{em} C_{em}}{2\pi^2} \left(\frac{\sigma}{C_{em}T}\right) T^2, \tag{7.28}$$

and is presented at the end of this work, including the systematics developed in the following sections.

When estimating the systematics of our procedure, an essential source of uncertainty is the fit Ansatz itself. Because of the general lack of information in an ill-posed inversion problem, and the fact that we apparently add strong information by the choice of our Ansatz, it is not excluded that other Ansaetze fit the data as well. In the next section we thus supplement the analysis by developing several structural changes in our Ansatz, and discuss what conclusion could be drawn from the respective modified Ansatz. Finally, the fit procedure is applied using each new Ansatz, and the results are presented.

7.2.1 Spectral function Ansatz: Breit-Wigner peak + free continuum

In the fit of our Ansatz ρ_{ans} to the extrapolated continuum data we want to provide as much physical information as possible. From the continuum extrapolations shown in Fig. 7.2 we see that for all three temperatures the extrapolation results almost agree with the data on the corresponding finest lattice from the midpoint down to $\tau T \simeq 0.15 - 0.20$. This is also where the coarsest lattice starts to bend upwards. As the ratios are supposed to approach $R_{ii} \longrightarrow T^2/\chi_q$ in the limit $\tau T \longrightarrow 0$, the 'bending up' when going to shorter distances is a cutoff effect. Since we want to be sure to include only continuum data into our fit procedure, we aim for $\tau T \sim 0.2$ and in practice take the distance which yields the χ^2/dof closest to unity when fitting Ansatz ρ_{ans}. This amounts to $\tau T_{\mathrm{min}} = 0.187, 0.232, 0.229$ for $T = 1.1T_c, 1.2T_c, 1.4T_c$, respectively, which will also be used as a definite choice of fit intervals for all following fits.

The fits of ρ_{ans} to the continuum extrapolated correlator data show a good convergence behavior and yield as a result the three fit parameters Γ, c_{BW}, k and their respective statistical fit errors, see Tab. 7.5. The relative statistical fit errors of the parameters are roughly $25 - 40\%$ for $c_{BW}T/\Gamma$ and $20 - 30\%$ for Γ/T. Note that the former has been calculated taking into account the correlation of the two parameters. The dimensionless

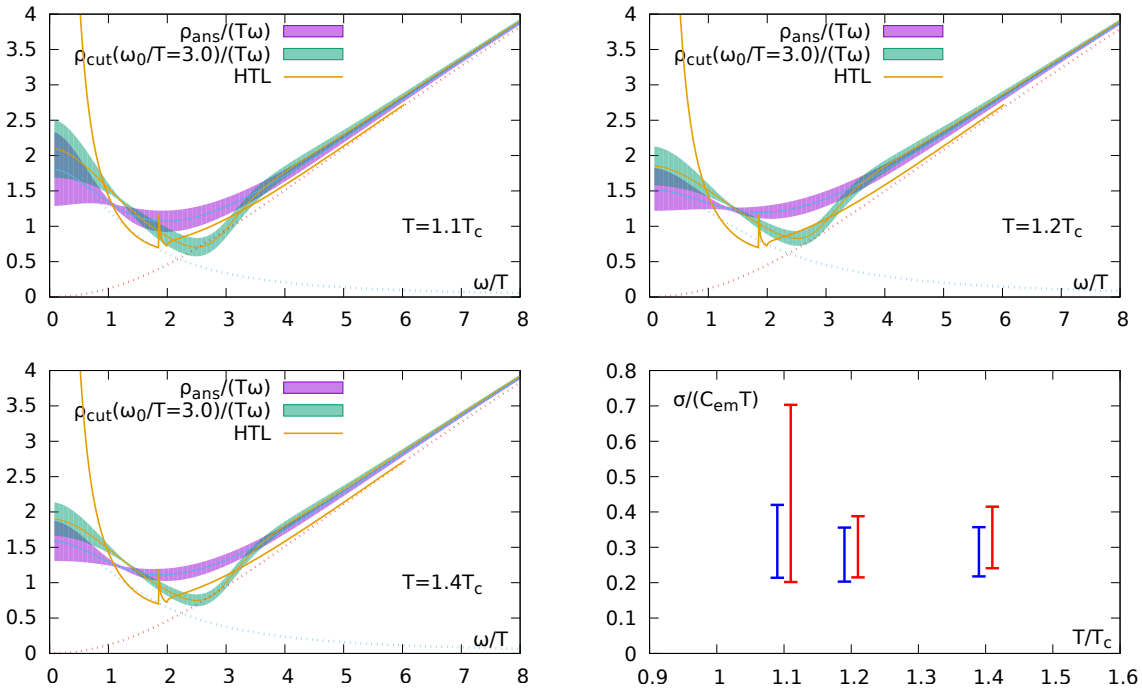

Figure 7.6: The spectral functions resulting from the fit using ρ_{ans} and ρ_{cut} (see Sec. 7.2.4) for all temperatures. The dotted lines are the Breit-Wigner and the free contributions separately to guide the eye. Note the consistently higher intercept of the spectral functions with the cut applied. *Bottom right:* The final results for the electrical conductivity for all three temperatures as resulting from Ansatz ρ_{ans} and an upper systematical error from the ansatz ρ_{cut} (see Sec. 7.2.4) (left, blue), and as resulting from Ansatz ρ_{R} (right, red).

modification k to the large frequency free behavior is small, but distinctly larger than zero in all cases. However, within errors there is no visible trend for the available range of temperatures. The values of χ^2/dof vary around unity and show that the fit to the data performs reliably. Using these parameters and their correlation matrix we construct the resulting spectral function, normalized by the frequency, with its corresponding statistical errorband in Fig. 7.6 (*left*) and (*top right*). The *HTL* result [93], introduced in Sec. 4.3.3, is also plotted and lies mostly below our estimate of the spectral function. In the low frequency region it cannot reproduce a (finite) transport peak, as its low ω

T	$\sigma/(C_{\mathrm{em}}T)$	Γ/T	$c_{BW}T/\Gamma$	k	χ^2/dof
$1.1T_c$	0.302(88)	2.86(1.16)	0.528(154)	0.038(8)	1.15
$1.2T_c$	0.254(51)	3.91(1.25)	0.425(85)	0.029(9)	0.52
$1.4T_c$	0.266(48)	3.33(89)	0.445(80)	0.040(7)	1.13

Table 7.5: Results of fitting the Ansatz ρ_{ans} for all three temperatures.

behavior is $\rho_{HTL} \sim \omega^x$, with $x < 1$. As an intermediate step in our analysis, we also give the electrical conductivity from this Ansatz in Tab. 7.5 for all three temperatures with the corresponding fitting error.

7.2.2 Spectral function Ansatz: flat transport region + free continuum

The Ansatz used so far is motivated by kinetic theory computations and argumentations. On the other hand, in the strong coupling limit the vector spectral function can be obtained from the AdS/CFT correspondence, see Sec. 4.3.3. The resulting spectral function in the low frequency region usually has no peak structure [97], consisting of a flat, 'featureless' shape in ρ/ω and then going over into the typical large frequency behavior. A simple Ansatz roughly showing this behavior is given by

$$\begin{aligned}\rho_{\text{flat}}(\omega) =& a\chi_q\omega\left(1-\widetilde{\Theta}(\omega,\omega_0,\Delta_0)\right)\\ &+(1+k)\rho_{\text{free}}(\omega)\widetilde{\Theta}(\omega,\omega_1,\Delta_1),\end{aligned} \tag{7.29}$$

with ω_i and Δ_i chosen such that ρ/ω then results in the desired shape. The functions $\widetilde{\Theta}(\omega_i,\Delta_i)$ are smoothed Heaviside functions

$$\widetilde{\Theta}(\omega,\omega_i,\Delta_i) = \left(1+\exp\left(\frac{\omega_i^2-\omega^2}{\omega\Delta_i}\right)\right)^{-1}, \tag{7.30}$$

which become sharp Heaviside functions in the limit $\Delta_i \to 0$. The cut on the first term is needed to make sure the large frequency regime is not affected by the low frequency constant contribution, and vice versa. This is of course a very rough model: not only is there a certain arbitrariness in the choice of ω_i and Δ_i, but in general there are many possible expressions that approximately describe the desired functional shape. Also, details like the exponentially damped oscillations are not built into this model. For these reasons we do not give definite results for the electrical conductivity or the soft photon rate, and merely utilize the model to test a non-peaked, flat low frequency region in ρ/ω. Technically, this change of the Ansatz, compared to the previous case, aims at making a statement about the *resolution* of our fit method regarding the low frequency region of the spectral function.

When fitting ρ_{flat} to the data, we tune the cut positions ω_i and the smoothing parameters Δ_i in such a way that the result from the fit roughly describes the characteristic, featureless ADS/CFT solution. The fits work well for a range of cuts at ω_i and smoothing parameters Δ_i. Throughout all temperatures they yield good fit qualities of $\chi^2/\text{dof} \sim 1.1$ for $T = 1.1T_c, 1.4T_c$ and $\chi^2/\text{dof} \sim 0.5$ for $T = 1.2T_c$, see Fig. 7.7 for the resulting spectral functions. The interpretation of this is first, that qualitatively this type of solution, being featureless in the low frequency region, fits our data just as well as a broad Breit-Wigner peak, motivated by kinetic theory, does. This implies that our

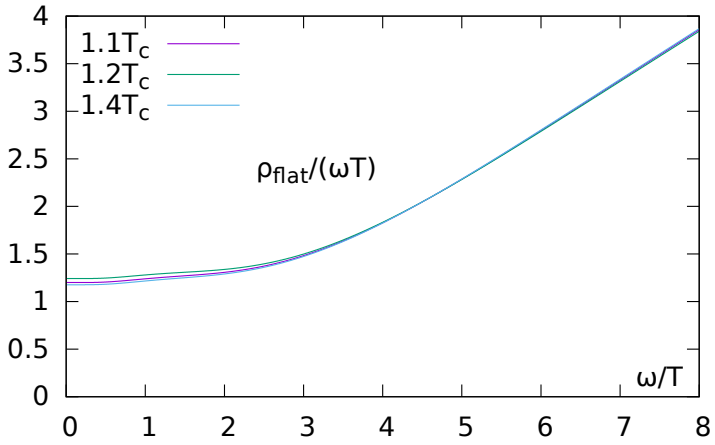

Figure 7.7: The spectral function resulting from the fit of the (coarse) model ρ_{flat} for all temperatures.

method, with regard to the available data, does not have the resolution to differentiate between these two extreme shapes with regard to the quality of the fit. The second point to make is that the solution from this type of Ansatz always yields an electrical conductivity, that is close to the lower bound of the results presented in Tab. 7.5, i.e. when using ρ_{ans}.

7.2.3 Crosscheck at low frequency

As a rather technical crosscheck, instead of using a Breit-Wigner peak for the low frequency part of the spectral function, we change it to be a real δ function with variable height, i.e. the Ansatz employed in this section is given by

$$\rho_\delta(\omega) = a\chi_q\omega\delta(\omega) + (1+k)\rho_V^{\text{free}}(\omega). \tag{7.31}$$

Up to the parameters k and a, this is just the free case. Theoretically, when turning off interactions, the conductivity should approach infinity, since no force changes the state of motion of a charge. Using the Kubo formula, this is clearly reflected in the above Ansatz ρ_δ for $\omega \to 0$, i.e. it is not compatible with a finite conductivity. Thus, performing the fit using this Ansatz we can check whether this wrong assumption works out with our interacting data, which should definitely yield a *finite* conductivity.

Performing the fit with Ansatz ρ_δ we find that the procedure yields values of $\chi^2/\text{dof} \sim 1.5$ for the two lower temperatures, and $\chi^2/\text{dof} \sim 2.5$, for $1.4T_c$, which also quantitatively shows a decrease in fit quality. Looking at the correlators resulting from the fitted parameters, shown in Fig. 7.8 (*left*) for all temperatures, we see that the reconstructed curves underestimate the correlator data points systematically by an amount of one standard deviation or more. Specifically, the fitted second thermal moments, shown at

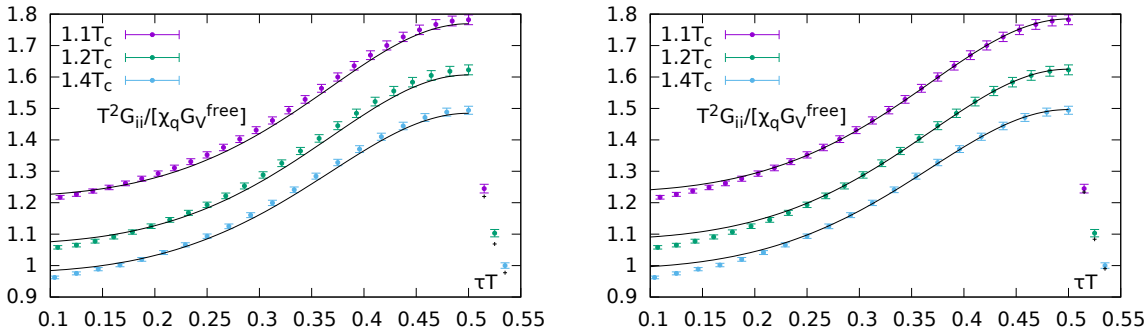

Figure 7.8: Resulting correlators when fitting with a genuine delta peak in the low frequency region. The points at $\tau T > 0.5$ are the second thermal moments and their fit results, respectively. *Left*: Fit including the covariance of the data. Note how the second thermal moments are described much worse than the corresponding correlator data points. *Right*: Fit without the covariance of the data. Note how the uncorrelated fit yields a much better reconstruction of the correlator data than the correlated fit.

$\tau T = 0.535$ in the plot, drastically deviate from the data. We conclude that the Ansatz does not describe the data sufficiently, and also place an emphasis on the importance of accurately determined thermal moments for the analysis. However, one peculiarity in this case is that, when we perform the fit *without* the covariance matrix in the minimizing χ^2 term, i.e. minimizing only with respect to the diagonal (variance) terms, we end up with a function that reconstructs the data points reasonably well at large distances, see Fig. 7.8 (*right*), with a $\chi^2/\text{dof} \sim \mathcal{O}(0.1)$. The latter is a typical sign for missing correlations in the fit procedure, see the discussion in Sec. 2.6.2. In this case, the second thermal moment is not quite as well reproduced compared to the data points of the ratio $R_{ii}(\tau T)$, but still distinctly better than in the fully correlated case. Reversing the argument, we see that the a priori insufficient fit Ansatz ρ_δ, which yields no finite conductivity by construction, fails to describe the data *only* if the information of the full covariance matrix is incorporated in the fit. In this sense we find that including covariances in the fit procedure measurably enhances our resolution of the spectral function in the low frequency region.

7.2.4 Uncertainties from the high frequency region

In order to check for uncertainties arising from the way we model the high frequency behavior in ρ_{ans}, we introduce a low-frequency cutoff multiplied to ρ_V^{free}, as proposed in [145], so that in total the modified Ansatz is given by

$$\begin{aligned}\rho_{\text{cut}}(\omega, \omega_0, \Delta_0) = \rho_{\text{BW}}(\omega) \\ + (1+k)\rho_V^{\text{free}}(\omega)\widetilde{\Theta}(\omega, \omega_0, \Delta_0).\end{aligned} \tag{7.32}$$

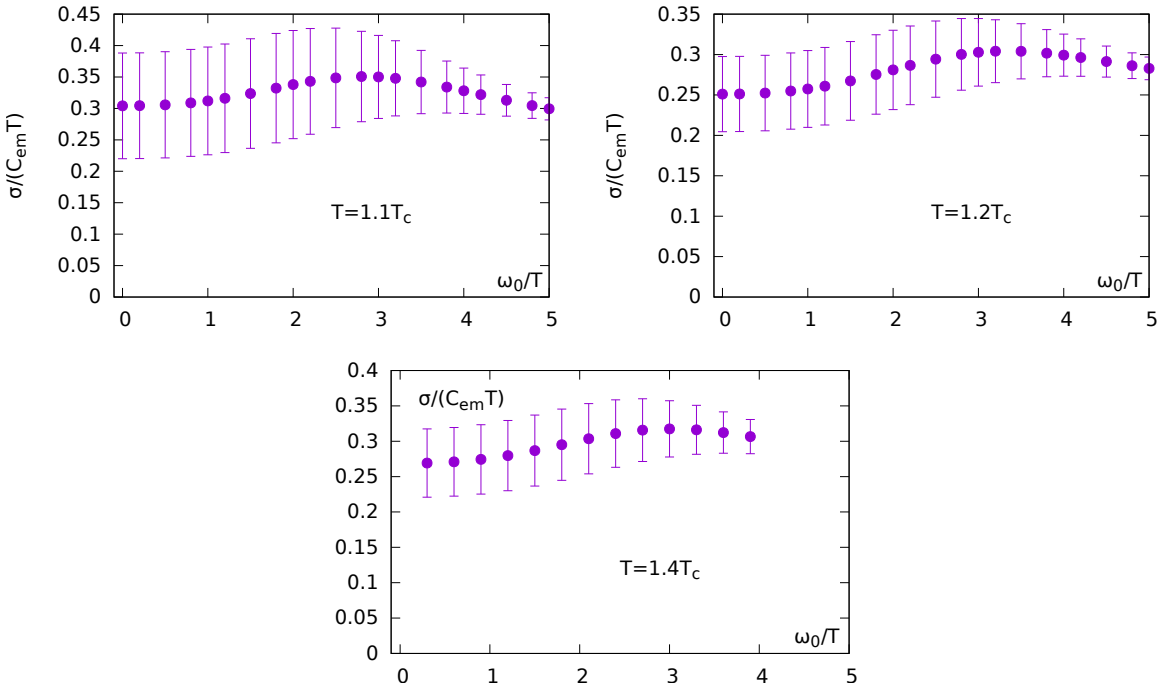

Figure 7.9: The increase of electrical conductivity upon increase of the cutoff ω_0/T in (7.30). It reaches its maximum around $\omega_0/T \simeq 3$ for all three temperatures. The smoothing parameter is fixed to $\Delta_0/T = 0.5$ throughout the analysis.

The cutoff factor $\widetilde{\Theta}(\omega, \omega_0, \Delta_\omega)$ is a representation of the Heaviside function for $\Delta_\omega \longrightarrow 0$, see equation (7.30) Consider that our choice in ρ_{ans} to account for the large frequency regime is essentially the free vector spectral function. However, this function has positive contributions for all positive frequencies $\omega > 0$, and it influences the Breit-Wigner peak for small frequencies. Thus we probe for this influence by cutting off its low frequency part and observing how the fit results react on this.

In order to fit the function ρ_{cut} to the continuum extrapolated data, we first of all set the width of the smeared Heaviside function to $\Delta_0/T = 0.5$. We varied the value of Δ_0/T and found that the result does not strongly depend on it. Applying the cut to different frequencies ω_0/T, however, has direct effect on the resulting electrical conductivity, illustrated in Fig. 7.9. As can be seen, the electrical conductivity, and thus the intercept of the spectral function normalized by the frequency, $\rho(\omega/T)/(\omega T)$, rises slightly when moving the cut to higher frequencies, showing that the peak rises in height. Around $\omega_0/T \simeq 3$ also Γ/T starts to rise sharply, i.e. at that point the peak is becoming much broader to compensate for the missing free contribution in the low ω regime, and thus $\sigma \sim c_{BW}/\Gamma$ falls off again. The fit itself still works well over a long range of ω_0 in the sense that χ^2/dof does not change much. However, raising ω_0/T further will finally make the model not fit the data anymore. This can be understood by noting that for low

frequency and large width, such that $\omega/\Gamma \ll 1$, the Breit-Wigner peak can be expanded,

$$\frac{\rho(\omega/T)}{\omega T} \sim \frac{\Gamma/T}{(\Gamma/T)^2 + (\omega/T)^2} = \frac{T}{\Gamma}\frac{1}{1+(\omega/\Gamma)^2} \approx \frac{T}{\Gamma}\left(1 - \mathcal{O}\left[\frac{\omega^2}{\Gamma^2}\right]\right), \tag{7.33}$$

and thus the leading order contributes a constant. As we saw in the fit to the Ansatz ρ_{flat}, this behavior leads to an equally good fit as a peaked structure at low frequencies. Of course, when finally ω_0/T becomes too large, this Ansatz does not mimic ρ_{flat} anymore, because too much of the continuum contribution is suppressed, and hence the fit performs worse. For the electrical conductivity, we can include its maximal deviation from the result obtained using the untruncated Ansatz as an upper systematical error, see Fig. 7.6 (*bottom right*). The corresponding spectral function ρ_{cut}, with the cut applied at $\omega_0/T = 3$, is shown in Fig. 7.6 (*top*) and (*bottom right*) for all three temperatures.

In our standard Ansatz ρ_{ans} we model the large frequency behavior as a scaled non-interacting continuum spectral function, which is just the tree level result from perturbation theory. Another approach would thus be to instead incorporate a higher order perturbative calculation of the vector channel spectral function, to be used as the large frequency part of our Ansatz for the spectral function. To this end, we pick the large frequency part of the high order solution shown in equation (4.87). In this case we still incorporate a factor multiplying the perturbative spectral function, C, to account for modifications from the surrounding medium, uncertainties in the renormalization etc. The modified Ansatz thus is given by

$$\begin{aligned} \rho_{\text{R}}(\omega, T) &= \rho_{\text{BW}}(\omega, T) + C\rho_{\text{impr}}(\omega, T), \\ \text{with} \qquad \rho_{\text{impr}} &= \frac{3\omega^2}{2\pi}\tanh\left(\frac{\omega}{2T}\right) R(\omega^2). \end{aligned} \tag{7.34}$$

Fitting our data with the Ansatz ρ_{R} and listing the results in Tab. 7.6, we generally find that the transport peak becomes a bit narrower and higher, when compared to ρ_{ans}, with the most pronounced effect at $T = 1.1T_c$, where the peak rises one third in height. However, the strong effect at $1.1T_c$ is accompanied by huge errors of both the transport peak's width and height, of $50 - 80\%$. The resulting spectral functions for all three temperatures are shown in Fig. 7.10. The parameter C is slightly smaller than unity in all cases, and for $1.1T_c$ and $1.4T_c$ it is even compatible with unity within its errors. From (7.34) we see, comparing to the large frequency part of $\rho_{\text{ans}}(\omega)$, that the factor $(1 + k)$ corresponds to a factor of $CR(\omega^2)$ in the improved case. On the one hand this makes the improvement of the large frequency part explicit, as what was the correction coefficient

T	$\sigma/(C_{\text{em}}T)$	Γ/T	$c_{BW}T/\Gamma$	C	χ^2/dof
$1.1T_c$	0.452(251)	1.62(1.09)	0.790(438)	0.993(7)	1.11
$1.2T_c$	0.301(87)	2.89(1.18)	0.504(145)	0.984(8)	0.53
$1.4T_c$	0.326(87)	2.38(85)	0.548(146)	0.996(7)	1.12

Table 7.6: Results of fitting the Ansatz ρ_{R} for all three temperatures.

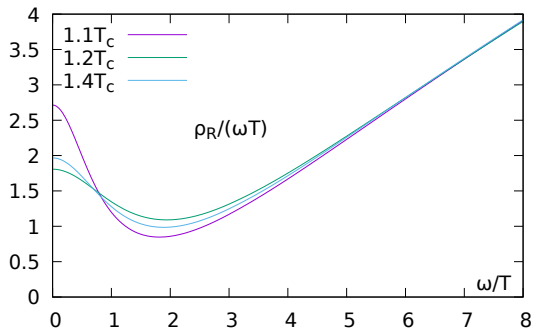

Figure 7.10: The resulting spectral function when utilizing perturbative input.

before now depends on the frequency. On the other hand, from a purely technical point of view, the remaining *correction constant* C becomes less important for the fit itself, as its deviation from unity is small, and partly negligible within its errors. To state a final result from this Ansatz, we plotted the maximum and minimum electrical conductivity, with errors coming from the fit, as the respective right bar of the paired bars in Fig. 7.6 (*Bottom right*).

7.2.5 Discussion

Comparing the three models ρ_{ans}, ρ_{flat} and ρ_{R} in Fig. 7.11 (*top left*), we see that the area under the spectral functions will likely become very similar above a certain frequency. For example, the smallness of $\rho_{\text{flat}}/(\omega T)$ close to the origin, compared to the more peaked solutions, is made up for in the region above $\omega/T \approx 1$. Indeed, we found that from a rather sharp peak to a fully flat behavior, all solutions are equally good ones in terms of stability and χ^2. This is in essence the sum rule mentioned in Sec. 5.1.1, and to further investigate this, Fig. 7.11 (*top right*) shows the primitive integral of $\rho/(\omega T)$ for all three cases. We find that above $\omega/T \gtrsim 3$ the areas under the curves are almost the same. Explicitly, the sum rule states that the area under ρ/ω in the peak region is in our case given by

$$\int_{\text{small }\omega} \mathrm{d}\left(\frac{\omega}{T}\right) \frac{\rho\left(\frac{\omega}{T}\right)}{\omega T} = \frac{2\pi}{3} N_c, \tag{7.35}$$

where we suppressed a factor of C_{em}, which is not contained in our definition of the spectral function. We plot this value as a straight line for reference. This reflects the equally good fit results of the different Ansaetze ρ_{ans}, ρ_{flat} and ρ_R, and shines a light on the predicted difficulty of fixing the shape of the low frequency regime of the spectral function unambiguously. The area fixing sum rule also reflects the small electrical conductivities obtained by fitting ρ_{flat}, compared to the other Ansaetze, that inhibit peaked structures. Concerning the width of the peaks, in both Ansaetze ρ_{ans} and ρ_R, which feature a Breit-Wigner peak at small frequency, we generally find $\Gamma/2 \sim \mathcal{O}(T)$ in all of

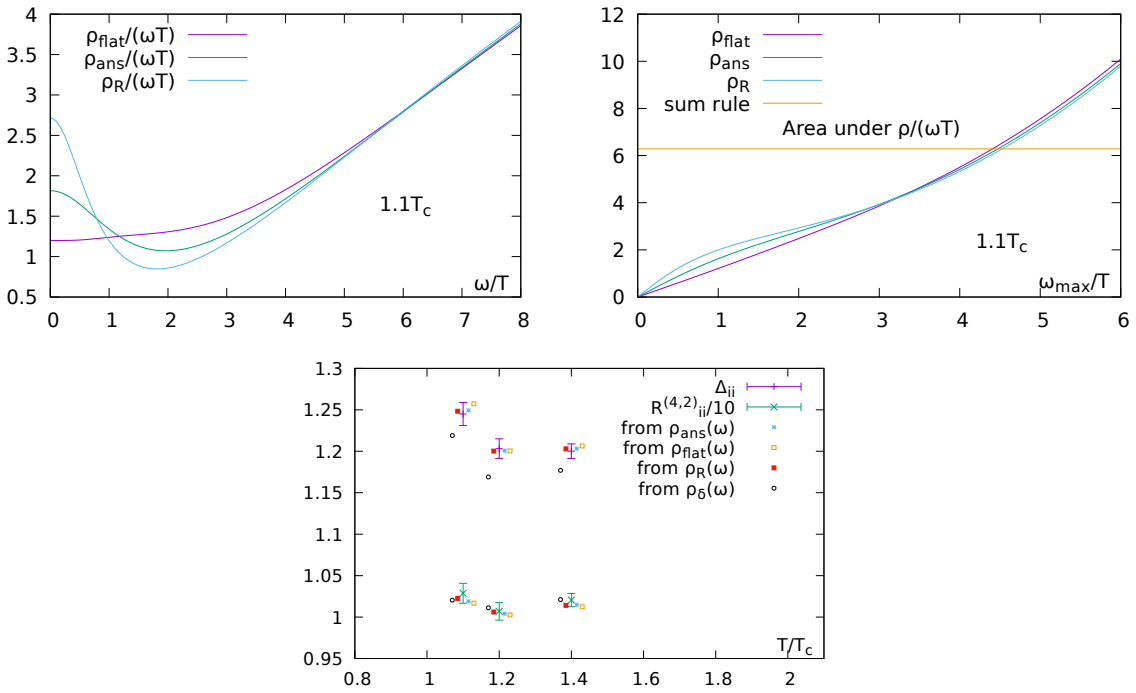

Figure 7.11: *Top left*: The solutions of different Ansaetze compared for $T = 1.1T_c$. Note that the difference between ρ_{R} and ρ_{ans} is most pronounced at $T = 1.1T_c$. *Top right*: Integrating $\rho/(\omega T)$ up to ω_{max}, i.e. numerically computing its primitive function for $T = 1.1T_c$. *Bottom*: The thermal moments for all T and their respective reconstructions from the fit, shown for all three models ρ_{ans}, ρ_{flat} and ρ_{R}.

our fits. As has been shortly discussed in Sec. 4.3.2, a width of this order is typical for a strongly coupled regime, and the corresponding scale for a weakly coupled plasma would be $\Gamma/2 \sim \mathcal{O}(gT)$ or smaller [12]. Thus our fitting results, obtained using the Ansaetze motivated from kinetic theory and from the AdS/CFT correspondence, both suggest a rather strongly coupled medium from $1.1T_c$ to $1.4T_c$.

We find that utilizing the covariance of the data points in the fit generally increases the resolution of the procedure with respect to the low frequency region, as described in Sec. 7.2.3, and also generally enhances the quality of the fit, in the sense that the errors on the resulting parameters are smaller compared to fits without the covariance matrix. The role of the second thermal moment as a constraint in the fit, however, turns out to be a more subtle one: On the one hand, when ignoring the covariance of the data, fitting with the second thermal moment as a constraint essentially also shows the effect of reducing the errors on the resulting fit parameters, as opposed to not constraining the fit with the thermal moment. But this effect does not appear when fitting with the full covariance of the data, showing that the information on the curvature of the correlation function is already largely contained in the statistical correlation. On the other

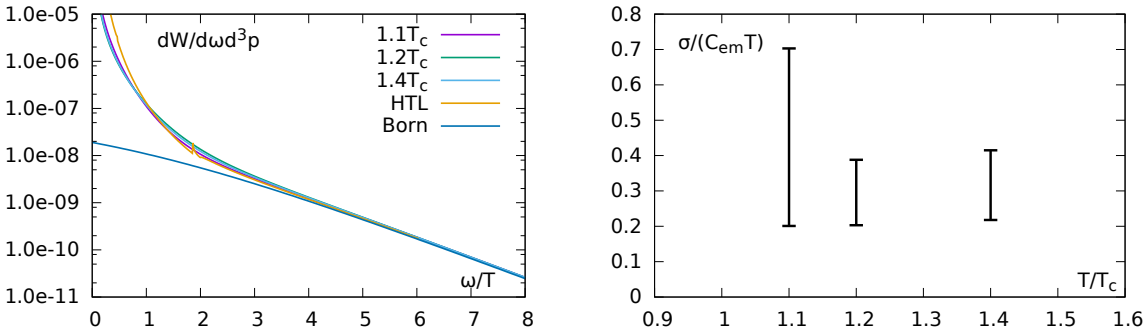

Figure 7.12: *Left*: The thermal dilepton rate as obtained from ρ_{R} as a function of ω/T, accompanied by the HTL rate and the non interacting Born rate. *Right*: The final results for the electrical conductivity. They incorporate the full systematics, i.e. the minimum and maximum conductivities, respectively, of ρ_{ans} and ρ_{R}.

hand, in the fit of $\rho_\delta(\omega)$, done with the full covariance of the data, the badly reproduced second thermal moment still serves as a very strong indication that the fit breaks down. This observation motivates us to also show the reconstruction of the extrapolated second thermal moment and the ratio of fourth to second thermal moments in Fig. 7.11 (*bottom*) for all temperatures. The reconstructed values from the fits (apart from $\rho_\delta(\omega)$) generally are in accord with the second thermal moments extracted from the data, which underlines that our fits work well from the point of view of fit quality. Although the second thermal moment is especially sensitive to the low frequency region of the spectral function, at the current state of data accuracy we cannot clearly differentiate between the models ρ_{ans}, ρ_{R} and ρ_{flat} using this observable. Considering that for $T = 1.1T_c$ and $T = 1.4T_c$ the thermal moment for ρ_{flat} deviates from the data visibly, but within errors, increasing the accuracy of the thermal moments data might provide a handle for this. The ratios $R_{ii}^{(4,2)}$ are not included in the fit as a constraint, but a posteriori (re)constructed from the data and resulting fit parameters, respectively. They compare within errors, although for $T = 1.1T_c$ and $T = 1.4T_c$ the results from the fit do not compare well. Note that the value from ρ_δ compares as well as any other reconstructed value, unlike in the case of the second moments discussed above. As expected in Sec. 5.2 from a rather qualitative argument, we thus see here explicitly that the ratios of fourth to second thermal moment are indeed far less sensitive to the low frequency region than the second thermal moments.

Our final results for the electrical conductivity for all three temperatures are summarized in Fig. 7.12 (*Right*). In the plot we show the respective minimum and maximum value resulting from the two Ansaetze ρ_{ans} and ρ_{R}, to incorporate the full systematics found in our analysis. They are comparable to recent studies using MEM and dynamical clover-improved Wilson sea quarks at finite lattice spacing [18, 148, 149]. For a comparison of different calculations of the electrical conductivity see [150]. The resulting

thermal dilepton rates, obtained from the spectral function ρ_{R} via the first expression of (3.5), are shown in Fig. 7.12 (*left*) for all three temperatures and a sum of squared charges of $C_{em} = \sum_i q_i^2 = 5/9$, corresponding to two valence quark flavors u and d. Our rates are qualitatively comparable to the rate obtained by an HTL calculation [93], see Sec. 4.3.3, in the large frequency region, as well as to the leading order (Born) rate. However, compared to the HTL computation, our results show an enhancement in the intermediate region $\omega/T \sim 2$ and a qualitatively different behavior for small frequency, as the leading term for $\omega \to 0$ is different (see also Fig. 7.6). Finally, the soft photon rate is obtained for all temperatures from the electrical conductivity via (7.28), and $C_{em} = 5/9$, as

$$\begin{aligned}
\omega \frac{\mathrm{d}R_\gamma}{\mathrm{d}p^3}\bigg|_{1.1T_c} &= \{5.00 - 17.48\} \times 10^{-5} T_c^2, \\
\omega \frac{\mathrm{d}R_\gamma}{\mathrm{d}p^3}\bigg|_{1.2T_c} &= \{6.01 - 11.48\} \times 10^{-5} T_c^2, \\
\omega \frac{\mathrm{d}R_\gamma}{\mathrm{d}p^3}\bigg|_{1.4T_c} &= \{8.78 - 16.71\} \times 10^{-5} T_c^2.
\end{aligned}$$

The soft photon rates at the two higher temperatures show a slight trend to rise with temperature, but this is within errors, and for the lower bound alone this trend is true for all T. However, the lowest temperature suffers from a large upper bound, that is also seen in the determined electrical conductivity.

7.2.6 Conclusion and outlook

Using non-perturbatively improved Wilson Clover valence fermions we performed continuum extrapolations of light vector channel correlation functions at three temperatures. The extrapolations yield reliable results with errors at the sub-percent level. A consequence of bootstrapping the extrapolation is that the covariance matrix of the data can be computed and is shown to permit stable fits. Employing a phenomenologically motivated Ansatz for the corresponding spectral function, these are used to perform a fully correlated χ^2-minimization and to obtain results for the spectral functions and thus the electrical conductivities via a Kubo relation, the thermal dilepton rates and the soft photon rates. The second thermal moments, obtained from a separate continuum extrapolation, are found to be sensitive to the low frequency region of the spectral function, while the ratios of the fourth to the second thermal moment are sensitive to a region at larger frequency. Different systematics related to the Ansatz are investigated. We find an essential improvement of the fit with respect to the low frequency region when performing the fit fully correlated, as opposed to neglecting the covariances of the data. Fitting a form of Ansatz inspired by the phenomenology of a strongly coupled QGP shows a comparable fit quality to the Ansatz motivated by a quasiparticle description, which implies that our procedure at this time does not resolve a difference between these two differently shaped spectral functions. This difficulty is reflected by the fact that the different spectral functions, extracted from our non-perturbative data, all fulfill

a sumrule that is valid in the low frequency region. However, by observing the resulting peak widths from the fits of a Breit-Wigner peak, we find that they are of the order of $\Gamma/2 \sim \mathcal{O}(T)$, as opposed to the smaller scale $\Gamma/2 \sim \mathcal{O}(gT)$, which reveals that both the peaked Ansaetze and the flat Ansatz hint at a strongly coupled medium. The use of a perturbative estimate for the large frequency part of the spectral function is found to generally increase the upper bound of the electrical conductivity. The electrical conductivities are in accordance with earlier results obtained by MEM and χ^2-minimization methods. We find no significant temperature dependence in the temperature range investigated, as was expected from the weak temperature dependence of the correlation functions. The thermal dilepton rates are compared to the HTL and leading order rates and show almost no temperature dependence in the analyzed temperature region, either. The lower bound on the determined soft photon rates clearly follows a trend by rising with temperature. However, the overall large errors, especially at $T = 1.1T_c$, make it difficult to determine a general trend.

The use of a higher order perturbative estimate for the large frequency behavior of our Ansatz opens two concrete possibilities. First, because for two temperatures the resulting C is compatible with unity within errors, we mark that in this sense further improvements might make it superfluous and thus reduce the number of parameters in the fit. Second, the low frequency behavior of the perturbative estimate is merely leading order. By incorporating additional perturbative input there, the resolution of the fit in the low frequency region might increase. Furthermore, although the quenched approximation has its merits by permitting generally high statistics and large lattices, in order to extract physics, large dynamical lattices are needed.

7.3 The Method of Backus and Gilbert

After approaching the problems of reconstructing spectral functions by performing fits to different Ansaetze, we now present a study that uses the method of Backus and Gilbert to reconstruct spectral function *directly* from data. While it does not rely on strong assumptions such as specific Ansaetze and yields a quantitative estimate for how well it can resolve the spectral function, given a specific set of data, note that this is an exploratory study, performed merely on a single data set, and serves as a first step to lay out its possible uses in future work. In the literature, the method of Backus and Gilbert has recently been employed in two studies [151, 152]. An especially interesting application is shown in [152], where the Backus Gilbert method is used to compare spectral functions, obtained by phenomenological computations, with spectral functions obtained from lattice calculations. The authors argue that for a meaningful comparison, phenomenological spectral functions should be filtered by the resolution function, provided by the Backus Gilbert method. This is a way to imprint the concept of resolution, that is naturally obtained within the Backus Gilbert method from non-perturbative lattice data, onto phenomenological models, which usually lack this concept. Concretely,

they compute $\hat{\delta}(\omega'/T, \omega/T)$, then convolute

$$\hat{\rho}_{\text{pheno}}(\omega'/T) = \int \mathrm{d}\left(\frac{\omega}{T}\right) \hat{\delta}(\omega'/T, \omega/T)\rho_{\text{pheno}}(\omega/T), \tag{7.36}$$

and compare $\hat{\rho}_{\text{pheno}}$ to the spectral function obtained in lattice calculations.

We will use the Backus Gilbert method in a much more direct way, by extracting solutions and the corresponding resolution function. As it turns out, a very interesting question is how to find a useful mapping $\theta(\omega/T)$ to fix the local regularization parameter for each single solution in frequency space. In the following, we first present some important preliminaries with respect to the application of the method, before turning to the application itself.

7.3.1 Practical considerations

For brevity we introduce the notation $\bar{\omega} \equiv \omega/T$, and the Fredholm equation connecting the Euclidean correlator and the spectral function becomes

$$G(\tau T) = \frac{1}{2\pi}\int_0^\infty \mathrm{d}\left(\frac{\omega}{T}\right) K(\omega/T, \tau T)\rho(\omega/T) \tag{7.37}$$

$$\equiv \frac{1}{2\pi}\int_0^\infty \mathrm{d}\bar{\omega} K(\bar{\omega}, \tau T)\rho(\bar{\omega}). \tag{7.38}$$

Computation of $\vec{R}$ and $\mathbf{W}$ require integrations of the kernel with respect to $\bar{\omega}$, see (5.43) and (5.46). Because the kernel has a pole of order one at $\bar{\omega} = 0$, it has to be regularized in order to make the above integrals convergent. An immediate modification would be to rewrite

$$\begin{aligned}\int_0^\infty \mathrm{d}\bar{\omega} K(\bar{\omega}, \tau T)\rho(\bar{\omega}) &= \int_0^\infty \mathrm{d}\bar{\omega} K(\bar{\omega}, \tau T)\alpha(\bar{\omega})\frac{\rho(\bar{\omega})}{\alpha(\bar{\omega})} \\ &= \int_0^\infty \mathrm{d}\bar{\omega} K'(\bar{\omega}, \tau T)\rho'(\bar{\omega}),\end{aligned} \tag{7.39}$$

and choose $\alpha(\bar{\omega})$ accordingly. In the course of this thesis we work with two different kernel modifications,

$$K_1 \equiv K(\bar{\omega}, \tau T)\alpha_1(\bar{\omega}) = \frac{\cosh(\bar{\omega}(1/2 - \tau T))}{\sinh(\bar{\omega}/2)}\tanh(\bar{\omega}/2), \tag{7.40}$$

$$K_2 \equiv K(\bar{\omega}, \tau T)\alpha_2(\bar{\omega}) = \frac{\cosh(\bar{\omega}(1/2 - \tau T))}{\sinh(\bar{\omega}/2)}\frac{\bar{\omega}^2}{\tanh(\bar{\omega}/2)}. \tag{7.41}$$

Kernel K_1 merely cures the divergence for $\bar{\omega} \to 0$, leaving the high frequency behavior untouched, as $\tanh(\bar{\omega}/2) \xrightarrow{\bar{\omega}\to\infty} 1$. Kernel K_2 achieves the same for the low frequency region, and additionally changes the expected large $\bar{\omega}$ (leading order) behavior of $\rho \sim \bar{\omega}^2$

to $\rho' \sim$ const in (7.39). The known asymptotics for $\bar{\omega} \to \infty$ is thus explicitly given to the method as additional information, which in turn only has to resolve the deviation from this asymptotic behavior. Note that the integrals $\vec{R}$ and $\mathbf{W}$ for kernel K_2 have to be solved numerically, while the integral $\vec{R}$ for kernel K_1 is given by the handy expression

$$R_i = \int_0^\infty \frac{\mathrm{d}\bar{\omega}}{2\pi} K_1(\bar{\omega}, \tau T_i) = \frac{1}{2\cos(\pi(1/2 - \tau T_i)}. \tag{7.42}$$

Additionally, because the method of Backus and Gilbert in general imposes no built in constraint on the *positivity* of the spectral function, we are free to subtract another function $H(\tau T)$ and write

$$\begin{aligned} G(\tau T) - H(\tau T) = \int_0^\infty \mathrm{d}\bar{\omega} K(\bar{\omega}, \tau T) \left\{\rho(\bar{\omega}) - h(\bar{\omega})\right\} \equiv \int_0^\infty \mathrm{d}\bar{\omega} K(\bar{\omega}, \tau T) \rho^{(-)}(\bar{\omega}), \\ \text{with} \qquad \int_0^\infty \mathrm{d}\bar{\omega} h(\bar{\omega}) K(\tau T, \bar{\omega}) = H(\tau T). \end{aligned} \tag{7.43}$$

A possible use of this is to take out the large frequency behavior of ρ, analogous to using Kernel K_2. In order to remove the first order pole in $K(\bar{\omega}, \tau T)$, we will in this case adopt $K_1 \equiv K(\bar{\omega}, \tau T)\alpha_1(\bar{\omega})$, as the large frequency behavior is already accounted for:

$$\int_0^\infty \mathrm{d}\bar{\omega} K(\bar{\omega}, \tau T) \rho^{(-)}(\bar{\omega}) \equiv \int_0^\infty \mathrm{d}\bar{\omega} K_1(\bar{\omega}, \tau T) \rho'(\bar{\omega}). \tag{7.44}$$

The complete spectral function would then be given by

$$\rho(\bar{\omega}) = \alpha_1(\bar{\omega})\rho'(\bar{\omega}) + h(\bar{\omega}), \tag{7.45}$$

i.e. especially we need both the correlator H and its spectral function h in order to perform the subtraction and later construct the full result. The corresponding variance (5.49) in this case transforms like

$$\begin{aligned} \mathrm{Var}(\rho(\bar{\omega})) &= \langle (\rho(\bar{\omega}))^2 \rangle - \langle \rho(\bar{\omega}) \rangle^2 \\ &= \langle [\alpha_1(\bar{\omega})\rho'(\bar{\omega}) + h(\bar{\omega})]^2 \rangle - \langle \alpha_1(\bar{\omega})\rho'(\bar{\omega}) + h(\bar{\omega}) \rangle^2 \\ &= \alpha_1^2(\bar{\omega}) \mathrm{Var}(\rho'(\bar{\omega})). \end{aligned} \tag{7.46}$$

Concerning the choice of spectral functions $h(\bar{\omega})$, we can subtract more than just the tree level asymptotics for $\bar{\omega} \to \infty$ by using the perturbatively computed spectral functions and correlators introduced in Sec. 4.3.3. The perturbative solution (4.87), relying on the 5-loop result, yields a much more refined large frequency behavior already at finite $\bar{\omega}$, compared to dividing out the tree level $\bar{\omega}^2$ behavior that is only valid asymptotically. We actually utilize only the high frequency part and discard the free theory peak, as we have in the fitting procedure, see (7.34). We (mis)label this contribution 'vacuum'. The thermal, interpolated computation, enumerated (3) in Sec. 4.3.3, adds a real transport

peak in the low frequency region. We label this contribution 'thermal'. By providing our method with both inputs as additional information, we will see whether a transport peak appears or, respectively, the existent transport peak gets modified in course of minimizing (5.50) for each $\bar{\omega}$.

Having a closer look at the interior of the Backus-Gilbert method, we classify three distinct components that form a given solution.

- The first one is the kernel, which influences the spread integral (5.43) and the constraint (5.46), forming the minimizing functional $\mathcal{A}$ when contracted with $\vec{q}(\bar{\omega})$.
- The second component is the covariance of the data, which constitutes the matrix S in (5.49), and, together with the vectors $\vec{q}(\bar{\omega})$, represents the minimizing functional $\mathcal{B}$. The vectors $\vec{q}(\bar{\omega})$ themselves are hence only dependent on the kernel and the covariances, but *not on the averaged data points*. This implies that both the spread and the variance of the solution do not depend on the averaged data points.
- The averaged data points are the third component, and are needed only when constructing the solution $\rho(\bar{\omega})$.

Before turning to the analysis, we still have to motivate a prescription for choosing $\theta(\bar{\omega})$ for each $\bar{\omega}$. As mentioned earlier, the best solution for a tradeoff problem is usually sought in the kink of the L-curve, i.e. at the point with largest curvature. Because there is one L-curve for each frequency $\bar{\omega}$, and remembering that both $\mathcal{A}$ and $\mathcal{B}$ depend implicitly on θ, we choose to minimize

$$\mathcal{A}^2(\bar{\omega}, \theta)\sin(\phi) + \mathcal{B}^2(\bar{\omega}, \theta)\cos(\phi), \tag{7.47}$$

with respect to θ for each $\bar{\omega}$. The newly introduced angle $\phi \in [0, \pi/2]$ is independent of $\bar{\omega}$ and thus leaves us with one parameter to tune the amount of regularization in the procedure globally, i.e. for all $\bar{\omega}$ at once. A large ϕ suppresses the variance term, and thus means small overall regularization, as mainly the resolution term is subject to the minimization. A small ϕ consequently implies strong regularization, while the statistical uncertainty is reduced. Reducing a very large number $N_{\bar{\omega}}$ of angles $\theta(\bar{\omega})$ to choose from to a single angle ϕ via a prescription like this of course is a very strong implicit assumption, because it decreases the degrees of freedom of the problem essentially to one. In some cases we decided to minimize the sum of squared distances to the input data,

$$\sum_{\tau T} \left(G^{\text{input}}(\tau T) - G^{\phi}(\tau T)\right)^2, \tag{7.48}$$

from all the solutions parameterized by ϕ, which determines the angle ϕ whose tuning of resolution and variance fits the data best in order to obtain an 'optimal' solution. Note, however, that strictly speaking all ϕ produce valid results, as all solutions on the L-curve are, theoretically, valid solutions of the problem. However, we expect the extreme cases

$\phi = 0$ and $\phi = \pi/2$ to be fully overregularized and underregularized, respectively. As such, they will yield solutions that do not reconstruct the input data well, because an underregularized solution will tend to oscillate wildly and be very unstable, while an overregularized solution will have extremely broad resolution and thus severely smear out the solution. Hence, we expect to find a well fitting solution somewhere between these two extremes. This approach gives us control over the global amount of regularization and its effect on the solution, very much like the single parameter λ in the Tikhonov regularization, see Sec. 5.1.2.

7.3.2 Results

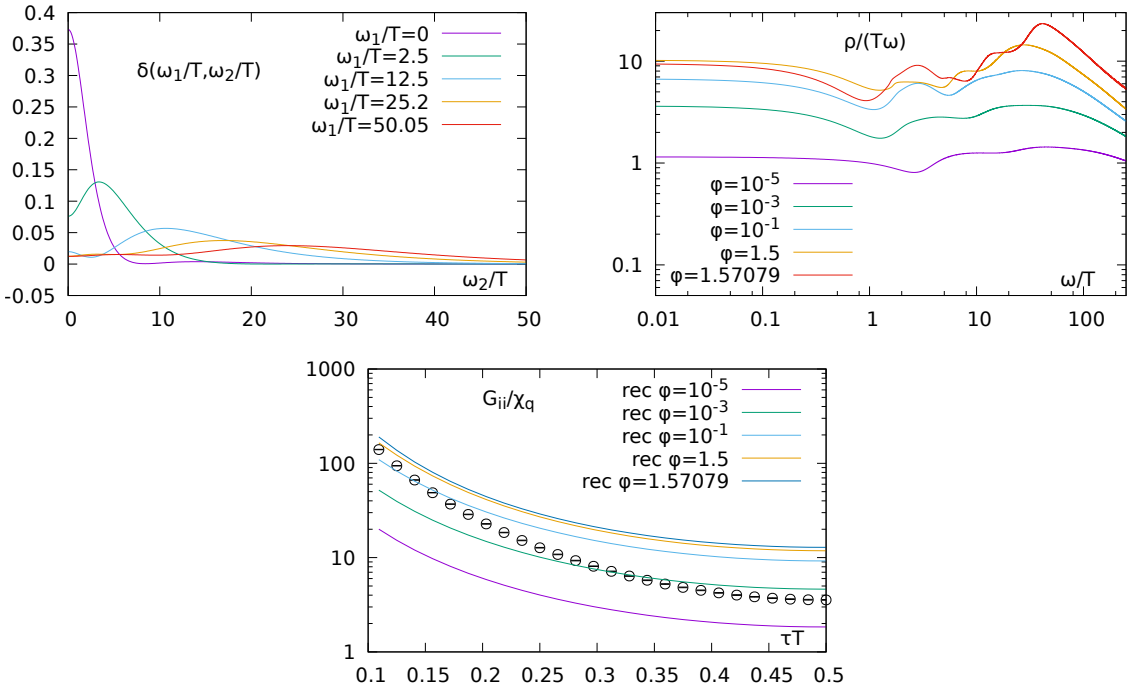

Figure 7.13: *Top left*: The resolution function δ, corresponding to *case 1*, for a number of frequencies. *Top right*: The resulting spectral function in log − log scale. *Bottom*: Reconstruction of the input correlator G_{ii}.

In what follows from here, we apply the method of Backus and Gilbert to our continuum extrapolated correlator data $G_{ii}(\tau T)$ at $T = 1.1T_c$, see Sec. 7.1.2, by using the two different kernels K_1 and K_2 to compare the general features of the solutions, i.e. resolution, variance and the dependence of the solution ρ, as well as its reconstructed correlator $G^{\phi}(\tau T)$, on the global regularization parameter ϕ. With these results at hand we proceed to work with the perturbative estimates to increase the amount of information given to the method. To name the different cases, we thus investigate:

Case 1 the kernel K_1 and data G_{ii} as input,

Case 2 the kernel K_2 and data G_{ii} as input,

Case 3 the kernel K_1 and data $G_{ii} - G_V^{\text{vacuum}}$ as input,

Case 4 the kernel K_1 and data $G_{ii} - G_V^{\text{thermal}}$ as input.

A range $\phi \in [10^{-5}, 1.57079]$ is considered, leading from a highly regularized regime to an almost unregularized regime. Generally, all distances in the interval $0.1 < \tau T \leq 0.5$ are used as input data.

We start with *case 1* and consider the reconstruction of the input correlator in Fig. 7.13 (*bottom*). In fact, no angle ϕ can make the correlator G^ϕ fit the input data for all distances. The only effect of changing ϕ is a constant factor (visually, the almost constant shift between the solutions in logarithmic scale), while the curvature of G^ϕ is generally not large enough to describe the input data. The reason for this can be found in the resolution function $\hat{\delta}(\bar{\omega}_1, \bar{\omega}_2)$, shown for several $\bar{\omega}_1$ in Fig. 7.13 (*top left*), as a function of $\bar{\omega}_2$. For definiteness these resolution functions are obtained at $\phi = 0.1$. While for small $\bar{\omega}_1$ we see clear peak structures, centered around $\bar{\omega}_2 = \bar{\omega}_1$, they obviously become broader in $\bar{\omega}_2$ with growing $\bar{\omega}_1$, the resolution is becoming increasingly asymmetric, and the peak is not centered around $\bar{\omega}_2 = \bar{\omega}_1$ anymore. Looking at the solution $\rho/\bar{\omega}$, shown in Fig. 7.13 (*top right*), we observe

1. that it falls off beyond $\bar{\omega} \sim 20 - 50$, depending on the amount of regularization applied, instead of keeping a roughly linearly rising behavior, as is expected by the asymptotic behavior $\rho(\bar{\omega}) \sim \bar{\omega}^2$. This is of course attributed to the observed loss of resolution (or 'signal') in this regime.

2. that the solution depends strongly on the regularization parameter ϕ even for very small frequencies, in the sense that the solutions $\rho(\bar{\omega})$ for increasing ϕ are constantly growing. Subsequently, the reconstructions plotted in Fig. 7.13 (*right*) also depend strongly on ϕ,

The strong dependence on the regularization parameter also in the low frequency region and the failure in reconstructing the curvature of the correlation function, which is hence attributed to the early loss of signal in the spectral function, leads us to the conclusion that no meaningful solution can be extracted utilizing the data $G_{ii}(\tau T)$ and the kernel K_1 alone.

In order to improve the method, it was proposed above to supply information about the large frequency behavior of the solution explicitly, by dividing out the asymptotic $\bar{\omega}^2$ dependence. This is realized by using kernel K_2 in the Backus Gilbert procedure together with the continuum extrapolated input data G_{ii}. In Fig. 7.14 (*top left*) the resolution kernels $\hat{\delta}(\bar{\omega}_1, \bar{\omega}_2)$ are plotted for several frequencies $\bar{\omega}_1$ at $\phi = 10^{-1}$. The loss of signal observed in the former case also occurs in this case, but at somewhat higher frequency $\bar{\omega}_1$ than in *case 1*. This indicates that we were successful in providing additional

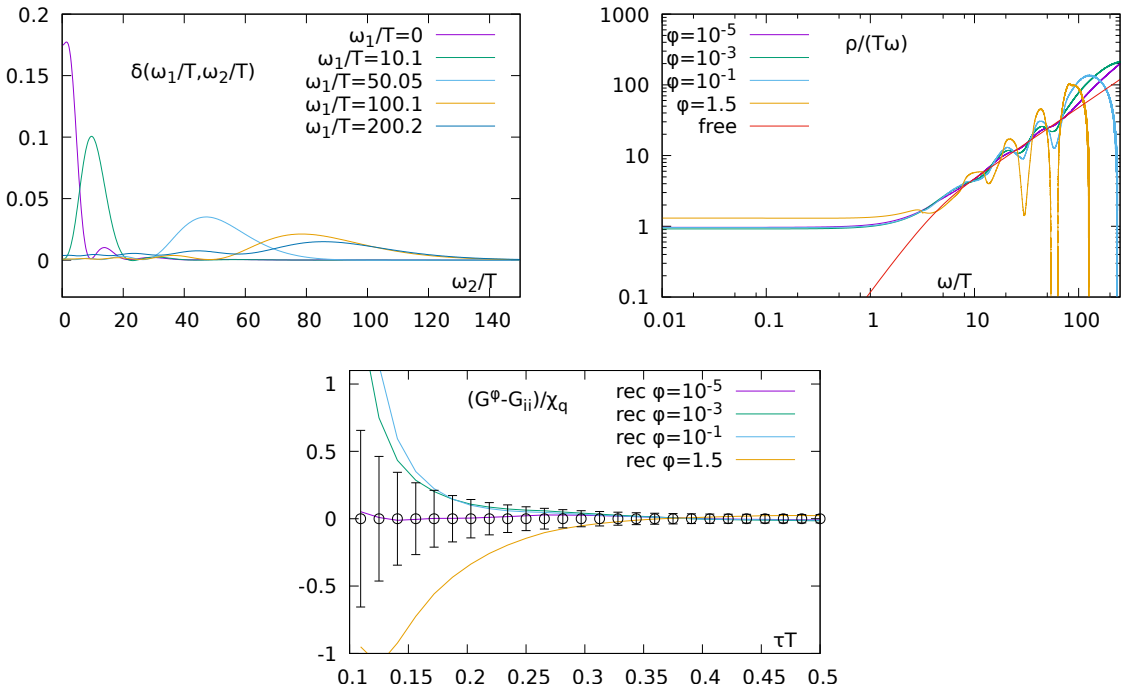

Figure 7.14: *Top left*: The resolution function δ, corresponding to *case 2*, for a number of frequencies. *Top right*: The resulting spectral function in $\log - \log$ scale. *Bottom*: Difference of the correlator to the correlator reconstruction.

information to the Backus Gilbert method by modification of the kernel. In Fig. 7.14 (*top right*) the solution is shown. The plot reveals that the high frequency region shows an oscillating behavior and, at some $\bar{\omega}$, whose precise value depends on ϕ, drops in a loss of signal as observed in the former case. Analogously to the resolutions, the drop occurs at larger frequencies. Thus, the observed improvement of resolution directly shows in the resulting solutions $\rho(\bar{\omega})$. In addition, the dependence of $\rho(\bar{\omega})$ on ϕ in the low frequency region is very weak, as opposed to *case 1*. Its course is very flat and does not exhibit a peak structure. The amplitude of the oscillations at large frequency depends on the amount of regularization. They are generally strongest (and set in earliest) for solutions featuring a smaller overall regularization, i.e. larger ϕ. Also, the free and massless continuum spectral function is shown to guide the eye. As can be seen in the figure, the solution oscillates around the free spectral function, before finally losing signal and dropping. The reconstruction of the correlation functions is shown in Fig. 7.14 (*bottom*), but this time the difference of the reconstruction and the input data is visualized for clarity. It works obviously much better than before and yields good results for large distances and for a wide range of regularization parameters. For small distances τT, we see that only the very small value of $\phi = 10^{-5}$ reconstructs the correlator successfully, which corresponds to a large degree of regularization and the spread term is highly suppressed in the minimization of (7.47), and thus the solution is dominated by the regularization error. It thus seems that for larger ϕ the large frequency region of the spectral function is

not stable enough for a reconstruction, because it suffers from too much oscillation. On the other hand, consider that in the plot the difference of reconstruction and input data is shown, and hence for the small distances the deviations are of the order of less than 1%.

We now undertake the final step and incorporate the two perturbative solutions as additional input via (7.43) and (7.44). Note that the subtraction of either of the perturbative solutions has no effect on the covariances of the data, because they are no statistical quantities, i.e.

$$\begin{aligned}\langle\Big\{G_i - G_i^{\text{pert}} - (\hat{G}_i - G_i^{\text{pert}})\Big\}\Big\{G_j - G_j^{\text{pert}} - (\hat{G}_j - G_j^{\text{pert}})\Big\}\rangle \\ = \langle\Big(G_i - \hat{G}_i\Big)\Big(G_j - \hat{G}_j\Big)\rangle.\end{aligned} \tag{7.49}$$

Furthermore, because the vectors $\vec{q}(\bar{\omega})$ depend only on the covariances and the specific kernel, they are the same as the corresponding vectors obtained by using kernel K_1 and the data G_{ii} alone, i.e. *case 1*. The solution of the subtracted problem can be split using (5.39),

$$\rho^{-}(\bar{\omega}) = \vec{q}(\bar{\omega}) \cdot \Big(\vec{G}_{ii}(\tau T) - \vec{G}^{\text{pert}}(\tau T)\Big) \equiv \rho_1(\bar{\omega}) - \vec{q}(\bar{\omega}) \cdot \vec{G}^{\text{pert}}(\tau T), \tag{7.50}$$

where ρ_1 is the solution of *case 1*, obtained with the same kernel K_1, but without subtracting the perturbative part. We see that the resulting spectral function is a modified version of this first result above, which suffered from a resolution problem for rather small values of $\bar{\omega}$, and thus did not permit a reconstruction of the correlator. Since the relative difference of our non-perturbative data and the perturbative spectral function is small compared to either correlator, we read (7.50) as a rather small correction to the full spectral function, which is constructed by adding the perturbative input onto it via (7.45),

$$\rho(\bar{\omega}) = \rho^{(-)} + \rho_{\text{pert}}(\bar{\omega}) = \rho_{\text{pert}}(\bar{\omega}) + \vec{q}(\bar{\omega}) \cdot \Big(\vec{G}_{ii}(\tau T) - \vec{G}^{\text{pert}}(\tau T)\Big). \tag{7.51}$$

The solutions $\rho^{(-)}$ are shown in Fig. 7.15 (*top left*), for *case 3*, i.e. subtracting the vacuum perturbative result, and in Fig. 7.16 (*top left*), for *case 4*, i.e. with the thermal perturbative result subtracted. The modifications for moderate choices of the regularization parameter ϕ indeed show up as slight changes from the respective perturbative result, increasing the spectral function in the low frequency region for the vacuum case, while the strong peak of the thermal perturbative result is slightly reduced. In the large frequency region, we see that there still are modifications by the Backus Gilbert method, but, considering that the complete spectral function $\rho(\bar{\omega})$ is dominated by the perturbative contribution ρ_{pert} at large frequencies, these contributions do not alter the complete spectral function much. This can be explicitly seen in the respective *top right* plot in the figures, where the solution $\rho/(\omega T)$ indeed behaves very stable in the large frequency region with respect to changing ϕ. The region around $\bar{\omega} \sim 1$ is still sensitive to the amount of regularization applied. The reconstruction of the correlators from these

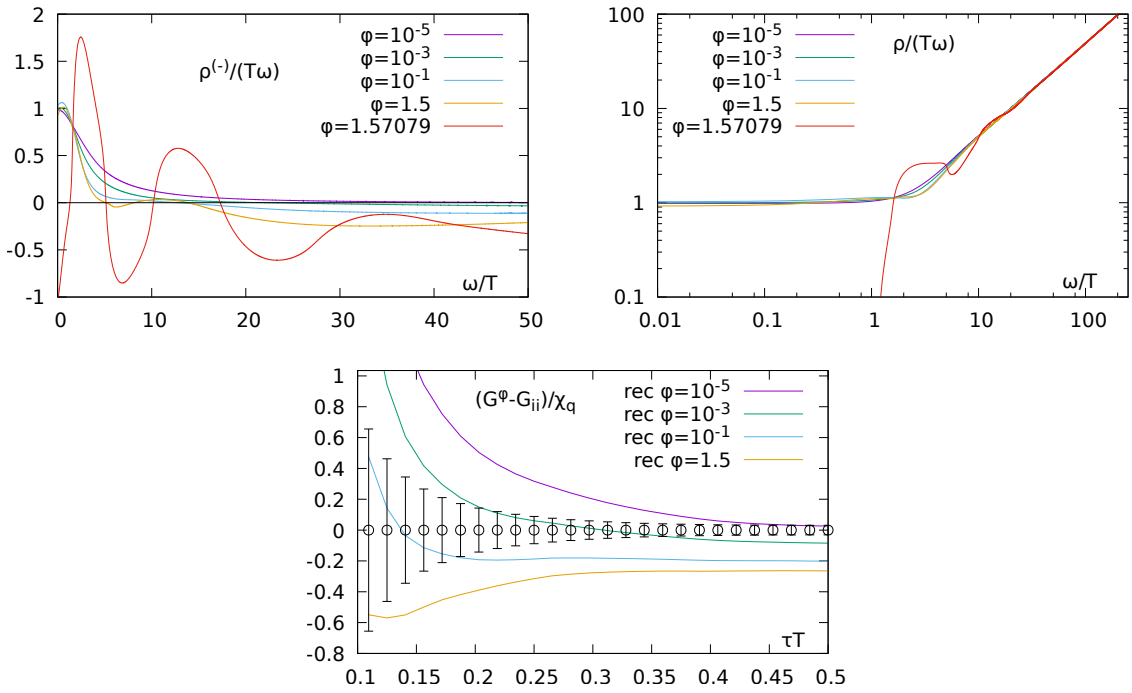

Figure 7.15: *Top left*: The difference $\rho^{(-)}(\bar{\omega}) = \rho(\bar{\omega}) - \rho_{\text{vacuum}}(\bar{\omega})$. Note the relatively small modifications for moderate choices of ϕ. *Top right and bottom*: The solution $\rho(\bar{\omega})$ and its reconstructed correlators.

spectral functions accordingly works well, compared to *case 1*, see Fig. 7.16 (*bottom*) and Fig. 7.15 (*bottom*). However, in both cases the reconstruction depends stronger on the regularization parameter ϕ than in *case 2*, and particularly, in *case 3* this dependence is slightly stronger than in *case 4*.

In order to make a definite choice of the regularization parameter, minimizing (7.48) can find the best ϕ in both cases, resulting in the parameters presented in Tab. 7.7. We furthermore plot the tradeoff curves, or L-curves, which display the balance between variance and resolution, in Fig. 7.17 (*top left*). Note that these tradeoff curves are valid for *case 1*, *case 3* and *case 4*, because they all share the same solution vectors $\vec{q}(\bar{\omega})$, as shown in equation (7.49). Marked in the four curves, which correspond to

Scheme	ϕ	χ^2/dof
K_1 & $(G_{ii} - G_{\text{vac}})$	0.084	0.042
K_1 & $(G_{ii} - G_{\text{thermal}})$	0.076	0.009

Table 7.7: The best ϕ for *case 3* and *case 4*, obtained by fitting the correlator reconstruction to the input data, under the restriction of the global minimization prescription (7.47).

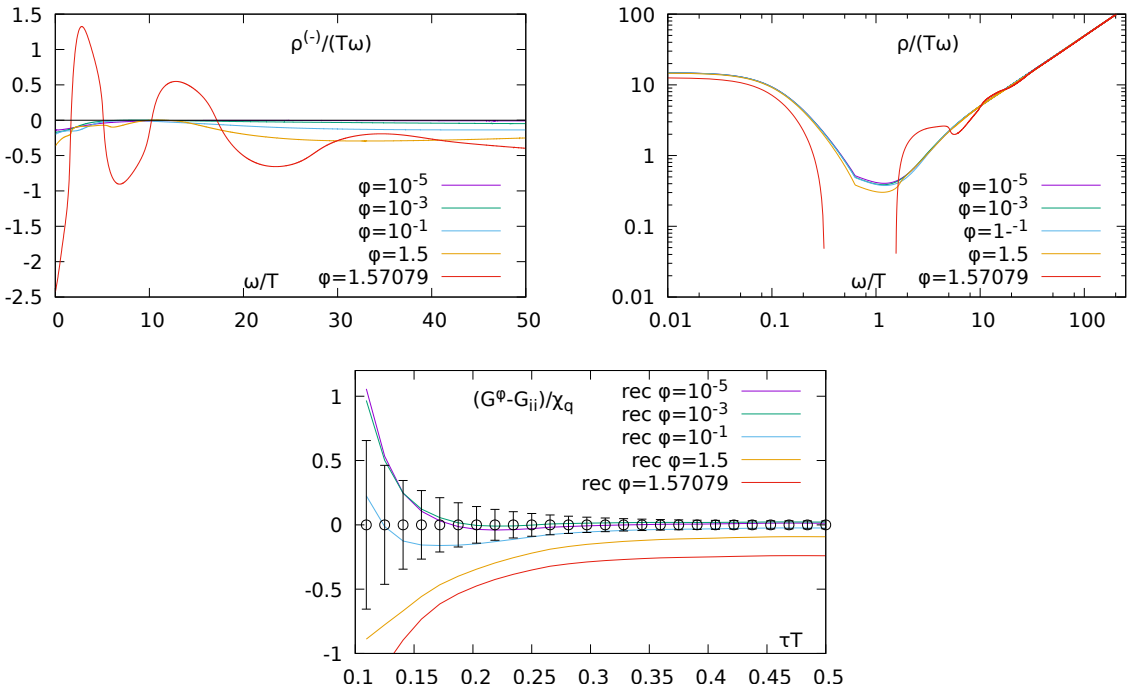

Figure 7.16: *Top left*: The difference $\rho^{(-)}(\bar{\omega}) = \rho(\bar{\omega}) - \rho_{\text{thermal}}(\bar{\omega})$. Note the relatively small modifications for moderate choices of ϕ. *Top right and bottom*: The solution $\rho(\bar{\omega})$ and its reconstructed correlators.

$\bar{\omega} = 0,\ 1,\ 2,\ 3$, are the points that result from several choices of the local regularization parameter $\theta(\bar{\omega})$, fixed by the global parameter ϕ. The violet filled triangle corresponds to the best ϕ of *case 3*, found above, and indeed lies for all $\bar{\omega}$ close to the kink of the tradeoff curve. Note how the tradeoff curves at different $\bar{\omega}$ vary in shape. In order to assess this effect in more detail, we plot the found parameterizations $\theta(\bar{\omega})$ for a range of increasing $\phi = 10^{-5}, 10^{-3}, 8.4 \cdot 10^{-2}, 10^{-1}, 1.57079$, from top to bottom, as black lines in Fig. 7.17 (*top right*). The y-axis denotes the exponent of the local regularization parameter θ in base 10, i.e. $y = -3 \leftrightarrow \theta = 10^{-3}$. Color coded in this plot is the variance $\text{Var}(\theta, \bar{\omega})$, which shows an intriguing structure of 'valleys' with a low variance, for small $\bar{\omega}$ and small θ. At larger frequencies, these valleys disappear and the variance is almost a constant in $\bar{\omega}$ for fixed θ. It can be seen that the found curves $\theta(\bar{\omega})$ follow this structure at lower frequencies, and flatten out for larger frequencies. The same plot, but with the spread $\mathcal{A}$ color coded in the background, is shown in Fig. 7.17 (*bottom*), featuring a quite similar structure overall. Note how the spread inevitably increases at large frequencies, which shows the loss of resolution in that region, which is worse for a more regularized solution. Together with the corresponding plot for the variance, the tradeoff that has to be made between spread and variance becomes explicit in the plots. The course of $\theta(\bar{\omega})$ is characterized by the global minimization prescription (7.47), which we chose in the beginning of this study, inspired by the typical treatment of ill-posed problems in the framework of Tikhonov regularization. However, instead of looking for

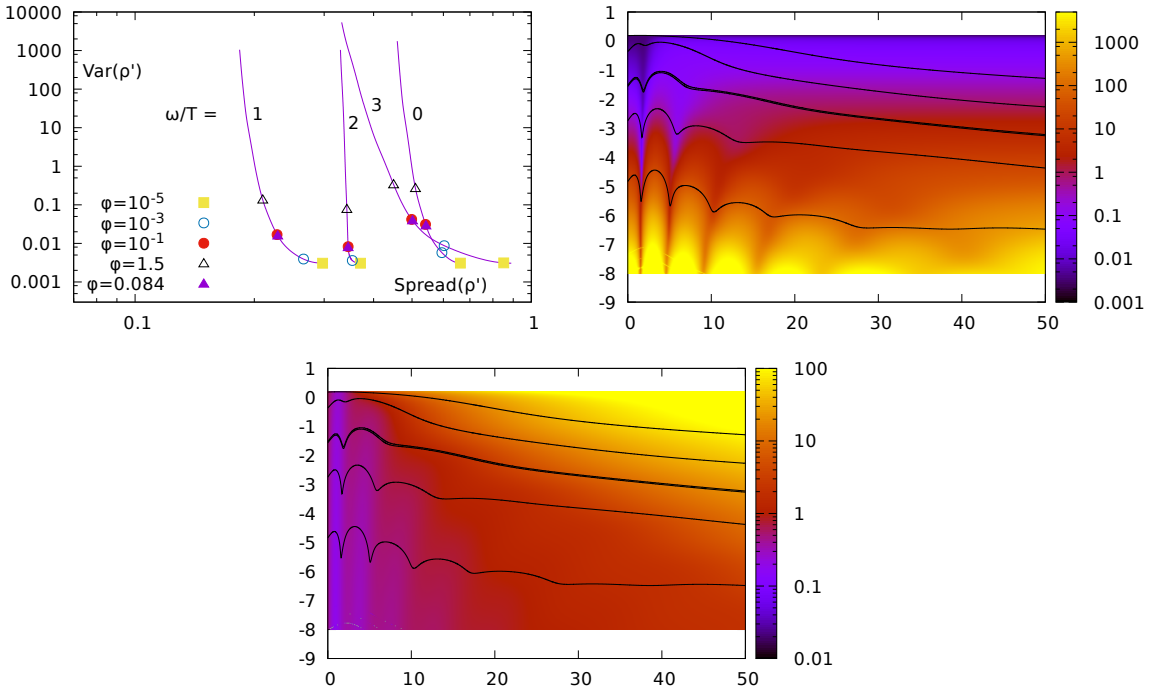

Figure 7.17: *Top left*: The tradeoff curves for $\bar{\omega} = 0,\ 1,\ 2$ and 3. Note how the curves shift with $\bar{\omega}$. *Top right*: The local regularization parameter θ as a function of $\bar{\omega}$. Color coded in the background is the corresponding statistical variance $\mathcal{B}$. *Bottom*: The same plots, with the spread $\mathcal{A}$ color coded in the background. Note how the spread is inevitably becoming large for large $\bar{\omega}$.

the corresponding kink in the L-curve, these plots suggest other choices to fix $\theta(\bar{\omega})$. For example, one could take $\theta = \text{const}_{\bar{\omega}}$, or fix $\theta(\bar{\omega})$ to be a line of either constant variance or constant spread.

7.3.3 Conclusion and comparison to the fit procedure

The method of Backus and Gilbert is applied to the continuum extrapolated correlator data set $G_{ii}(\tau T)$ at $T = 1.1T_c$, making four different choices of Kernels and/or utilizing perturbative additional input. A definite choice for the local regularization parameter $\theta(\bar{\omega})$ is made by minimizing, for all $\bar{\omega}$ at once, the squared sum of spread and statistical variance via one global regularization parameter ϕ. The perturbative input has no influence on the covariance of the data, and thus the spread and variance only depend on the kernel used. For both used kernels, we measure the resolution at a specific choice of ϕ, and subsequently investigate the resulting spectral function $\rho/(\omega T)$ and its respective correlator reconstruction $G^{\phi}(\tau T)$. We find that using kernel K_1, without any additional information supplied, yields no unambiguous solution $\rho/(\omega T)$ due to a strong loss of resolution at higher frequencies, and thus no reliable correlator reconstruction.

Using kernel K_2 without additional input and kernel K_1 with two kinds of perturbative input, respectively, we find overall much better correlator reconstructions. The additive perturbative inputs fix the large frequency behavior by construction, and the method of Backus and Gilbert is found to merely provide corrections to the respective perturbative spectral function. The fact that these corrections are small for large frequencies suggests to focus on the low frequency region in this case. From here, we now refer to the solution to *case n* as ρ_n for clarity. Providing only the kernel K_2 also shows to improve the spectral function $\rho_2/(\omega T)$ at large frequencies compared to $\rho_1/(\omega T)$, but suffers from the loss of resolution more directly compared to fixing the large frequency region with additive input. In the region of small $\bar{\omega}$, we find good qualitative agreement between the behavior of $\rho_3/(\omega T)$ and $\rho_2/(\omega T)$, which both reproduce a flat region with a finite intercept. The solution $\rho_4/(\omega T)$ shows a slight reduction of the input peak at low frequencies, and because $\rho_3/(\omega T)$ and $\rho_4/(\omega T)$ still show a vastly different low frequency behavior, we conclude that there is a very strong dependence of the solution on the details of the additional input information. The investigation of L-curves, for single frequencies, and planes of spread and variance, as a function of θ and $\bar{\omega}$, eludicates the tradeoff aspect of the method, with respect to the possible choices of the mapping $\theta(\bar{\omega})$.

We now turn to comparing the results of this section to the results from the fit procedure conducted in Sec. 7.2. In Fig. 7.18 (*right*) the solutions of the Breit-Wigner ansatz $\rho_{\text{ans}}/(\omega T)$ and the Ansatz $\rho_{\text{flat}}/(\omega T)$ from the fit procedure are plotted as their respective errorbands. Additionally, we plot the solutions $\rho_3/(\omega T)$ and $\rho_4/(\omega T)$, with ϕ taken according to Tab. 7.7, and their respective errorbands computed via (7.46). It is clearly visible how the statistical error of $\rho_4/(\omega T)$ becomes very small for $\bar{\omega} \to 0$, which indicates how strongly the perturbative input fixes the result in this case. The solution $\rho_3/(\omega T)$ is qualitatively comparable to $\rho_{\text{flat}}/(\omega T)$, but has a smaller intercept at $\omega/T = 0$ and lies overall lower for $\omega/T \lesssim 1$. The differently shaped spectral functions

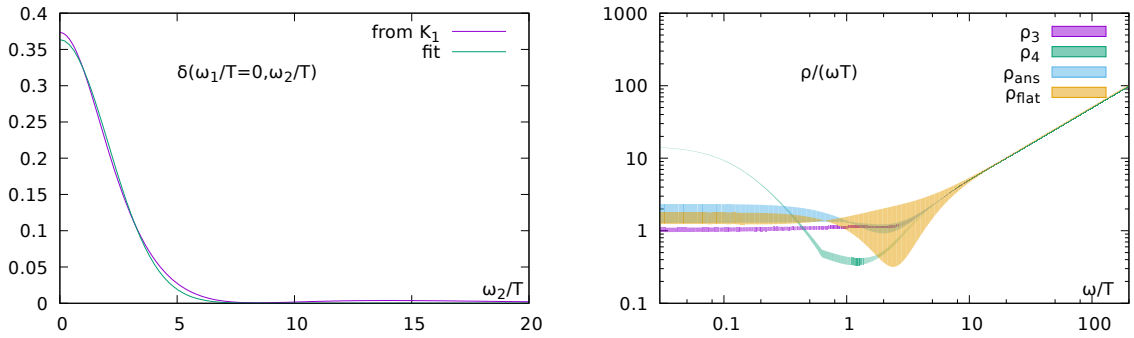

Figure 7.18: *Left*: A gaussian fit to the resolution function for kernel K_1. *Right*: A comparison of $\rho_3/(\omega T)$, $\rho_4/(\omega T)$ and the fit results $\rho_{\text{ans}}/(\omega T)$ and $\rho_{\text{flat}}/(\omega T)$.

in this plot, which all constitute valid solutions to the Fredholm equation, illustrate how difficult it is to fix the exact shape in the low frequency region. However, in the fit procedure, Ansaetze with a deliberately different low frequency region were chosen to

assess the resolution of the procedure, but the Backus Gilbert Method provides us with a direct, and measurable, expression of the resolution. To investigate the resolution in the low frequency region in a more precise fashion, we measure of the width of the resolution peak. We choose to fit a gaussian $g(\bar{\omega}) = A \exp(-\bar{\omega}^2/b^2)$ to the peak at $\bar{\omega}_1 = 0$ for kernel K_1, see Fig. 7.18 (*left*). Although the shape of the peak is not so well described by a gaussian, we take the resulting width $b \approx 3T$ as an approximate measure of resolution in the low frequency region. From the plots of our solutions $\rho/(\omega T)$ we see that the high frequency behavior, characterized by the free and the perturbative solutions, respectively, effectively sets in around $\omega/T \gtrsim 3$. Because in the fit procedure we come to the same result by investigating the effect of the sum rule on the spectral functions resulting from the fit, we confirm the limited resolution around $\bar{\omega} = 0$ using the Backus Gilbert method.

8 Summary and conclusions

In this work we studied the in-medium modification of hadronic correlation functions and determined spectral and transport properties from meson operators containing different quark flavors, from degenerate light, strange and charmed mesons as well as open-charm.

We presented results from phenomenological computations to formulate our expectations of spectral functions from in-medium mesons in general, and to shape a picture of the qualitative change of in-medium spectral functions from the corresponding non-interacting spectral functions. The existing computations of the latter for hidden flavor were extended to account for open flavor, i.e. non-degenerate quark masses, in the continuum and in the Wilson fermion formulation. The computed expression for the non-interacting open flavor meson spectral functions shows that a structure at small, but distinctly finite, frequency appears. This is, in the relevant channels, shown to constitute the corresponding zero mode in the limit of degenerate quark masses. We motivated Ansaetze for the vector meson spectral function to fit to the vector correlators in the light quark sector, featuring both the typical shapes resulting from a hydrodynamical description at strong coupling, as well as a quasiparticle description at weak coupling.

At temperatures in the deconfined phase the vector correlators in the light quark sector do not contain any bound state contributions and the corresponding spectral functions show a perturbative-like behavior already at moderate frequencies. Using continuum extrapolated correlators in the quenched approximation at vanishing momentum, this enables us to determine a continuum estimate of the dilepton rate, the soft photon rate, the electrical conductivity, and also, for the first time, their temperature dependence in the range between $1.1T_c$ and $1.4T_c$. Continuum extrapolations can be, and have been, performed at non vanishing momentum, for the first time giving rise to the photon rate at larger frequencies from continuum extrapolated lattice data, and are a part of future work. The continuum extrapolated vector current data exhibit almost no temperature dependence, and the fits to the latter show the difficulties of fixing the low frequency behavior of the spectral function. Although we measurably enhanced the resolution by performing fully correlated fits, and the use of second thermal moments provides valuable additional information, both the peaked low frequency region, motivated by a quasiparticle description, and flat low frequency region, motivated by hydrodynamical considerations, turn out to reproduce the input correlator data equally well. However, the resulting width of the peaked solutions is $\Gamma/2 \sim \mathcal{O}(T)$, and thus parametrically large enough to still hint at a rather strongly coupled plasma in the investigated temperature region. Utilizing perturbative input for the large frequency region shows to potentially reduce the number of parameters needed in our Ansatz. At all temperatures we compute

the electrical conductivity, the dilepton rate and the soft photon rate. The method of Backus and Gilbert confirms the difficulties of fixing the small frequency shape of the spectral function in a twofold way. First, we retrieve both peaked and flat solutions from the method, depending on the input information, and second, the method yields a quantitative estimate of its resolution in the low frequency region, which we find to be $\Delta\omega = 3T$ around vanishing frequency. This is in accord with our findings from the fitted spectral functions, inserted into a low frequency sum rule.

Using these different Ansaetze and analyses we were able to reliably estimate the systematic uncertainties of the electric conductivity, dilepton and soft-photons rates in this temperature regime. Although still based on the quenched approximation, these results and the methodology elaborated here will serve as important foundations for future studies including dynamical fermions, where a continuum extrapolation so far is out of reach, but may be possible with future computing resources. The mild temperature dependence observed in this study may be related to the quenched approximation where the deconfinement transition is of first order and effects of this transition turn in very close to T_c. This may change when including light dynamical degrees of freedom. Close to the transition region, one could expect that these will become important and furthermore the transition changes from first order to a cross-over for physical quark masses.

In the heavy quark sector, it is expected that bound states survive in the QGP and for charmonium and bottomonium states, one expects a sequential melting pattern. The interesting temperature region for the melting of charmonia is between $1.0T_c$ and $1.5T_c$. A further important topic concerns strange mesons and open-charm mesons and the question about their thermal modifications around the transition region and if they are melted already within this region. As the present study was performed at temperatures of $0.95T_c$ and $1.11T_c$, i.e. very close below and above the transition region, dynamical light quark degrees of freedom are important and we used gauge field configurations generated with physical $2 + 1$ HISQ flavors for this study, together with corresponding zero temperature calculations. Although limited to one lattice size, this combination allowed to study the medium modifications of spatial correlation functions and screening masses, as well as the modification of temporal correlators using the ratio G/G_{rec}, which effectively removes most cutoff effects, and allows for a qualitative discussion of modifications of bound states and the spectral and transport properties in this sector in comparison to the vacuum. We use a standard Wilson action on top of the HISQ sea to compute meson correlation functions, and yet the extracted screening correlation functions are very comparable to earlier computations using HISQ sea and valence quarks on slightly smaller lattices. The screening correlators turn indeed out to be very sensitive to in-medium effects, especially when compared to the temporal correlation functions. For strange and strange-charm flavored mesons this indicates strong bound state modifications already in the transition region. The screening masses extracted at both temperatures show differences compared to the pure HISQ study, which are especially strong in the case of charmonium. This might indicate that the used lattices are

yet too coarse to perform charmonium spectroscopy, or effects coming from our Wilson-on-HISQ approach. However, apart from a shift, the extracted screening masses of the S-wave channel with all flavor contents show the expected behavior in the transition region. The analysis of temporal correlation functions shows overall much smaller modifications above T_c, but still we find signs for appearing zero mode contributions in all relevant investigated mesons, and a modification of bound states for the S-wave channels of strange and strange-charmed correlators already slightly above T_c.

As an outlook, we propose to increase the statistics of the open flavor mesons on the dynamical lattices to reduce the statistical error, from which especially the study of G/G_{rec} would profit, and also include the quark line disconnected contribution to the correlators, as soon as the statistics is high enough. Complementary to that, it is important to gain a more refined understanding of the lattice spacing artifacts, as well as the systematical effects that arise from the Wilson-on-HISQ approach. The former can be reduced by utilizing improvements of the valence quark action, possibly by determining c_{sw} in non-perturbative lattice calculations for this specific setup. The latter is one aspect of cutoff errors in general, and comparisons to correlation functions at both vanishing and finite temperature, as well as corresponding (screening) masses, computed on the same gauge field background with HISQ valence quarks, can lead to a quantitative understanding of the effects induced by the mixing of different actions. Such a study is underway. With an understanding of these effects at hand, computations at smaller lattice spacings, and subsequently continuum extrapolations of the extracted correlation functions, become possible.

Bibliography

[1] K. A. Olive et al. "Review of Particle Physics". In: *Chin. Phys.* C38 (2014), p. 090001. DOI: 10.1088/1674-1137/38/9/090001.

[2] Serguei Chatrchyan et al. "Observation of a new boson at a mass of 125 GeV with the CMS experiment at the LHC". In: *Phys. Lett.* B716 (2012), pp. 30–61. DOI: 10.1016/j.physletb.2012.08.021. arXiv: 1207.7235 [hep-ex].

[3] Adrian Cho. "Higgs Boson Makes Its Debut After Decades-Long Search". In: *Science* 337.6091 (2012), pp. 141–143. ISSN: 0036-8075. DOI: 10.1126/science.337.6091.141. eprint: http://science.sciencemag.org/content/337/6091/141.full.pdf. URL: http://science.sciencemag.org/content/337/6091/141.

[4] Wikipedia (User: Laurascudder). *Eightfold Way (physics)*. [Online; accessed 20-Feb-2016; under CC BY-SA 3.0]. 2007. URL: https://en.wikipedia.org/wiki/Eightfold_Way_(physics).

[5] Murray Gell-Mann. "The Eightfold Way: A Theory of strong interaction symmetry". In: (1961). DOI: 10.2172/4008239.

[6] C. Gattringer and C. Lang. *Quantum Chromodynamics on the Lattice: An Introductory Presentation*. Lecture Notes in Physics. Springer Berlin Heidelberg, 2009. ISBN: 9783642018497.

[7] Maarten Golterman. "Applications of chiral perturbation theory to lattice QCD". In: *Modern perspectives in lattice QCD: Quantum field theory and high performance computing. Proceedings, International School, 93rd Session, Les Houches, France, August 3-28, 2009*. 2009, pp. 423–515. arXiv: 0912.4042 [hep-lat]. URL: http://inspirehep.net/record/840837/files/arXiv:0912.4042.pdf.

[8] H.J. Rothe. *Lattice Gauge Theories: An Introduction*. EBSCO ebook academic collection. World Scientific, 2005. ISBN: 9789812560629.

[9] I. Montvay and G. Münster. *Quantum Fields on a Lattice*. Cambridge Monographs on Mathematical Physics. Cambridge University Press, 1997. ISBN: 978052 1599177.

[10] Yuri L. Dokshitzer. "Calculation of the Structure Functions for Deep Inelastic Scattering and e+ e- Annihilation by Perturbation Theory in Quantum Chromodynamics." In: *Sov. Phys. JETP* 46 (1977). [Zh. Eksp. Teor. Fiz.73,1216(1977)], pp. 641–653.

[11] M.E. Peskin and D.V. Schroeder. *An Introduction to Quantum Field Theory*. Advanced book classics. Addison-Wesley Publishing Company, 1995. ISBN: 9780201503975.

[12] Harvey B. Meyer. "Transport Properties of the Quark-Gluon Plasma: A Lattice QCD Perspective". In: *Eur.Phys.J.* A47 (2011), p. 86. DOI: 10.1140/epja/i2011-11086-3. arXiv: 1104.3708 [hep-lat].

[13] Johann Rafelski. "Connecting QGP-Heavy Ion Physics to the Early Universe". In: (2013). [Nucl. Phys. Proc. Suppl.243-244,155(2013)]. DOI: 10.1016/j.nuclphysbps.2013.09.017. arXiv: 1306.2471 [astro-ph.CO].

[14] Miklos Gyulassy. "The QGP discovered at RHIC". In: *Structure and dynamics of elementary matter. Proceedings, NATO Advanced Study Institute, Camyuva-Kemer, Turkey, September 22-October 2, 2003*. 2004, pp. 159–182. arXiv: nucl-th/0403032 [nucl-th].

[15] Schäfer, Thomas and Teaney, Derek. "Nearly Perfect Fluidity: From Cold Atomic Gases to Hot Quark Gluon Plasmas". In: *Rept. Prog. Phys.* 72 (2009), p. 126001. DOI: 10.1088/0034-4885/72/12/126001. arXiv: 0904.3107 [hep-ph].

[16] Derek A. Teaney. "Viscous Hydrodynamics and the Quark Gluon Plasma". In: (2009). arXiv: 0905.2433 [nucl-th].

[17] Helmut Satz. "Charm and beauty in a hot environment". In: *Sense of Beauty in Physics: Miniconference in Honor of Adriano Di Giacomo on his 70th Birthday Pisa, Italy, January 26-27, 2006*. 2006. arXiv: hep-ph/0602245 [hep-ph].

[18] Heng-Tong Ding, Frithjof Karsch, and Swagato Mukherjee. "Thermodynamics of strong-interaction matter from Lattice QCD". In: *Int. J. Mod. Phys.* E24.10 (2015), p. 1530007. DOI: 10.1142/S0218301315300076. arXiv: 1504.05274 [hep-lat].

[19] F. Karsch and E. Laermann. "Thermodynamics and in medium hadron properties from lattice QCD". In: (2003). arXiv: hep-lat/0305025 [hep-lat].

[20] Juhee Hong and Derek Teaney. "Spectral densities for hot QCD plasmas in a leading log approximation". In: *Phys.Rev.* C82 (2010), p. 044908. DOI: 10.1103/PhysRevC.82.044908. arXiv: 1003.0699 [nucl-th].

[21] M. Laine, A. Vuorinen, and Y. Zhu. "Next-to-leading order thermal spectral functions in the perturbative domain". In: *JHEP* 09 (2011), p. 084. DOI: 10.1007/JHEP09(2011)084. arXiv: 1108.1259 [hep-ph].

[22] Martin Luscher. "Advanced lattice QCD". In: *Probing the standard model of particle interactions. Proceedings, Summer School in Theoretical Physics, NATO Advanced Study Institute, 68th session, Les Houches, France, July 28-September 5, 1997. Pt. 1, 2*. 1998, pp. 229–280. arXiv: hep-lat/9802029 [hep-lat]. URL: http://alice.cern.ch/format/showfull?sysnb=0270921.

[23] Martin Luscher et al. "Chiral symmetry and O(a) improvement in lattice QCD". In: *Nucl. Phys.* B478 (1996), pp. 365–400. DOI: 10.1016/0550-3213(96)00378-1. arXiv: hep-lat/9605038 [hep-lat].

[24] B. Sheikholeslami and R. Wohlert. "Improved continuum limit lattice action for QCD with Wilson fermions". In: *Nuclear Physics B* 259.4 (1985), pp. 572 – 596. ISSN: 0550-3213. DOI: http://dx.doi.org/10.1016/0550-3213(85)90002-1. URL: http://www.sciencedirect.com/science/article/pii/0550321385900021.

[25] M. Luscher and P. Weisz. "O(a) improvement of the axial current in lattice QCD to one loop order of perturbation theory". In: *Nucl. Phys.* B479 (1996), pp. 429–458. DOI: 10.1016/0550-3213(96)00448-8. arXiv: hep-lat/9606016 [hep-lat].

[26] Martin Luscher et al. "Nonperturbative O(a) improvement of lattice QCD". In: *Nucl.Phys.* B491 (1997), pp. 323–343. DOI: 10.1016/S0550-3213(97)00080-1. arXiv: hep-lat/9609035 [hep-lat].

[27] Karl Jansen and Rainer Sommer. "O(a) improvement of lattice QCD with two flavors of Wilson quarks". In: *Nucl. Phys.* B530 (1998). [Erratum: Nucl. Phys.B643,517(2002)], pp. 185–203. DOI: 10.1016/S0550-3213(98)00396-4. arXiv: hep-lat/9803017 [hep-lat].

[28] N. Yamada et al. "Non-perturbative O(a)-improvement of Wilson quark action in three-flavor QCD with plaquette gauge action". In: *Phys. Rev.* D71 (2005), p. 054505. DOI: 10.1103/PhysRevD.71.054505. arXiv: hep-lat/0406028 [hep-lat].

[29] G. Peter Lepage and Paul B. Mackenzie. "On the viability of lattice perturbation theory". In: *Phys. Rev.* D48 (1993), pp. 2250–2264. DOI: 10.1103/PhysRevD.48.2250. arXiv: hep-lat/9209022 [hep-lat].

[30] T. DeGrand and C. DeTar. *Lattice Methods for Quantum Chromodynamics*. World Scientific, 2006. ISBN: 9789812567277.

[31] Holger Bech Nielsen and M. Ninomiya. "No Go Theorem for Regularizing Chiral Fermions". In: *Phys. Lett.* B105 (1981), p. 219. DOI: 10.1016/0370-2693(81)91026-1.

[32] Zoltan Fodor and Christian Hoelbling. "Light Hadron Masses from Lattice QCD". In: *Rev. Mod. Phys.* 84 (2012), p. 449. DOI: 10.1103/RevModPhys.84.449. arXiv: 1203.4789 [hep-lat].

[33] E. Follana et al. "Highly improved staggered quarks on the lattice, with applications to charm physics". In: *Phys. Rev.* D75 (2007), p. 054502. DOI: 10.1103/PhysRevD.75.054502. arXiv: hep-lat/0610092 [hep-lat].

[34] David H. Adams. "The Rooting issue for a lattice fermion formulation similar to staggered fermions but without taste mixing". In: *Phys. Rev.* D77 (2008), p. 105024. DOI: 10.1103/PhysRevD.77.105024. arXiv: 0802.3029 [hep-lat].

[35] A. Bazavov et al. "Strangeness at high temperatures: from hadrons to quarks". In: *Phys. Rev. Lett.* 111 (2013), p. 082301. DOI: 10.1103/PhysRevLett.111.082301. arXiv: 1304.7220 [hep-lat].

[36] A. Bazavov et al. "The chiral and deconfinement aspects of the QCD transition". In: *Phys. Rev.* D85 (2012), p. 054503. DOI: 10.1103/PhysRevD.85.054503. arXiv: 1111.1710 [hep-lat].

[37] F. Karsch et al. "Signatures of charmonium modification in spatial correlation functions". In: *Phys. Rev.* D85 (2012), p. 114501. DOI: 10.1103/PhysRevD.85.114501. arXiv: 1203.3770 [hep-lat].

[38] J. J. Binney et al. *The Theory of Critical Phenomena: An Introduction to the Renormalization Group*. New York, NY, USA: Oxford University Press, Inc., 1992. ISBN: 0198513933, 9780198513933.

[39] H. Satz. *Extreme States of Matter in Strong Interaction Physics: An Introduction*. Lecture Notes in Physics. Springer Berlin Heidelberg, 2012. ISBN: 9783642239083.

[40] David J. Gross and Frank Wilczek. "Ultraviolet Behavior of Non-Abelian Gauge Theories". In: *Phys. Rev. Lett.* 30 (26 1973), pp. 1343–1346. DOI: 10.1103/PhysRevLett.30.1343. URL: http://link.aps.org/doi/10.1103/PhysRevLett.30.1343.

[41] Martin Luscher et al. "Nonperturbative determination of the axial current normalization constant in O(a) improved lattice QCD". In: *Nucl.Phys.* B491 (1997), pp. 344–364. DOI: 10.1016/S0550-3213(97)00087-4. arXiv: hep-lat/9611015 [hep-lat].

[42] M.L. Bellac. *Thermal Field Theory*. Cambridge Monographs on Mathematical Physics. Cambridge University Press, 2000. ISBN: 9780521654777.

[43] N. Cabibbo and E. Marinari. "A New Method for Updating SU(N) Matrices in Computer Simulations of Gauge Theories". In: *Phys. Lett.* B119 (1982), pp. 387–390. DOI: 10.1016/0370-2693(82)90696-7.

[44] A. D. Kennedy and B. J. Pendleton. "Improved Heat Bath Method for Monte Carlo Calculations in Lattice Gauge Theories". In: *Phys. Lett.* B156 (1985), pp. 393–399. DOI: 10.1016/0370-2693(85)91632-6.

[45] Michael Creutz. "Overrelaxation and Monte Carlo simulation". In: *Phys. Rev. D* 36 (2 1987), pp. 515–519. DOI: 10.1103/PhysRevD.36.515. URL: http://link.aps.org/doi/10.1103/PhysRevD.36.515.

[46] A. D. Kennedy. "Algorithms for dynamical fermions". In: (2006). arXiv: hep-lat/0607038 [hep-lat].

[47] S. Duane et al. "Hybrid Monte Carlo". In: *Phys.Lett.* B195 (1987), pp. 216–222.

[48] M. A. Clark and A. D. Kennedy. "The RHMC algorithm for two flavors of dynamical staggered fermions". In: *Nucl. Phys. Proc. Suppl.* 129 (2004). [,850(2003)], pp. 850–852. DOI: 10.1016/S0920-5632(03)02732-4. arXiv: hep-lat/0309084 [hep-lat].

[49] MILC collaboration. URL: http://physics.indiana.edu/~sg/milc.html.

[50] Constantia Alexandrou. "Selected results on hadron structure using state-of-the-art lattice QCD simulations". In: *45th International Symposium on Multiparticle Dynamics (ISMD 2015) Kreuth, Germany, October 4-9, 2015*. 2015. arXiv: 1512.03924 [hep-lat]. URL: http://inspirehep.net/record/1409500/files/arXiv:1512.03924.pdf.

[51] C. B. Lang. "Hadron Structure and Spectrum from the Lattice". In: 2015. arXiv: 1512.05545 [nucl-th]. URL: http://inspirehep.net/record/1410092/files/arXiv:1512.05545.pdf.

[52] N. Brambilla et al. "Heavy quarkonium: progress, puzzles, and opportunities". In: *Eur. Phys. J.* C71 (2011), p. 1534. DOI: 10.1140/epjc/s10052-010-1534-9. arXiv: 1010.5827 [hep-ph].

[53] Liuming Liu et al. "Excited and exotic charmonium spectroscopy from lattice QCD". In: *JHEP* 07 (2012), p. 126. DOI: 10.1007/JHEP07(2012)126. arXiv: 1204.5425 [hep-ph].

[54] D. Griffiths. *Introduction to Elementary Particles*. Physics textbook. Wiley, 2008. ISBN: 9783527406012.

[55] Sasa Prelovsek. "Lattice QCD review of charmonium and open-charm spectroscopy". In: *Proceedings, 6th International Workshop on Charm Physics (Charm 2013)*. 2013. arXiv: 1310.4354 [hep-lat]. URL: http://inspirehep.net/record/1260560/files/arXiv:1310.4354.pdf.

[56] Christian Hoelbling. *Lecture 'Data Analysis'*. Lattice Practices, Zeuthen, 2012.

[57] Christian Hoelbling. "Lattice QCD: concepts, techniques and some results". In: *Acta Phys. Polon.* B45.12 (2014), p. 2143. DOI: 10.5506/APhysPolB.45.2143. arXiv: 1410.3403 [hep-lat].

[58] Christopher Michael and A. McKerrell. "Fitting correlated hadron mass spectrum data". In: *Phys. Rev.* D51 (1995), pp. 3745–3750. DOI: 10.1103/PhysRevD.51.3745. arXiv: hep-lat/9412087 [hep-lat].

[59] L. Levkova and C. DeTar. "Charm annihilation effects on the hyperfine splitting in charmonium". In: *Phys. Rev.* D83 (2011), p. 074504. DOI: 10.1103/PhysRevD.83.074504. arXiv: 1012.1837 [hep-lat].

[60] Alexei Bazavov et al. "In-medium modifications of open and hidden strange-charm mesons from spatial correlation functions". In: *Phys. Rev.* D91.5 (2015), p. 054503. DOI: 10.1103/PhysRevD.91.054503. arXiv: 1411.3018 [hep-lat].

[61] R. Rapp, J. Wambach, and H. van Hees. "The Chiral Restoration Transition of QCD and Low Mass Dileptons". In: *Landolt-Bornstein* 23 (2010), p. 134. DOI: 10.1007/978-3-642-01539-7_6. arXiv: 0901.3289 [hep-ph].

[62] Edward V. Shuryak and O. V. Zhirov. "Is the Explosion of a Quark - Gluon Plasma Found?" In: *Phys. Lett.* B171 (1986), pp. 99–102. DOI: 10.1016/0370-2693(86)91006-3.

[63] T. Matsui and H. Satz. "J/ψ Suppression by Quark-Gluon Plasma Formation". In: *Phys. Lett.* B178 (1986), p. 416. DOI: 10.1016/0370-2693(86)91404-8.

[64] K. Yagi, T. Hatsuda, and Y. Miake. *Quark Gluon Plasma. From Big Bang to Little Bang*. Cambridge University Press, 2005.

[65] C. Y. Wong. *Introduction to high-energy heavy ion collisions*. 1995.

[66] J. Cleymans. "Maximal Net Baryon Density in the Energy Region Covered by NICA". In: *Phys. Part. Nucl. Lett.* 8 (2011), pp. 797–800. DOI: 10.1134/S154747711108007 arXiv: 1005.4114 [nucl-th].

[67] Peter Senger. "The Compressed Baryonic Matter Experiment at FAIR". In: *JPS Conf. Proc.* 8 (2015), p. 022001. DOI: 10.7566/JPSCP.8.022001.

[68] Miklos Gyulassy et al. "Jet quenching and radiative energy loss in dense nuclear matter". In: (2003). arXiv: nucl-th/0302077 [nucl-th].

[69] R. Rapp and J. Wambach. "Chiral symmetry restoration and dileptons in relativistic heavy ion collisions". In: *Adv. Nucl. Phys.* 25 (2000), p. 1. DOI: 10.1007/0-306-47101-9_1. arXiv: hep-ph/9909229 [hep-ph].

[70] Heng-Tong Ding. "Hard and thermal probes of QGP from the perspective of Lattice QCD". In: *Nucl. Phys.* A932 (2014), pp. 500–507. DOI: 10.1016/j.nuclphysa.2014.08.066. arXiv: 1404.5134 [hep-lat].

[71] Heng-Tong Ding. "Thermodynamics of heavy-light hadrons". In: *PoS* LATTICE2014 (2014), p. 184. arXiv: 1412.5735 [hep-lat].

[72] L. D. McLerran and T. Toimela. "Photon and dilepton emission from the quark-gluon plasma: Some general considerations". In: *Phys. Rev. D* 31 (3 1985), pp. 545–563. DOI: 10.1103/PhysRevD.31.545. URL: http://link.aps.org/doi/10.1103/PhysRevD.31.545.

[73] Guy D. Moore and Jean-Marie Robert. "Dileptons, spectral weights, and conductivity in the quark-gluon plasma". In: (2006). arXiv: hep-ph/0607172 [hep-ph].

[74] Agnes Mocsy, Peter Petreczky, and Michael Strickland. "Quarkonia in the Quark Gluon Plasma". In: *Int. J. Mod. Phys.* A28 (2013), p. 1340012. DOI: 10.1142/S0217751X13400125. arXiv: 1302.2180 [hep-ph].

[75] F. Karsch, D. Kharzeev, and H. Satz. "Sequential charmonium dissociation". In: *Phys. Lett.* B637 (2006), pp. 75–80. DOI: 10.1016/j.physletb.2006.03.078. arXiv: hep-ph/0512239 [hep-ph].

[76] F. Karsch and H. Satz. "The Spectral analysis of strongly interacting matter". In: *Z. Phys.* C51 (1991), pp. 209–224. DOI: 10.1007/BF01475790.

[77] M. Laine et al. "Real-time static potential in hot QCD". In: *JHEP* 03 (2007), p. 054. DOI: 10.1088/1126-6708/2007/03/054. arXiv: hep-ph/0611300 [hep-ph].

[78] A. Beraudo, J. P. Blaizot, and C. Ratti. "Real and imaginary-time Q anti-Q correlators in a thermal medium". In: *Nucl. Phys.* A806 (2008), pp. 312–338. DOI: 10.1016/j.nuclphysa.2008.03.001. arXiv: 0712.4394 [nucl-th].

[79] Yannis Burnier, Olaf Kaczmarek, and Alexander Rothkopf. "Quarkonium at finite temperature: Towards realistic phenomenology from first principles". In: *JHEP* 12 (2015), p. 101. DOI: 10.1007/JHEP12(2015)101. arXiv: 1509.07366 [hep-ph].

[80] J.I. Kapusta and C. Gale. *Finite-Temperature Field Theory: Principles and Applications*. Cambridge Monographs on Mathematical Physics. Cambridge University Press, 2006. ISBN: 9781139457620.

[81] H.-T. Ding. "Charmonium Correlation and Spectral Functions in Quenched Lattice QCD at Finite Temperature". PhD thesis. Bielefeld University, 2010.

[82] A. Francis. "Thermal Dilepton Rates from Quenched Lattice QCD". PhD thesis. Bielefeld University, 2011.

[83] Gert Aarts and Jose M. Martinez Resco. "Continuum and lattice meson spectral functions at nonzero momentum and high temperature". In: *Nucl.Phys.* B726 (2005), pp. 93–108. DOI: 10.1016/j.nuclphysb.2005.08.012. arXiv: hep-lat/0507004 [hep-lat].

[84] S. Stickan et al. "Free meson spectral functions on the lattice". In: *Nucl. Phys. Proc. Suppl.* 129 (2004). [,599(2003)], pp. 599–601. DOI: 10.1016/S0920-5632(03)02654-9. arXiv: hep-lat/0309191 [hep-lat].

[85] F. Karsch et al. "Infinite temperature limit of meson spectral functions calculated on the lattice". In: *Phys. Rev.* D68 (2003), p. 014504. DOI: 10.1103/PhysRevD.68.014504. arXiv: hep-lat/0303017 [hep-lat].

[86] D. B. Carpenter and C. F. Baillie. "Free Fermion Propagators and Lattice Finite Size Effects". In: *Nucl. Phys.* B260 (1985), p. 103. DOI: 10.1016/0550-3213(85)90312-8.

[87] P. A. Baikov, K. G. Chetyrkin, and Johann H. Kuhn. "Order alpha**4(s) QCD Corrections to Z and tau Decays". In: *Phys. Rev. Lett.* 101 (2008), p. 012002. DOI: 10.1103/PhysRevLett.101.012002. arXiv: 0801.1821 [hep-ph].

[88] Edward V. Shuryak. "Correlation functions in the QCD vacuum". In: *Rev. Mod. Phys.* 65 (1 1993), pp. 1–46. DOI: 10.1103/RevModPhys.65.1. URL: http://link.aps.org/doi/10.1103/RevModPhys.65.1.

[89] P. Resibois and M. de Leener. *Classical Kinetic Theory of Fluids*. A Wiley-interscience publication. John Wiley & Sons, 1977. ISBN: 9780608153704.

[90] Peter Petreczky and Derek Teaney. "Heavy quark diffusion from the lattice". In: *Phys. Rev.* D73 (2006), p. 014508. DOI: 10.1103/PhysRevD.73.014508. arXiv: hep-ph/0507318 [hep-ph].

[91] Peter Brockway Arnold and Laurence G. Yaffe. "Effective theories for real time correlations in hot plasmas". In: *Phys. Rev.* D57 (1998), pp. 1178–1192. DOI: 10.1103/PhysRevD.57.1178. arXiv: hep-ph/9709449 [hep-ph].

[92] Y. Burnier and M. Laine. "Massive vector current correlator in thermal QCD". English. In: *Journal of High Energy Physics* 2012.11 (2012). ArXiv ePrint: 1210.1064, pp. 1–26. DOI: 10.1007/JHEP11(2012)086.

[93] Eric Braaten and Robert D. Pisarski. "Soft Amplitudes in Hot Gauge Theories: A General Analysis". In: *Nucl.Phys.* B337 (1990), p. 569. DOI: 10.1016/0550-3213(90)90508-B.

[94] Eric Braaten, Robert D. Pisarski, and Tzu Chiang Yuan. "Production of soft dileptons in the quark-gluon plasma". In: *Phys. Rev. Lett.* 64 (19 1990), pp. 2242–2245. DOI: 10.1103/PhysRevLett.64.2242. URL: http://link.aps.org/doi/10.1103/PhysRevLett.64.2242.

[95] Y. Burnier and M. Laine. "Towards flavour diffusion coefficient and electrical conductivity without ultraviolet contamination". In: *Eur. Phys. J.* C72 (2012), p. 1902. DOI: 10.1140/epjc/s10052-012-1902-8. arXiv: 1201.1994 [hep-lat].

[96] T. Altherr and P. Aurenche. "Finite Temperature QCD Corrections to Lepton Pair Formation in a Quark - Gluon Plasma". In: *Z. Phys.* C45 (1989), p. 99. DOI: 10.1007/BF01556676.

[97] Derek Teaney. "Finite temperature spectral densities of momentum and R-charge correlators in N=4 Yang Mills theory". In: *Phys. Rev.* D74 (2006), p. 045025. DOI: 10.1103/PhysRevD.74.045025. arXiv: hep-ph/0602044 [hep-ph].

[98] Ofer Aharony et al. "Large N field theories, string theory and gravity". In: *Phys. Rept.* 323 (2000), pp. 183–386. DOI: 10.1016/S0370-1573(99)00083-6. arXiv: hep-th/9905111 [hep-th].

[99] Gert Aarts. "Transport and spectral functions in high-temperature QCD". In: *PoS* LAT2007 (2007), p. 001. arXiv: 0710.0739 [hep-lat].

[100] Juan Martin Maldacena. "The Large N limit of superconformal field theories and supergravity". In: *Int. J. Theor. Phys.* 38 (1999). [Adv. Theor. Math. Phys.2,231(1998)], pp. 1113–1133. DOI: 10.1023/A:1026654312961. arXiv: hep-th/9711200 [hep-th].

[101] M. Asakawa, T. Hatsuda, and Y. Nakahara. "Maximum entropy analysis of the spectral functions in lattice QCD". In: *Prog.Part.Nucl.Phys.* 46 (2001), pp. 459–508. DOI: 10.1016/S0146-6410(01)00150-8. arXiv: hep-lat/0011040 [hep-lat].

[102] P. de Forcrand et al. "Meson correlators in finite temperature lattice QCD". In: *Phys. Rev.* D63 (2001), p. 054501. DOI: 10.1103/PhysRevD.63.054501. arXiv: hep-lat/0008005 [hep-lat].

[103] Gert Aarts and Jose Maria Martinez Resco. "Transport coefficients, spectral functions and the lattice". In: *JHEP* 0204 (2002), p. 053. DOI: 10.1088/1126-6708/2002/04/053. arXiv: hep-ph/0203177 [hep-ph].

[104] Gert Aarts and Jose M. Martinez Resco. "Transport coefficients from the lattice?" In: *Nucl. Phys. Proc. Suppl.* 119 (2003). [,505(2002)], pp. 505–507. DOI: 10.1016/S0920-5632(03)01597-4. arXiv: hep-lat/0209033 [hep-lat].

[105] Per Christian Hansen. *Discrete Inverse Problems: Insight and Algorithms*. SIAM, 2010. ISBN: 0898716969, 9780898716962.

[106] Albert Tarantola. *Inverse Problem Theory and Methods for Model Parameter Estimation*. Philadelphia, PA, USA: Society for Industrial and Applied Mathematics, 2004. ISBN: 0898715725.

[107] A. Carpio et al. *Inverse Problems and Imaging: Lectures given at the C.I.M.E. Summer School held in Martina Franca, Italy, September 15-21, 2002*. Lecture Notes in Mathematics. Springer Berlin Heidelberg, 2009. ISBN: 9783540785477.

[108] William H. Press et al. *Numerical Recipes 3rd Edition: The Art of Scientific Computing*. 3rd ed. New York, NY, USA: Cambridge University Press, 2007. ISBN: 0521880688, 9780521880688.

[109] Charles W Groetsch. *The theory of Tikhonov regularization for Fredholm equations of the first kind*. Vol. 105. Pitman Advanced Publishing Program, 1984.

[110] O. Forster. *Analysis 3*. Analysis. Vieweg + Teubner, 2009. ISBN: 9783834807045.

[111] Per Christian Hansen. "Regularization Tools Version 4.0 for Matlab 7.3". In: *Numerical Algorithms* 46.2 (2007), pp. 189–194. ISSN: 1017-1398. DOI: 10.1007/s11075-007-9136-9.

[112] Per Christian Hansen. "Analysis of Discrete Ill-Posed Problems by Means of the L-Curve". In: *SIAM Review* 34.4 (1992), pp. 561–580. DOI: 10.1137/1034115. eprint: http://dx.doi.org/10.1137/1034115. URL: http://dx.doi.org/10.1137/1034115.

[113] PerChristian Hansen. "The discrete picard condition for discrete ill-posed problems". English. In: *BIT Numerical Mathematics* 30.4 (1990), pp. 658–672. ISSN: 0006-3835. DOI: 10.1007/BF01933214. URL: http://dx.doi.org/10.1007/BF01933214.

[114] P. C. Hansen. "The L-Curve and its Use in the Numerical Treatment of Inverse Problems". In: *in Computational Inverse Problems in Electrocardiology, ed. P. Johnston, Advances in Computational Bioengineering*. WIT Press, 2000, pp. 119–142.

[115] M. Asakawa, T. Hatsuda, and Y. Nakahara. "Maximum entropy analysis of the spectral functions in lattice QCD". In: *Prog. Part. Nucl. Phys.* 46 (2001), pp. 459–508. DOI: 10.1016/S0146-6410(01)00150-8. arXiv: hep-lat/0011040 [hep-lat].

[116] Gert Aarts et al. "Spectral functions at small energies and the electrical conductivity in hot, quenched lattice QCD". In: *Phys. Rev. Lett.* 99 (2007), p. 022002. DOI: 10.1103/PhysRevLett.99.022002. arXiv: hep-lat/0703008 [HEP-LAT].

[117] Yannis Burnier and Alexander Rothkopf. "Bayesian Approach to Spectral Function Reconstruction for Euclidean Quantum Field Theories". In: *Phys. Rev. Lett.* 111 (2013), p. 182003. DOI: 10.1103/PhysRevLett.111.182003. arXiv: 1307.6106 [hep-lat].

[118] Alexander Rothkopf. "Improved Maximum Entropy Method with an Extended Search Space". In: *PoS* LATTICE2012 (2012), p. 100. arXiv: 1208.5162 [physics.comp-ph].

[119] H. T. Ding et al. "Charmonium properties in hot quenched lattice QCD". In: *Phys. Rev.* D86 (2012), p. 014509. DOI: 10.1103/PhysRevD.86.014509. arXiv: 1204.4945 [hep-lat].

[120] Takashi Umeda. "Study of constant mode in charmonium correlators at finite temperature". In: *PoS* LAT2007 (2007), p. 233. arXiv: 0710.0204 [hep-lat].

[121] P. Petreczky. "On temperature dependence of quarkonium correlators". In: *Eur. Phys. J.* C62 (2009), pp. 85–93. DOI: 10.1140/epjc/s10052-009-0942-1. arXiv: 0810.0258 [hep-lat].

[122] Saumen Datta et al. "Behavior of charmonium systems after deconfinement". In: *Phys. Rev. D* 69 (9 2004), p. 094507. DOI: 10.1103/PhysRevD.69.094507. URL: http://link.aps.org/doi/10.1103/PhysRevD.69.094507.

[123] A. Jakovác et al. "Quarkonium correlators and spectral functions at zero and finite temperature". In: *Phys. Rev. D* 75 (1 2007), p. 014506. DOI: 10.1103/PhysRevD.75.014506. URL: http://link.aps.org/doi/10.1103/PhysRevD.75.014506.

[124] H. Ohno et al. "Charmonium spectral functions with the variational method in zero and finite temperature lattice QCD". In: *Phys. Rev.* D84 (2011), p. 094504. DOI: 10.1103/PhysRevD.84.094504. arXiv: 1104.3384 [hep-lat].

[125] P. Petreczky et al. "Charmonium at finite temperature". In: *Nucl. Phys. Proc. Suppl.* 129 (2004). [,596(2003)], pp. 596–598. DOI: 10.1016/S0920-5632(03)02653-7. arXiv: hep-lat/0309012 [hep-lat].

[126] H. Ohno, H. T. Ding, and O. Kaczmarek. "Quark mass dependence of quarkonium properties at finite temperature". In: *PoS* LATTICE2014 (2014), p. 219. arXiv: 1412.6594 [hep-lat].

[127] Wojciech Florkowski and Bengt L Friman. "Spatial dependence of meson correlation functions at high temperature". In: *Zeitschrift für Physik A Hadrons and Nuclei* 347.4 (1994), pp. 271–276.

[128] G. Backus and F. Gilbert. "The Resolving Power of Gross Earth Data". In: *Geophysical Journal* 16 (Oct. 1968), pp. 169–205. DOI: 10.1111/j.1365-246X.1968.tb00216.x.

[129] T. J. Loredo and R. I. Epstein. "Analyzing gamma-ray burst spectral data". In: *APJ* 336 (Jan. 1989), pp. 896–919. DOI: 10.1086/167060.

[130] Maarten F. L. Golterman and Jan Smit. "Selfenergy and Flavor Interpretation of Staggered Fermions". In: *Nucl. Phys.* B245 (1984), p. 61. DOI: 10.1016/0550-3213(84)90424-3.

[131] A. Bazavov et al. "Fluctuations and Correlations of net baryon number, electric charge, and strangeness: A comparison of lattice QCD results with the hadron resonance gas model". In: *Phys. Rev.* D86 (2012), p. 034509. DOI: 10.1103/PhysRevD.86.034509. arXiv: 1203.0784 [hep-lat].

[132] M. Cheng et al. "Equation of State for physical quark masses". In: *Phys. Rev.* D81 (2010), p. 054504. DOI: 10.1103/PhysRevD.81.054504. arXiv: 0911.2215 [hep-lat].

[133] Susumu Okubo. "Note on unitary symmetry in strong interactions". In: *Prog. Theor. Phys.* 27 (1962), pp. 949–966. DOI: 10.1143/PTP.27.949.

[134] H. Leutwyler. "Principles of chiral perturbation theory". In: *Hadrons 94 Workshop Gramado, Brazil, April 10-14, 1994*. 1994, pp. 1–46. arXiv: hep-ph/9406283 [hep-ph]. URL: http://inspirehep.net/record/374074/files/arXiv:hep-ph_9406283.pdf.

[135] A. Bazavov et al. "The melting and abundance of open charm hadrons". In: *Phys. Lett.* B737 (2014), pp. 210–215. DOI: 10.1016/j.physletb.2014.08.034. arXiv: 1404.4043 [hep-lat].

[136] M. Cheng et al. "Meson screening masses from lattice QCD with two light and the strange quark". In: *Eur. Phys. J.* C71 (2011), p. 1564. DOI: 10.1140/epjc/s10052-011-1564-y. arXiv: 1010.1216 [hep-lat].

[137] Hideaki Iida, Yu Maezawa, and Koichi Yazaki. "Hadron properties at finite temperature and density with two-flavor Wilson fermions". In: *PoS* LATTICE2010 (2010), p. 189. arXiv: 1012.2044 [hep-lat].

[138] Gert Aarts et al. "Charmonium at high temperature in two-flavor QCD". In: *Phys. Rev.* D76 (2007), p. 094513. DOI: 10.1103/PhysRevD.76.094513. arXiv: 0705.2198 [hep-lat].

[139] Szabolcs Borsanyi et al. "Charmonium spectral functions from 2+1 flavour lattice QCD". In: *JHEP* 04 (2014), p. 132. DOI: 10.1007/JHEP04(2014)132. arXiv: 1401.5940 [hep-lat].

[140] Szabolcs Borsányi et al. "Spectral functions of charmonium with 2+1 flavours of dynamical quarks". In: *PoS* LATTICE2014 (2015), p. 218. arXiv: 1410.7443 [hep-lat].

[141] Philipp Gubler, Kenji Morita, and Makoto Oka. "Charmonium spectra at finite temperature from QCD sum rules with the maximum entropy method". In: *Phys. Rev. Lett.* 107 (2011), p. 092003. DOI: 10.1103/PhysRevLett.107.092003. arXiv: 1104.4436 [hep-ph].

[142] Heng-Tong Ding, Olaf Kaczmarek, and Florian Meyer. *Thermal dilepton rates and electrical conductivity of QGP from the lattice*. ... to appear, 2016.

[143] Jacopo Ghiglieri et al. *Lattice constraints on the thermal photon rate.* ... to appear, 2016.

[144] M. Müller. "Meson correlations and spectral functions in the deconfined phase". PhD thesis. Bielefeld University, 2013.

[145] H.-T. Ding et al. "Thermal dilepton rate and electrical conductivity: An analysis of vector current correlation functions in quenched lattice QCD". In: *Phys.Rev.* D83 (2011), p. 034504. DOI: 10.1103/PhysRevD.83.034504. arXiv: 1012.4963 [hep-lat].

[146] Stephan Durr et al. "Precision study of the SU(3) topological susceptibility in the continuum". In: *JHEP* 04 (2007), p. 055. DOI: 10.1088/1126-6708/2007/04/055. arXiv: hep-lat/0612021 [hep-lat].

[147] B. Beinlich et al. "String tension and thermodynamics with tree level and tadpole improved actions". In: *Eur. Phys. J.* C6 (1999), pp. 133–140. DOI: 10.1007/s100520050326. arXiv: hep-lat/9707023 [hep-lat].

[148] Alessandro Amato et al. "Electrical conductivity of the quark-gluon plasma across the deconfinement transition". In: *Phys.Rev.Lett.* 111.17 (2013), p. 172001. DOI: 10.1103/PhysRevLett.111.172001. arXiv: 1307.6763 [hep-lat].

[149] Bastian B. Brandt et al. "Thermal Correlators in the ρ channel of two-flavor QCD". In: *JHEP* 1303 (2013), p. 100. DOI: 10.1007/JHEP03(2013)100. arXiv: 1212.4200 [hep-lat].

[150] Carsten Greiner et al. "Low Mass Dilepton Rate from the Deconfined Phase". In: *Phys.Rev.* C83 (2011), p. 014908. DOI: 10.1103/PhysRevC.83.014908. arXiv: 1010.2169 [hep-ph].

[151] Bastian B. Brandt et al. "Pion quasiparticle in the low-temperature phase of QCD". In: *Phys. Rev.* D92.9 (2015), p. 094510. DOI: 10.1103/PhysRevD.92.094510. arXiv: 1506.05732 [hep-lat].

[152] Bastian B. Brandt et al. "Charge transport and vector meson dissociation across the thermal phase transition in lattice QCD with two light quark flavors". In: (2015). arXiv: 1512.07249 [hep-lat].

Acknowledgments

A good third of my life I have spent at Bielefeld University. That leaves a lot of people to say 'thank you' to:

- Thanks to the (former and current) members of the Lattice group in Bielefeld, and to the people at BNL and in Wuhan,
- Thanks Prof. Laermann, for accompanying me for almost my whole academic life,
- Olaf for fruitful discussions and giving me the possibility to learn all that I know today,
- Christian, for answering all my questions about physics and supercomputers,
- Thank you, thank you, thank you Gudrun and Susi for all that you have done for me!
- Many, many thanks go to the DAAD, who enabled me to go to China.
- Thank you Heng-Tong, it was a great time, in every respect!
- Thanks to all the students, postdocs and professors there! You made me feel like home.

And what would a Bachelor/Master/PhD student be without fellow students? Thanks to all the people who have come, or gone, or both, and made being a student in Bielefeld such a great experience!

- Thanks Andi, Flomo, Johannes, Jonas, Matthi, Rebe, Rene, Stephan, Vanessa, Verena and Victor for the good start.
- Thanks Ioan, Nirupam and Sama for coffee breaks.
- Thanks Daniel, Isabel, Song, Thomas, for discussions at lunch!

Last but not least, I would like to thank my whole family, without whom I never could have done all this, thank Adam and Marcel for a long time, and thank my wife Gudrun, who is always there for me. Te iubesc, Luceafarul meu!

Disclaimer

I hereby declare that the work done in this dissertation is that of the author alone with the help of no more than the mentioned literature and auxiliary means.

Bielefeld, 2016/02/26

_____

Florian Meyer